Institute for Earth and Environmental Sciences
Geoscience

Earthquake-induced landsliding: Earthquakes as erosional agents across timescales

Kumulative Dissertation
zur Erlangung des akademischen Grades
"doctor rerum naturalium"
(Dr. rer. nat.)
in der Wissenschaftsdisziplin Geomorphologie

eingereicht an der
Mathematisch-Naturwissenschaftlichen Fakultät
der Universität Potsdam

Odin MARC

Potsdam, den 1st of Oktober 2016

Published online at the
Institutional Repository of the University of Potsdam:
URN urn:nbn:de:kobv:517-opus4-96808
http://nbn-resolving.de/urn:nbn:de:kobv:517-opus4-96808

Acknowledgments

There are many individuals that have contributed to make the years I spent in Potsdam doing my PhD a rich and very enjoyable experience.

First of all I am very grateful to my supervisor Niels Hovius, that I have been really lucky to meet. More than a great scientist he has been an unexpected source of inspiration on many other aspects, providing me with opinions and advices on many more issues than the "narrow" topic with which this dissertation is concerned.

Then I want to thank Patrick Meunier, that has also been key in defining and completing many of the scientific objectives of this thesis. I have appreciated very much its wide curiosity and knowledge in natural and social science, and especially in physics and philosophy, that has fuelled many discussions in or out of the office. He also turned out to be more than an good advisor and I am grateful about that.

I also want to thank to Christoph Sens-Schönfelder, with who I learnt a lot about ambient noise seismology and rock "healing", and all my other co-authors, Taro Uchida, Shin-Ichiro Hayashi, Tolga Gorum, Mako Ohzono, Ya-Ju Hsu, Kaoru Sawazaki, Manuel Hobiger. They were all essential to the completion of the work I am presenting here.

I am also very thankful to the extremely rich scientific atmosphere of the geomohphology section 5.1 of the GFZ, with its extremely diverse skills and visions on the science they do, but a very collaborative and friendly atmosphere. Thanks a lot to Jens, Micha, Kristen, Arnaud, Anne, Taylor, Dirk and Christoff.

I also want to thanks the PhD student that I met here, especially Rob Emberson and Antonius Golly, with who I shared office, and therefore many enjoyable tips, discussions and debates, fieldtrips, and occasionally beds or tents. Thanks also to the younger PhD students that actually "rejuvenated" the group, Steffi, David and Johanna.

My PhD was not quite focussed on field works, but I have been very pleased to join many field campaigns where I gained a lot of experience and knowledge as well as friendship and memories. Many thanks to Christoff Andermann for introducing me to Nepal and the fascinating Himalayas, to Bhairab Sitaula for being much more than a guide in Nepal, to Taro Uchida and Hayashi Shin-Ichiro that organized my stay and work in Japan and gave me so much insights on the life and culture of this amazing

country, to Arnaud Burtin and its seismometers in ever more remote places, to Kristen Cook for her knowledge of Taiwan and her skills at pilotting drones, and to all the other "unfortunate" members of the landslide grain size counting team, Patrick, Anne, Jens, Arnaud, and Antonius.

Thank you Ananda, for being present, even through the distance.

Finally, I am also grateful for the EU Marie-Curie ITN fellowship TOPOMOD, that basically funded my work at the GFZ, and additionally gave me several opportunities to meet other students and research teams within this European network. Thanks to all the other TOPOMOD PhD, Post-docs and PI for the broad ranging discussions, field trips and other sources of fun.

Contents

Contents v

List of Figures ix

List of Tables xii

Abstract xiii

Zusammenfassung xv

1 Introduction 1

1.1 Erosion, climate and tectonics . . . 1

1.2 Landslide processes . . . 3

1.2.1 Theoretical and empirical understanding . . . 3

1.2.2 Landslide role in steep terrain . . . 6

1.3 Earthquake processes . . . 7

1.3.1 Fault and earthquakes . . . 8

1.3.2 Seismic waves and ground shaking . . . 9

1.4 Earthquake-induced landslides . . . 10

1.5 Main questions and outline . . . 13

1.6 Author's contribution and publications . . . 15

2 Amalgamation in landslide maps: effects and automatic detection 17

2.1 Introduction . . . 18

2.2 Landslide Mapping and Amalgamation . . . 20

2.3 Data . . . 21

2.4 Quantifying effects of amalgamation . . . 22

2.5 Automatic detection of amalgamation . . . 25
2.6 Discussion . . . 28
2.7 Conclusion . . . 31

Link **33**

3 A seismologically-consistent expression for the total area and volume of earthquake-triggered landsliding. **35**
3.1 Introduction . . . 37
3.2 Data and Methods . . . 38
3.2.1 Earthquake and Landslide Data . . . 38
3.2.2 Estimation of Total Landslide Volume . . . 40
3.2.3 Case Specific Corrections . . . 42
3.3 Modeling the Volume of Seismically Induced Landslides . . . 42
3.3.1 Model development . . . 44
3.3.2 Assumptions and Their Consequences . . . 48
3.3.3 Model Uncertainties . . . 51
3.4 Landscape Sensitivity . . . 51
3.4.1 Topographic Steepness . . . 51
3.4.2 Prediction of Total Area . . . 53
3.5 Discussion . . . 55
3.5.1 Strength and Limitations of our Prediction . . . 55
3.5.2 Application to Earthquake Scenarios . . . 63
3.6 Conclusion . . . 64
3.7 Supplementary materials to Chapter 3 . . . 66

Link **85**

4 Transient changes of landslide rates after earthquakes. **87**
4.1 Introduction . . . 88
4.2 Cases, data and methods . . . 88
4.3 Precipitation variability and landsliding . . . 89
4.4 Enhanced post-seismic landsliding . . . 90
4.5 Temporary substrate weakening . . . 92

4.6 Conclusion . . . 94
4.7 Supplementary materials to Chapter 4 . . . 96
4.7.1 Landslide mapping . . . 96
4.7.2 Landslide volume computation . . . 96
4.7.3 Climatic forcing . . . 97
4.7.4 Landslide statistics and probability density function . . . 98

Link **103**

5 Co-evolution of shallow seismic velocity changes and landslide rates after earthquakes. **105**
5.1 Introduction . . . 106
5.2 Cases, data and methods . . . 106
5.3 Results . . . 107
5.4 Discussion . . . 109
5.5 Conclusion . . . 111
5.6 Supplementary materials to Chapter 5 . . . 112
5.6.1 Supplementary methods . . . 112

Link **123**

6 The mass balance of earthquakes and earthquake sequences. **125**
6.1 Introduction . . . 126
6.2 Methods . . . 127
6.2.1 Uplift Modeling . . . 127
6.2.2 Landslide Modeling . . . 127
6.3 Mass Balance of single earthquakes . . . 128
6.4 Mass balance of earthquake sequences . . . 130
6.5 Long-term Mass balance of faults . . . 131
6.6 Discussion and conclusions . . . 132
6.7 Supplementary materials to Chapter 6 . . . 135
6.7.1 Supplementary methods . . . 135

7 Conclusions **138**

8 Synthesis **142**

8.1 Discussion . . . 142

8.1.1 Coseismic landsliding . . . 142

8.1.2 Bedrock fracturing and earthquake strong-motion . . . 143

8.1.3 Earthquake mass balance . . . 144

8.1.4 Landslide hazard . . . 145

8.2 Future work . . . 146

8.2.1 Automatic mapping of individual landslides . . . 146

8.2.2 Quantification of rock strength . . . 146

8.2.3 Developing software for automatic earthquake-induced landsliding hazard assessment . . . 147

Bibliography **148**

List of Figures

1.1 Interactions between erosion, climate, and tectonics 2

1.2 Landslide area-volume scaling 4

1.3 Landslide frequency-size distributions 5

1.4 Behaviour of a threshold landscape 7

1.5 Scaling relationships for earthquake length and corner frequency 8

1.6 Empirical scaling of the total volume of earthquake-induced landslides with seismic moment 11

1.7 Post-earthquake increase and restauration of fluvial sediment transport 12

1.8 Mass balance of the 2008 Wenchuan earthquake 13

2.1 Amalgamation in the landslide inventory map of the 2008 Wenchuan earthquake 19

2.2 Examples of amalgamation in several inventories 19

2.3 Amalgamation effect on landslide area-frequency distributions. 24

2.4 Flowchart of the algorithm for automatic detection of amalgamation. . . 27

2.5 Example of automatic detection of amalgamation 29

3.1 Estimated total landslide volume for 40 earthquakes and comparison of empirical fit against moment and of our seismologically-consistent prediction 43

3.2 Conceptual sketch of the model and of the correction associated with flat topography 50

3.3 Probability distribution of local topographic slopes in the epicentral areas of the 11 earthquakes with comprehensive landslide inventories . . . 52

3.4 Total landslide volume prediction residuals against landscape modal slope 54

3.5 Total landslide area prediction and its dependency on modal slope, mean asperity depth and area-frequency distribution exponent 56

3.6 Predicted vs. estimated total landslide volume for 40 earthquakes 58

3.7 World map with the locations of the 40 shallow earthquakes considered in this study. . . . 76
3.8 Landsat image (February 1992) of the epicentral area of the 1991 Limon (Costa Rica) earthquake . . . 77
3.9 Landslide volume density as a function of the horizontal peak ground acceleration (normalized by $1g$) in the Chi-Chi epicentral area . . . 78
3.10 Sensitivity analysis of the seismologically-consistent expression for total landslide volume . . . 79
3.11 Same as figure 3.3 of the main text but for the areas of the 29 earthquakes in our compilation for which we do not have comprehensive landslide maps. . . . 80
3.12 Model residuals against all input parameters . . . 81
3.13 Model residuals for different source term frequencies . . . 82
3.14 Estimated against predicted of total landslide volume when source depth is the hypocentral depth . . . 82
3.15 Estimated against predicted of total landslide volume when normal faults produce as much shaking as reverse faults . . . 83
3.16 Landslide area-frequency distribution for our 11 exhaustive inventories 84

4.1 Total landslide volume per unit mapped area against cumulative precipitation proxy, P, in the ChiChi (Taiwan) area . . . 90
4.2 Precipitation normalized landslide rate against time in the (A) Chi-Chi, Taiwan (B) Niigata, Japan (C) Finisterre, Papua New Guinea, and (D) Iwate, Japan, earthquake epicentral areas. . . . 91
4.3 Landslide area-frequency distributions for the background and post-seismic intervals . . . 94
4.4 Hydrograph from station 1510H049, on the Chenyoulan river, Choshui catchment, Taiwan . . . 100
4.5 Total landslide volume per unit area for each mapping interval plotted against the total rainfall during the same interval, in the epicentral areas of 3 intermediate earthquakes . . . 100
4.6 Recovery time estimated for the 4 studied earthquakes against their moment magnitude . . . 101
4.7 Normalized Difference Vegetation Index (NDVI) map derived from Landsat 5 imagery, before and after the Chi-Chi earthquake . . . 101
4.8 Time series of climate normalized landslide rate in (A) Number, (B) Area and (C) Volume . . . 102

5.1 Co-evolution of landslide rates, seismic velocity and GPS displacement in the epicentral area of the Chi-Chi (Taiwan) earthquake . . . 108

5.2 Co-evolution of landslide rates, seismic velocity and GPS displacement in the epicentral area of the Niigata and Iwate earthquakes, in Japan . . 108
5.3 Seismic velocity changes in Niigata epicentral area 115
5.4 Seismic velocity changes in Chi-Chi epicentral area 116
5.5 Seismic velocity changes in Iwate epicentral area 117
5.6 GPS displacements in Niigata epicentral area 118
5.7 GPS displacements in Chi-Chi epicentral area 119
5.8 GPS displacements in Iwate epicentral area 120
5.9 GPS displacements in Iwate epicentral area 121
5.10 Regional surface deformation in Chi-Chi epicentral area 122

6.1 Uplift and erosion caused by an earthquake above its causative fault . . 129
6.2 Mass balance of characteristic earthquake sequences for different scenarios 131
6.3 Mass balance of earthquake sequences following a Gutenberg-Richter distribution, for different scenarios 133

List of Tables

2.1 Confusion matrix of the algorithm for automatic detection of amalgamation 28

3.1 Data summary for published information about earthquake-induced landsliding 67

3.2 Summary of the methods used to estimate total landslide volume and its uncertainty from published information 74

4.1 Summary of the different images used to produce the landslide inventories 99

5.1 Summary of the relaxation times estimated for landsliding, seismic velocity and post-seismic displacement for three earthquakes 107

5.2 Summary of the relaxation time constants and confidence intervals for post seismic GPS displacement 114

Abstract

Earthquakes deform Earth's surface, building long-lasting topographic features and contributing to landscape and mountain formation. However, seismic waves produced by earthquakes may also destabilize hillslopes, leading to large amounts of soil and bedrock moving downslope. Moreover, static deformation and shaking are suspected to damage the surface bedrock and therefore alter its future properties, affecting hydrological and erosional dynamics. Thus, earthquakes participate both in mountain building and stimulate directly or indirectly their erosion. Moreover, the impact of earthquakes on hillslopes has important implications for the amount of sediment and organic matter delivered to rivers, and ultimately to oceans, during episodic catastrophic seismic crises, the magnitude of life and property losses associated with landsliding, the perturbation and recovery of landscape properties after shaking, and the long term topographic evolution of mountain belts. Several of these aspects have been addressed recently through individual case studies but additional data compilation as well as theoretical or numerical modelling are required to tackle these issues in a more systematic and rigorous manner.

This dissertation combines data compilation of earthquake characteristics, landslide mapping, and seismological data interpretation with physically-based modeling in order to address how earthquakes impact on erosional processes and landscape evolution. Over short time scales (10-100 s) and intermediate length scales (10 km), I have attempted to improve our understanding and ability to predict the amount of landslide debris triggered by seismic shaking in epicentral areas. Over long time scales (1-100 ky) and across a mountain belt (100 km) I have modeled the competition between erosional unloading and building of topography associated with earthquakes. Finally, over intermediate time scales (1-10 y) and at the hillslope scale (0.1-1 km) I have collected geomorphological and seismological data that highlight persistent effects of earthquakes on landscape properties and behaviour.

First, I compiled a database on earthquakes that produced significant landsliding, including an estimate of the total landslide volume and area, and earthquake characteristics such as seismic moment and source depth. A key issue is the accurate conversion of landslide maps into volume estimates. Therefore I also estimated how amalgamation - when mapping errors lead to the bundling of multiple landslide into a single polygon - affects volume estimates from various earthquake-induced landslide inventories and developed an algorithm to automatically detect this artifact. The database was used to test a physically-based prediction of the total landslide area and volume caused by earthquakes, based on seismological scaling relationships and a statistical

description of the landscape properties. The model outperforms empirical fits in accuracy, with 25 out of 40 cases well predicted, and allows interpretation of many outliers in physical terms. Apart from seismological complexities neglected by the model I found that exceptional rock strength properties or antecedent conditions may explain most outliers.

Second, I assessed the geomorphic effects of large earthquakes on landscape dynamics by surveying the temporal evolution of precipitation-normalized landslide rate. I found strongly elevated landslide rates following earthquakes that progressively recover over 1 to 4 years, indicating that regolith strength drops and recovers. The relaxation is clearly non-linear for at least one case, and does not seem to correlate with coseismic landslide reactivation, water table level increase or tree root-system recovery. I suggested that shallow bedrock is damaged by the earthquake and then heals on annual timescales. Such variations in ground strength must be translated into shallow subsurface seismic velocities that are increasingly surveyed with ambient seismic noise correlations. With seismic noise autocorrelation I computed the seismic velocity in the epicentral areas of three earthquakes where I constrained a change in landslide rate. We found similar recovery dynamics and timescales, suggesting that seismic noise correlation techniques could be further developed to meaningfully assess ground strength variations for landscape dynamics. These two measurements are also in good agreement with the temporal dynamics of post-seismic surface displacement measured by GPS. This correlation suggests that the surface healing mechanism may be driven by tectonic deformation, and that the surface regolith and fractured bedrock may behave as a granular media that slowly compacts as it is sheared or vibrated.

Last, I compared our model of earthquake-induced landsliding with a standard formulation of surface deformation caused by earthquakes to understand which parameters govern the competition between the building and destruction of topography caused by earthquakes. In contrast with previous studies I found that very large ($M_w > 8$) earthquakes always increase the average topography, whereas only intermediate ($M_w \sim 7$) earthquakes in steep landscapes may reduce topography. Moreover, I illustrated how the net effect of earthquakes varies with depth or landscape steepness implying a complex and ambivalent role through the life of a mountain belt. Further I showed that faults producing a Gutenberg-Richter distribution of earthquake sizes, will limit topography over a larger range of fault sizes than faults producing repeated earthquakes with a characteristic size.

Zusammenfassung

Erdbeben gestalten die Erdoberfläche, sie tragen langfristig zum Aufbau von Topografie sowie zur Landschafts- und Gebirgsbildung bei. Die von Erdbeben erzeugten seismischen Erschütterungen können Gebirge jedoch auch destabilisieren und grosse Mengen an Boden sowie Grundgestein zum Abrutschen bringen und zerrüten. Erdbeben wirken daher sowohl auf die Gebirgsbildung als auch auf ihre Denudation. Ein detailliertes Verständnis der Auswirkungen von Erdbeben auf Hangstabilität ist eine wichtige Voraussetzung um die Zusammenhänge mit anderen Prozesse besser nachzuvollziehen: der kurzfristige Transport von Sedimenten und organischem Material in Flüsse und ihre Ablagerung bis in die Ozeane; der Verlust von Leben und Infrastruktur durch Hangrutschungen verbunden mit episodischen, katastrophalen, seismischen Ereignissen; die Störung und Wiederherstellung von Landschaftseigenschaften nach Erdbeben; sowie die langfristigen topographischen Entwicklung von ganzen Gebirgsketten. Einige dieser Forschungsfragen wurden kürzlich in einzelnen Fallstudien betrachtet aber zusätzliche Datenerfassung, theoretische und numerische Modellierung sind erforderlich, um diese Prozesse detaillierter zu erfassen.

In dieser Dissertation werden Daten zu Eigenschaften der Erdbeben sowie aus Hangrutsch kartierungen und die Interpretation seismologischer Daten mit physikalischer Modellierung kombiniert, um die folgende übergreifende Frage zu beantworten: Wie beeinflussen Erdbeben die Erosionsprozesse in der Landschaftsentwicklung? Auf einer kurzen Zeitskala (10-100 s) und einer mittleren räumlichen Skala (10 km), habe ich versucht sowohl unser Prozessverständnis zu vertiefen als auch Vorhersagen Ãijber das gesamte Volumen der Rutschungen welche durch seismische Beben in der unmittelbaren Umgebung von Epizentren ausgelöst wurden, zu treffen und zu verbessern Auf einer langen Zeitskala (1-100 ky) und über einen Gebirgsgürtel (100 km) habe ich die durch Erdbeben ausgelösten konkurrierenden Prozesse von Abflachung von Topografie durch Erosion und den Aufbau von Topografie durch Hebung, modelliert. Auf einer mittleren Zeitskala (1-10 Jahre) und einer relativ kleinen Hangskala (0,1-1 km) habe ich geomorphologische und seismologische Daten erhoben, welche die anhaltenden Auswirkungen von Erdbeben auf Landschaftseigenschaften und deren Dynamic hervorheben.
Zuerst habe ich eine Datenbank von Erdbeben erstellt, welche erhebliche Hangrutschungen ausgelöst hatten, einschliesslich einer Schätzung des gesamten Hangrutschungsvolumens und der Erdbebencharakteristiken wie z.B. seismischer Moment und Lage des Hypozentrums. Ich habe auch beurteilt, wie die Kartierung von Erdrutschen die Abschätzungen des Gesamtvolumens fehlerhaft beeinflussen können und prÃd'sentiere einen Algorithmus, um solche Fehler automatisch zu erkennen. Diese Datenbank

wurde verwendet, um eine physisch-basierte Vorhersage der durch Erdbeben verursachten gesamten Hangrutschungsflächen und Volumen zu testen, welche auf seismologischen Skalierungsbeziehungen und auf einer statistischen Beschreibung der Landschaftseigenschaften basiert.
Zweitens untersuchte ich den Einfluss von starken Erdbeben auf die Landschaftsdynamik durch das Vermessen der temporalen Entwicklung der Suszeptibilität von Hangrutschungen. Ich habe gezeigt, dass die stark erhöhte Hangrutschrate nach dem Erdbeben schrittweise nach einigen Jahren zurückging. Diesen Rückgang Ãijber die Zeit interpretiere ich als die Zerrüttung von oberflächennahem Gestein durch das Erdbeben und die Heilung der dadurch entstandenen Risse über der Zeit Meine Daten deuten darauf hin, dass die Zerrüttungen und die anschliessende Heilung des Festgesteins in dem epizentralen Gebieten mit ambienten, seismischen Hintergrundrauschen überwacht werden kann. Möglicherweise wird die Heilung zusätzlich durch andauernde post-seismische Deformation angetrieben.
Am Ende der Arbeit vergleiche ich meine entwickelten Modelle von erdbebenbedingten Hangrutschungen mit einer Standardformel für erdbebenverursachte Oberflächendeformierung. Mit diesem Vergleich zeige ich welche Parameter den Wettstreit zwischen der Hebung von Topografie und der gleichzeitigen Zerstörung von Topografie durch Erdbeben bestimmen. Ich zeige, dass nur mittlere - $M_w \sim 7$ - Erdbeben die Topografie reduzieren können im Gegensatz zu stärkeren - $M_w > 8$ - Beben die immer einen effektive Bildung von Topografie verursachen. Meine Ergebnisse zeigen die komplexen Zusammenhänge von Erdbeben in der Gebirgsbildung.

Chapter 1

Introduction

Earthquakes represent an iconic process of Earth sciences, both for the hazard they pose throughout the world and for their role in tectonic deformation. However, in steep terrain ground shaking associated with earthquakes may also trigger widespread landsliding. The detailed effects and implications of these earthquake-induced landslides on natural hazards and surface processes remain a challenging question that I have tried to address in this thesis. I am first introducing this topic within the broader context of research on interactions and feedbacks between tectonics, climate and erosion. Then, I review some important aspects of earthquake and landslide processes before focussing on the state of the art knowledge about earthquake-induced landsliding and presenting the current research questions that I address in this dissertation.

1.1 Erosion, climate and tectonics

Erosion is the sum of all physical and chemical processes redistributing mass at the surface of the Earth. It encompasses processes of weakening, wearing, dissolving or breaking rocks into mobile products, such as sediment or solutes, as well as processes transporting away from their source areas. Erosion agents are extremely varied and act on different scales, from the microscopic, root or microbial enhanced weathering (e.g., Bennett et al., 1996) to typhoon or earthquake-induced extensive landsliding on regional scales (e.g., Keefer, 1994). Among the most common and universal agents of erosion are hillslope processes, such as the various types of landslides, where gravity drives an unstable mass of material towards the valley bottom, and incising and transporting water bodies such as rivers and glaciers.

The evolution of landscapes is set by the competition between tectonic or non-tectonic forms of uplift (such as isostatic uplift) and erosion. In mountain belts tectonic activity can result in large, shallow earthquakes whereas older mountain belts or cratonic areas may rather be dominated by isostatic re-adjustment or dynamic topography supported by mantle convection (e.g., Braun, 2010). Although considered a major contributor of uplift (Avouac, 2007), earthquakes are not the only agents of tectonic uplift in active mountain belts, as diverse aseismic components of crustal deformation such as postseismic (e.g., Rousset et al., 2012) and interseismic (Grandin et al., 2012; Ching et al., 2011) deformation or creeping faults may also produce uplift.

The competition between surface uplift and erosion is further complicated by the nu-

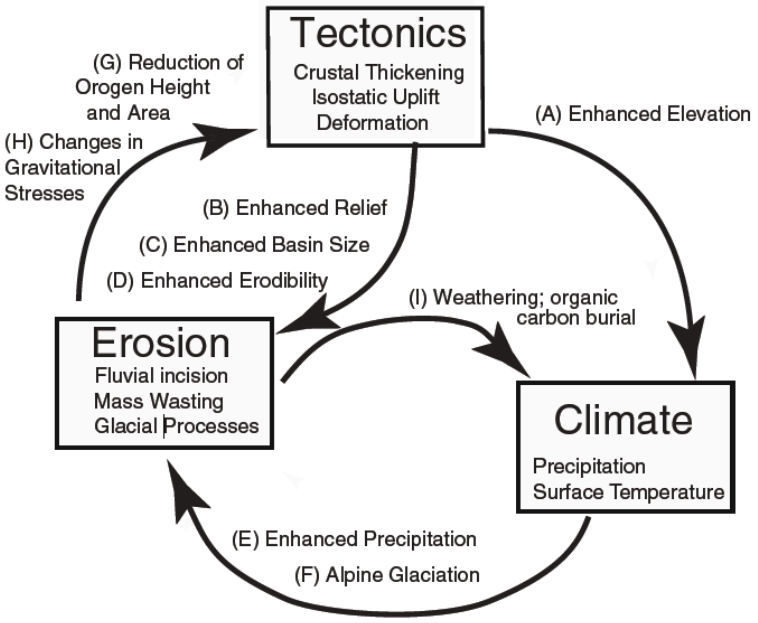

Figure 1.1 – Interactions and feedbacks pathways for tectonics, climate, and erosional processes. After Willett et al. (2006)

merous feedbacks existing between tectonics, erosion, and climate (Willett et al., 2006)(Figure 1.1). It has become clear that these three domains strongly influence each other but a lively debate is still ongoing about which is the dominant driver in each orogen and at which timescale. Below I present a non exhaustive overview of the multiple and complex processes that link climate, erosion and tectonics.

In many places, surface elevation is the long term product of uplift due to tectonic activity, and must be maintained in order to allow erosion to persist. From the early work of Ahnert (1970) the relation between topographic slope and erosion rate has been established. Further, a number of studies have observed and conceptually modeled a non linear relationship between slope and erosion (Granger et al., 1996; Montgomery and Brandon, 2002; Portenga and Bierman, 2011). Additionally, tectonic activity and deformation through faulting has been proposed as an important mechanism of rock-mass fracturing, decreasing rock strength and enhancing future erosion (Molnar et al., 2007). Moreover, seismic waves generated by earthquakes are an important trigger of earthquake-induced landslides (Keefer, 1994) that are important erosional agents in most steep mountain terrain (Hovius et al., 1997; Shroder, 1998).

In the opposite direction erosion may also affect and drive tectonic activity by changing the distribution of mass at the surface of the Earth and therefore the distribution of stress in the subsurface. This may lead to isostatic compensation producing uplift and focussing further erosion, as proposed in various models and as deduced from observations (Willett, 1999; Champagnac et al., 2012). At a more local scale erosional unloading can also change the stress on fault systems, possibly changing fault slip rate or loading state (Maniatis et al., 2009; Steer et al., 2014).

On the other hand, many of the most efficient agents of erosion are dependent on precipitation, whether rain or snow, and also on temperature. Variations of the amount of precipitation or in the frequency of intense storms may increase landslide occurence (Iverson, 2000; Dadson et al., 2003) and fluvial incision and transport (Hartshorn et al.,

2002; Stark et al., 2010). Some research suggests that glaciers may be the most efficient agent of erosion, responsible for a general increase in erosion rate with the onset of glaciation during the Pleistocene and able to durably limit maximum topography (Egholm et al., 2009; Herman et al., 2013). Many other processes are climate mediated and modulate erosion, such as freeze and thaw cycles weakening the rock (Walder and Hallet, 1985), or vegetation root-system enhancing ground cohesion (Sidle et al., 2006), and tighten the link between climate and erosion.
Erosion is thought to affect climate by modulating the atmospheric concentration of dioxide carbon. Silicate weathering may be a significant long term sink of CO_2 (Brady, 1991; Raymo and Ruddiman, 1992). Erosion can also harvest carbon fixed in organic matter and may remove it from the atmosphere if the organic matter bearing sediments are buried rapidly enough (cf., France-Lanord and Derry, 1997; Hilton et al., 2008, 2011a).
Finally on longer timescales, tectonics have direct influences on climate. Active volcanism releases large amounts of greenhouse gases affecting global temperature, while the formation of tall mountain belts such as the Andes or the Himalayas leads to orographic precipitation and regional changes in the atmospheric circulation (e.g., Insel et al., 2009; Barnes et al., 2012). Climate controls, at short and long timescales, from seasonal patterns to glaciation, the spatial distribution of water bodies weigh on the lithosphere, leading to a modulation of microseismicity or post-glacial rebound (e.g., Bollinger et al., 2007; Hampel et al., 2007).
One of the important challenges for deepening our understanding of these complex interactions is to go beyond gross characterization of the tectonic, climatic and erosional processes. Many initial insights were gained by reducing tectonic forcing to uplift and erosion to average lowering or river incision. Still, we need to describe and understand the individual processes performing tectonic and geomorphic work in order to constrain their interactions and feedbacks. Focussing on the coupling between tectonics and erosion, earthquake and landslides represent key processes of each domain, the role and characteristics of which need to be accounted for. In active mountain belts, a significant part of uplift is caused by earthquakes that also have a dynamic component, with seismic waves disturbing the landscape over very short time scales. In turn, erosion in steep terrain is strongly modulated by hillslope processes, and especially landslides, that are sensitive to the strong-motion caused by seismic waves (Meunier et al., 2007). These processes are major agents of the tectonic and erosional dynamics and it seems essential to focus on them and on the details of their interactions in order to understand the couplings and feedbacks existing between tectonics and erosion.

1.2 Landslide processes

1.2.1 Theoretical and empirical understanding

Research on landslide processes is broadly aimed at answering three types of questions that deal with their location and timing, their size, and their travel-path. Where, and how often, will landslides initiate? How large/deep will the area that fails be? How far will the mobilized material travel? The two first questions have important implications for the erosive action of landsliding and all are essential for natural hazard prevention. In the following I summarize our basic understanding of the landslide

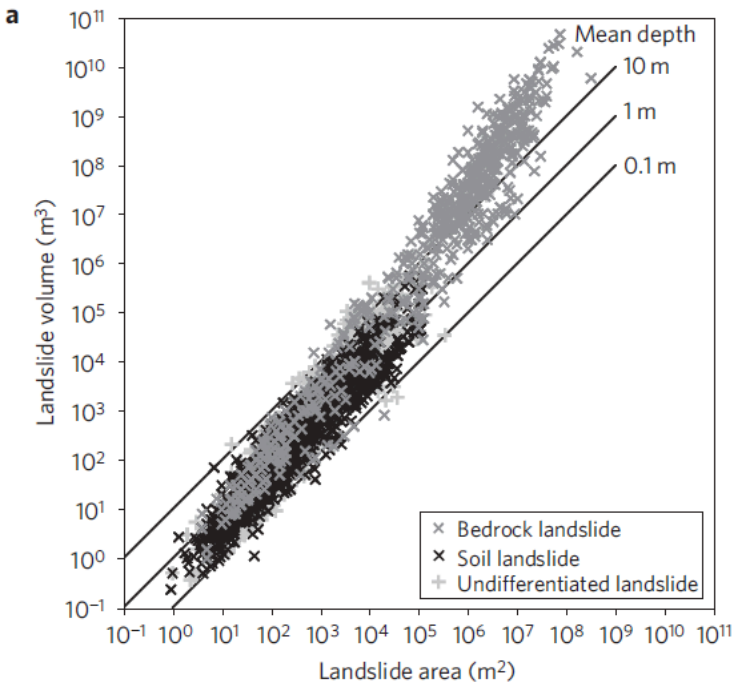

Figure 1.2 – Landslide volume against landslide area estimated for a compilation of more than 4000 landslides surveyed in the field. Soil, bedrock and undifferentiated landslides are plotted with different symbols and exhibit slightly different scaling. After Larsen et al. (2010)

processes relevant for these three questions.
The main theoretical framework used to understand landslide initiation is that of frictional theory, in which driving and resisting forces or moment are compared on a potential surface of failure (e.g., Newmark, 1965). The ratio of resisting and driving forces or stresses can be rewritten as a safety factor, FS, taking the following general form:

$$FS = \frac{\tan\phi(P-p)+Co}{\tau}, \tag{1.1}$$

with ϕ the friction angle of the material, P the pressure normal to the failure surface, p the water pore pressure, Co the cohesion of the material and τ the shear stress on the failure surface. P and τ are both the result of the projection of the weight of the mass on the slope of the failure surface. When the safety factor of a slope is greater than one it is theoretically stable whereas below one the slope is prone to failure. This simple expression allows understanding of how various processes affect landslide probability. Water infiltration changes the weight of the mass above the failure surface but also reduces the friction on it because the pore pressure increases, therefore leading to failure (Iverson, 2000). Cohesion may be increased by tree roots (Sidle et al., 2006) as well as by clay deposits (Selby, 1982), whereas processes fracturing the bedrock such as frost (Walder and Hallet, 1985) or ground shaking (Sleep, 2010) will reduce cohesion and enhance failure. Seismic waves also add transient stresses that may repeatedly reduce the FS by increasing τ or opposing P until failure (Newmark, 1965). Safety factor analysis is widely used both for rain-triggered landslides and earthquake-induced landslides (e.g., Wu and Sidle, 1995; Shou and Wang, 2003; Gorsevski et al., 2006; Baum et al., 2010) but lacks a physical description of the mechanical processes at play when a rupture initiates (Stark and Guzzetti, 2009), whether it is fracturing and crack propagation

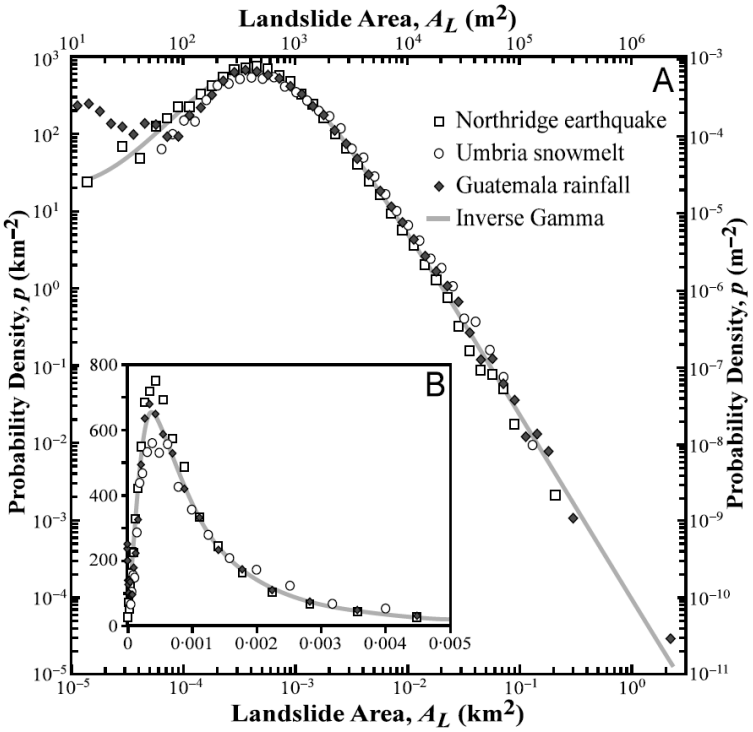

Figure 1.3 – Dependence of landslide probability density on landslide area, for three landslide inventories caused by: the 1994 Northridge (California) earthquake, heavy rainfall in Guatemala and snowmelt in Umbria (Italy). Note that in spite of the different triggers and affected regions the three inventories are very similar and can be fit with a single inverse gamma distribution. After Malamud et al. (2004a)

within bedrock or plastic deformation in soil.
More exhaustive description of the physical process may be found in recent numerical simulations. However, they are limited to case studies because they require very detailed information about the structure and geotechnical properties and are computationally expensive. Therefore, our understanding of landsliding at the landscape scale, whether due to large triggering events or integrated over a longer period, is mostly empirical. Two important empirical scaling relationships for landslides have emerged out of a number of studies. The first one is the relation between landslide area and volume or area and mean depth (Figure 1.2), observed across many orders of magnitude (e.g., Guzzetti et al., 2009a; Larsen et al., 2010) and apparently valid for subaerial and submarine landslides (ten Brink et al., 2006). This scaling must in part relate to the mechanical properties of the substrate, and it has been inferred that the soil thickness constrains the area-volume scaling for shallow landslides (Larsen et al., 2010). In parallel, the scaling between landslide size and frequency has been shown to be a power-law with a roll-over at the mode of the distribution (e.g., Hovius et al., 1997; Brardinoni and Church, 2004; Malamud et al., 2004a; ten Brink et al., 2006). As for the volume area scaling, such distributions seem to hold for every type of landsliding and trigger (Figure 1.3). In detail, models, experiments and observations have tried to relate the power-law scaling exponent to physical parameters, such as the material strength and cohesion (Densmore et al., 1998; Stark and Guzzetti, 2009; Frattini and Crosta, 2013; Gallen et al., 2015), to the geometry or level of heterogeneity of the material (Katz and Aharonov, 2006; Brunetti et al., 2009) or to the moisture distribution in a landscape

(Pelletier et al., 1997). Though the roll-over may be due to the impossibility to detect smaller landslides with low resolution imagery (Stark and Hovius, 2001), it may also persist for exhaustive catalogues and has been interpreted to result from a mechanical transition, whether a strength increase or a change in heterogeneity, going from the soil layer to shallow bedrock (Katz and Aharonov, 2006; Stark and Guzzetti, 2009; Frattini and Crosta, 2013). The most recent models (e.g., Stark and Guzzetti, 2009; Frattini and Crosta, 2013) are converging somewhat but still give different quantitative solutions. Additionally, mapping errors or incompleteness are frequent, rendering uncertain any attempt to deduce local rock properties from landslide inventories. The forward problem of anticipating the frequency distribution of landslide sizes is equally difficult. Theoretical progress together with efforts to find new ways to estimate and monitor slope properties, such as friction and cohesion or pore pressure, at a meaningful scale, are long term objectives to better understand and predict landslide occurence and size. After landslide initiation a phase of downslope movement occurs until deposition in a river channel or on a less steep slope. The distance from the landslide initiation point to its deposition area may be called the runout length and is of primary interest in the field of natural hazards. Indeed some large landslides have been observed to have extremely long runout and to cause significant property and human loss (e.g., Evans et al., 2009; Iverson et al., 2015). Various theories and observations have been gathered to understand the processes at play within this mobile phase, such as flash-heating, air cushions or fragmentation energy (cf., Legros, 2002; Staron and Lajeunesse, 2009; Lucas et al., 2014). Further research to understand landslide initiation, size and mobility is not only important to mitigate natural hazards, but also because landslides have been recognized as a key erosion agent in steep terrain.

1.2.2 Landslide role in steep terrain

Over the past two decades many mountain belts have been described as threshold landscapes - i.e., landscapes with steady-state topography in which the hillslopes have reached their maximal slope or relief - and therefore display relatively stable slope distribution across large variations of erosion or uplift rate (Burbank et al., 1996). Such landscapes are considered to have attained a critical slope, set by large scale bedrock strength (Schmidt and Montgomery, 1995), and therefore to respond with increased frequency of landsliding to any increase in uplift rate or river incision rate (Burbank et al., 1996; Montgomery and Brandon, 2002; Larsen and Montgomery, 2012) (Figure 1.4). The few studies that have investigated this, have confirmed that landslide and uplift rates are spatially correlated and that lithology and rock strength have a detectable topographic fingerprint (Korup, 2008; Korup and Schlunegger, 2009; Larsen and Montgomery, 2012). More recent analysis with very high resolution topographic data obtained by Lidar has suggested more complex variations between topographic indices, such as mean slope or skewness, and erosion rates, highlighting the need for better process scale understanding of hillslope erosion in threshold landscapes (DiBiase et al., 2012).
Nevertheless, the dominant role of bedrock landsliding in threshold landscapes is consistent with several studies that found that erosion attributed to landsliding seemed to match mean catchment denudation rates (Hovius et al., 1997, 2000; Gallo and Lavé, 2014). The predominance of landslides as a sediment source has also been found in some less steep catchments dominated by slow moving landslides (Mackey and Roer-

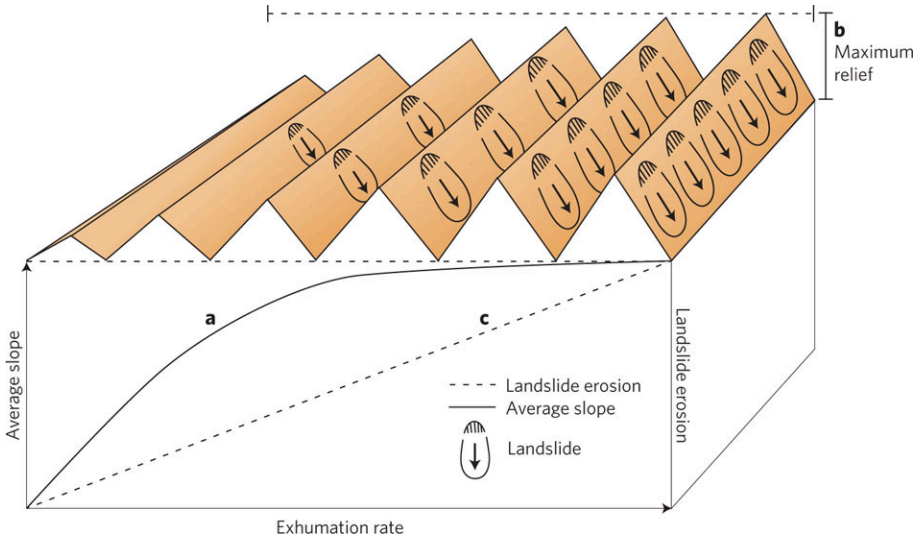

Figure 1.4 – Sketch of a landscape evolving from low angle hillslope to threshold hillslopes. As uplift rates increase (a), the relief of the mountain range will rise, but only up to a certain point (b). This upper limit to topographic development is commonly attributed to the attainment of a threshold hillslope, beyond which landslide erosion (c) will keep pace with uplift and stream incision, limiting the height of the mountain range. After Roering (2012).

ing, 2011). Landslides are also important in the way they affect river channels, by delivering large amounts of sediment that impede bedrock incision or dam the channel for long timescales (Lague, 2010; Korup et al., 2010; Yanites et al., 2010) or by shaping incipient drainage networks (Hovius et al., 1998).
We have seen that landsliding may be one of the dominant players of erosion in the steep, bedrock dominated landscapes that are typical of many active mountain belts. Catastrophic landsliding may happen without obvious triggers but the two most common triggers of landsliding are rainstorms and earthquakes. Though earthquakes are much less frequent than storms, they exert a spectacular forcing on hillslopes that can lead to tens of thousands of slope failures and the mobilization of very large volumes of debris (Keefer, 1994, 1984). Therefore, earthquakes are an outstanding and direct link between tectonic and erosional processes, but with a still unquantified contribution to the long term erosion budget of a mountain belt.

1.3 Earthquake processes

A review of fault and earthquake mechanics is outside the scope of this thesis. Instead, this section aims to summarize some of the basic facts and theories used to describe earthquakes and seismic waves responsible for the ground shaking. Ground shaking is essentially the convolution of a source term, a wave travel term and a site term. First, I review some essential aspects of fault rupture during earthquakes that define the source term, and then I discuss how travel and site effects modulate the seismic wave amplitude and associated ground shaking.

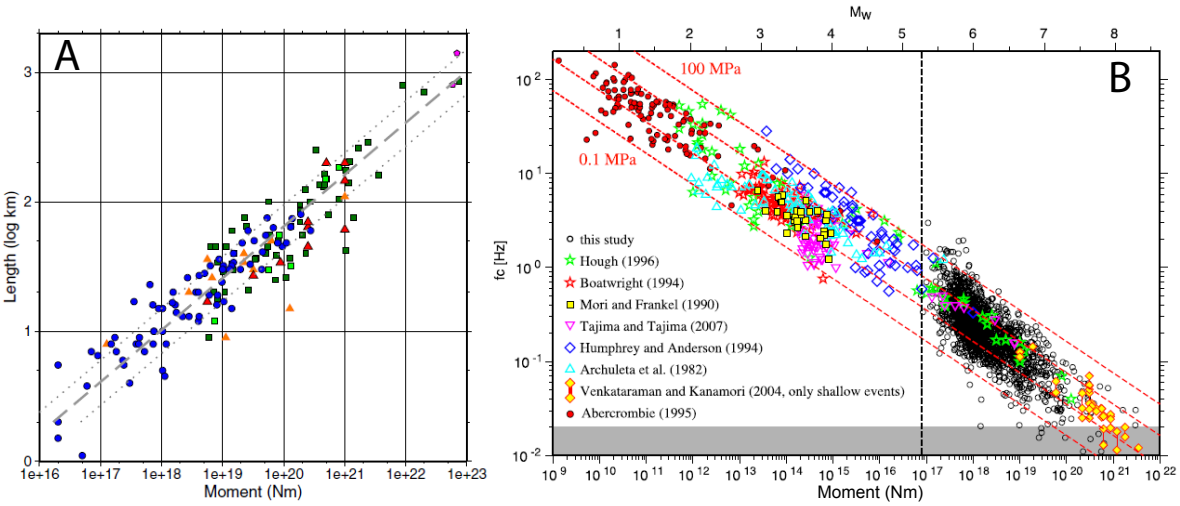

Figure 1.5 – Scaling relationships for earthquake length and corner-frequency. A: fault length against seismic moment for dip-slip earthquakes, with a model with a 2/5 scaling exponent and its 1σ uncertainties shown as dashed and dotted lines. From Leonard (2010). B: Corner frequency against seismic moment and moment magnitude, after Allmann and Shearer (2009). The dashed lines show constant stress drops of 0.1, 1, 10, and 100 MPa. The gray shaded area shows the resolution limit of the data. The vertical dashed line marks the lower magnitude cutoff of the data.

1.3.1 Fault and earthquakes

Earthquakes can be explained as the sudden release of elastic strain that has accumulated on faults due to regional crustal shearing motions. The faults are considered quasiplanar breaks in the rock that are relatively weak due to repeated motion, and therefore prone to the localization of displacement during earthquakes. When strain reaches a threshold, best-described as a Coulomb failure criterion, abrupt frictional sliding occurs, releasing energy through heating and fracturing of the rocks as well as seismic waves. Importantly, once sliding starts, the friction on the fault plane is reduced to a dynamic friction coefficient, lower than the pre-failure static one, promoting the acceleration of the rupture and the occurence of an earthquake instead of stable sliding. As long as regional deformation continues, the cycle of fault loading and rupture may repeat many times over the active life-time of the fault.
Important scaling relations exist between, fault dimensions earthquakes and energy release. The seismic moment, Mo, that is the total energy released by an earthquakes can be linearly related to the mean static displacement, $\bar{D}$, averaged over the fault area, A, with:

$$Mo = \mu A \bar{D} = \mu L W \bar{D} \tag{1.2}$$

with μ the shear modulus of the crust, and L and W the length and width of a simplified rectangular fault. Observations of aftershock distributions have allowed to constrain fault plane sizes revealing robust power-law scaling between Mo and L, W and $\bar{D}$ (Scholz, 1982; Leonard, 2010). These scalings have important implications for the static stress drop, $\Delta\sigma$, that is the difference between pre- and post-failure stress averaged over the ruptured fault. This stress drop is proportional to the ratio between $\bar{D}$ and the characteristic rupture dimension, that is L or W. Scaling between $\bar{D}$ and L and W suggests that the stress drop is independent of the moment (Leonard, 2010). This

is consistent with stress drop catalogues based on seismic measurements of the corner frequency of the seismic source emission spectra, that report a median stress drop of about 5 MPa for a very large range of moment (Allmann and Shearer, 2009; Leonard, 2010; Baltay et al., 2011). Stress drop is an important seismic source parameter because, through a simplified crack model, it can be related to the emission spectra of seismic waves and therefore to ground shaking (Brune, 1970; Hanks and McGuire, 1981; Baltay and Hanks, 2014). Beyond the source term, the effects along the wave path and at the sites are essential to understand ground shaking, and this is discussed next.

1.3.2 Seismic waves and ground shaking

During wave propagation, elastic energy is reduced because of both geometric spreading and attenuation. Geometric spreading simply reflects the fact that, as a wave is travelling away from its source, the wave front is expanding, and the energy associated with the wave in a given point of this wave front must be reduced to conserve the total energy (Wallace and Lay, 1995). This is purely geometric and for body waves that travel away from a point source, the energy is distributed at the surface of a sphere, meaning that the energy density decay is proportional to $1/R^2$, where R is the distance of travel from source to site. In contrast, surface waves, that are conducted within a shallow layer close of the surface, that is an expanding cylinder, have an energy decay following $1/R$. As the wave amplitude scales with the square root of the energy, the amplitude decay due to the spreading of body waves and surface waves follows $1/R$ and $1/R^{1/2}$, respectively (Wallace and Lay, 1995). Further, the wave amplitude is reduced by inelastic attenuation, due to energy loss through heat or damage of the medium during each cycle, and by scattering of waves on discontinuities that reflect and refract them, splitting the energy into different waves (Wallace and Lay, 1995). These processes are complex and often described through an exponential decay of the amplitude with distance. Importantly, these processes are strongly frequency dependent, as higher frequency waves perform more cycles for a given travel distance and interact with smaller, more frequent, discontinuities. This means that high frequency waves (i.e., $> 10Hz$) are attenuated to very small amplitudes and accelerations over relatively small distances (i.e., a few tens of kilometers). However, at lower frequencies (0.1-1Hz) and at distances below 60-80 km, these non-linear effects remain relatively small compared to the attenuation due to geometric spreading (Boore and Atkinson, 2008).
In addition, ground motion can also be affected by what are commonly termed seismic site effects, related to the amplification of seismic waves when they reach the surface. Various processes may produce site effects, the most common being either the transition from a stiff media to a softer one (typically the transition from bedrock to sedimentary layers). When large, continuous layers of soft sediments cover stronger bedrock, as in many shallow sedimentary basins, they may trap seismic waves and act as a wave-guide for surface waves, or even enter in resonace with a certain seismic wave frequency, and therefore experience much larger displacement amplitudes. These site effects associated with sedimentary layers are of great concern for cities or buildings. However, in steep terrain where bedrock outcrops in many sites and soil is often discontinuous, these effects may be of lesser importance compared with topographic amplification. Topographic amplification refers to the fact that seismic waves entering a topographic ridge are reflected and refracted by the surface, progressively

focussing upward with constructive interference of the reflected waves leading to enhanced ground motion at topographic highs or convexities (e.g., Bouchon, 1973; Davis and West, 1973). Thus, topographic amplification strongly depends on the characteristic topographic length scale and on the wave frequency, which determines whether constructive interference will occur.
I have reviewed some of the important processes modulating ground shaking caused by earthquakes. Inspecting the safety factor equation, Eq. 1.1, it can be seen that the stability of a given hillslope may be significantly changed by the cyclic accelerations associated with ground shaking, as they affect P and τ, the normal and shear stresses on potential failure planes. If sufficient ground shaking occurs in regions with many marginally stable slopes, then widespread landsliding can occur. Next, I discuss the importance and current understanding of this process.

1.4 Earthquake-induced landslides

The importance of earthquakes in terms of natural hazards and global erosion has long been recognized through case studies (Mathur, 1953; Garwood et al., 1979; Harp et al., 1981, 1984; Pearce and O'Loughlin, 1985) and compilations of events (Keefer, 1984, 1994; Hancox et al., 1997; Rodriguez et al., 1999). The seminal work of Keefer (1984, 1994) has defined many key questions, such as: How many landslides will be triggered by an earthquake depending on its seismic characteristics? What volume will be transported downslope (Figure 1.6)? How large is the surface area affected by seismically-induced landslides? How does surface rock strength modulate the occurence of earthquake-induced landslide? Twenty years later most of these questions are still research challenges, in part because high quality datasets are very difficult to obtain. Most of the earthquakes used in early compilation work (Keefer, 1984, 1994; Rodriguez et al., 1999) were poorly documented both from geophysical and geomorphological point of view, impeding detailed quantitative analysis.

However, at the end of the 1990s the Northridge (USA) and the Chi-Chi (Taiwan) earthquakes were recorded by a number of geophysical instruments (e.g., Shin and Teng, 2001; Wald et al., 1996) whilst triggering a very large number of landslides that were mapped in detail (Harp and Jibson, 1996; Liao and Lee, 2000). These two events have yielded iconic landslides inventories from which many qualitative and quantitative insights into earthquake-induced landslide (EQIL) have been derived. These include the influence of ground shaking (Khazai and Sitar, 2004; Meunier et al., 2007), of slope gradient, lithology and rock strength (Parise and Jibson, 2000; Lin et al., 2008), of slope aspect (Parise and Jibson, 2000; Meunier et al., 2008), and site effects and topographic amplification (Harp and Jibson, 2002; Meunier et al., 2008; Lee et al., 2010). In the last decade or so, with the availability of high resolution satellite imagery, the spread of Geographic Information Systems easing the production of digitized maps and the growing interest in landsliding, many new inventories have been created and landslide positions and characteristics have been correlated to a variety of topographic and seismic parameters (e.g., Yagi et al., 2007, 2009; Meunier et al., 2008; Parker et al., 2011; Gorum et al., 2011, 2013; Xu et al., 2013, 2014b,c). New insights have been gained through this proliferation of catalogues. The link between the spatial pattern of landsliding and ground shaking has been tightened through new observations and new

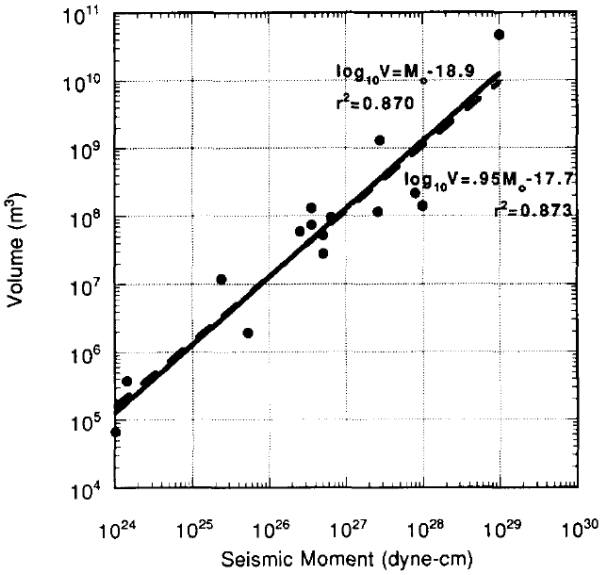

Figure 1.6 – Total landslide volume against earthquake moment for 15 earthquakes worldwide. The data is well fit by a linear trend. After Keefer (1994).

methods (Yuan et al., 2013; Meunier et al., 2013). These advances are suggesting that our understanding and ability to model earthquake strong-motion can be further used to gain insights on EQIL. Moreover, using EQIL patterns to gain information on poorly instrumented or historical earthquakes is also of great interest. EQIL have been considered as a potential tool to determine the strength of near-surface materials (Gallen et al., 2015).

The impact of earthquake strong-motion and landsliding on the ensuing erosional dynamics of the affected area has also been interrogated through recent studies. A prolonged increase in suspended sediment transported by rivers and in landslide rate has been reported after some earthquakes (Koi et al., 2008; Hovius et al., 2011; Dadson et al., 2004; Lin et al., 2008; Saba et al., 2010; Wang et al., 2015) (Figure 1.7), and has been interpreted as a possible consequence of ground cracking and/or rock weakening caused by the ground motion (Hovius et al., 2011; Owen et al., 2008). Using clast size and geochemical properties along cores of lake sediment near the Alpine Fault of New Zealand, a distinct post-seismic phase of sediment accumulation of about 50 years was detected after each of the last major earthquakes (Howarth et al., 2012). These studies suggest that the coseismic landslides may be only a fraction of the erosion caused by large earthquakes, and that landscapes need significant time, up to decades, to recover from seismic disturbances, with important implications for erosion dynamics and hazard managment.

Additionally, the total landslide volume caused by the M_w7.6 1999 Chi-Chi (Taiwan) and M_w7.9 2008 Wenchuan (China) earthquakes were found to be on the same order and larger than the earthquake surface uplift, respectively, sparking debate about the role of earthquakes within mountain building (Hovius et al., 2011; Parker et al., 2011; Molnar, 2012) (Figure 1.8). Although it turned out that the landslide volume for the Wenchuan case was significantly overestimated, recent work suggests that very large earthquakes may produce more erosion than average uplift (Li et al., 2014). The original calculations driving this debate were flawed, mainly due to mapping errors, emphasizing the need for new methods of landslide mapping and quality assessment (cf.,

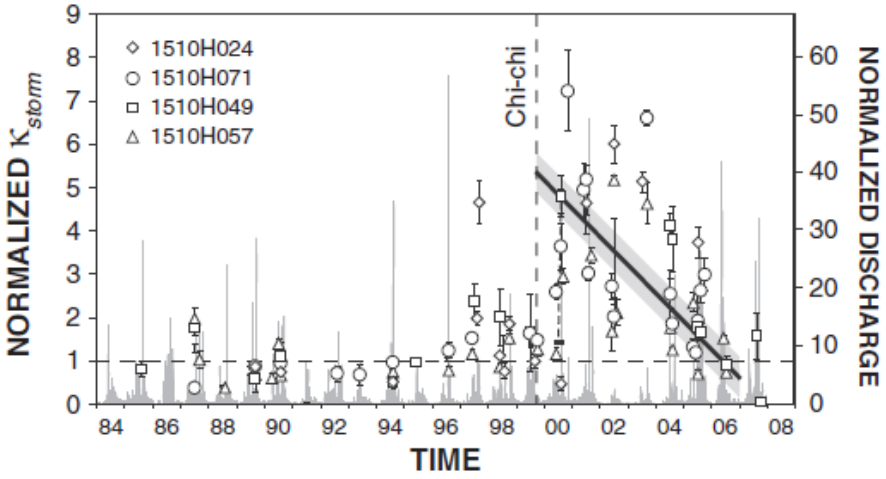

Figure 1.7 – Time evolution of the unit sediment concentration in major storm floods after the 1999 Chi-Chi earthquake, κ_{storm}, at 4 stations in the Choshui catchment, Taiwan (error bars show 1σ range). For direct comparison, values have been normalised to the mean of values prior to September 1999 at a station. Water discharge, normalised to the average of 1984-2007 ($\sim 150 m^3 s^1$), is shown in the background. After Hovius et al. (2011).

Guzzetti et al., 2012).

The current grand challenges for the community working on earthquake-induced landsliding can be summarized as follows. The first challenge is to better predict the amount of landsliding and its spatial pattern. This requires better integration of seismological aspects such as accurate spatial maps of ground shaking, the importance of topography in focussing and amplifying waves, and the relation between the shaking at a site and the ground failure and its geometry. Additionally, we need to find new ways to characterize hillslopes in terms of rock strength and general susceptibility to shaking. This is a long-term goal, as each component described above is a significant challenge, and all seem required in order to have an effective and detailed prediction of the effects of EQIL at short timescales.
The two next challenges are important for the whole landslide research community but are specifically harder to reach when studying EQIL because of the very large number of landslides produced at the same time.
The second challenge is to develop automatic mapping algorithms, suitable for intensely affected areas: though the amount of data is increasing, the field is still relatively data-poor and obtaining good quality inventories manually requires significant effort. Further, refining automatic detection algorithms based on various type of imagery is an important topic. Finding ways to map or constrain the fine geometry of landslides, with higher resolution images or differential DEMs are also important avenues to explore. Up to now, only the location and surface area of landslides are routinely obtained, but we have no direct ways to measure their depth, or subdivide them into a scar, transport and deposit area. These are technical objectives but they are important in order to solve the other challenges.
The third challenge is to couple the effects of widespread landsliding together with other surface process systems. Few studies have addressed the landscape response to widespread landsliding, and it is essential for many theoretical and applied pur-

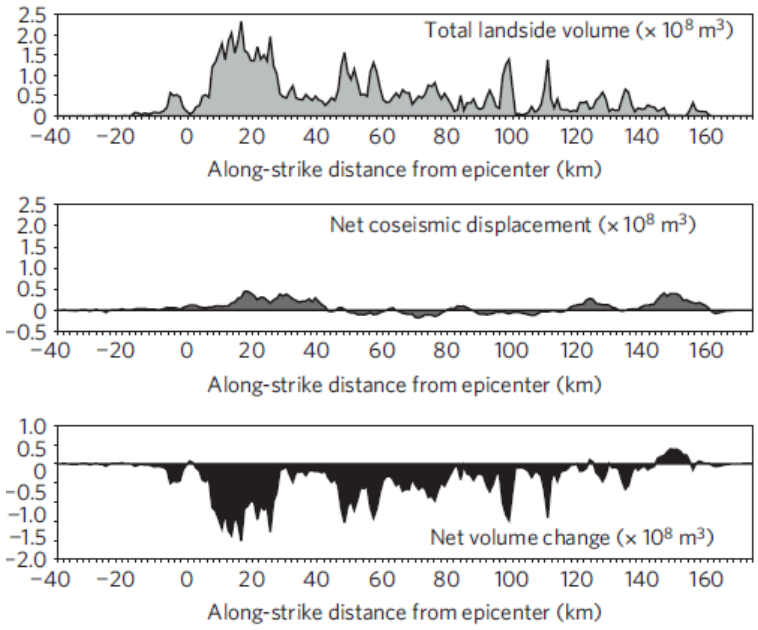

Figure 1.8 – Comparison of erosion and uplif associated with the M_w7.9 2008 Wenchuan (China) earthquake. From top to bottom: Landslide volume derived from the global bedrock landslide scaling relationship applied to individual landslides within each 1-km wide strip. Net coseismic volume change in each 1-km wide strip. Net volume change determined by subtracting landslide volumes from coseismic volume change. All data are projected onto a rupture-parallel line at 1 km intervals. Modified after Parker et al. (2011).

poses to understand how river networks will cope with the new sediment, and how geochemical and geobiochemical processes, such as weathering, soil formation and organic carbon sequestration, will be affected by EQIL. This requires both acquisition of detailed data on the interactions between landsliding and these other processes, and modelling of the propagation, over intermediate timescales, of the EQIL perturbation through the different process zones of the landscape.
The fourth challenge is to understand the feedbacks between erosion and tectonics, operating over long timescales of one or several seismic cycles, requiring exploration of how earthquakes affect the evolution of topography, and how EQIL and their evacuation influence fault development and activity or isostatic patterns.
These different challenges are entangled and lie at the interface of multiple fundamental disciplines of the Earth sciences. This thesis only addresses some subcomponents of them, as detailed below.

1.5 Main questions and outline

The recent proliferation of new catalogues of EQIL and the observations suggesting unrecognized short term and long term effects of earthquakes on the erosional dynamics of mountain belts (Hovius et al., 2011; Parker et al., 2011) have led to a series of questions that I have tried to address within this dissertation. These key research questions mainly pertain to the 1st and 4th challenges that I have described above:

1/ First of all, what volume of debris is mobilized through EQIL and can this

be better correlated to seismological parameters? The single published global analysis has an order of magnitude of scatter and accounts only for the seismic moment magntiude (Keefer, 1994) (Figure 1.6), whereas more recent case studies suggest that other parameters, such as ground shaking and earthquake depth, must be taken into account (Meunier et al., 2007, 2013). To answer this question also requires the collection of unbiased landslide inventories and to ask what mapping errors may remain unnoticed in landslide inventories (e.g., Li et al., 2014).
In Chapter 2, *Amalgamation in landslide maps: effects and automatic detection*, I assess the errors caused by amalgamation -the bundling of several landslides into a single mapped polygon- in several EQIL inventories. I quantify the magnitude of errors on estimates of the total volume of landslides and on the characterization of landslide frequency-size distributions. I present and test an algorithm based on the polygon shape and position within a digital elevation model to automatically detect amalgamated polygons.
In Chapter 3, *A seismologically-consistent expression for the total area and volume of earthquake-induced landslide populations*, I present a new analytical expression to predict the total volume or area of landslides caused by an earthquake. I build this relationship by considering the statistical relation between landsliding and ground shaking, a source term for wave emission as a function of earthquake size, the attenuation of seismic waves with distance and the sum effect of multiple seismic sources, the number of which scales with the fault size. Further, I account for the availability of steep hillslopes in the epicentral areas and for their characteristic steepness, which controls their sensitivity to shaking. The model is calibrated and tested against a database of 40 earthquakes for which EQIL has been constrained. The accuracy and limitations of the model are discussed.

2/ Second, I explore the intermediate timescale, to try to understand not just the instantaneous mass wasting caused by the shaking, but also the impact on the landscape in the following years or decades after the main shock. If earthquakes do stimulate hillslope erosion (Hovius et al., 2011; Owen et al., 2008; Saba et al., 2010) (Figure 1.7), is it related to ground cracking or to another process, and to what extent and for how long are the hillslopes perturbed? How can we monitor post-earthquake erosional change and relaxation?
In Chapter 4, *Transient changes of landslide rates after earthquakes*, I quantify the evolution of landslide rates in the epicentral areas of 4 earthquakes. I produce a time series of landslide maps and show that the landslide volume and area are non-linear function of the total rainfall. However, landsliding for a given rainfall amount increased up to 20 times in the years following all earthquakes and then recovered over a time span that apparently scales with the earthquake magnitude. This transient increase in the landslide susceptibility is not explained by landslide reactivation, water-table elevation or root-system disturbance. I propose instead that it is due to ground damage due to shaking, and that the recovery is likely due to a healing process, which remains to be determined.
In Chapter 5, *Co-evolution of shallow seismic velocity changes and landslide rates after earthquakes*, I compare the evolution of landslide rates in epicentral areas with subsurface seismic velocities obtained from the autocorrelation of ambient noise, finding that these two observables co-evolve. This supports the common hypothesis that seismic velocity drop and recovery is dominated by shallow ground cracking due to the strong-

motion, and that the recovery is related to crack healing and closure. Time-series of surface displacement of GPS stations in the same areas also show similar changes through time, suggesting that deep tectonic deformation may be a driver of the healing of surface rocks.

3/ Directly following from the first question, we can attempt to understand how much net topography building is achieved by earthquakes in active mountain belts (Figure 1.8). Can earthquake induced erosion be modelled accurately enough to go beyond existing case studies (Hovius et al., 2011; Parker et al., 2011) and to understand which parameters govern the proportion of the earthquake uplift that is eroded through landsliding? And what is the contribution of post-seismic landsliding to the mass balance of earthquakes ?
In Chapter 6, *The mass balance of earthquakes and earthquake sequences*, I combine the landslide model developed in Chapter 3 and the standard formulation used to compute the surface deformation of an earthquake to determine which earthquakes may have a negative mass balance, i.e., produce more erosion than uplift. I assess the role of different parameters such as the earthquake depth, the fault geometry and the landscape steepness in modulating the mass balance of single earthquakes and of earthquake sequences. Earthquake sequences are modeled based on two plausible end-member: as a series of characteristic earthquakes or as a sequence following a Gutenberg-Richter distribution of earthquake magnitudes. I find that intermediate size earthquakes ($M_w 67.3$) may cause more erosion than uplift, controlled primarily by seismic source depth and landscape steepness, and less so by fault dip and rake. Earthquake sequences with a Gutenberg-Richter distribution have a greater tendency to lead to predominant erosion, than repeating earthquakes of the same magnitude, but fault large enough to produce $M_w > 8$ will always be constructive over long timescales.

This dissertation ends with Chapter 7, which summarizes the work presented in Chapter 2-6, and Chapter 8, which integrate the thesis within the broader discourse of geomorphology and natural hazards research before suggesting some future work.

1.6 Author's contribution and publications

The bulk of the work described in the following chapters has been performed by the author. Chapters 2-6 are published or awaiting publication in international peer-reviewed journals:

Chapter 2 Marc, O. and Hovius, N.: Amalgamation in landslide maps: effects and automatic detection, Nat. Hazards Earth Syst. Sci., 15, 723–733, doi: 10.5194/nhess-15-723-2015, 2015.
OM and NH contributed equally to conceptualizing the study, and writing the manuscript; OM conducted all data analysis, wrote the algorithm and designed all artwork.

Chapter 3 Marc, O., Hovius, N., Meunier, P., Gorum, T., and Uchida, T.: A seismologically consistent expression for the total area and volume of earthquake-triggered landsliding, Journal of Geophysical Research: Earth Surface, 121, 640–663, doi: 10.1002/2015JF003732, 2016b.
OM, NH and PM conceived the study and wrote the manuscript with input from TU

and TG. OM assembled and complemented the data base with help from TU and TG, and performed all analyses, assisted by PM and NH. OM designed all artwork.

Chapter 4 Marc, O., Hovius, N., Meunier, P., Uchida, T., and Hayashi, S.: Transient changes of landslide rates after earthquakes, Geology, 43, 883–886, doi: 10.1130/G36961.1, 2015.
OM, NH and PM conceived the study and wrote the manuscript with input from TU and SH. OM mapped the landslides and performed all analyses, assisted by PM and NH. TU and SH delivered landslide maps and assistance on collecting and using Japanese data.

Chapter 5 Marc, O., Sens-Schönfelder, C., Hovius, N., Meunier, P., Hobiger., M., Hsu, Y.J., Ohzono, M., and Sawazaki, K.: Co-evolution of shallow seismic velocity changes and landslide rates after earthquakes, Science, About to be submitted.
OM, CSS, NH and PM conceived the study and wrote the manuscript with input from all others. CSS and MH performed the noise correlations. YJH and MO extracted GPS displacement and computed surface areal strain. OM and CSS performed all other analyses. OM designed all artwork.

Chapter 6 Marc, O., Hovius, N., and Meunier, P.: The mass balance of earthquakes and earthquake sequences, Geophysical Research Letters, In Review.
OM, NH and PM conceived the study and wrote the manuscript. OM conducted all numerical computations and designed all artwork.

During the course of his PhD, the author has contributed to the following publications that are not included in the present thesis:

Emberson, R., Hovius, N., Galy, A., and Marc, O.: Chemical weathering in active mountain belts controlled by stochastic bedrock landsliding, Nature Geoscience, 9, 42–45, doi: 10.1038/ngeo2600, 2015.

Kober, F., Zeilinger, G., Hippe, K., Marc, O., Lendzioch, T., Grischott, R., Christl, M., Kubik, P. W., and Zola, R.: Tectonic and lithological controls on denudation rates in the central Bolivian Andes, Tectonophysics, 657, 230–244, doi: 10.1016/j.tecto.2015.06.037, 2015.

Chapter 2

Amalgamation in landslide maps: effects and automatic detection

Abstract

Inventories of individually delineated landslides are a key to understanding landslide physics and mitigating their impact. They permit assessment of area-frequency distributions and landslide volumes, and testing of statistical correlations between landslides and physical parameters such as topographic gradient or seismic strong motion. Amalgamation, i.e. the mapping of several adjacent landslides as a single polygon, can lead to potentially severe distortion of the statistics of these inventories. This problem can be especially severe in datasets produced by automated mapping. We present 5 inventories of earthquake-induced landslides mapped with different materials and techniques and affected by varying degrees of amalgamation. Errors on the total landslide volume and power-law exponent of the area-frequency distribution, resulting from amalgamation, may be up to 200% and 50%, respectively. We present an algorithm based on image and DEM analysis, for automatic identification of amalgamated polygons. On a set of about 2000 polygons larger than $1000m^2$, tracing landslides triggered by the 1994 Northridge earthquake, the algorithm performs well, with only $2.7 - 3.6\%$ wrongly amalgamated landslides missed and $3.9 - 4.8\%$ correct polygons wrongly identified as amalgams. This algorithm can be used broadly to check landslide inventories and allow faster correction by automating the identification of amalgamation. [1]

1. Originally published as: Marc, O. and Hovius, N.: Amalgamation in landslide maps: effects and automatic detection, Nat. Hazards Earth Syst. Sci., 15, 723–733, doi: 10.5194/nhess-15-723-2015, 2015

2.1 Introduction

Regional landslide maps are a crucial component of many landslide related studies (Guzzetti et al., 2012) : they are necessary to improve our understanding of landslide rupture mechanics and test conceptual models, to produce landslide risk and vulnerability maps, to understand how different climatic and tectonic mechanisms can trigger landslides, and to estimate how mass wasting contributes to sediment production and landscape evolution (Montgomery and Dietrich, 1994; Meunier et al., 2007, 2008; Hovius et al., 1997). Such maps used to be created by manual mapping from remote sensed imagery, often accompanied by partial field checks (e.g., Harp et al., 1981; Harp and Jibson, 1996) . Due to the high cost and time associated with manual mapping of thousands or tens of thousands of landslides over large areas, automated mapping techniques are increasingly used (e.g., Martha et al., 2010; Mondini et al., 2011; Parker et al., 2011). These techniques have specific associated errors, amongst which amalgamation, that is the bundling of several adjacent landslides into a single map polygon, is prominent. Amalgamation typically occurs when the spatial density of landslides is high and the resolution of images from which they are mapped relatively low, making it difficult to differentiate multiple landslides in a perturbed area. Automatic mapping algorithms designed to detect change of surface properties, irrespective of the shape of the changed area, are especially prone to this effect. If uncorrected, amalgamation can lead to severely mistaken results and interpretations in many domains. For example, studies using landslide maps to estimate the volume of debris produced, whether to understand sediment transfer dynamics (Hovius et al., 2000; Yanites et al., 2010), organic matter mobilisation (Hilton et al., 2011b), average erosion rates (Hovius et al., 1997) or mountain building (Parker et al., 2011), rely on empirical laws giving landslide volume as a function of landslide area (Guzzetti et al., 2009a; Larsen et al., 2010). In this approach, landslide depth is assumed to scale with area, giving rise to strongly non-linear area-volume relations, which assign disproportionate importance to landslides with the largest surface areas. Accurate landslide area mapping, differentiating precisely between individual events is therefore of the essence (Li et al., 2014). This also applies to studies considering the area-frequency distribution of landslides, whether to assess landslide hazard and risk associated with extreme events (Malamud et al., 2004b), or to understand the underlying physics of the distribution (Pelletier et al., 1997; Stark and Guzzetti, 2009; Frattini and Crosta, 2013). Finally, any attempt to understand the physics of landslide triggering from mapped landslide patterns could suffer from the effects of wrongly mapped landslide outlines and artificial prominence of large disturbed areas (Montgomery and Dietrich, 1994; Meunier et al., 2008).

Here, we survey why and where amalgamation can occur, and determine the minimum error it has introduced to estimates of total landslide volume and the area-frequency distribution of several landslide inventories. Subsequently, we propose an algorithm able to automatically detect amalgamation when provided with a raster file of polygon shapes and a DEM. Performance of this algorithm is tested on a representative subset of the inventory of landslides triggered by the Northridge earthquake. We finish with a short discussion of the benefits and limitations of this approach and possible alternatives.

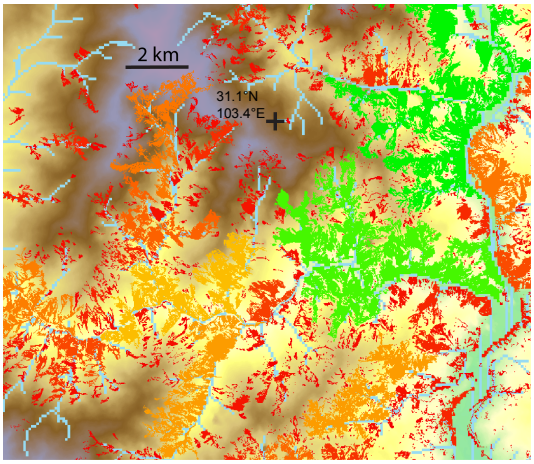

Figure 2.1 – Some polygons from the Parker et al. (2011) dataset, representing landsliding caused by the 2008 Wenchuan earthquake. Polygons are color coded by size (red being the smaller polygons) and overlaid on a DEM and a river network. The density of landsliding is correctly estimated but dozens of small landslides have been connected along slope or even across rivers or ridges.

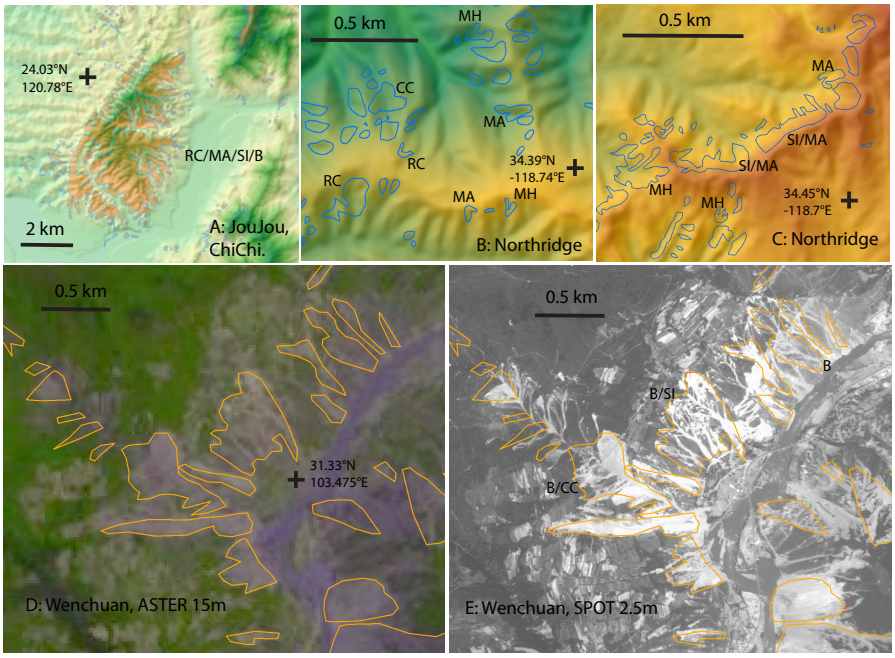

Figure 2.2 – A, B, C: Landslide polygons on a DEM topography showing examples of amalgamation in the ChiChi and Northridge inventories. Geometric and topographic inconsistencies that signal amalgamation are specified as follow: RC for ridge crossing, CC for channel crossing, MH for multi-headed (multiple source area), MA for multi-armed (multiple deposit areas), SI for slope inconsistencies (polygon elongated perpendicular to the slope) and B for blurring due to insufficient resolution to differentiate different disturbed areas. D, E: Some polygons mapped by Gorum et al. (2011) after the Wenchuan earthquake overlaid on a 15m-resolution ASTER image (D) and on a 2.5m-resolution SPOT 5 image (E), of the same area. Note the presence of amalgamation but also the significant mapping extent exaggeration when mapping on low resolution relative to the landslide density .

2.2 Landslide Mapping and Amalgamation

Most landslide inventories are derived from analysis of optical or multispectral imagery, exploiting the typical texture, colour and spectral properties of freshly disturbed areas (Guzzetti et al., 2012). Often, landslides are conspicuous because they clear vegetation that has a very different appearance or radiation intensity spectrum. When landslides are mapped as polygons, whether by men or machine, the general assumption is that the polygon represents a single landslide, most often combining a scar area, a deposit area and sometimes a runout area. A mapped polygon is therefore assumed to contain direct or indirect information on the location and size and, implicitly, the volume of one landslide but also potentially about the slope where the landslide initiated and terminated, the runout distance, the drop of potential energy, or the triggering mechanism, such as the local peak ground acceleration or pore pressure at the time of failure.

Amalgamation, the combination of several individual adjacent landslides in a single polygon, can be due to the actual coalescence of landslides, or the apparent contiguity of disturbed areas in images with low resolution or poor contrast between affected and unaffected areas (Figure 2.1). Indeed,where landsliding is very dense, several adjacent landslides may have joint runout areas or overlapping deposits, or scars separated by a distance too short to be resolved by the available imagery. At a given resolution, multispectral images contain more information than optical images, which may help in delineating individual landslides but this does not always preclude amalgamation in landslide mapping. Even where image resolution would permit accurate mapping of individual landslides, amalgamation can occur when the primary goal of the mapper is not to map landslide extent precisely, but rather to rapidly evaluate the area affected by slope failure. This seems common for maps predating widespread use of landslide area-volume relationships as well as for more recent inventories, underlining the current lack of care in avoiding or at least flagging amalgamation. In automatic mapping, algorithms that are not object oriented will usually classify single pixels based on their various bulk properties (Guzzetti et al., 2012). If adjacent pixels are classified as disturbed, then the algorithm will combine them in a single polygon, regardless of how many separate landslides are contained within. When image resolution is not very high, then automatic algorithms can bundle hundreds of small landslides, located within a limited area with high propensity to failure, into a single, apparently very large landslide polygon.

A striking example of amalgamation can be found in the JouJou Mountain area of Taiwan, where pervasive shallow landsliding occurred during the M_w 7.6 ChiChi earthquake in 1999 (Figure 2.2) (Liao and Lee, 2000). In available maps, these landslides have been merged into a few complex shaped polygons, blanketing the steep, gullied hills and covering $9.8km^2$. However, a separate, local survey has found more than one thousand individual, shallow failures, many of which adjoined without making larger landslides (Lee et al., 2010). Together, these landslides had a total area of $7.22km^2$, implying a significant area exaggeration by the automated mapping procedure.The implications of this extreme amalgamation are far reaching. For example, using common landslide area-volume relations (Guzzetti et al., 2009a; Larsen et al., 2010), the total volume of the six largest, automatically mapped polygons in the area would be estimated at about $0.19km^3$, with the largest polygon ($4.13km^2$) alone contributing about $0.11km^3$. If the total area occupied by these six polygons is arbitrarily repartitioned

into 1000 landslides of roughly equal size, set by the characteristic local ridge spacing and slope lengths of $\sim 100 - 150m$, then a 17-fold reduction of the estimated landslide volume would result. This estimate could be refined with access to the local landslide data (Lee et al., 2010), which can be seen to have a non-uniform area-frequency distribution with hundreds of landslides with areas of $100m^2$ and one landslide of $0.1km^2$.
In this example, amalgamation of landslides is easily recognizable due to the complex shape of polygons straddling multiple topographic features, with surface areas much larger than permitted by the characteristic length scale of the topography. Formally, the merging of several landslides can result in a range of geometric or topographic inconsistencies, such as multi-branched polygons, or polygons with orientations inconsistent with local topographic slope or transgressing ridgelines or channels (Figure 2.2). We consider that these features are unlikely characteristics of individual landslides, even though failure on multiple scarps, divergence in runout, runout crossing rivers and spreading on the opposing valley side or occasional overtopping of dividing ridges are known to happen.
Some polygons may also appear topographically and geometrically consistent, although they are, in fact, a combination of several adjacent landslides close to or below the resolution of available images, the combined effect of which is to alter the visual or spectral properties of a larger area. This blurring can conjugate amalgamation and an exaggeration of the area affected by landslides, but it cannot be identified without use of very high-resolution images (Figure 2.2). It is, therefore, out of the scope of our study and remains a challenge and a caveat for landslide mapping.

2.3 Data

The recognition of geometric and topographic inconsistencies in landslide inventories is a key to identification of amalgamation of individual landslides and mitigation of its effects. To develop a method for detection of amalgams in large landslide datasets, and to evaluate the effects of amalgamation on scientifically interesting derivatives of these datasets, we have focused on earthquake cases. Large earthquakes can trigger many thousands of landslides in a limited area, reducing possible effects of geological heterogeneity on landslide populations and their statistics. Moreover, by focusing on landslides with a shared trigger mechanism, we have removed possible complications due to convolution of trigger-specific effects from our analysis. Finally, earthquake-induced landslide populations tend to span a very large range of landslide sizes, allowing robust computation of area-frequency statistics, one of the key attributes affected by amalgamation.
We have used 5 published inventories of earthquake-induced landslides, mapped over areas of $10^3 - 10^4 km^2$. Together, these inventories cover a range of mapping approaches from manual mapping with extensive field checking, to fast automated mapping with limited supervision and verification. The 1994 M_w 6.6 Northridge earthquake in California triggered more than 10,000 landslides, which were mapped manually from airphotos, with field checks at selected sites (Harp and Jibson, 1996). The same approach was used to map more than 6,000 landslides triggered by a M_w 7.6 earthquake in 1976 in Guatemala (Harp et al., 1981). The 1999 M_w 7.6 ChiChi earthquake in west Taiwan also caused severe landsliding, with more than 9,000 landslides larger than $625m^2$ (25

m x 25 m) mapped manually from SPOT satellite imagery (Liao and Lee, 2000). Finally, for the 2008, M_w 7.9 Wenchuan earthquake in China, many different maps of coseismic landslides exist (Ouimet, 2010; Qi et al., 2010; Dai et al., 2011; Gorum et al., 2011; Parker et al., 2011; Xu et al., 2014c), allowing comparison of independent and broadly equivalent datasets. We have used two catalogues containing 50,000 polygons apiece. One was mapped with a semi-automatic algorithm using 2.5 to 10 m-resolution SPOT 5 and EO-1 satellite imagery (Parker et al., 2011). The other was mapped by hand, mainly from 15 m-resolution ASTER imagery and locally higher resolution imagery (Gorum et al., 2011). In all these inventories, the entire area perturbed by a landslide, including scar, runout and deposit, is delineated by a single polygon.
In addition to these five inventories, we have used Aster GDEM-30 m data to evaluate the topographic context of mapped landslide polygons and as an input of our algorithm for detection of amalgams. In the case of the Wenchuan earthquake, we have also used 15 m-resolution ASTER images and 2.5 m-resolution SPOT 5 images from the epicentral area, taken shortly after the earthquakes, to verify the different landslide maps.

2.4 Quantifying effects of amalgamation

The earthquake-induced landslide inventories summarized above are too large for comprehensive manual verification. To assess the possible effects of amalgamation in these data sets, we have focused on the largest polygons in each inventory. These polygons dominate landslide volume estimates and can strongly influence the best fits to area-frequency distributions. Thus, by checking and correcting a limited number of large polygons, the quality of derivatives of landslide inventories can be substantially improved. In checking individual polygons, we considered as anomalous any polygon displaying a geometrical or topographical inconsistency such as branching, traversing of ridges or rivers or orientation inconsistent with the local topographic slope. These polygons were compared with local topographic data and, when appropriate split to make residual polygons more consistent with the general topography. Nevertheless it is clear that without high-resolution imagery, many landslide polygons were redefined in a relatively crude way.
We have used published area-volume relationships to estimate the volume of landslides from the mapped disturbed areas (Larsen et al., 2010). It was assumed that landslides with area > $100,000 m^2$ involved bedrock, and that smaller landslides were mixed bedrock and soil failures. Landslide maps typically do not distinguish between scar and deposit, lumping the two in one area measure. According to Larsen et al. (2010), scars and deposits have area-volume relations with the same power-law exponent, implying constant size ratios between scar and deposit areas of 1.1 and 1.9 for mixed and bedrock landslides, respectively. Hence, we have estimated the scar area by dividing the mapped landslide area by 2.1 and 2.9 for mixed and bedrock landslides, respectively, assuming that runout was equal to the scar length. Then we converted scar area A, into volume V, for bedrock and soil landslides with $V = aA^b$ with a=0.146 and 0.234 and b=1.33 and 1.41 for mixed and bedrock landslides, respectively. Computed landslide individual and total volumes appear to be consistent with field estimates for cases where the whole perturbed area was mapped.
Comprehensive landslide inventories have a typical area-frequency distribution with

a roll-over and a power-law decay with an exponent, ρ, commonly within a narrow range of values (Malamud et al., 2004a). The roll-over can be caused by censoring of the small landslides due to the mapping resolution (Stark and Hovius, 2001), but can also be related to the physics of landsliding and the transition from cohesion-controlled to friction-controlled hillslope stability with increasing landslide area and depth (Katz and Aharonov, 2006; Stark and Guzzetti, 2009). The roll-over and power-law decay have also been attributed to a combination of the size distribution of continuous local topographic slopes and the distribution of moisture or increasing cohesion with depth (Pelletier et al., 1997; Frattini and Crosta, 2013). We have assessed the impact of amalgamation by comparing the area-frequency distribution of the original datasets with that of our partially corrected datasets. Because the frequency decay with increasing landslide size is usually modeled as a power-law, a specific functional form does not have to be prescribed if we only consider the distribution at areas ten times larger than the roll-over. For these large areas we have obtained ρ with a linear least-square regression of the log-transformed data (Figure 2.3).

In many cases a larger number of smaller polygons were also visibly amalgamated, but we did not correct them, due to the effort and uncertainties involved. Thus, the estimates of errors on total landslide volume and the power law exponent of the landslide area-frequency distribution due to amalgamation, presented below, are likely minimum values. Next, we review the individual landslide inventories and highlight the varying degrees to which they are affected by amalgamation and its effects.

Landslides induced by the 1976 Guatemala and 1994 Northridge earthquakes were mapped in detail, apparently to record where landslides had occurred, but not necessarily to distinguish the boundaries of individual landslides. We have inspected all 356 polygons with an area larger than $10,000m^2$ in the Northridge inventory and all 90 polygons exceeding $100,000m^2$ in the Guatemala dataset. Together, these polygons represent 56% and 73% of the uncorrected volume of the landslide populations of the Northridge and Guatemala earthquakes, respectively. 162 out of 356 and 51 out of 90 of these polygons were found to be amalgams of several landslides. They were split according to their shapes and relation to the local topography. This resulted in a reduction of the total volume of landslides by 16% in the Northridge case and 35% in the Guatemala case, and an increase of the area-frequency scaling exponent, by 16% and 22%, from 1.57 and 1.33 to 1.82 and 1.62, respectively (Figure 2.3). Because polygons smaller than the threshold represent only 44% and 27% of the total volume, respectively, and because they must be less amalgamated and have much smaller individual volumes, their correction would likely add only a minor contribution to the total volume change.

The ChiChi earthquake caused widespread landsliding in the mountains of central west Taiwan. An inventory of these landslides (Liao and Lee, 2000) contains 9272 polygons in an area 150 times larger than the JouJou Mountain, mentioned above, with a total estimated volume of about $0.73km^3$. We have inspected all 173 polygons larger $100,000m^2$, representing 85% of the total uncorrected volume of the ChiChi inventory. We have found that 100 of them needed corrections ranging from the splitting of minor branches to the artificial fragmentation of the largest polygons in the JouJou mountain area, where precise correction was impossible. Together, these corrections resulted in a volume reduction of 38% to $0.45km^3$, but an insignificant increase of the area-frequency scaling exponent by 5%.

The two inventories for the Wenchuan earthquake have similar total landslide areas

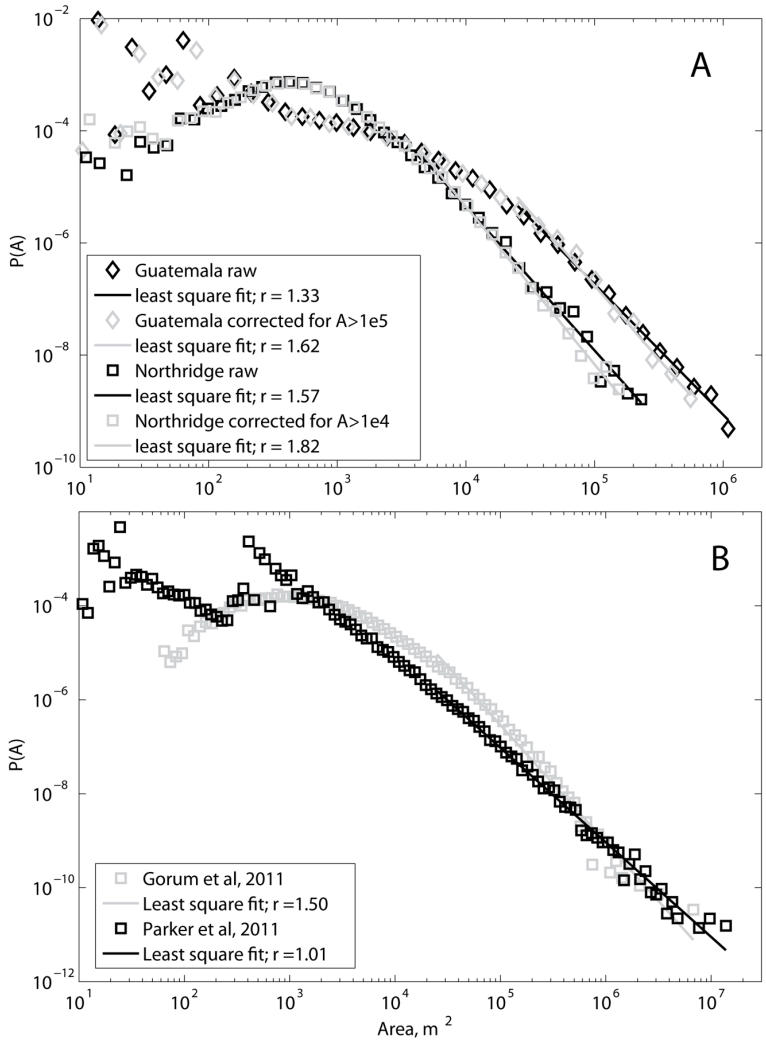

Figure 2.3 – Amalgamation effect on landslide area-frequency distributions. A: Comparison between the raw data from the coseismic landslide maps for to the 1976 Guatemala and 1994 Northridge earthquakes and the corrected catalogue where every amalgam larger than $100,000m^2$ and $10,000m^2$ was split, respectively. For the 2008 Sichuan earthquake, several landslide maps were published. Of these, the Parker et al. (2011) dataset is severely affected by amalgamation whereas the Gorum et al. (2011) dataset is relatively exempt from amalgams.

and similar total numbers of landslides, even though the mapping of Gorum et al. (2011) extended further to the north along the seismogenic fault. We have compared the maps where they overlap, along 150 km of the fault trace, where the majority of landslides occurred (e.g., Figure 2.2). There is good overall agreement between the data sets, but the manual mapping of Gorum et al. (2011) has clearly delineated many more individual slides (Figure 2.2). Many examples of amalgamation are evident in the Parker et al. (2011) data set (Figue 2.1), and although, there are some mapping discrepancies between the two inventories, this appears to be the main difference between them. It has resulted in a total landslide volume reduction of 69%, from $6.30km^3$ for the automated-mapping inventory (Parker et al., 2011) to $1.96km^3$ for the original manually-mapped inventory of Gorum et al. (2011). However, this inventory also contains amalgamation artefacts (Figure 2.2). We have visually checked all 152 landslides larger than $300,000m^2$, representing 51% of the total volume of the manual inventory

(including landslides mapped in areas not surveyed by Parker et al. (2011). Of these 87 required editing, leading to a final landslide volume estimate of $2.3km^3$ instead of $2.45km$, equivalent to a modest reduction of 6%.
The landslide polygon area-frequency distributions of the Wenchuan inventories also differ significantly (Figure 2.3). First, the amalgamated catalogue of Parker et al. (2011) yields a discontinuous distribution, which does not exhibit the roll-over commonly observed in well-mapped data sets (Malamud et al., 2004a; Brardinoni and Church, 2004). Instead the smaller polygons also have a decreasing frequency with increasing size, and they appear to be relatively infrequent compared to medium to large slides. In contrast, the manually mapped inventory has a area-frequency distribution with a rollover at $\sim 1000m^2$. The exponent on the best-fit power-law for this data set, after our correction for amalgamation is also much higher than for the Parker et al. (2011) inventory, $\rho = 1.5$ and $\rho = 1.0$, respectively, confirming the relative abundance of large, mostly amalgamated polygons in the latter (Figure 2.1,2.2). Correction for amalgamation effects results in a slight rise of the scaling exponent of the manually mapped inventory to $\rho = 1.6$.
From these analyses it is clear that amalgamation can significantly distort both landslide population volume estimates and the frequency distribution of mapped landslide areas. However, the frequency distribution itself does not necessarily betray amalgamation, and exhaustive visual screening can be prohibitively time consuming. In the following section, we propose an automatic algorithm, which can be used to differentiate correctly mapped and amalgamated polygons and allow faster and more comprehensive cleaning of affected data sets.

2.5 Automatic detection of amalgamation

Because amalgamation leads to geometric anomalies and unusual positions of putative landslides in the landscape it is possible to detect amalgams simply by looking at their shape and at the underlying topography. Following the criteria defined in section 2 (Landslide mapping and amalgamation) we have developed an algorithm able to guide a mapper or an end-user towards suspicious polygons, and facilitate a correction or an assessment of the catalogue quality. The algorithm requires a DEM, a raster made from the polygon shapefile and a text file with polygon ID and information. Below, we present the operation of the algorithm and assess its accuracy.
First, the algorithm considers the geometry of a landslide polygon. The branching of polygons is the most common and visible effect of amalgamation. This affects the relation between perimeter, P, and area A, of the polygons, biasing amalgams towards high P. These attributes are easily extracted from a landslide inventory with any GIS. A polygon with given P and A can be compared to an ellipse of equal P and A, and aspect ratio K. Using the Fagnano (1750) approximation, the ellipse perimeter can be written as:

$$P = \pi \left(\frac{3}{2b}(K+1) - \sqrt{Kb^2} \right) \tag{2.1}$$

where b is the small radius. Since $A = \pi K b^2$, it can be shown that the perimeter of any ellipse varies as

$$P = \left(\frac{3(K+1)}{2\sqrt{K}} - 1 \right) \sqrt{\pi A} \tag{2.2}$$

Rearranging (2), K can be found from P and A as the solution of a second order equation:

$$K = \frac{1}{2}\left(\frac{4}{9}\left(\frac{P}{\sqrt{\pi A}}+1\right)^2 - 2 + \sqrt{\left(\frac{4}{9}\left(\frac{P}{\sqrt{\pi A}}+1\right)^2 - 2\right)^2 - 4}\right) \tag{2.3}$$

Thus, any polygon can be described easily and objectively by the aspect ratio, K, of its equivalent ellipse. For reference, a circle would yield K=1, a square K=2.3 and rectangle twice as long as wide K=2.7. A polygon with high K is more likely to be incorrect whereas a polygon with $K < 2$ has a compact shape from which any mapping error cannot easily be recognized. Therefore, to accelerate the algorithm any polygon below a critical aspect ratio, K_c, is assumed to be correct (Figure 2.4).

A high K value may signal amalgamation or simply an elongated landslide, for example due to long runout. Therefore, K is a useful input parameter but ultimately it is necessary to explicitly consider the geometry of the polygon. This is achieved by reducing the mapped polygons to their skeleton with a standard image analysis method, which iteratively thins a solid polygon to a branched centre-line (Figure 2.5). From this skeleton, branch points and individual branches are easily found. However, even polygons with a relatively simple shape may have skeletons with some branching points and small branches pointing towards a polygon corner or irregular side. To eliminate these spurious branches, we impose an arbitrary threshold size ratio of branches relative to the longest branch, RB_c. A polygon with a main branch and several smaller branches, all of which are shorter than the main branch by a factor $1/RB_c$ or more is considered to be a correctly mapped, single landslide (Figure 2.4). All other polygons receive a score equal to the number of branches longer than the longest branch divided by RB_c, reflecting qualitatively the degree of amalgamation.

In a second step, the algorithm tests the consistency of a polygon with apparently correct geometry, with the local topography. This is done by extracting the DEM elevation along the longest branch of the polygon, which is assumed to be an adequate representation of the pathway of the landslide. First, the algorithm checks that the highest and lowest elevations along the branch coincide with the top and toe of the mapped landslide. A violation of this condition typically signals that the branch traverses a ridge or valley floor, or that two landslides were merged into a crescent shaped polygon, smooth enough not to be identified as a likely amalgam by the first part of the algorithm. If the polygon passes this second test, then a last check is made to see if the maximum variation of elevation along the main branch is above the minimum slope for landsliding, S_c (Figure 2.4). Polygons failing this test are typically oriented perpendicular to the main topographic slope over long distances, as a result of the lateral merging of several small, parallel failures along a ridge or cliff.

Thus, our algorithm is formally based on 3 adjustable parameters K_c, RB_c, and S_c. Of these, only RB_c may be substantially tuned, depending on the smoothness of the input raster, which in turn depends on the landslide mapping technique and the raster resolution. S_c is a physical parameter which should normally be close to a 10°threshold for landsliding (e.g., Meunier et al., 2007; Lin et al., 2008), thus requiring minimal tuning, unless the local substrate has exceptional properties. To minimize the number of false negatives (i.e. undetected amalgams), K_c should be set at a low value of about 2, so that only polygons without any geometrical complexity are screened out. Setting K_c at a higher value can be useful to assess the degree of amalgamation and isolate only those polygons that are likely to be composites of many landslides.

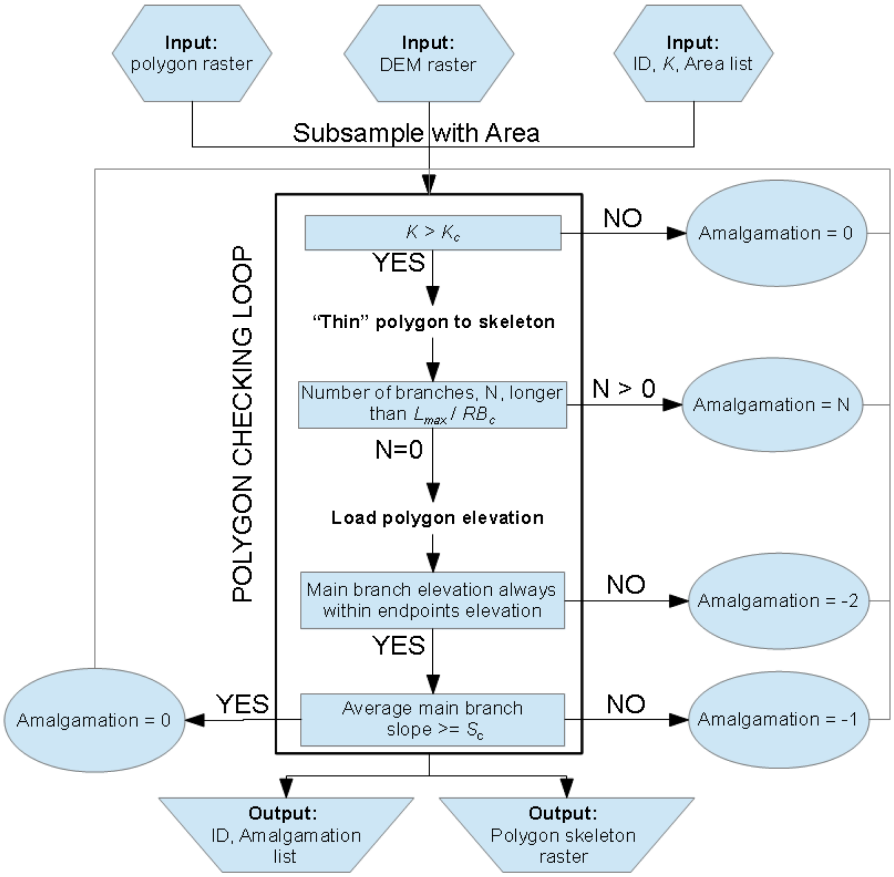

Figure 2.4 – Flowchart of the algorithm for automatic detection of amalgamation. Inputs are used to individually analyse polygons based on geometric and topographic characterictics, following a series of conditional tests that lead to a polygon score. A score of zero means that the polygon is considered clean and any other scores refer to some sort of amalgamation. K is the equivalent ellipse aspect ratio (see Eq 3), L_{max} is the length of the longest branch of a polygon, RB_c is an arbitrary critical length ratio and S_c is a critical slope angle.

To assess the accuracy of the algorithm we have applied it to an inventory of landslides triggered by the 1994 Northridge earthquake in southern California (Harp and Jibson, 1996). Within the bounds of the Santa Susanna Mountains, we manually screened all 2083 mapped polygons larger than $1000m^2$ for amalgamation. This is close to the rollover in the landslide area-frequency distribution of the inventory, so that the test set encompasses most of the landslide volume. The Santa Susanna subset is representative of the diversity of size and shape that can be found in the Northridge inventory in its entirety. Of all polygons in the subset, the amalgamation state of 136 (6.52%) could not be ascertained visually. These polygons were removed from the test data set before further analysis. Of the remaining 1950 polygons, 617 amalgams and 1187 single landslides were correctly classified by our algorithm. The algorithm missed 70 amalgams (3.6% of false negatives, that is undetected amalgams) and wrongly classified 76 single landslides as amalgams (3.9% of false positives, that is correct polygons classified as amalgams) (Table 2.1). About two thirds of all polygons classified as amalgams were detected using the branching criterium, in part because it is the most easily detectable feature but also because it is the first step of the algorithm. One third of amalgamation cases were only diagnosed by the second step of the algorithm, which considers the

Table 2.1 – Confusion matrix of the algorithm tested on the 1950 independently verified polygons larger than $1000m^2$, from an inventory of landslides triggered by the 1994 Northridge earthquake. Positive and negative conditions refers to polygons considered amalgamated and correct, respectively. Therefore, false positives are correctly mapped polygons erroneously identified as amalgams whereas false negatives are amalgams that remain undetected by the algorithm. Values are given as number of landslides and percent of the total population. The algorithm was run with the following parameters: Resolution 2m, $K_c = 2$, $S_c = 12°$and $RB_c = 5$ for the upper part of the table and $RB_c = 6$ for the lower part.

True positive: 617 (31.6%)	False positive: 76 (3.9%)	Positive predictive rate = 89.0%
False negative: 70 (3.6%)	True negative: 1187 (60.9%)	Negative predictive rate = 94.4%
Sensitivity = 89.8%	Specificity = 94.0%	Accuracy = 92.5%
True positive: 653 (33.5%)	False positive: 94 (4.8%)	Positive predictive rate = 87.4%
False negative: 52 (2.7%)	True negative: 1151 (59.0%)	Negative predictive rate = 95.7%
Sensitivity = 92.6%	Specificity = 92.5%	Accuracy = 92.5%

topographic context of a polygon. Taking results from these two steps together, the overall accuracy of the algorithm was very good, with 1804 of 1950 (92.5%) polygons in the test set classified correctly (Table 2.1). Thus, our algorithm provides a relatively rapid and accurate way to assess the quality of a dataset and a partial guide to manual correction. It can reduce the workload associated with manual splitting of amalgamated polygons, by shortening the amalgam identification phase, and enhancing the detection of smaller amalgamated polygons that may have only subtle distortions. However, the algorithm only yields a minimal number of branches and the automatic and accurate splitting of complex polygons based on detected branching geometry remains a challenge.

The algorithm can assess the quality of every polygon of an inventory as long as the raster resolution is high enough for a polygon to be made up by at least a few tens of cells, so that a skeleton can be defined. Therefore, at a raster pixel size of 2m, $100m^2$ polygons would have about 25 pixels and could be analysed by our algorithm. This is lower than the usual roll-over of landslide area-frequency distribution (e.g., Malamud et al., 2004a; Brardinoni and Church, 2004). DEMs with a high spatial resolution will also yield better results and the accuracy of the detection is helped by the fact that the algorithm uses raw elevation data rather than a local derivative such as slope, which is calculated over several adjacent cells.

2.6 Discussion

We have proposed an algorithm based on polygon geometry and topographic analysis, which allows automatic detection of polygons outlining amalgamated landslides with good but incomplete detection rates and minimal diagnostic error. However, depending on the objective of a study, even a few wrongly diagnosed polygons may be of concern. Therefore, the algorithm must be tuned towards a reduction of false negative results, by increasing RB_c or S_c, even if the rate of false positive results increases as a consequence. For example, raising RB_c from 5 to 6 in the analysis of landslides in the Santa Susanna Mountains results in a useful 24% reduction of false negative results, from 70 to 52 polygons out of 1950, and a concomitant increase of false positive results by 16% from 76 to 90 polygons (Table 2.1). However, increasing

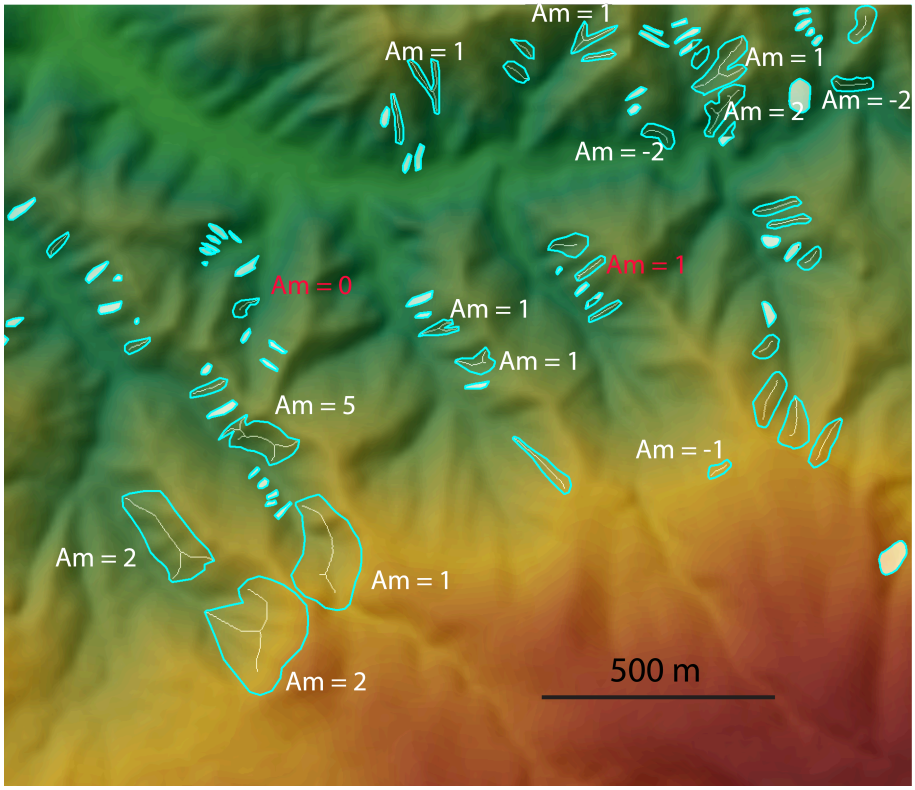

Figure 2.5 – Part of the Northridge landslide polygon inventory overlaid on a hillshaded DEM. The skeleton raster output is shown for all polygons larger than $1000m^2$ and with $K >= 2$ (35 polygons). Polygons with $K < 2$ are filled in white and considered clean. White labels show erroneous polygons detected by the algorithm, with positive numbers giving the number of secondary branches detected, -2 meaning ridge or river crossing and -1 indicating a slope smaller than 12°. Red labels show wrongly diagnosed or dubious results within this sample. Polygons with skeleton but no labels have been correctly classified as unamalgamated.

S_c to 15°or more may increase significantly the number of false positives but not necessarily the number of true positives as the most common type of amalgamation is related to multiple branches. An increase of false positives is not an issue, if amalgams detected by the algorithm are subsequently split manually. In that case, the operator can decide to leave an incorrectly diagnosed polygon intact. However, false negatives will go unnoticed and could have a large impact. Therefore, it is advisable to perform an additional manual check of the largest polygons in a data set, irrespective of how the classification algorithm has diagnosed them, especially for applications where the importance of polygons is proportional to their size. For example, one false negative within the 10 or 20 largest landslides in an inventory could significantly affect estimated total landslide volume.

A second, more fundamental issue is that the algorithm considers polygon geometry, in a way which does not allow detection of ellipsoid-shaped amalgams. Examples of this can be found, amongst others, in an inventory of landslides triggered by the 2008 Wenchuan earthquake (Gorum et al., 2011), where several landslides on the same slope were sometimes merged into larger, relatively smooth, polygons with a low K value and without any clear geometric or topographic indication of amalgamation (Figure 2.2). In this case, image resolution may have been too low to distinguish the separate landslides, or the mapper may have simplified the geometry for convenience. For such

amalgams, even if another criteria, such as alignment of the polygon long axis with the strike of the topographic slope, hints at possible amalgamation, high-resolution imagery would be required to test the diagnosis, as single landslides with similar shape and orientation may exist. Merger of parallel landslide outlines due to image resolution limitations may cause errors of similar magnitude as other types of amalgamation, which are more easily detected, and could critically affect the common argument that at a given pixel resolution small landslides are missed but everything above a cutoff lengthscale of a few cells is properly mapped. Because the high-resolution imagery required to check visually for the occurrence of low-K amalgamation, or any other type of amalgamation, is rarely available to end-users of landslide inventories, it is important that it is mitigated for by those who develop the mapping techniques and acquire the landslide inventories. This may not always concur with the principal objectives of a particular mapping effort, for example in natural disasters when rapid assessment of the location and total extent of landslides is of the essence. However, if a landslide inventory is to be of general use to the research community, then the risk of amalgamation must be suppressed, both in manual and automatic mapping.

Suppression of landslide polygon amalgamation is hampered by deeper issues, such as image resolution and the uncontrolled subjectivity introduced in binary landslide mapping, where every pixel either is or is not a landslide. We draw into question the general assumption that in a given inventory, every landslide larger than a few image pixels is correctly mapped (e.g., Liao and Lee, 2000). Instead, it is reasonable to expect that many disturbed areas mapped as single medium to large landslides could in fact consist of groups of smaller landslides, giving potentially significantly different erosion volumes and size statistics (Figure 2.2). Moreover, satellite imagery does not always yield unambiguous information about the number and shape of landslides which occurred on a given slope. Where this applies, subjective choices of the mapper are crystallized within the landslide inventory. A Bayesian approach to mapping, aimed at delivering probabilistic instead of binary maps (e.g., Mondini et al., 2013) could be helpful in testing the different possibilities of splitting complex disturbed areas (see Figure 2.2) and ultimately deliver more accurate, objective and reproducible datasets.

Short of a practicable, comprehensive solution, our method, which has a good reliability, can be used in several ways to mitigate for amalgamation in landslide maps, by helping the mapper to identify mistakes in automatic mapping, and the user to do the same in existing landslide maps. Notably, sorting mapped polygons by K value and size allows rapid, first order vetting of the largest landslides, which, when followed by manual splitting of amalgams, will be enough to yield a reasonable estimate of the total volume of landslides in an inventory. Then, for large populations, one could exclude all polygons with K values above a threshold and consider the correlation between the size or location of remaining landslides and physical parameters such as local topographic slope or triggering effects. Finally, a K value criteria might also be introduced in a semi automatic algorithm detecting landslides, to guide iteratively towards a sound splitting of adjoining landslides.

In the end, we must recall that amalgamation even if it may be a major source of errors, such as in the Wenchuan example , it is not the only one. Firstly, anthropogenic clearance or other disturbance of the landscape may be mistaken for a landslide, especially by automatic algorithms. Secondly, when scar, transport and deposit areas cannot be differentiated the volume of landslides with long runout may be substantially over-

estimated. Thirdly, when landslides are reactivated and previously stable parts of the landscape are not involved, then it may be hard for the mapper to delineate the area of the actual failure with accuracy and this new failure may also not yield a volume as large as expected from area-volume relationships. These issues may be difficult to deal with but their effects will be suppressed when high resolution imagery is used by an experienced mapper. Additionally, systematic ways of dealing with these issues, such as the flagging reactivated landslides, and the differentiation of the transport areas of debris flow or long runout landslides, should be practiced by mappers and also considered by users analysing old data.

2.7 Conclusion

We have shown that amalgamation, the bundling of several adjacent landslides into a single map polygon, is a common problem in landslide inventories and has inflated estimates of landslide volumes by up to a factor of three, and the power-law exponent of landslide area-frequency distributions by up to 50%. Even though the design of comprehensive and fully reliable automatic corrective method remains a challenge, we have presented and tested a practical algorithm for automatic detection of amalgamated polygons based on geometric and topographic considerations. The algorithm performs well, with an accuracy of 92.5% and only $2.7 - 3.6\%$ amalgams missed and $3.9 - 4.8\%$ correct mapped polygons wrongly classified. It can, therefore, be used to automate the identification of landslide amalgams, accelerate the evaluation of datasets, and guide the manual correction of amalgams. Thus, our algorithm is a first step towards setting a quality standard for landslide maps in order to derive scientifically and societally useful variables, such as risk estimates, erosion rates, organic matter fluxes, or correlations between landsliding and physical triggers, as accurately as possible. Further challenges lie in attempting to automatically correct amalgamation and in assessing how mapping errors due to resolution blurring propagate into final products derived from landslide maps.

Link

In Chapter 2, I have investigated the effect of amalgamation - the bundling of several landslides into a single mapped polygon - on common measures characterizing landslide inventories, such as total landslide volume and landslide frequency-size distribution. Errors could lead to up to a factor of 3 of total volume over-estimation and up to 50% change in the distribution scaling exponent. I have proposed an algorithm to automatically detect potentially erroneous polygons and isolate them or correct them. Detection and mitigation of such errors is required in order to confidently assess the amount of erosion produced by a given landsliding event, whether due to an earthquake or a storm. Therefore, removing amalgamation of landslide inventories is essential to adequately constrain the total landslide volume caused by earthquakes and test the predictions of any model of earthquake-induced landsliding, such as the model presented in Chapter 3. Accurate volume estimates are also important to quantify the temporal evolution of landslide rate before and after an earthquake, required in Chapter 4 to assess persistent effects of earthquakes on hillslope susceptibility, and in Chapter 6, where the contribution of both coseismic and post-seismic landsliding is compared to the uplift due to the earthquake.
In the next Chapter, I develop a seismologically-consistent model with the aim of predicting the total volume of landslides caused by a given earthquake. I build this expression by acknowledging important seismological aspects controlling the strong ground motions associated with an earthquake, which are responsible for the slope failures. Such models critically need to be tested and calibrated against a large number of earthquakes for which field reports or landslide maps give accurate constraints on the amount of landsliding.

Chapter 3

A seismologically-consistent expression for the total area and volume of earthquake-triggered landsliding.

Abstract

We present a new, seismologically consistent expression for the total area and volume of populations of earthquake-triggered landslides. This model builds on a set of scaling relationships between key parameters, such as landslide spatial density, seismic ground acceleration, fault length, earthquake source depth and seismic moment. To assess the model we have assembled and normalized a catalogue of landslide inventories for 40 shallow, continental earthquakes. Low landscape steepness systematically leads to over-prediction of the total area and volume of landslides. When this effect is accounted for, the model predicts within a factor of 2 the the total landslide volumes for 63% of the 40 events ($R^2 = 0.76$), against 23% of correct predictions ($R^2 = 0.46$) for the previously published empirical expression based on moment only. The prediction of total area is also sensitive to the landscape steepness, but less than the total volume, and seems also affected by controls on the landslide size-frequency distribution and possibly the shaking duration. Some outliers in terms of estimated total landslide volume are likely associated with exceptionally strong rock mass in the epicentral area, while others may be related to seismic source complexities ignored by the model. However, the close match between prediction and estimate for 63% of the events suggests that, despite the variety of lithologies and tectonic settings covered, rock mass strength is similar in many cases and that our simple seismic model is often adequate. This makes our expression suitable for integration into landscape evolution models, and application to the assessment of secondary hazards associated with earthquakes. [1]

1. This work was in the final round of review at JGR-ES. By the time of the final thesis publication it has been typo-edited, formatted and published as : Marc, O., Hovius, N., Meunier, P., Gorum, T., and Uchida, T.: A seismologically consistent expression for the total area and volume of earthquake-triggered landsliding, Journal of Geophysical Research: Earth Surface, 121, 640–663, doi: 10.1002/2015JF003732, 2016b.

Notation

Symbols with a bar are average values for the whole fault or affected area (ex: $\bar{R}_0$, $\bar{\alpha}$ ...).
All acceleration terms are normalized by the gravitational acceleration, and therefore non-dimensional.
a_c, Threshold acceleration for ground damage ()
a, Ground acceleration ()
A', V', Individual landslide area or volume (m^2 or m^3)
A, V, Estimated total landslide area or volume (m^2 or m^3)
A_p, V_p, Predicted total landslide area or volume (m^2 or m^3)
A_p^s, V_p^s, Predicted total landslide area or volume normalized for steepness (m^2 or m^3)
A_{topo}, Available topography corrector ($\%$)
b, Inferred acceleration due to waves at 1km from the seismic source and a given frequency (m)
b_{sat}, Saturation acceleration for the scaling of b (m)
C_1, C_2, Empirical constants for fault size scaling with moment (cf., Leonard, 2010)
e_5, e_6, e_7, Empirical constants for b scaling with moment (cf., Boore and Atkinson, 2008)
f, Seismic wave frequency (Hz)
H_s, Seismogenic zone thickness (km)
L, Fault plane length (km)
l_{asp}, Asperity length scale (km)
M_h, Hinge magnitude above which b saturates ()
Mo, Seismic moment (N.m)
M_w, Moment magnitude ()
P_{LSA}, P_{LSV}, Landslide area density (m^2/km^2) and landslide volume density (m^3/km^2)
R, Distance between earthquake source and considered topography (km)
R_0, High frequency waves source depth (i.e., mean asperity depth) (km)
R_H, Horizontal distance from the surface projection of the earthquake source (km)
R_{HMAX}, Maximal horizontal distance at which landsliding occur (km)
$\bar{S}$, dS, epicentral average and local deviation of the site effects amplification of a ()
S_{mod}, Modal slope of the affected hillslopes (i.e., affected topography excluding flat lands) (°)
T_{SV}, T_{SA}, Empirical steepness constant for total volume and total area (°)
α_A, α_V, Landscape propensity to failure for acceleration exceeding a_c ($m^2.km^{-2}$ or $m^3.km^{-2}$)
δ_A, δ_V, Material propensity to failure (independent of slope geometry) ($m^2.km^{-2}$ or $m^3.km^{-2}$)
λ,γ, Empirical constants for area-volume scaling of landslides ()
μ, Elastic shear modulus (Pa)
ρ, Landslide area-frequency distribution decay exponent ()
θ, Angular coordinate (°)

3.1 Introduction

Earthquake-triggered landslides are a major hazard and cause of secondary losses associated with earthquakes, with effects sometimes exceeding those of direct shaking (Bird and Bommer, 2004). Moreover, due to widespread triggered landsliding, earthquakes can be important drivers of continental erosion (Keefer, 1994; Malamud et al., 2004b) and they have been found to be important actors in mountain building and landscape evolution (Hovius et al., 2011; Li et al., 2014). Models permitting the prediction or rapid estimation of the total area or total volume of landsliding due to earthquakes can therefore aid in seismic hazard assessment and disaster management as well as explorations of landscape evolution in tectonically active settings.
Not surprisingly, seismic moment has been shown to be a first-order control on the area affected by landsliding (Keefer, 1984; Rodriguez et al., 1999) and the total volume of triggered landslides (Keefer, 1994). However, the scatter in simple relations between total landslide volume and earthquake moment amounts to an order of magnitude at least. This is because the spatial density of landslides is, all else being equal, set by the intensity of ground shaking (Meunier et al., 2007). Therefore, seismic wave attenuation and site effects determine the spatial distribution of landslides in detail (Meunier et al., 2008, 2013). Hence, a predictive and accurate model for the total volume of landslides caused by earthquakes should incorporate not only the earthquake magnitude (e.g., Keefer, 1994) but also effects such as the loss of seismic wave energy with distance from source or the non-linear scaling between seismic moment and ground shaking. Importantly, the effects of strong motion are modulated by the local topographic slope and the effective strength of its substrate (e.g., Parise and Jibson, 2000; Yagi et al., 2009; Gorum et al., 2011, 2013). These parameters are at the core of slope stability analysis (e.g., Newmark, 1965), which, although simplified, offers a physical description of the probability of failure of a given slope during an earthquake. Ultimately, then, knowledge of the earthquake rupture initiation and propagation, translated into a model of ground shaking accurate at the hillslope scale and coupled with a robust slope stability analysis would allow prediction of landslide areas and volumes without empirical calibration.
Efforts to predict slope failure have mainly taken the form of pseudostatic (e.g., Terzaghi, 1950), stress-deformation (e.g., Clough and Chopra, 1966) and permanent displacement (e.g., Newmark, 1965) analyses, the rationale, advantages and limitations of which have been comprehensively reviewed by Jibson (2011). These approaches require extensive and detailed knowledge of the spatial distribution of ground shaking, topographically induced driving stresses, and of the local rock mass strength (Dreyfus et al., 2013). It is, therefore, impractical at larger scales, even if recent work suggests that it can be used to invert rock strength a posteriori (Gallen et al., 2015). In the absence of the required local knowledge a priori, we propose not to model individual slope failures, and introduce a model based on average properties of the forcing mechanism (i.e., the shaking) and of the landscape (i.e., steepness, strength and hydrology) on which it acts. The model presented aims at the prediction of the bulk response of a landscape to earthquake strong ground motion, giving the total volume and area of the population of triggered landslides, based on seismological scaling relationships and empirically adjusted for geomorphic sensitivity. It should allow for estimation of secondary risks associated with an earthquake scenario with reduced predictive uncertainties, and for improved evaluation of the role of climatic and seismic forcing of

erosion in mountain belts where landsliding is the dominant erosion mechanism (Hovius et al., 1997). To determine the accuracy of this model, we have calibrated it against a compilation of landslide inventories for 40 earthquakes for which seismological information was available.
In this paper, we summarize the available landslide inventories and the methods used to obtain conservative estimates of total landslide volume they represent. Then, we derive a seismologically-consistent model predicting total landslide area and volume for a given earthquake and landscape. To support this, we constrain empirically the link between the probability distribution of the topographic slopes in an earthquake area and the landscape response to seismic shaking. Finally, precision and limitations of the model are discussed before we close with two example applications, exploring the possible landsliding triggered by an expected scenario earthquake on the Alpine Fault, bounding the Southern Alps of New Zealand and by the recent $M_w 7.8$ Gorkha earthquake in Nepal.

3.2 Data and Methods

3.2.1 Earthquake and Landslide Data

We compiled previously published information allowing estimation of total landslide area, A, and/or volume, V, for 40 shallow ($< 25km$), onshore earthquakes (Section 2.2, Suppl. Fig 3.7, Suppl. Table 3.7). The estimated numbers of triggered landslides range from $\sim 10^2$ to $\sim 10^5$ per event, affecting a wide range of climates (from arid to tropical to periglacial), lithologies (from carbonates to volcanic rocks and metasediments) and topographies (from active mountain ranges to fjords and volcanic landscapes). All types of landslides were considered, most inventories contain soil, mixed, and bedrock landslides and do not explicitly discriminate between them. Mapped landslides had variable amounts of displacement, but fissures and other disturbance with negligible displacement ($< 1m$) are ignored. The complexities of landslide mechanism and mobility are beyond the scope of this paper. For 10 cases, V could be derived from published landslide area inventories (Harp et al., 1981; Harp and Jibson, 1996; Liao and Lee, 2000; Yagi et al., 2007, 2009; Meunier et al., 2008; PWRI, 2009; Gorum et al., 2011, 2013, 2014), using empirical V-A relationships (Larsen et al., 2010). To this, we added the case of the 1991 Limon (Costa Rica) earthquake, for which we mapped the landslides from 30m-resolution Landsat images (Suppl. Fig 3.8). These inventories consist of mapped polygons delineating areas disturbed by landslides (i.e., scar, runout and deposit) but excluding debris-flow transport and deposition along channels. They were scanned and corrected for mapping errors including amalgamation (Marc and Hovius, 2015) and for completeness for landslides larger than $10,000m^2$, which dominate the total eroded volume (Hovius et al., 1997). The 29 other cases are less well constrained, because V was extrapolated based on published area-frequency distributions or on information about a limited number of large landslides (Bonilla, 1960; Govi and Sorzana, 1977; Pearce and O'Loughlin, 1985; Harp and Jibson, 1996; Jibson et al., 1994; Keefer, 1994; Schuster et al., 1996; Hancox et al., 1997; Antonini et al., 2002; Hancox et al., 2003, 2004; Jibson and Harp, 2006; Mahdavifar et al., 2006; Owen et al., 2008; Evans et al., 2009; Guzzetti et al., 2009b; Alfaro et al., 2012; Has et al., 2012; Gorum

et al., 2014; Xu et al., 2014a,b; Barlow et al., 2015; Tang et al., 2015) (see Suppl. Table 3.7, 3.7). Using landslide density gradients away from seismogenic faults or earthquake epicenters, we have ascertained that all comprehensive inventories and detailed field reports in our catalogue have sufficient spatial coverage to capture the bulk of landsliding caused by an earthquake. Amongst the 40 cases in our database, the total landslide area, A, could be constrained only for the 11 comprehensive inventories and six further cases with detailed mapping of large and intermediate size landslides (Suppl. Table 3.7). In the other 23 cases, information was limited to the larger landslides, which tend to dominate the total landslide volume, but not the total area. As an example, in our 11 comprehensive inventories, the 1% largest landslides represent $53 \pm 22\%$ of V but only $21 \pm 8\%$ of A.

Though other studies have considered relations between the total landslide number and earthquakes parameters (Keefer, 2002; Gorum et al., 2014), we did not focus on this statistic because we consider it the most ill-constrained. Importantly, the total landslide number is dominated by the smallest landslides. Such landslides are not systematically accessible for most earthquakes, and tend to be easily censored or amalgamated even with recent imagery (Stark and Hovius, 2001; Marc and Hovius, 2015). Therefore, even if the total landslide number is an important variable for landslide hazard, the available counts are not sufficiently robust in most cases, and we do not attempt to analyze or model them.

Our database includes earthquakes ranging from moment magnitude M_w 5 to 8.6 (Figure 3.1). These are mostly reverse fault earthquakes (N=25) but also strike-slip (N=11) and normal fault events (N=4), as determined from their focal mechanism. The hypocentral depths range from a few km to 24 km. However, it has been shown that the pattern of landsliding in two particularly well-constrained earthquakes is best explained by considering the main slip patch rather than the hypocentre as the dominant wave source (Meunier et al., 2013). From a seismological point of view, asperities on which most of the coseismic slip occurs are considered to be an important source of high frequency waves ($> 0.5Hz$) (Ruiz et al., 2011; Avouac et al., 2015), that we consider dominant for landslide triggering (See section 3.2). For about half of the earthquakes in our database, the mean asperity depth along the fault rupture, R_0, could be estimated from published seismological rupture inversions (Yoshida and Koketsu, 1990; Wald et al., 1991, 1996; Zeng and Chen, 2001; Hernandez et al., 2004; Hikima and Koketsu, 2005; Pathier et al., 2006; Tan and Taymaz, 2006; Elliott et al., 2007; Cirella et al., 2009; Hashimoto et al., 2011; Wei et al., 2011; Cheloni et al., 2012; Fielding et al., 2013; Sun et al., 2013; Zhang et al., 2014) (Suppl. Table 3.7). For less constrained cases, we set R_0 at the hypocenter, or at half the hypocentral depth when surface rupture occurred or when the earthquake exceeded M_w 7.5 (Given et al., 1982; Kawakatsu and Cadena, 1991; Kikuchi and Kanamori, 1991; Stein and Ekstrom, 1992; Anderson et al., 1994; Stevens et al., 1998; Doser et al., 1999; Abercrombie et al., 2000; McGinty et al., 2001; Januzakov et al., 2003; Berryman and Villamor, 2004; Hancox et al., 2004; Hamzehloo, 2005; Legrand et al., 2011; Alfaro et al., 2012; Has et al., 2012), with the exception of the 1991 Limon (Costa Rica) case. The 1991 Limon earthquake ruptured a listric fault with a hypocenter at $\sim 24km$ depth, on a flat detachment, which steepened sharply offshore (Suarez et al., 1995). Seismological evidence indicates that in this earthquake, most of the moment was released at 15-20km North of the hypocenter, along the flat detachment, and therefore we have set the mean asperity depth at 20km (Goes et al., 1993). Under-constrained events were assigned a larger uncertainty in the modeling (Suppl.

Table 3.7). Three events are very poorly constrained and we did not set a single mean asperity depth but rather a range of 1.5 to 4.5 km, 4 to 12 km and 8 to 24 km for the 1957 Daly City (USA), the 1950 Assam (India) and the 1855 Wairapa (New Zealand, NZ) earthquakes, respectively (Bonilla, 1960; Molnar and Qidong, 1984; Darby and Beanland, 1992).
We assume that this database is sufficiently large and comprehensive to distinguish first-order controls on earthquake-triggered landsliding from local, secondary effects.

3.2.2 Estimation of Total Landslide Volume

We used published area-volume relationships, $V' = \lambda A'^{\gamma}$ (Larsen et al., 2010), to estimate the volume of a landslide, V', from its mapped disturbed area, A'. Following Larsen et al. (2010) it was assumed that landslides with $A' > 10^5 m^2$ involved bedrock, and that smaller landslides were mixed bedrock and soil failures. Landslide maps typically do not distinguish between scar and deposit, lumping the two in one area measure, although the relevant volume, in fact, would be that of the landslide scar. As a systematic way to constrain runout variations is not available, we have applied a blanket correction to reduce the total area of a landslide to its scar area, thus obtaining a conservative volume estimate. According to Larsen et al. (2010), scars and deposits have area-volume relations with the same power-law exponent, implying constant size ratios between scar and deposit areas of 1.1 and 1.9 for mixed and bedrock landslides, respectively. Hence, we estimated the scar area by dividing the mapped landslide area by 2.1 and 2.9 for mixed soil and bedrock and solely bedrock landslides, respectively, assuming that runout distance was equal to the scar length. This may lead to an overestimation of landslide scar volume where runout was much longer, mostly for small slides, which do not contribute significantly to the total eroded mass. Conversely some large landslides on gentle slopes have overlapping scar and deposit areas, meaning that our correction may causes significant underestimation of the scar size and thus the landslide volume.
Rare field estimates of the volume of one or a few large earthquake-triggered landslides agree with our landslide volume estimates, supporting our assumption of a reduced proportionality of perturbed area to scar area. In Nagano, the mapping was derived from airphoto interpretation and seems restricted to scar areas. In this case, the uncorrected mapped area of the landslide on Ontake volcano gave a volume estimate of $\sim 20 Mm^3$, closer to the field estimate of $\sim 34 Mm^3$ (Voight and Sousa, 1994). Therefore, we did not apply an area correction to estimate the scar areas in this inventory.
We calculated the volume of every individual landslide in a catalogue, and summed to obtain a total volume of landslides for each earthquake. Uncertainties in our approach include the coefficient and exponent of the landslide area-volume relations, with reported standard deviations of 0.005 for both σ_λ and σ_γ for mixed bedrock-soil landslides and of 0.02 and 0.03 on σ_λ and σ_λ, respectively, for bedrock landslide scars (Larsen et al., 2010). For mapping errors, a standard deviation of 20% of the mapped area was arbitrarily assumed. Assuming no covariance between these three sources of uncertainties, we used Gaussian propagation of error to obtain $1 - \sigma$ uncertainties on the volume of each mapped landslide, V'. Further, the standard deviation on the total landslide volume for an earthquake was calculated assuming that the volume of each individual landslide was unrelated to that of any other, ignoring possible co-variance. Hence, the uncertainty on the total volume, reported in the supplementary Table 3.7,

depends heavily on the size distribution of landslides. When the total landslide volume is dominated by many medium sized landslides in a population, then the uncertainty on the total volume estimate is small, because it is unlikely that all important individual landslide volumes are biased in the same way (e.g., the 1994 Northridge (USA) and 2010 Haiti (Haiti) cases). However, when the total volume is dominated by a few very large landslides, then the uncertainties on their volumes are less likely to cancel out, which leads to a large uncertainty on the total volume estimate (e.g., 1984 Nagano (Japan) and 2008 Iwate (Japan) cases).
For earthquakes without exhaustive landslide inventories we estimated the total landslide volume using one of the following methods. In the best cases, published frequency area distributions were used to estimate the number of landslide for a given size range and converted to volumes as outlined above. However, for most larger earthquakes, volumes were reported only for a limited number of very large landslides, typically < 20 landslides $> 0.5Mm^3$ (Suppl. Table 3.7). For comparison, the ten largest landslides of 8 of our 11 comprehensive inventories comprised 20% to 86% of the total landslide volume, V, and $51\pm23\%$ on average, excluding the Haiti, Northridge and Limon cases, which did not have any landslides larger than $0.5Mm^3$. Hence, in some cases all the small landslides together could have a smaller volume than the uncertainties on the volume of the large landslides, but in other cases the total volume of small landslides could be five times that of the large ones. For simplicity, we assumed that the reported landslides were indeed the largest, that their volume V_L represented $\sim 66\%$ of V, and that the $2-\sigma$ uncertainty range of V extends between 75% and 400% of V_L, accounting for the uncertainties on the total landslide volume estimate in this way. Finally, for a few earthquakes (1950 Assam (India), 1989 Loma Prieta (USA), 1987 Reventador (Ecuador), 1980 Mammoth (USA) and 1983 Coalinga (USA)), an estimate of the total landslide volume was published without further information on uncertainties or on the size of individual landslides and for some others (2005 Kashmir (Pakistan), 2002 Avaj (Iran) and 2013 Lushan (China)) only the largest landslide was described. Assuming a universal area-frequency distribution, a total volume can be estimated from the largest landslide (Eq 27 and 33 of Malamud et al. (2004b)). This assumes implicitly a volume scaling that is biased upward ($V' \sim 0.05A'^{1.5}$), but given the other sources of uncertainty on the landslide area-frequency distribution and on the volume of the largest landslide, we simply use the relationship provided by Malamud et al. (2004b). Note that estimates from the previous methods are not inconsistent with, and mostly within a factor of 3 of this crudest type of estimate (Suppl. Table 3.7). Nevertheless, these eight cases are certainly the least constrained in our catalogue, and we therefore allocate an arbitrary uncertainty range of a factor 4 to them, greater than the uncertainty range of any other methods (Suppl. Table 3.7). Finally, the 2011 Lorca (Spain) and 2004 Rotoehu (NZ) earthquakes triggered only a few tens of slides and 100-200 small rock falls, and we estimated the total volume range based on field photographs and reported volumes. This too is crude, but, because of the limited number of landslides and the small size of the larger events, we consider the total landslide volume to be relatively well constrained compared with the eight uncertain cases discussed above.

3.2.3 Case Specific Corrections

Robust and uniform estimation of landslide volumes from available maps relies on the accuracy and consistency of mapping between the different datasets. An issue of particular importance in this respect is amalgamation, that is the bundling of multiple adjacent landslides into a single larger map polygon. Compounded with a landslide area-volume relation favouring the largest landslides, this can give rise to significant overestimation of the total landslide volume. We have discussed this issue, its consequences and how to detect associated mapping errors elsewhere (Marc and Hovius, 2015). Here, we briefly review how individual datasets have been corrected for its effects.
Amalgamation has affected a previous estimate of the volume of landslides triggered by the 2008 Sichuan (China) earthquake (Parker et al., 2011; Li et al., 2014), which, at $5 - 15km^3$, was substantially higher than our value of $2.3 \pm 0.25km^3$, even though we have used a landslide map with larger extent (Marc and Hovius, 2015). However, amalgamation is also evident in the mapping used for our volume estimate (Gorum et al., 2011) and we manually split the largest 152 landslides of the catalogue, which dominate the total volume. Because of our limited ability to comprehensively remove amalgamation across the full range of polygon sizes, the total landslide volume for the Sichuan event must be considered to have a slight upward bias. The same argument holds for the 1976 Guatemala (Guatemala), 1999 Chi-Chi (Taiwan) and 1994 Northridge (USA) earthquakes, for which the landslide inventories have been edited for amalgamation giving minimum volume reductions of 35%, 38% and 16%, respectively (Marc and Hovius, 2015). Finally, for the Aysen Fjord inventory we split 11 polygons larger than $0.1Mm^2$, including the three largest ones, into 37 and obtained a volume reduction of 29%. Although occasional amalgamation of relatively small landslides may also affect the other datasets, it is not considered to be a major source of errors and it was not mitigated for systematically.

3.3 Modeling the Volume of Seismically Induced Landslides

An empirical relation between total landslide volume, V, and the seismic moment, Mo, with the form of a sublinear power law, was first presented by Keefer (1994). It was based on 15 earthquakes, spanning a large range of magnitudes and hypocentral depths, including some subduction earthquakes. In assembling our extended database of 40 events, we eliminated the subduction earthquakes and focused only on continental, crustal events with an uncertainty assessment, as described in the previous section. Subduction events are typically deep ($> 30km$) and offshore, meaning that only a fraction of the emitted waves reach onshore high standing topography, after significant attenuation. Onshore strong ground motion in such earthquakes is commonly only moderate, yielding relatively small landslide numbers, areas and volumes (Lacroix et al., 2013; Wartman et al., 2013) (Fig. 3.1). In such cases, landsliding tends to be strongly influenced by site characteristics and site effects, negating several assumptions of our model approach. An orthogonal best fit to our data has the landslide volume scaling with the seismic moment to the power of three-halves ($Mo^{3/2}$, $R^2 = 0.6$), but it does not capture all physical processes and their associated parame-

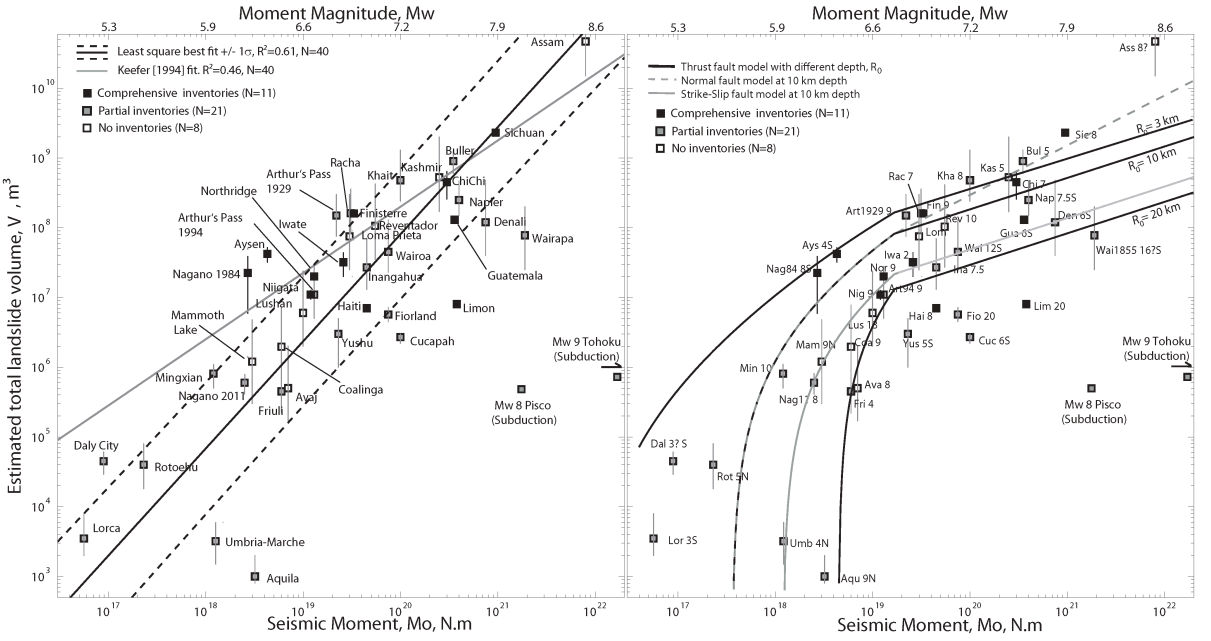

Figure 3.1 – A: Estimated total landslide volume with $2-\sigma$ uncertainties plotted against seismic moment for 40 shallow continental earthquakes (Suppl. Table 3.7). The gray line is the empirical relationship proposed by Keefer (1994), derived from a smaller database. The solid and dotted lines are the orthogonal least-squares best fit to our dataset and its $1-\sigma$ uncertainties. B: Comparison of the same data with our seismologically-consistent model. At this stage the model lines do not depend on any fitted parameters but only on earthquake observables.Name codes abbreviated to their first 3 character, followed by the mean asperity depth and S or N for strike-slip or normal events, respectively. The three black lines represent our analytical prediction of landslide volume dependency in moment for various mean asperity depths, R_0. The solid and dashed gray lines represent our predictions for normal and strike-slip fault mechanisms, respectively, for asperities at 10 km depth. For references, the estimated total volume of two subduction earthquakes (Tohoku (Japan) and Pisco (Chile)) are plotted. Landslide frequency-size distribution published by Lacroix et al. (2013); Wartman et al. (2013) were converted to volume, using the relationship of Larsen et al. (2010), and integrated to obtain the estimated total volume. Their volume is similar to the ones of events of $M_w \sim 6$.

ters, which are relevant to landsliding. More than one order of magnitude of scatter remains for a given earthquake moment (Figure 3.1), indicating that additional parameters affect the total volume of landslides triggered by earthquakes,

An accurate prediction of earthquake-triggered landslide volume requires the specific acknowledgment of the role of a range of seismological, topographic and mechanical parameters. The relation between ground shaking and landsliding has now been firmly established for a number of earthquakes (Harp and Jibson, 2002; Meunier et al., 2007; Yuan et al., 2013), highlighting the need to account for wave attenuation with distance from the earthquake source. Moreover, it is clear that hillslope-scale rock strength and local topographic attributes of gradient and relief modulate the propensity to failure of a landscape undergoing shaking (e.g., Schmidt and Montgomery, 1996; Parise and Jibson, 2000; Yagi et al., 2009; Gorum et al., 2013). Below, we combine recent observational constraints on earthquake-triggered landslides with seismological scaling relationships and a statistical approach to landscape sensitivity.

3.3.1 Model development

Typically, earthquake-triggered landslides are considered to occur when transient driving stresses on a potential failure plane due to variable ground shaking exceed the resisting stresses (Newmark, 1965). To predict the earthquake-triggered landsliding across a landscape, this approach requires the assessment of the stresses and mechanical properties over the whole topography (Dreyfus et al., 2013). We propose an alternative approach, relating landsliding primarily to strength reduction caused by ground shaking, and argue that it is adequate for modelling of landsliding at the landscape scale. We then consider effects modulating the ground shaking such as the scaling of seismic source emission with moment, the wave attenuation with distance from the source and the scaling of the number of point sources with the fault size. In order to develop a simple analytical solution for our model, we made three major simplifications or assumptions that are discussed in section 3.2.
We neglected scattering and inelastic effects on wave attenuation and considered only geometrical spreading (Assumption 1). We assigned to the landscape above the seismogenic fault a uniform geomorphologic sensitivity and assumed the seismic directivity of the shaking may be neglected (Assumption 2). Lastly, we assumed that landslides are triggered by relatively high frequency S-waves ($\sim 1Hz$) (Assumption 3).
To develop our model, we start with the widely observed relationship between landsliding and ground shaking a (Harp and Jibson, 2002; Khazai and Sitar, 2004), using the simple statistical approach introduced by Meunier et al. (2007):

$$P_{LSV} = \alpha_V(a - a_c) \tag{3.1}$$

where P_{LSV} is the landslide volume density and α_V is a volume sensitivity term that sets the hillslope propensity to failure for a given shaking (in $m^3.km^{-2}$), and a_c is the minimum acceleration required for landsliding to occur. Note that throughout this study all acceleration terms are normalized by the gravitational acceleration g and therefore dimensionless. Equation 3.1 was originally proposed for landslide area, with a landslide area density P_{LSA} and area sensitivity α_A (in $m^2.km^{-2}$), but it holds also for a volumic density and sensitivity (Suppl. Fig 3.9). Though the original correlation in Meunier et al. (2007) was obtained with measured peak ground accelerations, we propose that Eq. 3.1 holds with a being the characteristic ground acceleration in the range of frequencies relevant for landslide triggering (See section 3.2). Note also that although we focus on acceleration in this work, ground velocity and strain have also been discussed as potential landslide triggers (Harp et al., 2014).
As we are interested in the cumulative volume of landslides across the landscape, a_c should be a global, relatively constant parameter, rather than vary between individual slopes. Supporting this generalization is the observation that earthquake-triggered landslides mostly occur in very steep slopes, $> 35 - 50°$ (e.g., Parise and Jibson, 2000; Lin et al., 2008; Gorum et al., 2013). Such slopes are typically steeper than the friction angle of the underlying material, and remain stable because of cohesion. In soil covered slopes, clay or vegetation promote cohesion. In bedrock, even steeper slopes ($> 45°$) may retain some cohesion, in spite of jointing. Moreover, several studies have postulated or found non-linear soil behavior or bedrock strength reduction, due to a drop of cohesion or dynamic friction reduction, caused by earthquake strong-motion (e.g., Wen, 1994; Sleep, 2011b,a; Marc et al., 2015). Therefore we propose that a_c is the threshold acceleration at which a sudden drop of cohesion, transient or permanent,

occurs in slope materials. Even if a_c may vary with the material properties at individual locations, these variations are likely much smaller than the variations of cohesion observed in different material, making it a relatively constant parameter. This assumption is supported by the fact that Eq 3.1 holds for different earthquakes in different landscapes with an almost constant value for a_c between 0.1 and 0.2 (Meunier et al., 2007; Hovius and Meunier, 2012; Yuan et al., 2013). It is also consistent with non-linear soil behavior starting at 0.15 g (e.g., Wen, 1994).

However, the number of slope failures does not only depend on the magnitude of the shaking-induced strength reduction, but also on the frequency of slopes steeper than the friction angle and on their cohesion ambient pore pressure. Therefore, the geomorphological complexity of the exact distribution of topographic relief, slope gradients and cohesion, as well as, the hydrologic influence of pore pressure of the hillslopes in a landscape are bundled into α while the term $a - a_c$ contains only the seismological effects controlling the ground shaking. This makes Eq. 3.1 a statistical description of a simplified slope stability analysis where the shaking term and the slope properties are separated. Explicit modeling of α is a major challenge because the landslide area and volume density depends not only on the number of slope failures but also on the mechanical processes that will define the depth and extent of the ensuing landslides (e.g., Stark and Guzzetti, 2009). Below we use seismological scaling relationships to relate a to earthquake characteristics and propose a first order empirical constraint on α based on landscape properties.

The ground shaking a mainly depends on the inferred source acceleration b (the acceleration carried by waves at 1 km from the source), the wave attenuation between source and surface and on the site and directivity effects (Boore and Atkinson, 2008). In order to derive an analytical prediction we neglect non-linear attenuation of seismic waves (Assumption 1), considering only their geometrical spreading. We also neglect any effects of directivity but discuss below when this may affect our model accuracy (Assumption 2). Further we consider that the site response of any hillslope can be written as a constant average response over the whole landscape $\bar{S}$ plus a deviation term dS. Then,

$$P_{LSV} = \alpha_V \left(\frac{b.(\bar{S} + dS)}{R} - a_c \right) \tag{3.2}$$

with R the distance between the source and the landscape cell of interest. Eq 3.2 cannot be solved because the spatial distribution of site effects, represented by dS, remains a major unknown. However, we are not trying to resolve the spatial distribution of landsliding but only the total volume caused by a point source, V_{ps}, that is the spatial integral of P_{LSV}. By definition $\int^{\theta} \int^{R} dS(R,\theta) dR d\theta \rightarrow 0$ and we can neglect this term, giving:

$$V_{ps} = \int^{\theta} \int^{R_H} P_{LSV} R_H dR_H d\theta = \int^{\theta} \int^{R_H} \alpha_V \left(\frac{b.\bar{S}}{R} - a_c \right) R_H dR_H d\theta \tag{3.3}$$

where R_H and θ are polar coordinates of any point at the surface above the projection of the seismic source at a mean depth R_0, with R_H following $R^2 = R_0^2 + R_H^2$ (Fig. 3.2). To progress, we consider an average landscape sensitivity $\bar{\alpha}_V$ and a constant shaking behavior in all directions (i.e., independent of θ) (Assumption 2), yielding:

$$V_{ps} = 2\pi \bar{\alpha}_V \int_0^{R_{HMAX}} \left(\frac{b.\bar{S}}{\sqrt{R_0^2 + R_H^2}} - a_c \right) R_H dR_H \tag{3.4}$$

where R_{HMAX} is the horizontal distance from the wave source at which we expect the landsliding to end because the shaking drops below a_c, that is $R_{HMAX} = \sqrt{(b.\bar{S}/a_c)^2 - R_0^2}$. It is important to note that because we neglected the spatial variability of site effects (dS) and hillslope properties (α), our model does not retain any spatial information and only predicts a bulk landslide volume or area over the whole affected landscape. Integrating, we obtain:

$$V_{ps} = \pi \bar{\alpha}_V a_c R_0^2 \left(\frac{b.\bar{S}}{R_0 a_c} - 1 \right)^2 \tag{3.5}$$

Up to this point, only the ground shaking that a landscape would experience for a single point source of wave emission has been considered. However, during an earthquake waves are emitted as the rupture propagates along the fault length, L, and multiple sources, at a mean depth $\bar{R}_0$, will shake the landscape over an extended area, emitting multiple wave trains that will contribute to landsliding on a given hillslope (Meunier et al., 2013). The simplest model representing this considers that the total landslide volume for the whole fault, V_p, is the linear sum of all point sources along the fault, that is $V_p = N_{ps}.V_{ps}$, with N_{ps} the number of sources (Fig. 3.2A). N_{ps} cannot be constrained easily but it must scale at first order with the fault length L along which the rupture propagates, and then with parameters such as the rupture velocity and the antecedent stress distribution on the fault. Full representation of these effects is out of the scope of our study and instead we assume that the number of point sources is the number of asperities where high frequency waves are emitted, leading to:

$$V_p = V_{ps}.N_{ps} = \pi \bar{\alpha}_V a_c \bar{R}_0^2 \left(\frac{b.\bar{S}}{\bar{R}_0 a_c} - 1 \right)^2 \frac{L}{l_{asp}} \tag{3.6}$$

with l_{asp} the characteristic length of an asperity. Our approach considers the summed effect of multiple wave trains, which is equivalent to a shaking duration in the sense that ground shaking is applied several times on the landscape. Note, however, that sites are assumed to respond linearly, meaning that the possibility of material weakening or strengthening due to prolonged strong ground motion is ignored. Our approach ignores secondary effects that modulate shaking duration at a site, such as the source-site distance or the resonance effect due to sedimentary layers (Kempton and Stewart, 2006). Nevertheless, duration increases with $Mo^{1/3}$ (Kempton and Stewart, 2006), similar to the scaling of L/l_{asp} with $Mo^{2/5}$ (cf., Eq. 3.7), suggesting that most of the duration increase associated with moment is captured by our model. Because the areal landslide density P_{LSA} also scales with $a - a_c$ our prediction for the total area of landslide A_p would have exactly the same form as Eq. 3.5 and 3.6 but with a different landscape sensitivity term $\bar{\alpha}_A$. The parameter $\bar{S}$ is included to be consistent with current understanding of ground shaking but cannot be constrained in this paper and is therefore assumed to be constant. Neglecting the spatial variability of site effects (dS) and of geomorphic sensitivity α, as well as directivity of seismic waves are operational requirements that add potentially significant uncertainties to our prediction and these factors represent important challenges for future work. Hence, the model inputs are R_0, to be estimated for each earthquake, a_c, taken to be around 0.15 (cf., previous discussion after Eq. 3.1), L and b, varying mainly with the seismic moment, and $\bar{\alpha}_V$, varying with substrate strength, local topographic gradient and conditioning factors such as antecedent rain, and requiring empirical constraints.

The most up to date scaling relation between L and Mo (Leonard, 2010) states that:

$$L = \frac{Mo^{2/5}}{\mu C_1^{3/2} C_2} \tag{3.7}$$

with μ the shear modulus, assumed to be 3.3 GPa, and $C_1 = 16.5m^{1/3}$ and $C_2 = 3.7.10^{-5}$ constants derived empirically from many earthquakes (Leonard, 2010). This scaling holds for fault lengths of about 3.5 km to 225 km for thrust earthquakes of Mw 5 to 8. Therefore, we assume that $l_{asp} = 3km$, yielding 1 to 75 asperities or point sources for earthquakes in this magnitude range. Note that, because we assume a uniform l_{asp} for all earthquakes, a different value would not change any of the results of our studies apart from the numerical value of the material sensitivity (cf., Eq 3.11).

Strike-slip earthquakes need to be considered separately. When they reach a critical seismic moment, Mo^*, then their fault width reaches the size of the seismogenic layer. After this, fault width cannot grow and the scaling becomes:

$$\forall Mo > Mo^*, \quad L = \frac{Mo^{2/3}}{\mu C_1^{3/2}.H_s} \tag{3.8}$$

with, the seismogenic layer thickness assumed constant $H_s = 17km$ (Leonard, 2010). For the inferred source acceleration at a given frequency, b, we use the scaling relation proposed by Boore and Atkinson (2008):

$$b = b_{sat} \exp\left(e_5(M_w - M_h) + e_6(M_w - M_h)^2\right) \tag{3.9}$$

$$\forall M_w > M_h, \quad b = b_{sat} \exp\left(e_7(M_w - M_h)\right) \tag{3.10}$$

where M_w is the moment magnitude, $M_h = 6.75$ a hinge magnitude above which the acceleration carried by seismic waves saturates at b_{sat}, and $e_5 = 0.6728$, $e_6 = -0.1826$ and $e_7 = 0.054$ are constants for 1Hz waves, which we consider to be the most relevant for landsliding (Assumption 3), determined empirically from records of 58 earthquakes (Boore and Atkinson, 2008). Earthquake magnitude is derived from the moment based on the empirical relationship $M_w = 2/3(\log Mo - 9.1)$ (Hanks and Kanamori, 1979). Although this relationship is empirical, it is consistent with theoretical predictions based on earthquake emission spectra and attenuation (Baltay and Hanks, 2014). For earthquakes larger than $M_w \sim 6.8$ with numerous strong motion measurements, $b_{sat}.\bar{S}$ can be related to the epicentral ground acceleration a, with $a = b.\bar{S}/R_0$. However, only a few of the earthquakes in our database were large enough and sufficiently well instrumented for this approach. Hence we chose $b_{sat}.\bar{S} = 4000m$, meaning that large earthquakes with a shallow source depth of 5-10 km would have mean PGA above asperities of 0.4-0.8, ignoring ground shaking modulation due to site effects. This is consistent with strong motion measurements from the 1999 Chi-Chi (Taiwan) and 2008 Sichuan (China) earthquakes (Lee et al., 2001; Li et al., 2008).

A further consideration is that different types of earthquake focal mechanisms normally give rise to different ground motion, due to interactions between fault geometry and the free surface (Oglesby et al., 2000). Based on ground motion measurements, Boore and Atkinson (2008) have proposed similar b for strike-slip and reverse fault mechanisms, but 30% smaller b for normal faulting. Consequently, we prescribe $b_{sat}.\bar{S} = 2800m$ for normal fault earthquakes.

In our model, then, the critical moment, above which V_p assumes a non-zero value is

modulated by R_0 and ranges between $10^{16} - 10^{19} N.m$ (Figure 3.1 B). Above this critical moment, V_p rises sharply, driven by the exponential increase of the source acceleration (b) with increasing earthquake moment (Eq 3.9). After reaching the hinge magnitude, $M_h = 6.75$, the acceleration term saturates and V_p is primarily increasing due to fault length (L) growth with moment. Therefore, for these large events V_p is scaling as a power-law of the moment, with an exponent of 2/5 for dip-slip events, and an exponent of 2/3 for strike-slip events (Eq 3.7,3.8). These exponent values are much less than the exponent value of 1 or 3/2 obtained through direct fitting of a power law to the earthquake moment and landslide volume data (Figure 3.1). In the case of earthquake sequences in which earthquakes preceding or following the main shock have more than 30% of the main shock moment, we can compute and sum the associated landsliding of all events, neglecting any possible effects of transient preconditioning of the landscape (Marc et al., 2015). This was done for the 1980 Mammoth Lake (USA), the 1993 Finisterre (PNG), the 1997 Umbria-Marche (Italy), the 2002 Aysen (Chile) and the 2004 Niigata (Japan) earthquake sequences and the moment and depth of the subevents are reported in the supplementary Table 3.7.

3.3.2 Assumptions and Their Consequences

Three important assumptions enable a simple analytical solution of our model. The relevance and associated uncertainties of these assumptions are explored, briefly, in turn.

Assumption 1 is that geometrical spreading is dominant over inelastic attenuation. For S waves with frequency $f = 1Hz$ (cf., assumption 3) and velocity $V_s \sim 3km.s^{-1}$, the inelastic attenuation at a distance R, is $exp(-\pi f R/qV_s)$, with q the quality factor, typically ~ 100 in the uppercrust (Wallace and Lay, 1995). Therefore, at 10km, 20km and 25km the attenuation would reduce the shaking by about 10%, 19% and 23%, respectively. The integrated effect over a larger earthquake area would be somewhere within this range. Neglecting this effect causes over-estimation of the predicted total landslide volume Vp by about 15-20%, depending on the local q. In view of other sources of uncertainty in the model, neglecting inelastic attenuation seems practical and reasonable.

Assumption 2 is that we can use an average topographic sensitivity relevant for the landscape over the whole fault length. The topographic sensitivity may be relatively homogeneous in steep mountainous terrain with moderately uniform lithology, topography and climate, but not for events near coastlines (2007 Aysen (Chile) or 2010 Haiti (Haiti)), or at a mountain front (2011 Lorca (Spain) or 2013 Lushan (China)). For such cases, we cannot easily assess whether the shaking was equally distributed between flat and steep areas and therefore, we must ignore this complexity. However, it is possible to anticipate the amount of missing landsliding due to insufficient topographic steepness, i.e., areas where α_V tends to zero. Therefore, we subdivide the total area where shaking exceeded the critical acceleration into a zone of flat land where the modal value of the topographic slope distribution is below 8° and not likely prone to failure, and a zone where hillslopes are more likely to be sufficiently steep for landsliding to occur. We chose a modal slope of 8° because almost no earthquake-triggered landslides have been detected on slopes below $8-12^\circ$ (Parise and Jibson, 2000; Lin et al., 2008; Gorum et al., 2013). In our calculations of local slope gradients, we have consistently used the 30 m-Aster GDEM, which pairs a relatively high resolution with global coverage, to obtain comparable characterizations of the epicentral topographies for all

cases in our catalogue. For a given landscape and earthquake, we have computed the slope gradient distribution within $1km^2$ cells (i.e., 33 x 33 = 1089 pixels) above the fault and the expected P_{LS} pattern, knowing L, R_0 and b (Figure 3.2). This pattern is a first order approximation that neglects directivity and site effects, and therefore not necessarily suited to the prediction of landslide spatial distribution. However, it allows computation of the total percentage of V_p expected in sufficiently steep cells. This fraction is named A_{topo} (Figure 3.2). We note that using 6 or 10° as a threshold would change A_{topo} by less than 5% in most cases. Multiplying the total landslide volume obtained from Eq.3.6 by A_{topo} then yields a volume adjusted for the available topography. For very simple topography, A_{topo} can also be estimated safely based on symmetry (e.g., for coastal area or fault bounded topography $A_{topo} \sim 0.5$). This correction will fail if strong directivity effects apply. However we note that when A_{topo} is close to one ($> 50\%$ of our events) and the earthquake area has steep slopes in all directions, directivity is not likely to change the total landslide volume, unless a strong anisotropy in rock mass strength is aligned with the directivity. Given that significant directivity effects are not normally systematic on regional scales, we do not expect any general directivity-related bias, although it may affect the prediction of some cases, such as the 1994 Northridge (USA) earthquake (Figure 3.2). This correction will fail if strong directivity effects are present. However, we note that when A_topo is close to one ($> 50\%$ of our events, Suppl. Table 3.7), as steep slopes are available in all directions, directivity is not likely to change the total volume, unless a strong anisotropy in rock mass strength exists and is parallel to the directivity. Adding that significant directivity effects are not systematic, we do not expect a general bias related to directivity, although it can obviously affect the prediction of some events (Figure 3.2).

Assumption 3 is that the most relevant seismic waves for landslide triggering are S-waves with a frequency of about 1 Hz. For intermediate size earthquakes, landsliding is most intense at the epicenter (Meunier et al., 2007), where surface waves have not yet formed. This implies that body waves, and especially S-waves with larger accelerations, are the dominant landslide trigger. In larger earthquakes, surface waves may play a more important role in landslide triggering and neglecting them may cause the model to underpredict total landsliding. The exact frequency range over which landslides are efficiently triggered is difficult to constrain precisely but can be bracketed. Very high frequency waves, $> 10Hz$ would loose energy due to inelastic attenuation that would prevent landslide triggering at distances of 15-20 km or more from the source, contrary to common observations. On the other hand, at a shallow S-wave velocity of about $500 - 800m.s^{-}1$ (e.g., Picozzi et al., 2005) low frequency waves at 0.1 Hz have wavelengths of 5-8 km, unlikely to be responsible for shearing and damaging of hillslopes with lengths of 10-500 m to trigger landslides. Observations of landslide clustering on ridge crests where optimal topographic amplification of seismic waves is at about 1Hz lends direct observational support to our assumption (Meunier et al., 2008). In any case, the exact frequency band for landslide triggering is not a strict requirement and we have modelled our source term (Eq 9,10) for different frequencies (see Discussion).

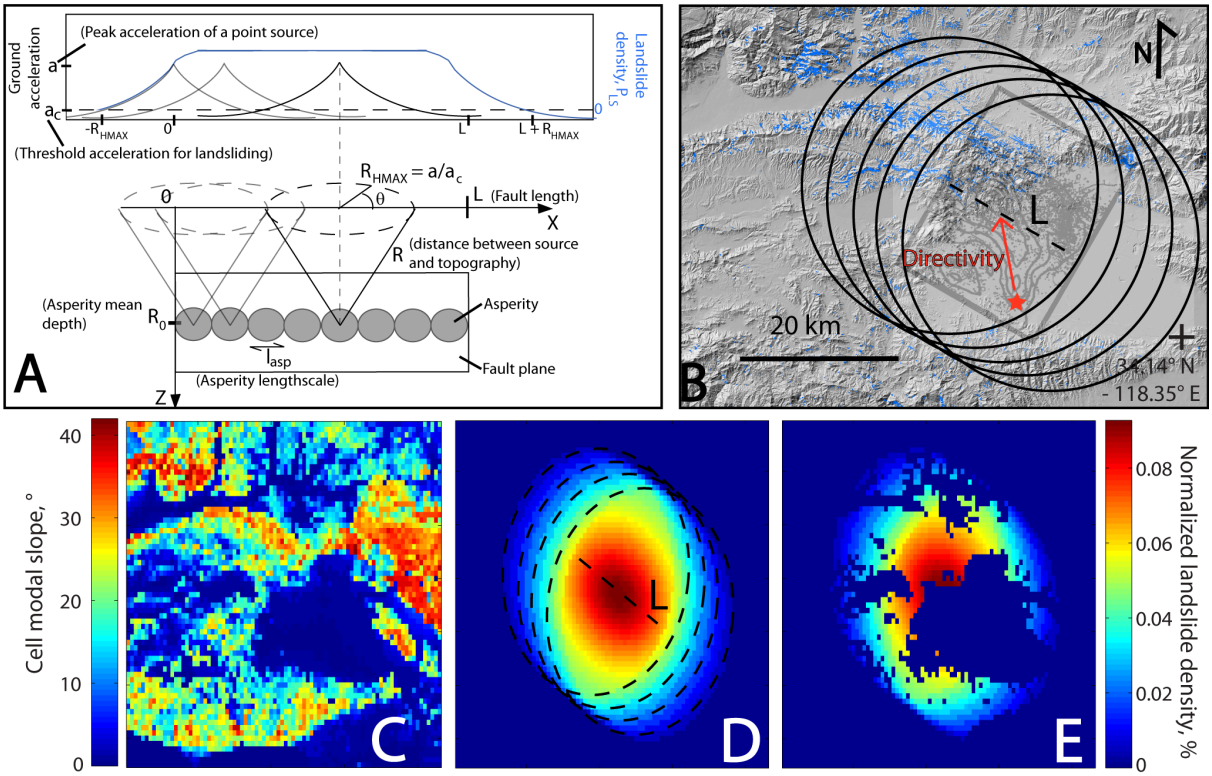

Figure 3.2 – A: Sketch of the geometry and relevant variables to describe the emission of seismic waves along a fault and their effect at the surface. B: Example of digital elevation model hillshade of the area affected by the 1994, M_w 6.6 Northridge earthquake. Triggered landslides are shown in blue (Harp and Jibson, 1996). The fault plane with slip contours and aftershocks is shown in black (Modified from Wald et al. (1996)). Multiple black circles represent areas affected by seismic waves emitted by sources along the fault, from which the surface projection is shown with a dashed black line. C : Modal slope map of the landscape affected by the 1994 Northridge earthquake, subdivided into $1km^2$ cells. D : Idealized shaking map converted into a normalized landslide density. Sources and their effect on the surface, identical to panels A and B are shown in black. E : Remaining normalized landslide density after setting all cells with a modal slope $< 8°$ to zero. The sum of all cell values of this map is between 0 and 1 and represents A_{topo}, a first order correction for topographic availability. This is only first order as the actual shaking map may be much more complex than the idealized representation in panel D. For example, in the particular case of Northridge, the directivity must have amplified the shaking to the north, meaning that the flatlands to the south did not limit landsliding as much as our simplification assumes.

3.3.3 Model Uncertainties

Our model requires precise knowledge of the seismic moment and source depth of an earthquake. For these parameters, we estimated a most likely value with a range of possible values. Without information on the uncertainty function we assumed it to be normal, implying that the estimated range of values represents a $2-\sigma$ range. It is assumed that the other model parameters, that is the rupture velocity, critical acceleration, saturation acceleration and hinge magnitude, have independent normal distributions with mean and standard deviation of 2000 ± 200 m/s, 0.15 ± 0.02, $4000 \pm 400m$ and 6.75 ± 0.1, respectively. We performed a Monte-Carlo simulation sampling 50,000 times for each parameter distribution and built a distribution of the predicted total landslide volume. This allowed us to constrain how the predicted volumes vary with the model parameters and with moment and depth uncertainties (Suppl. Fig 3.10). As the resulting landslide volume distributions are often strongly skewed, specification of a mean and standard deviation is not meaningful. Instead we used a percentile description, with the 25th, 50th and 75th percentile as our minimum, preferred and maximum prediction.

3.4 Landscape Sensitivity

We compare the general pattern of the volume estimates from landslide inventories with the model behavior, assuming $\alpha_V = 0.05$, for a thrust fault with a mean asperity depth of 10 km and a rugged topography with $A_{topo} = 1$. Model results for this specification intersect the bulk of our data within uncertainty (Figure 3.1B). Runs with shallower or deeper sources, at 3 or 20 km, predict total landslide volumes that bracket most of the estimates in our database. However, on closer inspection many individual data points do not lie near to their equivalent model depth curve (Figure 3.1 B). It is clear that the landscape sensitivity term α, in which geomorphic variables such as slope, strength and pore pressure have been bundled, cannot be kept constant. Quantitative controls on α_V are hard to derive theoretically. Therefore, we opted for an empirical approach. With no or very limited information about rock strength and antecedent moisture for most cases we start by constraining the dependency of the sensitivity term on the distribution of local slope gradients.

3.4.1 Topographic Steepness

In order to constrain the effect of topographic slope on the sensitivity of an entire landscape to seismic perturbation, we used first order statistical indicators of slope distribution. Slopes vary across upland landscapes, often with a unimodal probability distribution (Wolinsky and Pratson, 2005; Lin et al., 2008; Gorum et al., 2013) in which the most common, or modal slope is a relevant measure of the landscape steepness. For each earthquake, we extracted a slope histogram from the 30 m Aster GDEM for the area where our model predicted significant earthquake-triggered landsliding. This corresponds to the area used to determine A_{topo}, excluding any flat valley floors (i.e., cells with modal slope $< 8°$) (Figure 3.3, Suppl. Fig. 3.11). Against this modal slope,

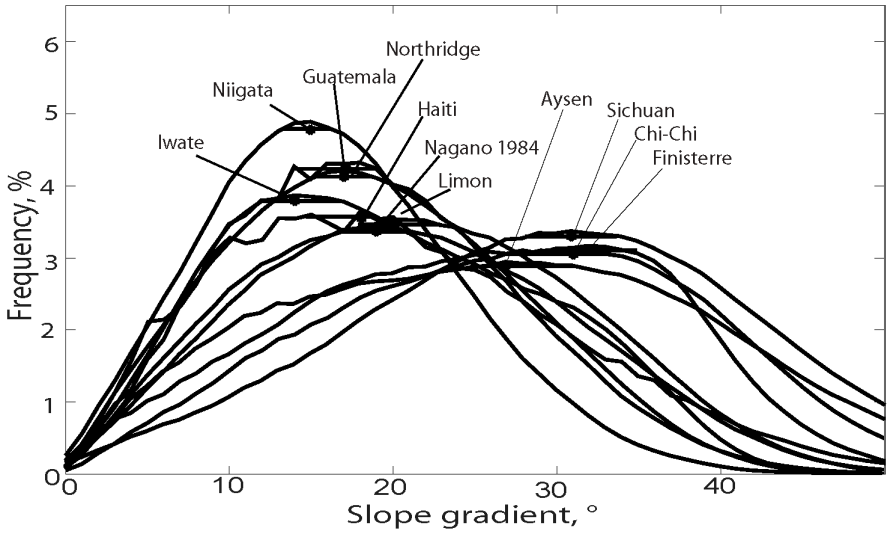

Figure 3.3 – Probability distribution of local topographic slopes in the epicentral areas of the 11 earthquakes with comprehensive landslide inventories. Black dots and bars show the modal slopes with an uncertainty range set arbitrarily at 98% of the modal frequency. The remaining distributions of our database are shown in the supplementary Figure 3.11. After removal of localized flat plains, all areas have unimodal slope distributions, but with diverse kurtosis or skewness.

we plotted the estimated total volume of landslides triggered by an earthquake divided by the volume predicted by the model, corrected for the available topography. Results are shown in Figure 3.4, where horizontal whiskers represent an arbitrary measure of steepness uncertainty given by the range of slopes reaching 98% of the modal frequency (Figure 3.3). Landslide volumes are predicted approximately correct for topographies with modal slope $S_{mod} \sim 35°$, but over-predicted for gentler topographies, up to 50-fold for landscapes with $S_{mod} \sim 12°$ (Figure 3.4). A general reduction of landslide incidence with decreasing landscape steepness is expected and explains much of our data. Eleven cases (1980 Friuli (Italy), 1987 Umbria (Italy), 1994 Arthur's Pass (New Zealand), 2002 Avaj (Iran), 2002 Denali (USA), 2004 Rotoehu (New Zealand), 2009 L'Aquila (Italy), 2010 Cucapah (Mexico), 2010 Yushu (China), 2011 Lorca (Spain), and 2011 Nagano (Japan)) remain as outliers compared to the broad trend defined by the residual data (Figure 3.4). This is not a surprise, as the landscape sensitivity must also depend on the geomechanical strength and hydrological saturation state of its hillslopes. Outliers may have a distinct hillslope strength or seismological specificities and we will discuss them later. Note that cases without source depth constraints, the 1957 Daly City (USA), 1950 Assam (India) and 1855 Wairapa (New Zealand) earthquakes, were not considered, because it is not meaningful to deduce the effects of steepness based on residuals that do not have good first order constraints. We assume that those cases within one standard deviation of our least-squares regression between modal slope and the logarithm of the predicted total landslide volume over the estimated total volume, S_{mod} vs $log(V_p/V)$, are adequately described by an average rock strength and moisture content, whatever that may be. Notably, the exponential function defined by those cases ($R^2 = 0.62$, N=26) has a very similar trend to the equivalent one defined by our 11 best constrained inventories ($R^2 = 0.67$, N=11, Figure 3.4). Therefore, we can

express the landscape sensitivity as a function of the landscape modal slope:

$$\forall b.\bar{S} > a_c R_0, \quad V_p^s = \pi \bar{\delta}_V a_c R_0^2 \left(\frac{b.\bar{S}}{R_0 a_c} - 1 \right)^2 . \frac{L}{l_{asp}} . \exp\left(\frac{S_{mod}}{T_{SV}} \right) A_{topo} \tag{3.11}$$

where $\bar{\delta}_V$ is an average material sensitivity term independent of slope geometry, but still incorporating the effects of rock strength and wetness of the landscape, and T_{SV} is a steepness scaling constant. $\bar{\delta}_V$ and T_{SV} were determined by orthogonal least-squares minimization of the logarithm of the residuals against the modal slope values, yielding $\bar{\delta}_V = 4174 \pm 212 m^3.km^{-2}$ and $T_{SV} = 11.6 \pm 0.6°$. This value of $\bar{\delta}_V$ can be taken to represent an average strength and pore pressure state of the fitted events. Apart from these two constants, every parameter in Eq. 3.11 has an unambiguous and distinct physical meaning, even if it sometimes refers to the average or mode of a variable parameter, and can be estimated for any earthquake scenario.
It must be emphasized that modal slope can only be a proxy for landscape sensitivity because most landslides associated with earthquakes occur at sites steeper than the modal slope of the landscape (Parise and Jibson, 2000; Lin et al., 2008; Gorum et al., 2013, 2014). Implicit in this treatment is the assumption that the occurrence of steep slopes (e.g., $> 35°$) scales with the modal slope. We performed the same analysis, using median instead of modal slope and obtained similar, but not better results.

3.4.2 Prediction of Total Area

The total area of landslides triggered by an earthquake must follow the same scaling with earthquake magnitude as landslide volume. However, α lumps the geomorphic controls on the probability of failure with those on the development and the final 3D geometry of a landslide (See section 3.1). As processes setting landslide runout and width may not depend on slope, strength or moisture in the same way than the ones setting landslide depth (for α_V only), we may expect a different dependency for $\bar{\alpha}_V$ and $\bar{\alpha}_A$. Initially, we chose a value $\bar{\alpha}_A = 0.05$, and compared our model predictions with 17 well-constrained cases. Fewer cases have well constrained total landslide area, because this measure is less dominated by the largest landslides and therefore cannot be extrapolated based on a limited number of large landslides. Similar to landslide volume, the ratio of estimated over predicted landslide area is also positively correlated with the modal slope of the landscape (Figure 3.5A). Events over-predicted (2002 Denali (USA), 2010 Yushu (China) or 2011 Nagano (Japan)) or under-predicted (1957 Daly City (USA)) in the volume domain (Fig. 3.4) are likewise mis-predicted in the area domain (Fig 3.5A). This is consistent with our interpretation that these events have a specific material sensitivity and/or violate our seismological assumptions, and we have ignored when determining the best-fit sensitivity constants in our total area prediction:

$$\forall b.\bar{S} > a_c R_0, \quad A_p^s = \pi \bar{\delta}_A a_c R_0^2 \left(\frac{b.\bar{S}}{R_0 a_c} - 1 \right)^2 . \frac{L}{l_{asp}} \exp\left(\frac{S_{mod}}{T_{SA}} \right) A_{topo} \tag{3.12}$$

with $\bar{\delta}_A$ and T_{SA} having a meaning analogous to $\bar{\delta}_V$ and T_{SV}. With an orthogonal least-squares minimization of the logarithm of the residuals against the modal slope values, we obtained $\bar{\delta}_A = 3445 \pm 325 m^2.km^{-2}$ and $T_{SA} = 15.8 \pm 1.5°$, indicating that topographic

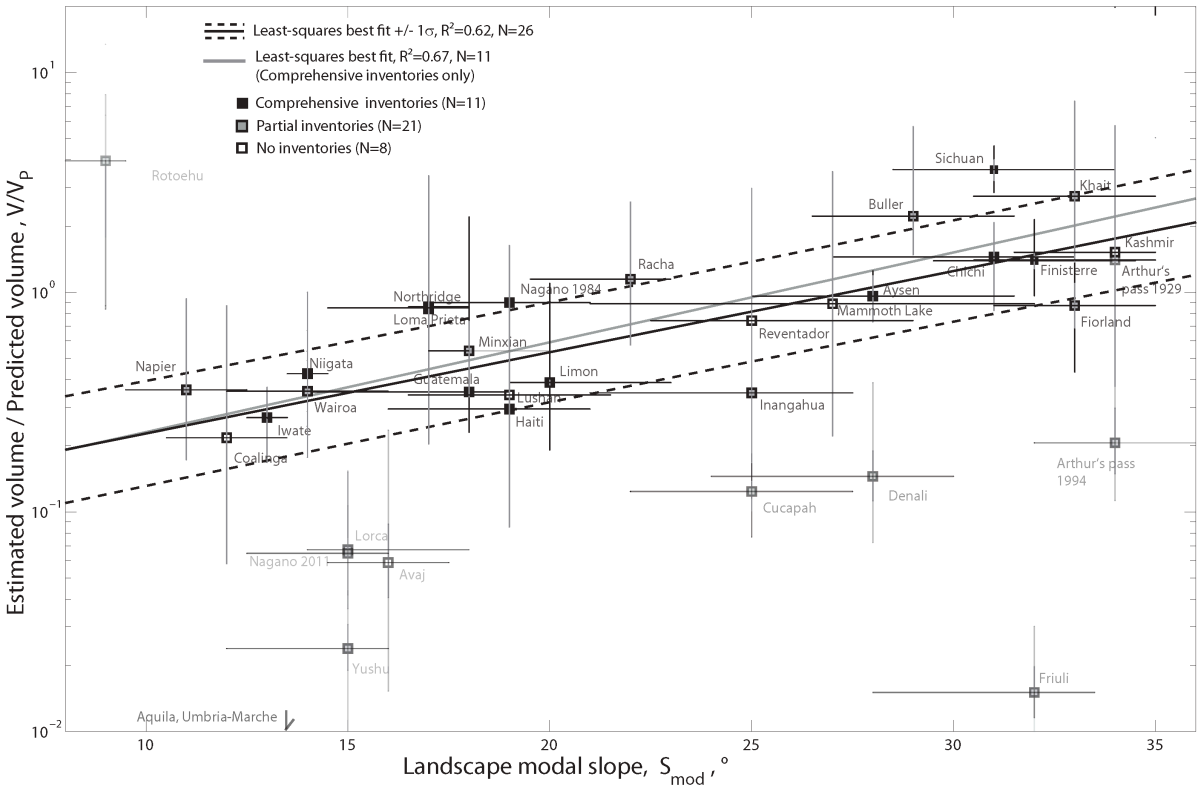

Figure 3.4 – Ratio of the estimated and predicted total volume of triggered landslides plotted against landscape modal slope for all events with sufficient data (i.e., excluding the 1950 Assam (India), 1957 Daly City (USA) and 1855 Wairapa (NZ) earthquakes) (N=37). The largely over-predicted Italian events (2009 Aquila and 1998 Umbria-Marche) (see Fig 3.6) plot outside of the frame. Gray and black bars represent the $2-\sigma$ uncertainties on the estimated volume for the preferred model and the 25-75th percentile of the distribution of model results against the mean estimated volume, respectively. Faded symbols are events excluded from the fit and assumed to have a different landscape sensitivity or seismological process from the bulk of our data (See discussion in section 5).

steepness is a lesser control on total landslide area than on total landslide volume. Even without the outliers, the best least-squares exponential fit only accounts for about 20% of the variance ($R^2 = 0.23$, N=13), further highlighting the limited control of landscape steepness on A. In the following discussion, we show that another parameter, related to the seismic source depth, is modulating A and is responsible for the poor variance reduction associated with landscape steepness. However, even if steepness appears a lesser control on landslide area than on volume, Eq. 3.12 yields predictions that are within a factor of 2 of the total area estimates for 11 out of 17 earthquakes (i.e., 65% success rate, Suppl. Fig 3.12) and $R^2 = 0.73, N = 17$.

3.5 Discussion

We derived expressions for the total volume and area of populations of earthquake-triggered landslides. These expressions aim to account for the principal characteristics of seismological and landsliding processes involved, and thereby to improve the accuracy and robustness of predictions of total landslide volume and area for relevant earthquake scenarios. In the following, the accuracy of our expressions is compared to previous and current empirical relationships. Then we discuss the limitations of our model in accounting for landscape properties and seismological complexities for both the landslide volume and landslide area predictions. We end with examples of applications to well-constrained settings with recurring large earthquakes, the Alpine fault of the Southern Alps, New Zealand, and to the 2015 Gorkha earthquake in Nepal.

3.5.1 Strength and Limitations of our Prediction

Accuracy Compared to the Empirical Relationships

The relationship of Keefer (1994) and our empirical fit of earthquake-triggered landslide volume against moment have scatter of one to two orders of magnitude (Figure 3.1). Moreover, in both relations, predicted landslide volume increases stronger with earthquake moment than in our model. Here, we briefly consider the accuracy and insight gained through our seismologically-consistent model compared to empirical approaches.

At the outset, it should be stressed that the landslide data used to test the accuracy of our model have diverse quality and uncertainties. Discrepancies between landslide volume estimates for poorly documented cases (1983 Coalinga (USA), 1980 Mammoth Lake (USA), 2002 Avaj (Iran), 1989 Loma Prieta (USA), 1987 Reventador (Ecuador), 2005 Kashmir (Pakistan), 2013 Lushan (China) and 1950 Assam (India)) and our model predictions may be due to inaccuracy of the published estimates as well as to the limitations of our model. Specifically, the landslide volume for the 1950 Assam earthquake was obtained using a constant landslide depth for all the perturbed areas, based on a few measurements only (Mathur, 1953). The published volume for this case is therefore likely an overestimate, but it is harder to decipher the uncertainties of the other cases. Other events such as Daly City, Wairapa or Rotoehu have relatively well constrained landslide volumes, but lack detailed seismological information and are therefore hard to predict.

Using Eq. 3.11, we predict the landslide volume triggered by a given earthquake with

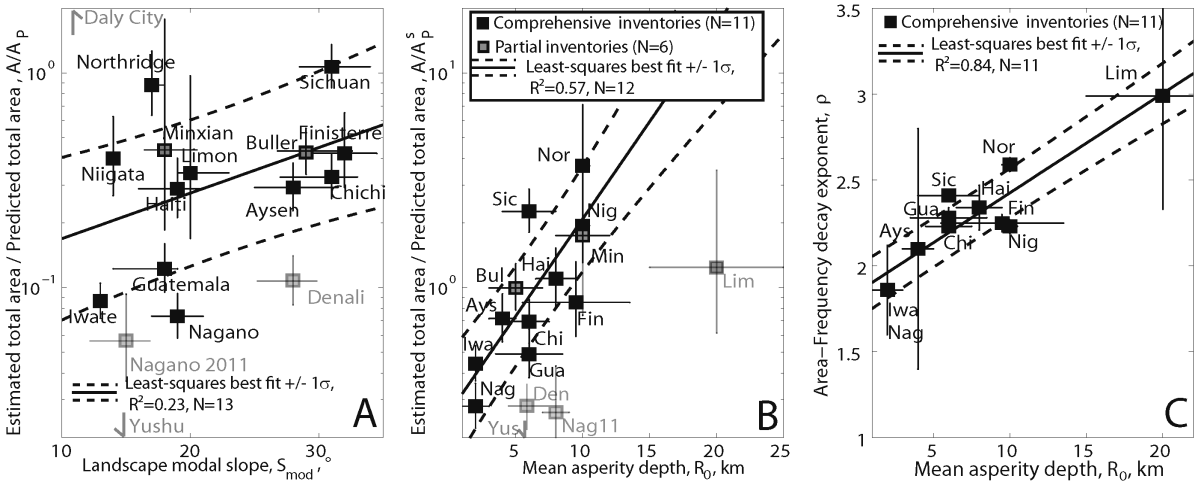

Figure 3.5 – A: Ratio of the estimated and predicted total area of triggered landslides plotted against landscape modal slope for all events with sufficient data (N=17). B: Ratio of the estimated and predicted total landslide area divided by the empirical slope correction from the left panel, plotted against the mean asperity depth R_0. Here, the 1991 Limon earthquake was ignored from the fit because its estimate of A is strongly under-estimated due to resolution censoring of the small landslides. C: Power-law decay exponent ρ of the landslide area-frequency distribution of our 11 comprehensive inventories (See Suppl. Figure 3.16) plotted against the mean asperity depth R_0. In panels A and B y-error bars represent model result uncertainties, that is 25-75th percentile of the distribution of model results. In the fit of Panel A and B, The 1957 Daly City (USA), the 2010 Yushu (China), the 2002 Denali (USA) and the 2011 Nagano, were eliminated because they likely violate key model assumptions or have a specific material sensitivity (See Section 5.1.4).

greater accuracy than with the empirical fit defined from our extended database or than with the Keefer (1994) relationship (Figure 3.1). As 63% of model predictions are within a factor 2 of the corresponding volume estimate, compared to only 23% for both empirical fits (Figure 3.6). For the 11 best constrained inventories, this success rate improves to 82%, against 45% and 18% for the Keefer (1994) relationship and our empirical fit, respectively (Figure 3.6). Thus, our model represents a significant improvement on the accuracy of landslide volume predictions. Also of interest is the fact that larger differences between model predictions and volume estimates provide insight into those factors that also affect the landslide response to earthquakes but have not been adequately represented in our model. It appears that many discrepancies are due at least in part to an ill-constrained material sensitivity term, $\bar{\delta}_V$. The fact that the final residuals of our model, V/V_p^s, has no remaining correlation with earthquake moment, nor with modal slope, mean asperity depth or fault type (Suppl. Fig. 3.12), strengthens our assertion that these parameters have been properly accounted for, and that other parameters govern the outliers. Such parameters include seismological complexities, specific rock mass strength or hydrological conditions

We also tested wave acceleration emission constants, b (Eq. 3.9), for different frequencies (Boore and Atkinson, 2008) and obtained similar, but not better results, for frequencies between 0.5Hz and 3Hz. However, frequency constants outside this range, such as $f = 0.25Hz$ or $f = 6Hz$ introduced a systematic bias with moment and much larger data misfits, supporting our assumption that frequencies of about 1Hz are the most relevant for landslide triggering (Suppl. Fig. 3.7).

Finally, we assessed the effect of using hypocentral depth instead of the mean asperity depth for R_0 (Suppl. Fig 3.14). For many earthquakes in our database, the difference between the hypocentre depth and the principal asperity depth is small, or assumed to be small. However, in 16 earthquakes considered here, the hypocentre was located substantially deeper than the asperity (Suppl. Table 3.7). The attendant reduction of the predicted landslide volume in these cases degrade the correlation with the landscape modal slope (Suppl. Fig. 3.14) and the final accuracy of the model, supporting our decision to consider that asperities are the most important sources of seismic wave responsible for triggering of landslides.

Landscape Sensitivity and Rock Strength

Landscape sensitivity to seismic perturbation is set not only by the steepness and relief of the local topography, but also by the geomechanical properties of the underlying soil and rock (Hoek and Brown, 1997; Schmidt and Montgomery, 1995). In our model, this is represented by the material sensitivity, $\bar{\delta}_V$, which was kept constant in our treatment, even though it must vary with rock mass strength and could explain some outliers. Before addressing the outliers we note that, with a constant material sensitivity, our model predicts total landslide volumes within a factor of 2 of estimated values in 25 cases in our catalogue, that is 63% (Figure 3.6), in spite of a large diversity of lithologies amongst these cases (Suppl. Table 3.7). Antecedent rainfall is not accurately quantified, but amongst these 25 cases only a few had heavy rainfall or notable drought preceding the earthquake, suggesting that the average rock mass strength of the various landscapes must be similar. Fracturing and subsequent weathering, resulting from either tectonic or geomorphic reasons (Molnar et al., 2007; Clarke and

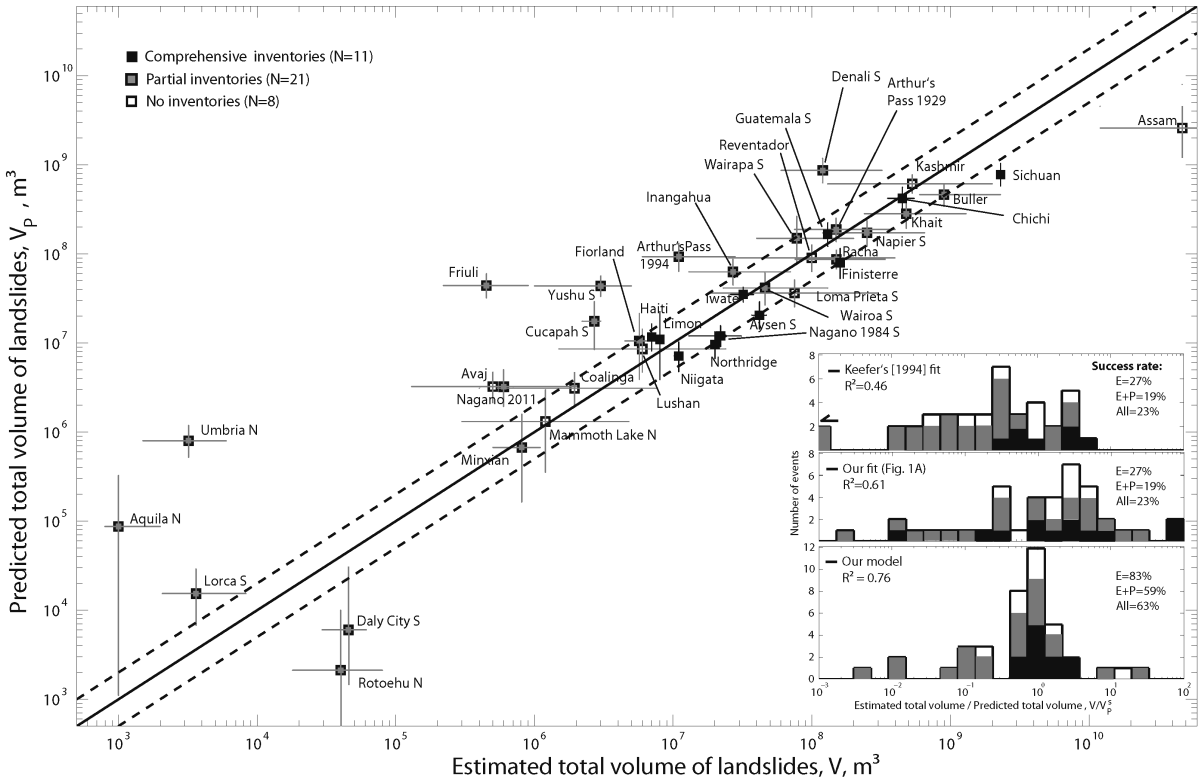

Figure 3.6 – Predicted total landslide volume plotted against estimated total landslide volume for 40 earthquakes in our database (Suppl. Table 3.7). For reference the one-one line, with a factor of 2 interval are shown as solid and dotted lines, respectively. Earthquakes on strike-slip or normal faults are indicated with (S) and (N) after the event name code. Inset: Histogram of the residuals of our model and the empirical fits of Figure 3.1. The black and grey fillings of the histograms refer to the number of comprehensive and partial inventories in each bin, respectively.

Burbank, 2010), is likely to have rendered a significant part of the landscape relatively weak (e.g., Schmidt and Montgomery, 1995) in the majority of our cases and independent of the lithology (Gallen et al., 2015). This does not preclude larger rock strength variations at the local scale from playing an important role in setting the spatial distribution of landslides (e.g., Parise and Jibson, 2000). Three Italian earthquakes (1976 Friuli, 1997 Umbria-Marche and 2009 L'Aquila), which occurred in terrain dominated by massive limestone cliffs, buck this trend. Landsliding due to these earthquakes was over-predicted by our model by two orders of magnitude, and consisted mainly of triggered rock falls and small rock avalanches (Govi and Sorzana, 1977; Antonini et al., 2002; Guzzetti et al., 2009b), even though many other earthquakes of similar magnitude have solicited significant landsliding. This suggests that the hillslopes in the epicentral areas of the these Italian earthquakes had a much greater than average strength, possibly due to the relatively high cohesion of calcareous substrate. The 1991 Racha (Georgia) earthquake is the only other case with substantial limestone in the epicentral area. Its estimated landslide volume is very close to that predicted by the model (Figure 3.6), but the landslide volume was dominated by a few giant earthflows that occurred in slopes underlain by clay (Jibson et al., 1994). These flows make up two thirds of the total landslide volume, suggesting that weak response to shaking in limestone areas may have been compensated by more abundant landsliding in weaker clay-rich substrates, coincidentally yielding a sum total landslide volume close to that predicted. In addition to the permanent effects of substrate quality, preconditioning of hillslope stability due to antecedent weather could also affect the sensitivity term. For most cases, the relevant meteorological information is lacking, but it is likely that many had some degree of substrate saturation and only some had exceptionally dry or wet conditions just before the earthquake. For example, the degree of hydrological saturation of hillslopes may have affected the 2002 Avaj (Iran) earthquake, which struck after prolonged drought. In this case large cracks in hillslopes, that could have become landslides in a wetter substrate, were widely observed (Mahdavifar et al., 2006). This may explain why the Avaj event is over-predicted by our model by a factor of 6. The 2010 Cucapah (Mexico) earthquake was also over-predicted by a factor of 6, possibly due to extremely dry conditions, although this case is difficult to evaluate because the topography above the 100km-long fault is very flat except for the narrow Sierra Cucapah (40 km long, 8 km wide) (Wei et al., 2011), yielding $A_{topo} \sim 10\%$ and suggesting our assumption that site effects average out is likely violated. In contrast, very intense rainfall occurred less than a few days before the 1984 Nagano and 2004 Niigata (Japan), possibly causing these earthquakes to have a landslide volume 2 and 1.6 times larger than the model prediction, respectively.

Seismological Complexities

Besides substrate sensitivity, discrepancies between predicted and estimated landslide volumes may relate to seismological complexities or violation of the seismological assumptions in the model. This is most clearly demonstrated in cases that appear not to have been strongly affected by the substrate issues discussed in the previous section. There are seven events where specificities of the ground shaking, rather than anomalous rock strength or preconditioning, likely explain why documented and predicted landslide volumes differ by more than a factor of four.

The 1957 Daly City (USA) and 2004 Rotoehu (NZ) cases had poorly constrained source depths with potentially major consequences for the predicted landslide volumes, as both earthquakes were close to the threshold for landslide triggering (M_w 5.3 and 5.4). In fact, for the range of mean asperity depths used, the 1957 Daly City (USA) earthquake should have produced between zero and half of the estimated landslide volume, according to our model. Additionally these cases are difficult to evaluate because the earthquakes struck in mostly flat or submerged areas ($A_{topo} \sim 15-20\%$, with $S_{mod} = 10°$), with occasional oversteepened slopes on ocean or lake shores ($> 45°$), where most landslides occurred (Bonilla, 1960; Hancox et al., 2004). In such cases, with only a small fraction of the topography steep enough for landsliding, our tenet that the mean shaking pattern is relevant and that the spatial pattern of site effects and directivity may be neglected is likely violated. Alternatively, the 2010 Yushu (China) earthquake triggered about seven times fewer landslides than expected from our model. The source depth of this earthquake is reasonably well constrained (Sun et al., 2013) and we could not find strong evidence of specific preconditioning or an anomalous rock mass strength. However, seismological observations indicate that the rupture propagated at speeds in excess of the seismic shear wave velocity, with $v_r \sim 5km/s$, that is in super-shear (Wang and Mori, 2012). During the 2002 Denali (USA) earthquake, the third fault segment ruptured in super-shear, and was observed to emit fewer high frequency waves than in sub-shear rupture (Frankel, 2004), with commensurately less attendant landsliding (Gorum et al., 2014). Thus, it is likely that these two earthquakes had less landsliding than our model predicted due to a reduction of high frequency wave emission in super-shear rupture. Super-shear has not been reported for any other cases in the database, but we cannot exclude that some older cases may have had super-shear ruptures that have remained unrecognized due to observational limitations.

The 2011 Nagano (Japan) earthquake induced about five times fewer landslides than expected from our model, possibly because the landscape was snow-covered. This has been reported to damp ground shaking in numerical simulation (McColl et al., 2012) and may also have played in the over-prediction of landslide volume for the 2002 Denali earthquake. The volume of landslides triggered by the 2011 Lorca (Spain) and 1994 Arthur's Pass (New Zealand) were about four times and eight times smaller than those predicted by our model, respectively. Both have reasonable depth constraints, on their epicenter at least, and no specifically dry conditions reported (Hancox et al., 1997; Alfaro et al., 2012). The Lorca areas contain possibly strong limestone cliffs, but also weaker marls and slates units, complicating any interpretation based on rock strength, while the Arthur Pass 1929 was adequately predicted with the average material sensitivity. For these cases, the volume mismatch remains unexplained. Discrepancies between predicted and estimated landslide volumes may also reflect some of the many aspects which have been overlooked in our model, such as strong local attenuation of seismic waves, seismic directivity or a geologic site effect pattern interacting with preferentially oriented topography, or specific seismic rupture processes affecting the relative importance of waves with 1-2Hz frequencies. This is also true for the smaller volume discrepancies of some other events, for example, we note that the three well-constrained earthquake sequences (in Aysen, Niigata, and the Finisterre Range) are undepredicted by about a factor 2, possibly reflecting a heightened propensity to failure after the initial damage of the hillslopes. The 2010 Haiti earthquake mobilized only half the expected landslide volume, probably because almost the entire hanging

wall of the seismogenic thrust was submerged and our topographic correction A_{topo} did not account for the fact that, in addition to possible directivity effects, the strongest shaking usually occurs in the hanging wall of thrust faults rather than in the footwall (Oglesby et al., 2000). The directivity effect present during the 1994 Northridge (USA) earthquake certainly focused strong shaking and landsliding North West of the fault (Figure 3.2B) meaning that our $A_{topo} = 0.45$ correction should rather be $\sim 0.6-0.7$ if we were to impose a shift of the strong motion to the North West, reducing significantly the current underestimation of this event. However, such case-specific effects seem to be of limited importance for the majority of our examples.

Fault Style Influence on Earthquake Triggered Landslides

Fault style has often been proposed to be a control on earthquake-triggered landsliding (e.g., Tatard and Grasso, 2013; Gorum et al., 2014) and numerical models and observations suggest it affects ground shaking (Oglesby et al., 2000). Our treatment involves a 30% reduction of waves emitted by normal fault earthquakes (Boore and Atkinson, 2008), as compared to reverse or strike-slip mechanisms. It also assumes that large magnitude strike-slip earthquakes will occur on longer faults and induce more landslides (see Eq 8). We have explored the effects of these two hypotheses. Most of the normal fault events are difficult to evaluate because of their small magnitude, but also because of specific lithological (1997 Umbria-Marche, 2009 L'Aquila) or topographic (2004 Rotoehu) constraints. Applying a reduction of shaking for normal faults, consistent with seismic observations (Oglesby et al., 2000; Boore and Atkinson, 2008), may improve the model accuracy, but our landslide data are too scarce and noisy to support it. Nevertheless, if the 30% reduction in wave emission for normal faults is not applied, then the landslide volumes predicted by the model increase substantially, predicting correctly the 2004 Rotoehu (NZ) event, while the 1980 Mammoth Lake (USA) event, which was the only well-predicted normal fault case becomes substantially over-predicted (Suppl. Fig 3.15). More well-constrained landslide inventories for normal fault earthquakes are needed to test this aspect of the model. Removing Eq (8) from our treatment reduces the fit quality of residuals against modal slope and results in under-prediction, by more than a factor of 2, of landslide volumes triggered by large strike-slip earthquakes such as the 1976 Guatemala and the 1931 Napier (NZ) earthquakes. However, our data do not support a major difference in earthquake-triggered landslide volume between strike-slip and reverse fault earthquakes (Fig 3.6,Suppl. Fig. 3.12). The same is true, in general, for integration of seismological complexities and sensitivity effects in our model and proper testing of predictions. The acquisition of high-quality landslide data for a larger number of earthquakes with different mechanisms remains an outstanding research challenge.

Total Landslide Area and Area-frequency Distribution

Residuals for total landslide area, A/A_p^s, are similar to those for volume, with 11 out of 17 of all well-constrained inventories within a factor of 2, or 65% of success, 4 within a factor of 5 and 2 significant outliers (Fig 3.5B, Suppl. Fig. 3.12). The estimated total landslide area, A is more sensitive to inclusion of small and intermediate size landslides ($< 50,000m^2$) than the total landslide volume. Low mapping resolu-

tion may cause significant reduction of A, because many small landslides cannot be mapped confidently, as is clearly the case for our mapping of the 1991 Limon (Costa Rica) earthquake which is likely to have a total landslide area 2 to 3 times larger as the estimated presented here. However, a lower resolution can also lead to an overestimation of the mapped area because disturbed areas may be blurred (Marc and Hovius, 2015). Therefore, we cannot exclude that resolution effects may bias the older events in the databse with a relatively low image quality, but it is unlikely to bias events mapped from high resolution imagery such as the 2004 Niigata, 1984 and 2011 Nagano, the 2008 Iwate, the 1976 Guatemala and the 1994 Northridge earthquakes (Suppl. Table 3.7). Notably, the area residuals appear to be correlated with the earthquake mean asperity depth ($R^2 = 0.58$, N=12, Fig 3.5B), with the exception of the 1991 Limon event, for which A is underestimated, and the 1957 Daly City, the 2002 Denali, the 2010 Yushu and the 2011 Nagano earthquakes for which the landslide volume prediction were poor. This trend is not visible for the volume residuals (Suppl. Figure 3.12), suggesting that a process specific to small and intermediate size landslides, which are less important in setting the total landslide volume, is modulating the total area estimate. This is supported by the very strong correlation ($R^2 = 0.84$, N=11, Fig 3.5B) between the mean asperity depth and the exponent ρ of the landslide area-frequency distribution for the 11 most comprehensive landslide inventories in this study (Fig 3.5C, Suppl. Fig. 3.16). Note that here we included the Limon case because landslides smaller than $\sim 1000m^2$ that could not be mapped, do not affect the fit of the decay exponent. Thus A is systematically under-predicted for deep earthquakes with a large number of small to medium size landslides relative to large landslides (large ρ), and A is consistently over-predicted for shallow earthquakes with relatively few small and medium size landslides. Because most of the 11 comprehensive inventories are for earthquakes at or above the hinge magnitude, $M_h = 6.75$ (i.e., when source accelerations b saturates), ground shaking is decorrelated from seismic moment and primarily depends on wave attenuation and the mean asperity depth. Thus, correlation between ρ and depth supports the tenet that the relative abundance of small and large earthquake-triggered landslides is modulated by the shaking properties, consistent with observation on the spatial distribution of landslide size for single earthquakes (Keefer and Manson, 1998; Khazai and Sitar, 2004). However, few mechanisms could explain a larger number of medium sized landslide for deeper earthquakes, as the shaking intensity due to such earthquakes is likely to be lower. Possibly our description of attenuation is too conservative, but this would not explain why the attenuation model should be different for the prediction of landslide volume and area. Alternatively, it could be argued that the shaking duration is an important control on small scale, shallow landsliding whereas larger and deeper landslides may be primarily controlled by the shaking intensity. In this case the increase of shaking duration with earthquake source depth (Kempton and Stewart, 2006), that is neglected in our model, may lead to the correlation we observe without affecting the predicted total landslide volume. Additional data are required to evaluate the effect of shaking duration and intensity on slope stability on specific length scales to be able and to better integrate these terms in our model framework.

3.5.2 Application to Earthquake Scenarios

Our model can be used when an earthquake is anticipated or after it has occurred. The seismic moment or the fault length, the mean asperity depth and the fault type may be specified based on paleo-earthquake information or initial seismological data. In either case, the active fault segment must be located, so that A_{topo} and the modal slope of the overlying area can be computed based on a 30m DEM, for consistency with our empirical correction for steepness (Fig. 3.2, 3.3). With these 5 quantities and their associated uncertainties, V_p and A_p and their uncertainties can be computed, using Eqs (11) and (12). Here, two examples are explored briefly: the 2015 Gorkha earthquake in Nepal, for which preliminary seismological and geomorphological data are available at the time of writing (Collins and Jibson, 2015; Kargel et al., 2015), but not yet a comprehensive landslide map, and an expected future large earthquake on the Alpine fault of New Zealand.

The $M_w 7.8$ Gorkha earthquake, which occurred in April 2015, had an estimated seismic moment of $72.10^{19} N.m$ and mean asperity depth of $15 \pm 2km$ (Avouac et al., 2015). From the available digital elevation data, we estimate $A_{topo} \sim 1$ and $S_{mod} = 33 \pm 2°$. With these constraints, our model prediction is: $V_p = 0.30(-0.11/+0.16)km^3$. We assume that the affected area has a rock strength similar to that of the majority of the cases in our data base, but because the ground was very dry at the time of the rupture, propensity to failure of hillslopes may have been relatively low, so that the model prediction may be somewhat high, perhaps by a factor 2. Note that we used a slip distribution inversion to accurately locate the mean asperity depth. Such inversions can typically be performed some days or weeks after the earthquake, depending on the availability and processing of InSAR, GPS and strong-motion data. However, a cruder landslide volume estimate could be made within 1 to 2 days after the earthquake, when first seismological constraints yielded similar moment estimates and a hypocentral depth between 15 and 25km, leaving a wide range of possible mean asperity depths, between half the shallow hypocenter (i.e., 8 km) and the deep hypocenter, at 25 km. With these initial constraints, the predicted total landslide volume was bracketed between $0.02 - 0.7km^3$.

Next, we consider the Alpine fault, bounding the Southern Alps of New Zealand to the west. This conspicuous tectonic feature has been shown to have consistently produced $M_w 8.1 \pm 0.1$ earthquakes , every 330 ± 30 years, over the last 8000 years (Berryman et al., 2012). The modal slope along the western Southern Alps is fairly constant, at about 32°(Clarke and Burbank, 2010), but decreases rapidly in the footwall of the fault, and as a representative slope we chose $30 \pm 2°$. The mean asperity depth where most of the wave emission is likely to occur cannot be predicted and is thus the major source of uncertainty. Instead of a single value, we can test two reasonable extremes for an earthquake of this size, 4 ± 1 and 8 ± 1 km. Along the $\sim 300km$ of the fault trace there are several sections where coastal plains or the ocean lie within 20 km of the fault, leading to a 30% reduction of the total available area, mostly in the footwall of the fault, and a correction $A_{topo} \sim 85 \pm 5\%$. The shallow and deep earthquake scenarios yield predicted total landslide volumes of 1.0 (-0.22/+0.28) km^3 and 0.7(-0.17/+0.23) km^3 and total areas of 420(-85/+105) km^2 and 290(-70/+90) km^2, respectively. Our model does not provide any information about the spatial distribution of these landslides. However, it is safe to assume that the landslides will be distributed along the fault trace, with the highest density within a radius of $\sim 20km$ that means an area of about $1200km^2$.

Hence, the average proportion of area affected by landslides along the fault is expected to be $2.4 - 3.5\%$. This bulk measure can be refined using various assumptions about the area likely to be affected more than average, based on local topographic steepness, or the expectation of stronger shaking in the hanging wall close to the fault (Oglesby et al., 2000). Coupled to a road or property density maps such estimates may help to quantify risk due to triggered processes. The total landslide volume is likely to be a key factor responsible for seismically induced changes in weathering and fluvial chemistry (Emberson et al., 2015; Jin et al., 2015). The total landslide area is crucial to evaluate the amount of standing biomass and soil biomass that will be harvested and may be buried, influencing the long term and short term carbon budget of the mountain belt (Hilton et al., 2011b). Moreover, the total landslide volume can be converted into mean erosion rates over the recurrence intervals, ($0.18-0.25 mm.yr^{-1}$), and compared to landslide erosion due to precipitation to assess the relative role of climate and seismicity in driving erosion in this setting (Hovius et al., 1997). Finally, as our model only requires DEM information and the prescription of the earthquake moment or fault length and depth, it can easily be integrated in landscape evolution models. This could enable assessment of the relative importance of earthquake erosion and the role of earthquakes in mountain building on longer time scales (Li et al., 2014). Beyond this, several issues are not addressed by our model, such as the precise location of the seismically triggered landslides, especially the larger ones that dominate the total landslide volume, the possible controls on the magnitude-frequency distribution of seismically-triggered landslides, and the amount and timing of debris reaching the river network and the dynamics of its fluvial export.

3.6 Conclusion

We developed a seismologically-consistent model relating the total volume and area of landslides triggered by an earthquake with the principal seismological characteristics of that earthquake and the main topographic attributes of the affected landscape. This model considers explicitly the effects of seismic moment, source depth and rupture mechanism on triggered landsliding. It also incorporates the modulating influence of landscape steepness, here defined as the modal slope of the affected topography, on the amount of landsliding, constrained using an extensive database of 40 shallow continental earthquakes ranging between M_w 5.1 to 8.6. However, variations of landscape sensitivity to seismic perturbation due to substrate strength remains elusive and has not been included in the model. This may be a cause of marked departures between predicted and estimated landslide volumes for some earthquakes in our database. However, model predictions are consistent with estimated total landslide volumes for a majority of events, although the precision of predictions is likely limited to a factor of 2 because of uncertainties on model input and simplifying assumptions. Predictions of total landslide area, with $R^2 = 0.73$ and 11 out of 17 events predicted within a factor of 2, appear to be less dependent on landscape steepness and may be affected by processes influencing the landslide area-frequency distribution, possibly the shaking duration. Nevertheless, our model significantly outperforms previous, empirical relations, with successful prediction rate (i.e., estimate within a factor of 2 of prediction) of 63% against 23% and $R^2 = 0.76$ against $R^2 = 0.46$. It also predicts a very

different scaling between landsliding and seismic moment for large earthquakes. Additionally, it anticipates explicit representation of the role of earthquakes in landscape evolution models, re-evaluation of seismically-driven erosion fluxes, and useful application to risk analysis for earthquake scenarios. Further development of the model should include the introduction of quantitative rock strength proxies and the inclusion of more complex seismological processes, to achieve greater accuracy in predicting the total amount and spatial pattern of landsliding caused by earthquakes.

3.7 Supplementary materials to Chapter 3

Introduction
The supporting information contains 2 data tables (one is uploaded as an additional excel file) summarizing the source, value and uncertainties of parameters used in the main text. Additionally it contains 10 figures that support the conclusions of the main text.
Suppl. Figure 3.7 shows the 40 earthquakes of our database on a world map.
Suppl. Figure 3.8 presents the imagery used to map and produce a new earthquake-induced landslide inventory for the 1991 Limon earthquake (Costa Rica).
Suppl. Figure 3.9 supports one of our model assumptions in showing that horizontal peak ground acceleration and landslide volume density seem linearly correlated.
Suppl. Figure 3.10 shows the model sensitivity to different parameters assessed through Monte Carlo simulations.
Suppl. Figure 3.11 complements the main text Figure 3 and shows the slope histograms of all the remaining earthquake areas.
Suppl. Figure 3.12 shows the final model residuals against depth, landscape steepness, fault type and seismic moment.
Suppl. Figure 3.13 shows the final model residuals against moment, obtained when we choose different frequencies (0.25 - 1 - 6Hz) for our seismic source scaling constants.
Suppl. Figure 3.14 shows the model accuracy changes when we consider the hypocenter as the source depth instead of the mean asperity depth.
Suppl. Figure 3.15 shows the model accuracy changes when we remove the assumption that normal fault earthquakes produce less ground shaking.
Suppl. Figure 3.16 shows the landslide area-frequency distribution for our 11 exhaustive inventories.

Table 3.1 – Data summary for published information about earthquake-induced landsliding. The techniques used to calculate landslide area and volume are indicated with: M= scanned and corrected inventory of mapped polygons converted to volume with empirical V-A relationship. N= estimation based on the total volume of $\sim 5-20$ very large bedrock landslides ($> 0.5Mm$). L= estimate from the literature. F= published frequency-size distribution converted to volume and integrated. B= extrapolation based on the largest landslides, assuming an universal frequency-size distribution. P = estimate based on field photographs and field report More details in section 2.2 and Table 3.7. Total number of landslides is an order of magnitude estimate only. Mapping resolution is given when the data comes from image interpretation. Unless indicated, all mapping studies included some field surveys. G indicates the data comes from field surveys and occasional aerial surveys only. Seismic moment, fault mechanism, mean depth of asperities (R_0) and fault style have been derived from published seismological studies. ! indicates events where we could access an earthquake source rupture inversion, whereas for other cases R_0 is based on hypocenter depth and other assumptions (see methods). * indicates that the event was an earthquake sequence, with aftershock or foreshock with seismic moment larger than 30% of the main shock. Fault type abbreviations are used as follows, SS for strike-slip, R for reverse and N for normal. Country abbreviations used are USA, for United States of America, NZ for New Zealand and PNG for Papua New Guinea. Modal slope estimates were extracted from 30m-Aster GDEM within the epicentral areas and ignoring flatlands ($< 8°$). The correction factor for available topography, A_{topo} was determined based on our average PGA decay approximation and the distribution of DEM cells with modal slope steeper than $8°$ (See Fig. 3.2). Typical landslide types reported are indicated with the following abbreviations: RF = rock fall, RA = rock avalanche, RS = rock slump, DSS = disrupted soil slides, SA = soil avalanche, SS = soil slump and EF= earth flow. Dominant lithologies grouped as volcanoclastic, V, sedimentary, S, metasedimentary, MS, metamorphic, M, igneous, I and limestone L. Climatic setting is also mentionned. The thick horizontal black line separates the 11 comprehensive inventories from the other 29 inventories in our catalogue.

Earthquake	Landslide volume estimate, V [km³] , (range)
1976, Guatemala, (Guatemala)	0.13 (0.115 – 0.145) (M)
1984, Nagano, (Japan)	0.022 (0.004 – 0.042) (M)
1991, Limon, (Costa Rica)	8.0e-3 (7.8e-3 – 8.2e-3) (M)
1993, Finisterre*, (PNG)	0.16 (0.147 – 0.173) (M)
1994, Northridge, (USA)	0.021 (0.02 – 0.022) (M)
1999, ChiChi, (Taiwan)	0.45 (0.26 – 0.64) (M)
2004, Niigata*, (Japan)	0.011 (0.0094 – 0.0126) (M)
2007, Aysen*, (Chile)	0.042 (0.032 – 0.052) (M)
2008, Iwate, (Japan)	0.032 (0.021 – 0.45) (M)
2008, Sichuan, (China)	2.3 (2.05 – 2.55) (M)
2010, Haiti, (Haiti)	7e-3 (6.8e-3 – 7.2e-3) (M)
1855, Wairapa (NZ)	0.078 (0.04 – 0.2) (N)
1929, Arthur's pass (NZ)	0.15 (0.075 - 0.4) (N)
1929, Buller, (NZ)	0.9 (0.05 – 0.23) (N)
1931, Napier, (NZ)	0.25 (0.12 – 0.73) (N)
1935, Wairoa, (NZ)	0.046 (0.023 – 0.13) (N)
1949, Khait, (Tadjikistan)	0.48 (0.24 – 1.3) (N)
1950, Assam, (India)	47 (12 – 200) (L)
1957, Daly city, (USA)	4.5e-5 (2.9e-5 – 6.1e-5) (F)
1968, Inangahua, (NZ)	0.027 (0.013 – 0.07) (N)
1976, Friuli, (Italy)	4.5 e-4 (2.2e-4 - 9e-4) (N)
1980, Mammoth Lake*, (USA)	1.2 e-3 (3e-4 – 4.8e-3) (L)
1980, Coalinga, (USA)	2 e-3 (0.5e-3 – 8e-3) (L)
1987, Reventador, (Ecuador)	0.1 (0.025-0.4) (L)
1989, LomaPrieta, (USA)	0.075 (0.02-0.3) (L)
1991, Racha, (Georgia)	0.16 (0.08-0.4) (N)
1994, Arthur's Pass, (NZ)	1.1e-2 (0.5e-2 – 2.8e-2) (N)
1997, Umbria-Marche, (Italy)	3.2 e-6 (1.5e-6 – 6e-6) (F)
2002, Avaj, (Iran)	5 e-4 (1.3e-4 – 2e-3) (B)
2002, Denali, (USA)	0.12 (0.06 – 0.32) (N)
2003, Fiorland (NZ)	5.7e-3 (4.5e-3 – 7.2e-3) (N)
2004, Rotoehu, (NZ)	4 e-5 (1.8 e-5 – 8 e-5) (P)
2005, Kashmir, (Pakistan)	0.53 (0.13 – 2) (B)
2009, L'Aquila, (Italy)	1 e-6 (0.8e-6 -2e-6) (F)
2010, Cucapah, (Mexico)	2.7e-3 (2.4e-3 – 3e-3) (F)
2010, Yushu, (China)	3e-3 (1e-3 – 5e-3) (F)
2011, Nagano, (Japan)	6e-4 (4.1e-4 – 8e-4) (F)
2011, Lorca, (Spain)	3.5e-6 (2e-6 - 8e-6) (P)
2013, Lushan, (China)	6e-3 (1.5e-3 – 2.4e-2) (B)
2013, Minxian, (China)	8e-4 (5e-4 – 1.1e-3) (F)

Landslide area estimate, A [km²]	Landslide number (Log10(N))	Mapping
61	3-4	(<1m)
1.72	2-3 (1m)	(<1m)
8.16	3 (30m)	(30m) No Field
56.6	3-4 (20m)	(20m) No Field
23.8	4 (1m)	(<1m)
128	4-5	(15m)
12	4	(<1m)
13	2-3	(1-2m) No Field
8.9	3	(<1m)
712	5	(15m)
8	3-4	(1-2m)
x	>2 ?	F
x	2-4	F
200	3-4	F
x	>2 ?	F
x	>2 ?	F
x	>2 ?	F
x	>2 ?	F
0.057	1-2	F
x	2-3	F
x	2	F
x	2-3	F
x	2-3	F
x	>2 ?	F
x	2-3	F
x	>2 ?	F
x	2	F
x	2	F
x	2	F
160	3	F
x	2-3	F
x	1-2	F
x	3	F
x	2	F
x	2	(2.5m)
1.2	3	(0.5-2.5m)
0.61	1-2	(<1m)
x	2	F
x	3-4	(0.5-5m)
0.76	3	(0.5m)

Mean asperity depth, R0 [km], (1 σ)	Hypocentral depth, km
6 (2.5)	12
3(1) !	4
20 (5)	24
9.5 (4) / 10 (4) / 12 (4)	19 / 20 / 24
10 (0.5) !	17
6 (1.5) !	10
10 (0.5) ! / 12(1)!	9 / 12
4(1) / 4 (1)	4 /
2 (0.5) !	8
6 (2) !	11
8(1.5) !	11
? (8-24)	16
6 (4)	12
5 (4)	10
7.5 (5)	15
12 (4)	12
8 (5)	16
? (4-12)	8
? (1.5-4.5)	3
7.5 (3)	15
4 (1) !	4
9 (4) / 14 (4) / 15 (4)	9
9 (2.5)	9
10 (4)	10
11(1.5) !	17
6 (1.5) !	6
9(3)	9
5(1) / 4 (1) !	5 / 4
8 (2)	8
6 (3) !	8
20(2) !	21
5(3)	5
5 (1) !	11
11 (2.5) !	10
6(2) !	6
5(3) !	17
8 (2)	8
3(1)	3
13 (3)	13
10 (4)	10

Smod [°] , (range)	A_{topo}	Mo [1e19 N.m] (2 σ) {Fault type}
18 (14 – 19)	0.5	32 (6) {SS}
19 (17 – 21)	0.75	0.28 (0.02) {SS}
20 (19 – 23)	0.4	38 (15) (R)
32 (29.5 – 34.5)	1	1.4 (0.15) + 0.72 (0.2) + 1.2 (0.4) {R}
17 (16.5 - 18)	0.5	1.3 (0.2) {R}
31 (27-33)	0.9	30 (10) {R}
14 (13.5 – 14.5)	0.7	0.88 (0.2) + 0.32 (0.05) {R}
28 (25 – 31.5)	0.85	0.25 (0.07) + 0.18 (0.05) {SS}
13 (12.5 – 13.5)	0.7	2.6 (0.2) {R}
31 (28.5-34)	1	95 (20) {R}
19 (16 – 21)	0.2	4.5 (1) {R}
25 (21.5-26)	0.25	190 (120) {SS}
34(30.5-35)	1	2.2 (0.7){SS}
29(26.5-31.5)	1	35 (12) {R}
11(9.5-12.5)	1	40(15) {S}
14 (12-16)	1	7.5(2.5) {S}
33 (30.5-35)	1	10 (8) {R}
33 (30-35)	1	800 (300*) {R}
9 (7.5-9.5)	0.15	9e-3 (3e-3*) {SS}
25 (21- 27.5)	0.6	4.5 (1.5) {R}
32 (28.5-33)	0.65	0.6 (0.15) {R}
27 (18 – 33)	1	0.29 (0.1) + 0.13 (0.4) + 0.11 (0.3) {N}
12 (10.5-13.5)	0.5	0.6 (0.2) {R}
25(22.5-29)	1	5.5 (2.5) {R}
17 (14.5-18)	1	3 (1*){SS}
22 (19.5-23)	1	3.2 (1) {R}
34 (32.5-36)	1	1.3 (0.3){R}
15 (12 - 18)	0.8	0.05(0.01) + 0.12 (0.02) {N}
16 (14.5-17)	0.27	0.7 (0.2) {R}
28 (24- 30)	0.65	75 (13) {SS-supershear}
32 (28.5-33)	0.3	7.5(2.5) {R}
9 (8-9.5)	0.2	0.023 (0.008) {N}
34 (31.5-35)	1	25 (5){R}
16 (14.5-17.5)	0.65	0.35 (0.05) {N}
25 (22-27.5)	0.08	10 (2) {SS}
15 (12-16)	0.85	2. 3 (0.3) {SS-supershear}
15 (12.5-16)	1	0.25 (0.08){R}
15 (14-18)	0.35	6.3 e -3 (1.5 e-3){SS}
19 (16.5-21.5)	0.8	1 (0.3) {R}
18 (17-20)	1	0.12(0.04) {R}

Landslide types reported	Main Lithology	Climatic setting
RS, RA, DSS, RF, SS	Volcanoclastic	Montane Temperate
RA, DSS, SA	Volcanoclastic	Temperate
DSS, SA, RA	Sedimentary	Tropical
RA, DSS, SA, RS	Volcanoclastic	Tropical
DSS, RF, RA, RS	Sedimentary	Dry Mediterranenan
RA, DSS, SA, RS	Metasedimetary	Sub Tropical
RA, DSS, SA, RS	Sedimentary / Volcaniclastics	Oceanic Temperate
RA, DSS, RF	Igneous / Volcanoclastic	Temperate
RA, DSS, SA, RS	Volcanoclastic / Igneous	Oceanic Temperate
RA, DSS, SA, RS	Metasedimetary / Igneous	Cool Sub Tropical
DSS, RF, RA	Sedimentary / Limestone	Tropical
RA, RS, DSS, SA, RF	Sedimentary	Oceanic Temperate
RA, RS,	Metasedimetary	Oceanic Temperate
RA, RS, DSS, SA,	Sedimentary	Oceanic Temperate
RA, RF	Sedimentary	Oceanic Temperate
DSS, RF, RA	Sedimentary	Oceanic Temperate
RA, SA, RF, DSS	Metamorphic / Loess	Semi-arid
RA, RS, DSS, SA, EF	Sedimentary	Tropical
RA, RS, DSS, EF	Sedimentary	Dry Mediterranenan
RA, DSS, RF	Sedimentary	Oceanic Temperate
RF, RA	Limestone	Mediterranenan
RF, RA	Metamorphic / Igneous	Montane Temperate
RF, RA, RS, DSS	Sedimentary	Dry Mediterranenan
DSS, SA, RA	Volcanoclastic / Sedimentary	Tropical
RF, RA, RS, DSS	Sedimentary	Dry Mediterranenan
RF, RA, DSS, EF	Limestone / Sedimetary	Humid Temperate
RF, RA, DSR	Metasedimetary	Oceanic Temperate
RF, RA	Limestone	Mediterranenan
RF, DSS, RS	Sedimentary	Arid
RF, RA	Sedimentary / Igneous	Periglacial
RF, RA,DSS	Metasidementary / Igneous	Oceanic Temperate
RA, DSS, SA	Volcanoclastic	Oceanic Temperate
RF, RA, DSS, RS	Sedimentary / Metasedimentary	Sub Tropical
RF, RA	Limestone	Mediterranenan
? , DSS	Igneous / Volcanoclastic	Arid
RA, DSS, RF, RS	Sedimentary	Alpine Sub-Arctic
RS, RA, DSS	Volcanoclastic	Temperate
RF, RA, DSS	Sedimentary	Mediterranenan
RF, RA, DSS, SA, SS	Metasedimetary	Cool Sub Tropical
RA, DSS, SA, RS	Sedimentary /Loess	Sub Tropical

Geomorpology Ref.	Seismology Ref.
Harp et al., 1981	Kikuchi and Kanamori, 1991
PWRI, 2010	Yoshida and Koketsu, 1990
This study	Goes et al., 1993 ; Suarez et al., 1995
Meunier et al., 2008	Stevens et al., 1998
Harp and Jibson, 1996	Wald et al., 1996
Liao and Lee, 2000	Zeng and Chen., 2001
Yagi et al., 2007	Hikima and Koketsu, 2005
Gorum et al., 2014	Legrand et al., 2011
Yagi et al., 2009	Suzuki et al., 2010
Gorum et al., 2011	Fielding et al., 2013
Gorum et al., 2013	Hashimoto et al., 2013
Hancox et al., 1997	Darby and Beanland, 1992
Hancox et al., 1997	Berryman and Villamor, 2004
Pearce and O'Loughlin, 1985 ; Hancox et al., 1997	Doser et al. 1999
Hancox et al., 1997	McGinty et al., 2001
Hancox et al., 1997	McGinty et al., 2001
Evans et al., 2009	Januzakov et al., 2003
Mathur, 1953	Molnar and Qidong, 1984
Bonilla, 1960	Bonilla, 1960
Hancox et al., 1997	Anderson et al., 1994
Govi and Sorzana, 1977	Cheloni et al., 2012
Keefer, 1994	Given et al., 1982
Keefer, 1994	Stein and Ekstrom, 1992
Schuster et al., 1996	Kawakatsu and Cadena, 1991
Keefer, 1994	Wald et al., 1991
Jibson et al., 1994	Tan and Taymaz, 2006
Hancox et al., 1997	Abercombie et al., 2000
Antonini et al., 2002	Hernandez et al., 2004
Mahdavifar et al., 2006	Hamzehloo, 2005
Jibson and Harp, 2006	Elliott et al., 2007
Hancox et al., 2003	McGinty et al., 2003
Hancox et al., 2004	Hancox et al., 2004
Owen et al., 2008	Pathier et al., 2006
Guzzetti et al., 2009	Cirella et al., 2009
Barlow et al., 2014	Wei et al., 2011
Xu et al., 2014a	Sun et al., 2013
Has et al., 2012	Has et al., 2012
Alfaro et al., 2012	Alfaro et al., 2012
Tang et al., 2015	Zhang et al., 2014
Xu et al., 2014b	Xu et al., 2014b

Table 3.2 – Summary of the methods used to estimate total landslide volume and its uncertainty from published information. V_A is the total volume and uncertainties estimated from converting into volume available landslide frequency-area distribution. V_P is the total volume estimated as 150% of the sum volume of (N) large, reported landslides, assumed to represent the largest triggered landslides (see Methods). In this case, the uncertainty range is assumed to be defined between 50-270% of V_P. When only area information was given, landslide volumes were derived with area-volume relationships (see Methods). V_M is the total landslide volume based on the volume of the largest landslide and assuming a universal frequency-area distribution (see Methods). V_{max} is the largest landslide volume reported. V_L is the landslide volume estimate reported by other authors (see Table 3.7 for references). For V_M and V_L the uncertainties are deemed large and assumed to extend between 25-400% of the estimated total volume. We consider V_A to be the most accurate, followed by V_P, and then V_M. The value in bold is the one considered further in the study and reported in Table 3.7. ** indicates that some deep-seated landslides with significant displacement (several meters), but not necessarily with catastrophic failure, were included in the total volume estimate.

Earthquake	V_A (km^3)	V_P (km^3) , [N]	V_M (km^3)	V_{max} 1e6 m^3	V_L (km^3)
Wairapa 1855	x	**0.078** [29]	0.067	11	x
Arthur Pass 1929	x	**0.15** [6]	0.47	72	0.059
Buller 1929	x	**0.9** [66]	1.47	210	1 - 1.3
Napier 1930	x	**0.25** [9]	0.19	30	x
Wairoa 1935	x	**0.046** [4]	0.12	20	x
Khait 1949	x	**0.48** [15-30?]	0.5	75	x
Assam 1950	x	x	x	x	**47**
Daly City 1957	**4.5e-5 [2.9e-5 - 6.1e-5]**	x	14e-5	0.03	6.7e-5
Inangahua 1968	x	**0.027** [10]	0.03	5	0.052
Friuli 1976	x	**4.5e-4** [11]	5e-4	0.1	x
Mammoth Lake 1980	x	x	1e-3	0.2	**1.2e-3**
Coalinga 1983	x	x	1e-3	0.2	**2e-3**
Reventador 1987	x	x	x	x	**0.076 ; 0.12**
Loma Prieta 1989	x	x	0.07	12	**0.075**
Racha 1991	x	**0.16** [7]**	0.33**	50**	x
Arthur Pass 1994	x	**0.011** [20]	0.011	2	x
Umbria Marche 1999	**3.2e-6 [1.5e-6 - 6e-6]**	x	0.8e-6	0.2e-3	x
Avaj 2002	x	x	**5e-4****	0.1**	x
Denali 2002	x	**0.12** [7]	0.12	20	x
Fiorland 2003	**5.7e-3 [4.5e-3 - 7.2e-3]**	x	x	x	x
Rotoehu 2004	**4e-5 (1.8e-5 - 8e-5) !**	x	x	x	x
Kashmir 2005	x	x	**0.5**	80	x
Aquila 2009	**1e-6 (8e-7 - 2e-6)**	x	2e-6	0.5e-3	x
Cucapah 2010	x	x	2.3e-4	0.05	**2.7e-3 [2.4e-3 - 3e-3]**
Yushu 2010	x	x	x	x	**3e-3 [1e-3 - 5e-3]**
Nagano 2011	**6e-4 (4.1e-3 âĂŞ 8e-4)**	x	7.5e-4	0.14	x
Lorca 2011	**3.5e-6 (2e-6 - 8e-6) !**	x	x	x	x
Lushan 2013	x	x	**6e-3**	1.2	x
Mingxian 2013	**8e-4 [5e-4 - 1.1e-3]**	x	13e-4	0.25	x

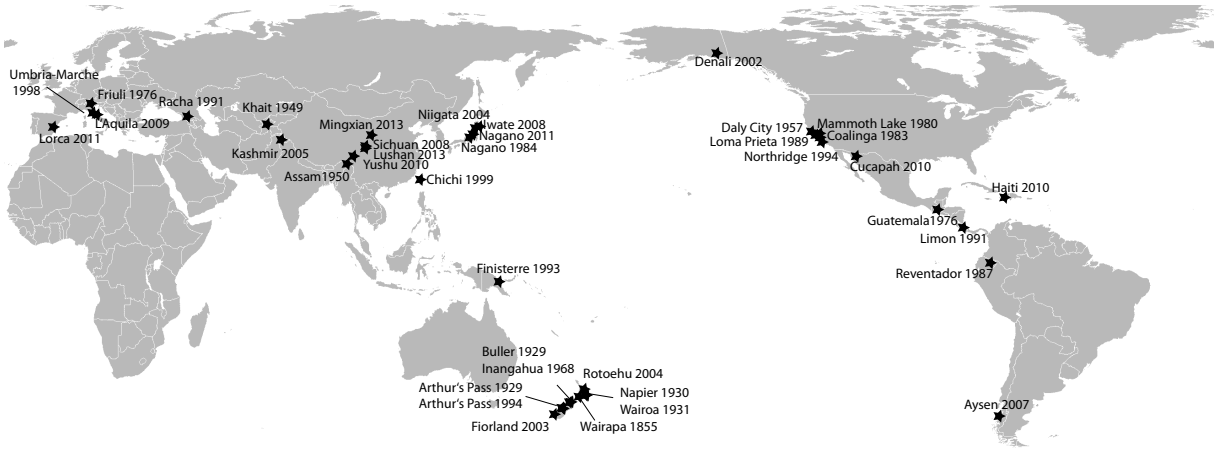

Figure 3.7 – World map with the locations of the 40 shallow earthquakes considered in this study.

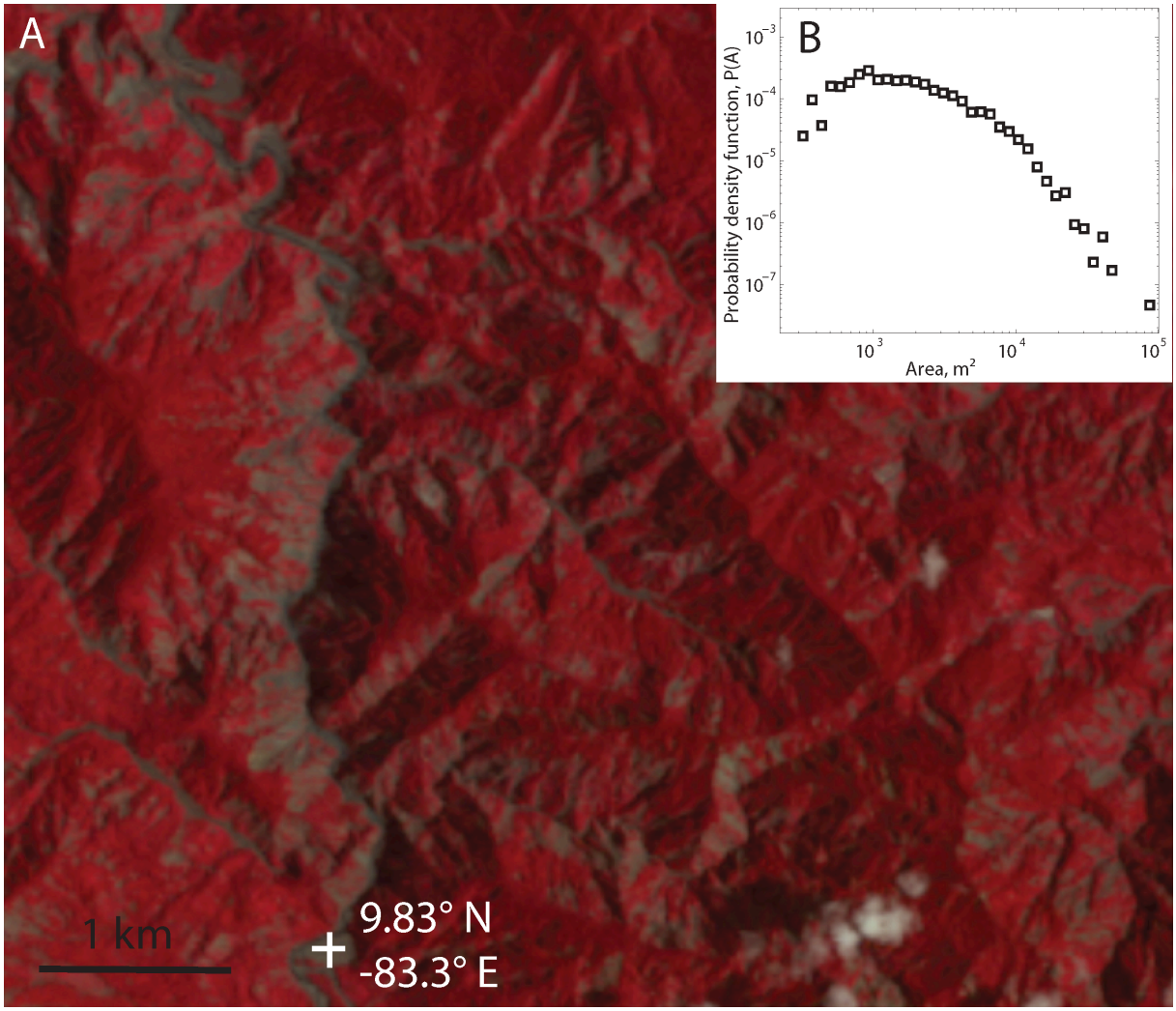

Figure 3.8 – Landsat image (February 1992) of the epicentral area of the 1991 Limon (Costa Rica) earthquake. Red represents vegetation whereas gray and white are bare rock or sediment and clouds, respectively. Visible landslides were mapped down to about $1000m^2$. The area-frequency distribution of 1643 large ($> 1000m^2$) mapped landslides is shown in the inset. The roll-over at $1000 - 3000m^2$ is likely due to resolution censoring. The total number of landslide is likely more than 3000.

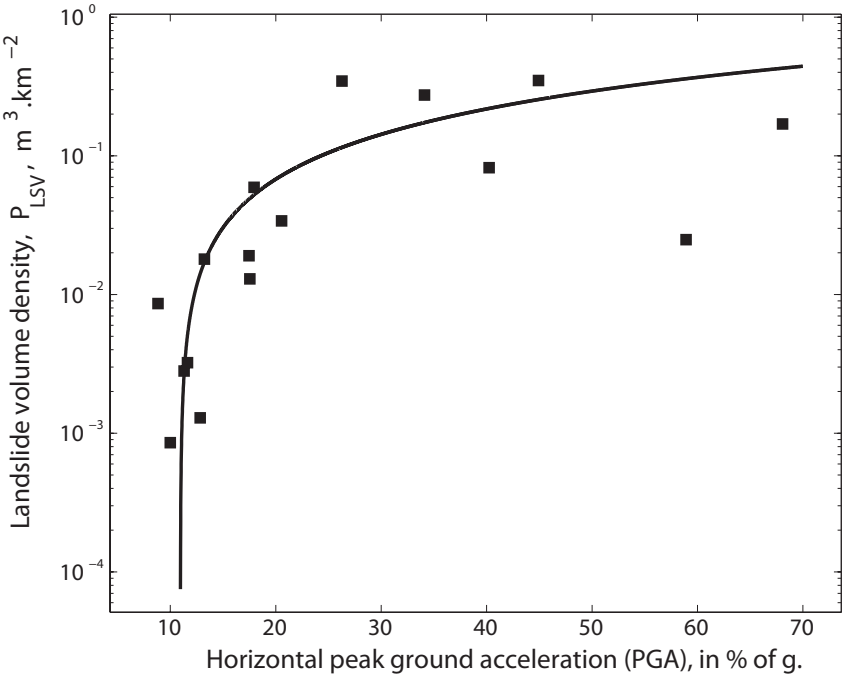

Figure 3.9 – Landslide volume density as a function of the horizontal peak ground acceleration (normalized by $1g$) in the Chi-Chi epicentral area. Available PGA records from seismic stations in Taiwan and landslide volume density were averaged within circular bins with increasing distance away from the earthquake epicenter. For reference the black curve represents the linear function $Y = 0.75(PGA - 0.11)$.

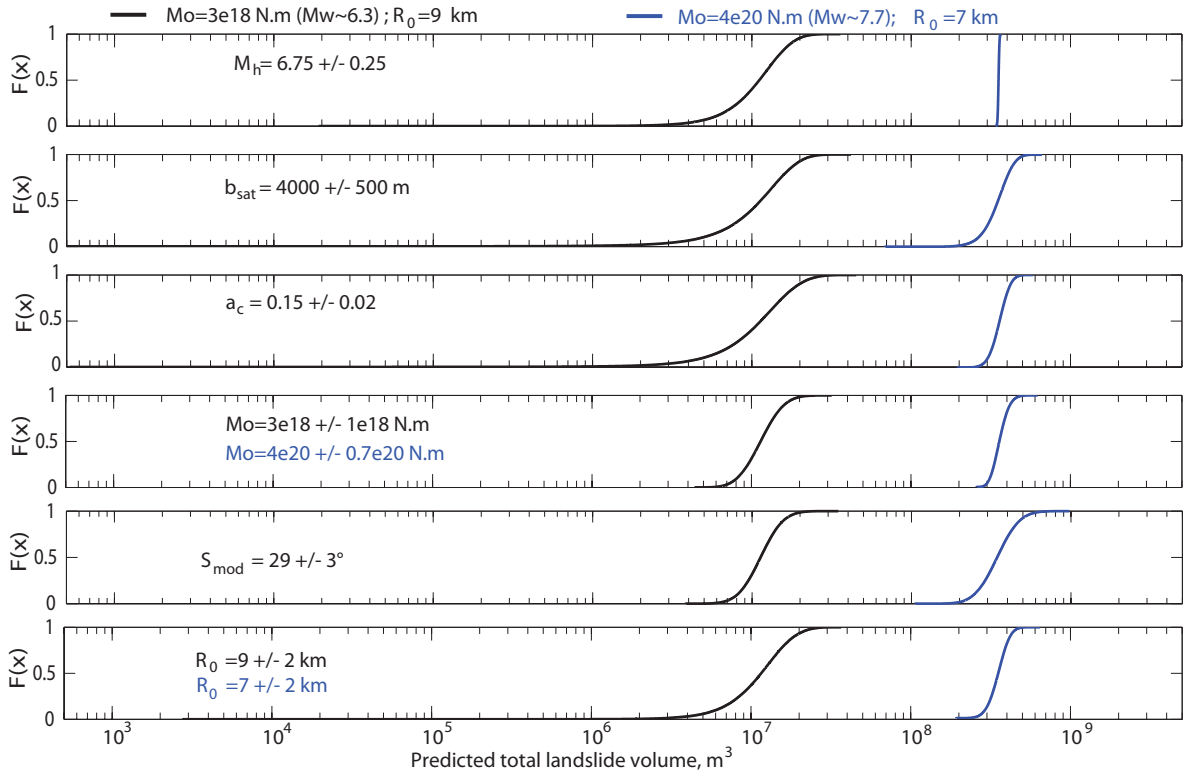

Figure 3.10 – Cumulative distribution of total landslide volume predictions for one relatively small and deep earthquake (in black) and a larger shallower one (in blue). In each panel a single parameter is varied while the others are kept constant at their mean value. Considered are the essential model parameters M_h, the hinge magnitude, b_{sat}, the saturation acceleration and a_c, the critical acceleration. Also considered are the key input data, the seismic moment Mo and the mean asperity depth, R_0 as well as the modal slope S_{mod} used to constrain the landscape sensitivity. In this exploration, the small, deep earthquake is in the very non-linear part of the model (i.e. before M_h) and is therefore much more sensitive to variations of the input parameters or of the model constant than the larger earthquake. Note that the model uncertainty ranges presented in Fig 4-6, are based on the same assumed variations of M_h, b_{sat} and a_c, and on input uncertainties reported in Table 3.7.

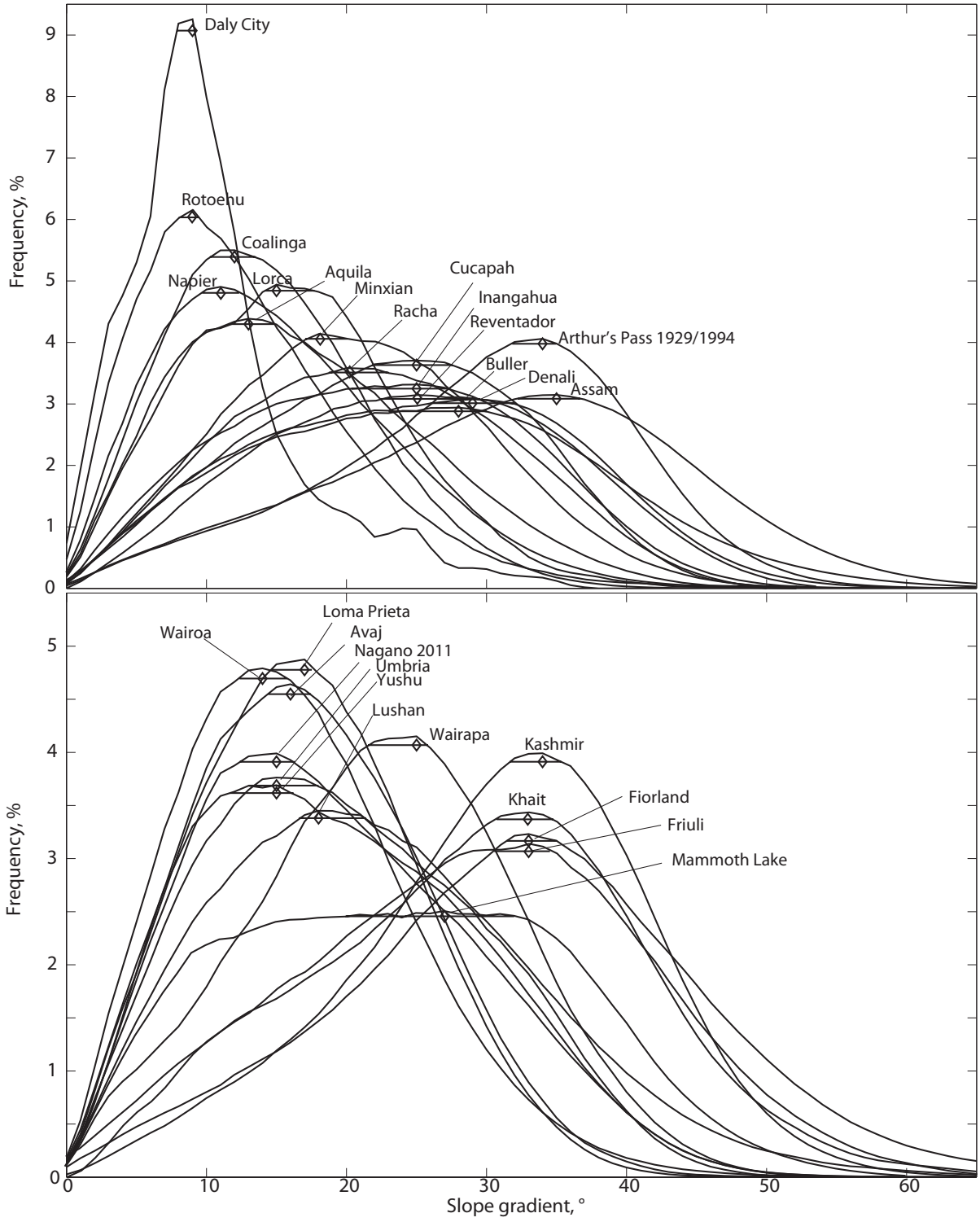

Figure 3.11 – Same as figure 3.3 of the main text but for the areas of the 29 earthquakes in our compilation for which we do not have comprehensive landslide maps.

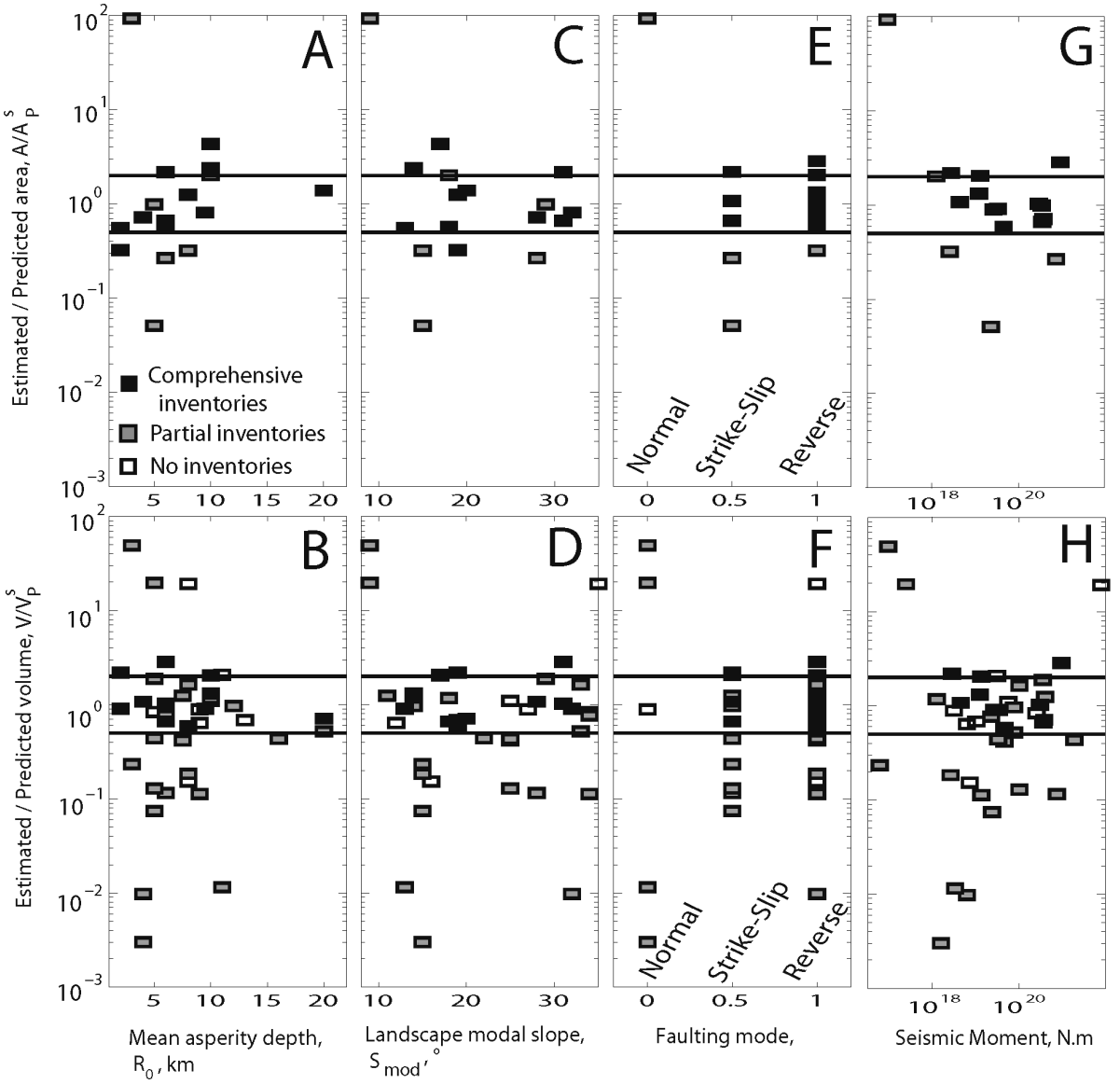

Figure 3.12 – Ratio of estimated total landslide area or volume over predicted total landslide area or volume plotted against asperity mean depth R_0 (A,B), landscape steepness, S_{mod} (C,D), faulting mode (E,F) and seismic moment (G,H). Note the absence of residual correlation in all panels except in panel A, suggesting that the mismatch between data and model prediction arises from factors not included in the model, (such as rock mass strength, hydrological state or shaking duration), and/or and/or from a discrepancy between actual earthquake characteristics and our seismological assumptions in some individual cases (See Section 3). Nevertheless, in the majority of cases, the ratio of estimated and predicted values is close to one, suggesting that for these cases the model assumptions are reasonable and the neglected factors are secondary relative to the ones considered.

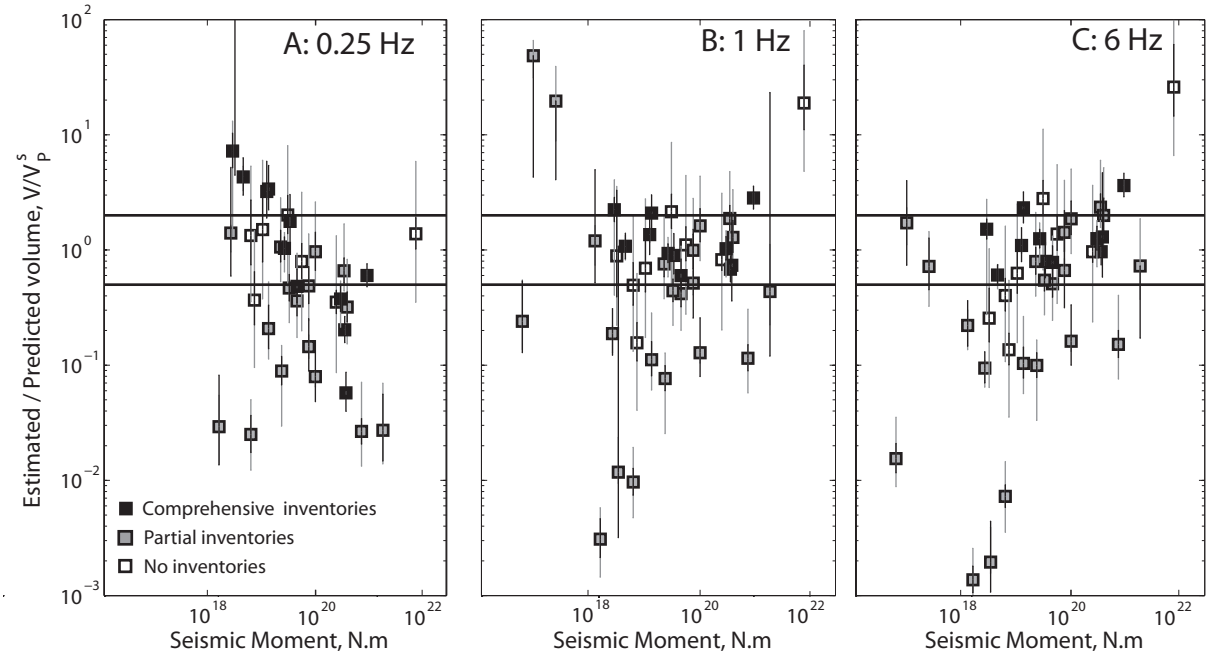

Figure 3.13 – Ratio of estimated total landslide volume over predicted total landslide volume plotted against earthquake seismic moment for different source term frequencies (Eq. 11) A: 0.25Hz, B: 1Hz, C: 6Hz.

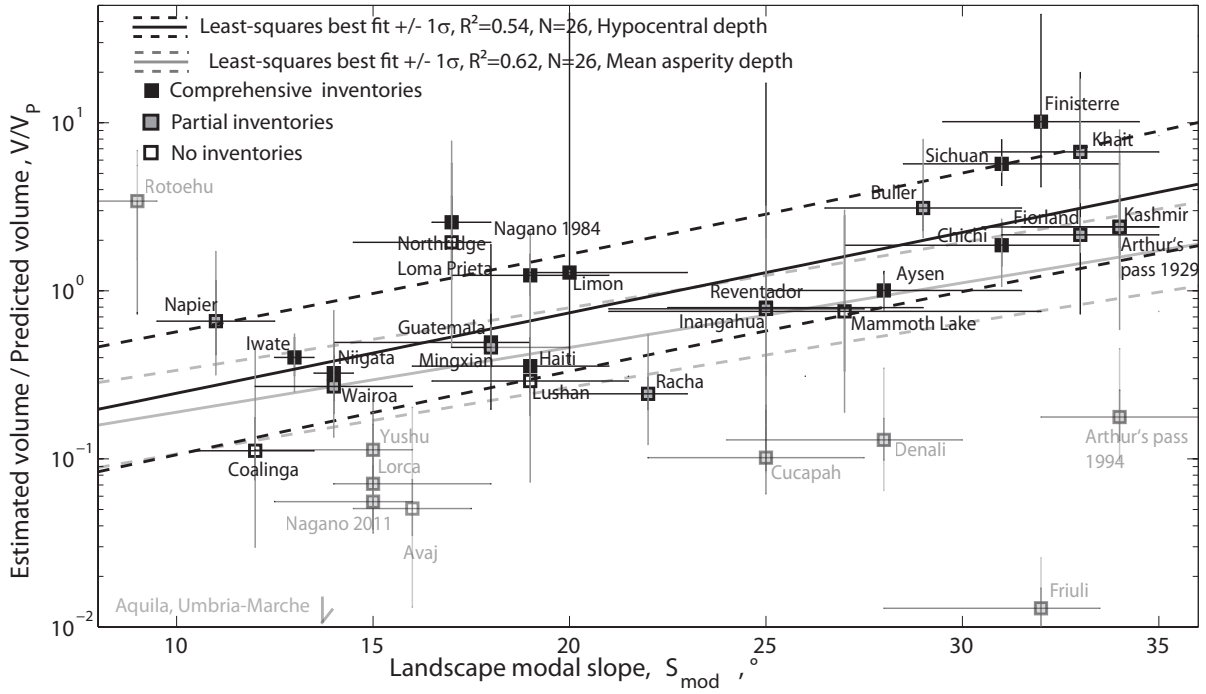

Figure 3.14 – Same as Figure 3.4 but with source depth set as the hypocentral depth. Therefore some events (e.g. Finisterre, Northridge, Napier, Buller, Khait, etc.) have a strongly reduced prediction and thus a residual larger than in Figure 3.4 resulting in a stronger control of the landscape modal slope and a larger scatter. For reference the fit obtained in Figure 3.4 is included.

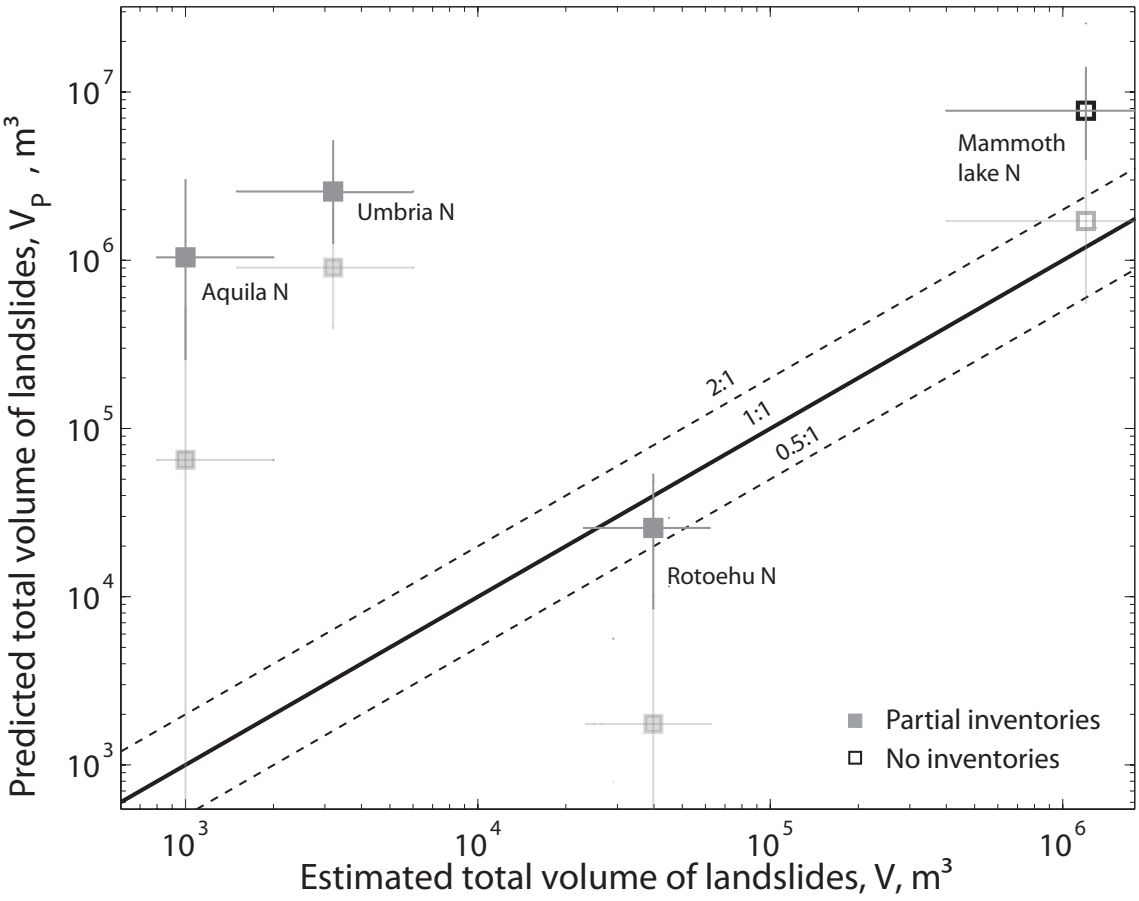

Figure 3.15 – Predicted total landslide volume plotted against estimated volume. In this prediction, normal faults are assumed to produce as much shaking as reverse slip and strike slip mechanisms. For comparison, the model prediction with 30% reduced shaking for normal faults (as in Figure 3.6) are shown in grey.

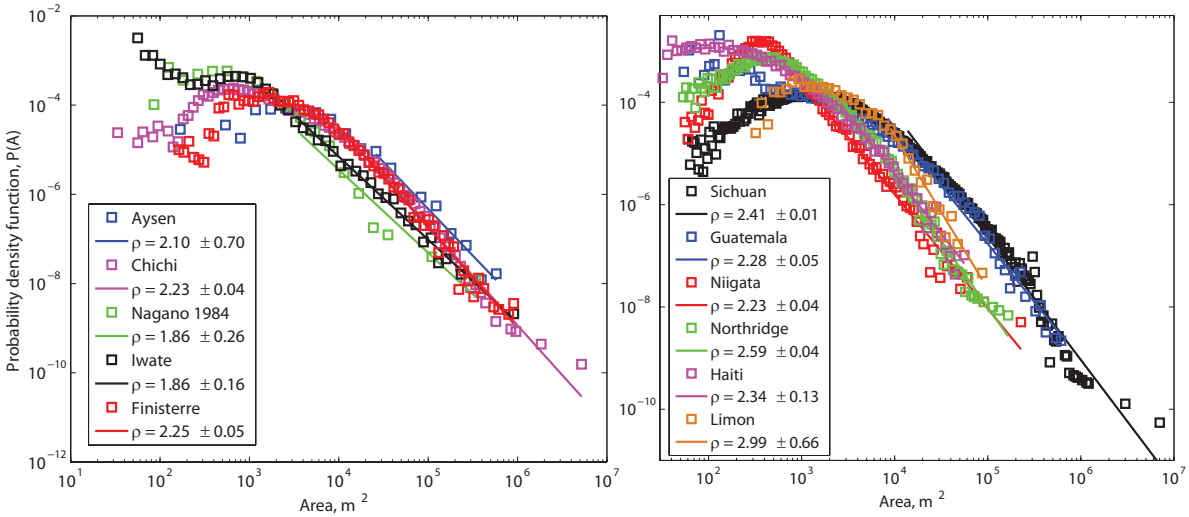

Figure 3.16 – Landslide area-frequency distribution for our 11 exhaustive inventories. Bins were logarithmically spaced between the smallest and largest landslide area of each catalogue, with a number of bins equal to the square root of the number of landslides in the inventory. The decay exponent and its $1-\sigma$ uncertainty were obtained by least-square minimization of the bins with a probability density 10 times smaller than the probability density at the roll-over to avoid to be biased by the roll-over of the distribution.

Link

In Chapter 3, I have proposed a new analytical prediction of the total landslide area and landslide volume caused by an earthquake. This seismologically-consistent prediction is derived from seismological and geomorphological scaling relationships and accounts for important processes such as wave attenuation, ground shaking saturation and fault size growth with moment. The landscape sensitivity to ground shaking is empirically constrained with the landscape modal slope, and by considering the proportion of the shaken area with hillslopes steep enough for landslides to occur. I have shown that this prediction has a higher accuracy compared to previous relationships, although it fails for settings with exceptional rock strength or earthquakes with exceptional ruptures. This prediction is easy to implement in landscape evolution models and for rapid assessment of earthquake secondary hazards.

The development of this relation is an important step towards understanding the net effect of earthquakes on long term topographic evolution, as discussed in Chapter 6. Furthermore, explicit use of seismological and geomorphological parameters will permit going beyond comparing earthquakes of different sizes and exploring which conditions may lead to earthquakes with a negative mass balance, i.e., more erosion than rock uplift. Its analytical form allows inexpensive computation of an earthquake mass balance and therefore evaluation of the net topographic change caused by many earthquakes over longer timescales.

In the development of the analytical model I also suggested that landslide response to shaking should be considered in the context of the fact that strong motion may cause damage in the ground and reduce cohesion, in addition to the force balance changes due to the transient accelerations of the ground (e.g., Newmark, 1965). If damage occurs above a threshold of shaking, then many slopes may be damaged by an earthquake but not fail coseismically. We would expect these slopes to be more sensitive to further perturbations and such persistent damage may explain the elevated fluvial sediment transport rates and landslide rates observed after some earthquakes (Saba et al., 2010; Hovius et al., 2011; Parker et al., 2015). These aspects will be quantified for various earthquakes in Chapter 4. We would also expect such ground damage to leave a signature in the geomechanical properties of the subsurface, possibly related to hydrological or seismological changes observed during and after earthquakes (Wang et al., 2004; Sawazaki and Snieder, 2013; Nakata and Snieder, 2012). The relations between co-seismic and post-seismic velocity changes in the subsurface, and ground damage and landslide rates will be discussed in Chapter 5.

Before comparing the prediction of Chapter 3 to the uplift caused by earthquakes, we will assess the contribution of post-seismic enhanced erosion that has been suggested to be significant by preliminary studies (Hovius et al., 2011). To this end, in Chapter 4, I will use time series of landslide maps from the epicentral areas of four intermediate

to large earthquakes (M_w 6.6 to 7.6) to assess the influence of earthquakes on the lingering landslide susceptibility of hillslopes. This requires correction for variable climatic forcing. I will also probe which mechanism best explains the observed changes, and estimates how the post-seismic erosion compares to the coseismic erosion.

Chapter 4

Transient changes of landslide rates after earthquakes.

Abstract

Earthquake impart an impressive forcing on epicentral landscapes, with immediate and often catastrophic hillslope response. However, their legacy on geomorphic process rates remains poorly constrained. We have determined the evolution of landslide rates in the epicentral areas of four intermediate to large earthquakes (M_w 6.6-7.6). In each area, landsliding correlates with the cumulative precipitation during a given interval. Normalizing for this meteorological forcing, landslide rates have been found to peak after an earthquake and decay to background values in 1-4 yr, with the decay timescale probably proportional to the earthquake magnitude. The transient pulse of landsliding is not related to external forcing such as rainfall or aftershocks, and we tentatively attribute it to the reduction and subsequent recovery of ground strength. Observed geomorphic trends are linked neither with groundwater level changes nor with root system damage, both of which could affect substrate strength. We propose that they are caused, instead, by reversible damage of rock mass and/or loosening of regolith. Qualitative accounts of ground cracking due to strong ground motion abound, and our observations are circumstantial evidence of its potential importance in setting landscape sensitivity to meteorological forcing after large earthquakes. [1]

1. Originally published as: Marc, O., Hovius, N., Meunier, P., Uchida, T., and Hayashi, S. Transient changes of landslide rates after earthquakes, *Geology, DOI:10.1130/1G36961.1, 2015. COPYRIGHT 2015 Geological Society of America. For permission to copy, contact editing.at.geosociety.org.*

4.1 Introduction

In steep terrain, large earthquakes can trigger widespread landsliding (e.g., Keefer, 1994; Meunier et al., 2007), which can persist long after coseismic activity has ceased. This may affect the socio-economic recovery of epicentral areas (e.g., Huang and Li, 2014), but also the sediment load of rivers and adds to the total erosional effect of an earthquake. High landslide activity has been observed, for example, during several years after the $M_w > 7.5$ 1999 ChiChi (Taiwan) and 2005 Kashmir earthquakes (Lin et al., 2008; Hovius et al., 2011; Saba et al., 2010). However, the magnitude of the geomorphic legacy of earthquakes and the manner of its decay have not been determined, in part because the seismic effect must be isolated from the strength of meteorological forcing and other potential controls on landsliding. For this, knowledge of the local relation between rainfall and landslide rate under normal, aseismic conditions is required.
We have compiled time series of landslide inventories in the epicentral areas of four intermediate and large earthquakes with similar mechanisms and source depths. These inventories span periods before, during and after the earthquakes and can be compared with matching records of precipitation and background seismicity. Normalizing for meteorological forcing, we demonstrate that landslide rates were significantly elevated for periods of 0.7-4.5 yr after these earthquakes, and that order-of-magnitude increases in landslide rate decreased exponentially to background values over this interval. Aftershocks and subsequent seismicity, and biological and hydrological effects of the earthquakes do not match this transient geomorphic response, leaving mechanical ground strength reduction and progressive healing as the probable cause of the observed geomorphic changes.

4.2 Cases, data and methods

Here, we consider four shallow thrust earthquakes of intermediate to large magnitude: the 1993 M_w 6.9 Finisterre (Papua New Guinea) earthquake (Stevens et al., 1998), the 1999 M_w 7.6 ChiChi (Taiwan) earthquake (Shin and Teng, 2001), and the 2004 M_w 6.6 Niigata (Hikima and Koketsu, 2005) and 2008 M_w 6.8 Iwate (Suzuki et al., 2010) earthquakes in Japan. For each of these earthquakes, we have assembled data to evaluate the co-evolution of mass wasting, seismicity and rainfall in epicentral catchments. The $39km^2$ Imokawa (Niigata) and $430km^2$ of the Hazama (Ichi-, Ni- and San-) and Iwai (Iwate) catchments in Japan have a temperate climate with winter snow and larger rainstorms in summer and fall. They are mostly underlain by young volcanic tuffs and ignimbrites. The Finisterre Mountains of Papua New Guinea are also dominated by volcaniclastic rocks, partially capped by marine sediments. They have orographically enhanced tropical rainfall throughout the year. Our landslide mapping covers a $1380km^2$ area mainly in the south flank of this mountain range. The Choshui catchment in Taiwan is composed of Neogene shales and sandstones, with greenschist facies metasediments in the eastern headwaters, and the climate is sub-tropical with typhoons. There, landslide mapping was restricted to three southern subcatchments with a total surface area of $1280km^2$.
We have used time series of satellite images or aerial photographs to map new landslides in vegetated topography and compute mobilization rates before, during and

after the earthquakes (see the methods section of Appendix 4.7, and Suppl. Table 4.1 therein). Time resolution is particularly high for the ChiChi earthquake case, with 34 map intervals over the period 1994-2006 and five intervals between 2009 and 2013. We covered 16 intervals between 1989 and 2010 for the Finisterre earthquake, 6 intervals between 2006 and 2013 for the Iwate earthquake, and 7 intervals between 1999 and 2009 for the Niigata earthquake. The length and number of intervals was limited by the available imagery. We computed the total volume of debris mobilized during a map interval with global area-volume scaling relationships Larsen et al. (2010) (see Appendix 4.7), avoiding landslide amalgamation to obtain conservative volume estimates (Marc and Hovius, 2015).
In each area, we have compiled records of ambient seismic activity and rainfall, the two main triggers of landsliding. The ambient seismicity, based on the catalogue of Storchak et al. (2013), comprises all earthquakes other than those mentioned above. This was restricted to earthquakes < 33 km depth and < 30 km away from the mapping area. The largest ambient earthquake in any of the records had M_w 6.3. Beyond the defined depth and distance range, earthquakes of this size are unlikely to trigger significant landsliding because of seismic wave attenuation (Meunier et al., 2007).
Meteorological conditions during map intervals were constrained with available data, which varies between cases. For the Japanese cases, we used daily precipitation (solid and liquid) measurements from local rain gauges, but for the New Guinea case, we were restricted to monthly total precipitation interpolated from distant stations (see the Appendix 4.7). In Taiwan mountain range, where rain data are scarce and discontinuous, we used daily records of river discharge near the outlet of the Chenyoulan catchment, (23.72 °N, 120.84 °E), a major subcatchment of the Choshui river. We filtered the hydrograph to remove the baseflow and obtain an equivalent daily precipitation averaged over the whole catchment (Eckhardt, 2005) (See Appendix 4.7, Suppl. Fig. 4.4).

4.3 Precipitation variability and landsliding

To isolate the long-term effects of large earthquakes on landslide rates, we first removed meteorological effects. During intervals without major seismic activity, the rate of landsliding should be related chiefly to the amount of precipitation (Iverson, 2000), but the nature of this relation is underconstrained and probably prone to local effects. We have sought to constrain the local relationship between the total landslide volume per unit of mapped area, V, over a mapping interval and the cumulative precipitation, P, during this interval (Table 4.1 ; Fig. 4.1) for the ChiChi case with data from 14 pre-earthquake intervals between 1994 and 1999. V correlates best with an exponential function of P ($R^2 = 0.89$). Hence, the total landslide volume, Vp, expected for an interval with known P can be found by:

$$Vp = A \exp\left(\frac{P}{B}\right) \tag{4.1}$$

where $A = 5m^3.km^{-2}$ and $B = 68mm$ are area-specific empirical constants, probably reflecting the area ś pre-earthquake susceptibility to slope failure and the geomorphic efficacy of rainfall (cf., Burtin et al., 2014), respectively (Fig. 4.1). Notably, the rate of landsliding during 2009-2014, significantly after the end of the transient geomorphic response to the ChiChi earthquake according to Hovius et al. (2011), fits well with

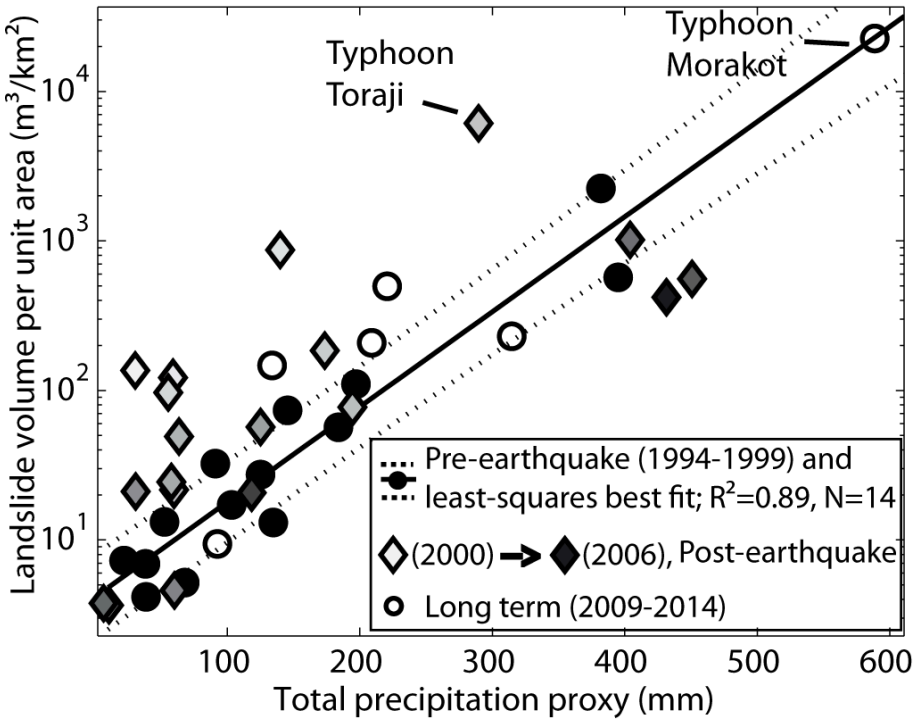

Figure 4.1 – Total landslide volume per unit mapped area against cumulative precipitation proxy, P, in the ChiChi (Taiwan) area. In this case, P is obtained by hydrograph filtering. Note that the pre-earthquake relationship between climate and landsliding is consistent with the long term data (post 2009).

Equation 4.1. This interval included the exceptional rainfall during passage of typhoon Morakot (Chien and Kuo, 2011), confirming the robustness of our empirical expression for the precipitation control on landslide rates over a large range of rainfall. It also suggests that intervals sufficiently long after a seismic perturbation can be used together with the pre-earthquake data to derive a climatic normalization.

The Niigata and Finisterre cases are less well constrained, but follow the same pattern as the ChiChi case, with landslide rates during post-seismic intervals systematically above background levels, determined before or longer after the earthquake (Fig. 4.5). Thus, it seems reasonable to define the climatic normalization based on post seismic data only, as necessary for the Iwate case (Fig.4.5). Ideally, the parameters of this normalization would relate to physical characteristics, such as rock strength, landscape steepness and pore water pressure. However, the nonlinear nature of Equation 4.1 indicates that the interval over which landsliding and precipitation are summed matters, and that a physically sound relationship between precipitation and landsliding must be based on individual rain events. Available remote sensed imagery stipulates that most of our landslide mapping intervals span multiple rain events, precluding an optimal approach. Despite this limitation, normalization for the rainfall control on landslide rates according to Equation 4.1 is adequate for our purpose.

4.4 Enhanced post-seismic landsliding

The ratio $V* = V/Vp$, should track non-climatic changes in the landslide rate, due either to secondary seismic forcing (i.e., aftershocks or ambient seismicity), or a

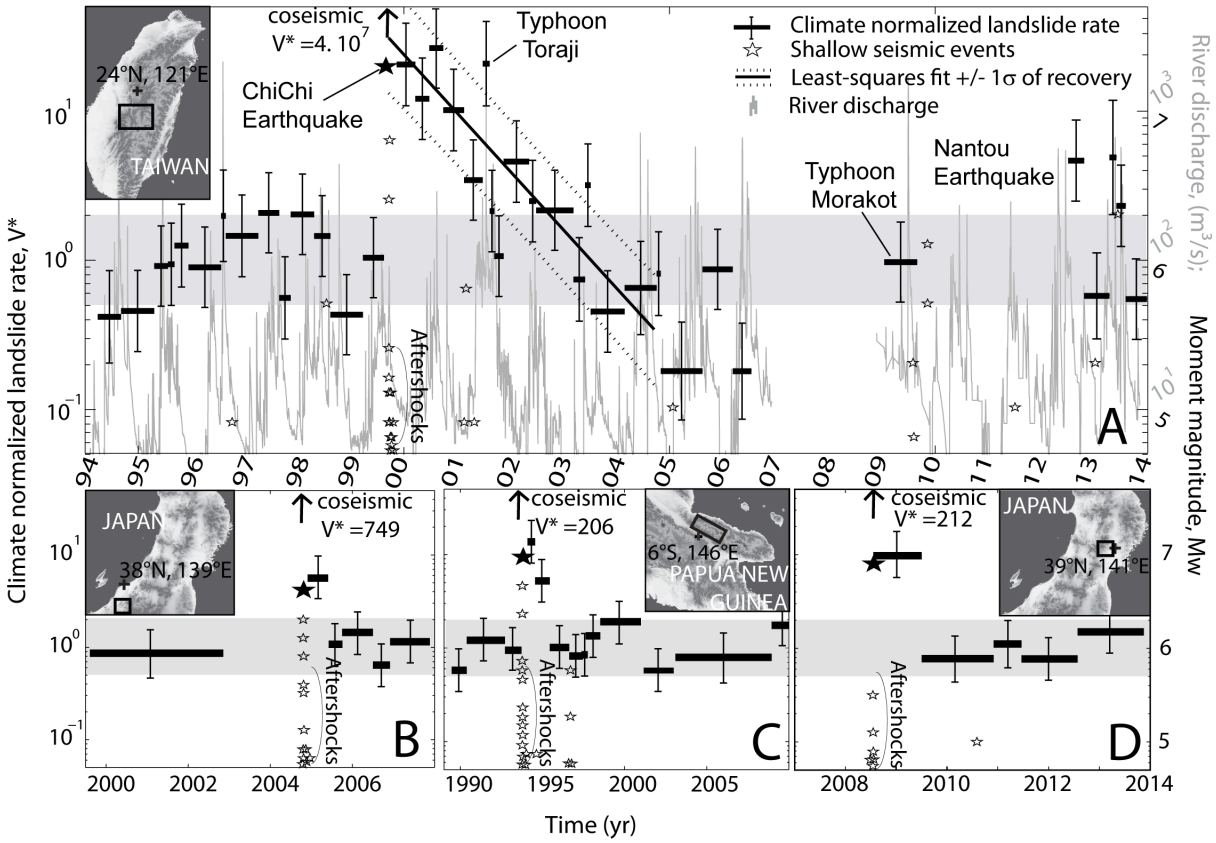

Figure 4.2 – Normalized landslide rate against time in the (A) Chi-Chi, Taiwan (B) Niigata, Japan (C) Finisterre, Papua New Guinea, and (D) Iwate, Japan, earthquake epicentral areas. The right hand y-axis shows the magnitude of local earthquakes and the river water dishcarge in (A). In each insets the black box shows the mapping area location. Each bar width represents the interval time span. Vertical whiskers represent the 1σ uncertainty on $V*$ obtained by propagating the uncertainty of our climate normalization Vp (Fig. 4.1, 4.5) and of our volume estimate V. Note that the coseismic intervals are plotting off the scale.

change in the susceptibility of the topography to slope failure. In this section we analyze the temporal evolution of the precipitation normalized landslide rate $V*$ to reveal and quantify the long-term effect of earthquakes on hillslope stability. In each case, the earthquake disturbance is characterized with the peak change of $V*$ after the coseismic interval, and the time until complete recovery, t_r, defined here as the return of $V*$ to within the range of values for background conditions.

In all cases, $V*$ is relatively constant before the earthquake, varying between 0.5 and 2, and then increases by several orders of magnitude in the coseismic interval (Fig. 4.2). After this, $V*$ decays rapidly over one to several years until values around 1, on timescales always exceeding by far the period of aftershocks, which typically lasts one to a few months (Fig. 4.2). The peak and decay sequence is best constrained for the ChiChi earthquake, with 16 intervals of 32-256 days, over which the evolution of $V*$ is well described by an exponential decay function ($R^2 = 0.76$). Scatter in this data set may be due to the limitations of the rainfall correction but also to local seismicity, such as the 2013 M_w 6.3 Nantou earthquake (Fig. 4.2), or the occurrence of rare large landslides, possibly unrelated to instantaneous rain forcing, for example in late 2012.

The exponential best fit to $V*$ values over the interval of landslide rate decay after the ChiChi earthquake defines a 22x (-13/+28, 1σ) increase of the normalized landslide rate, averaged over a year, with respect to the pre-earthquake period and a recovery time $t_r = 3.8 \pm 0.9$ yr. The other cases only have 1-2 intervals with elevated landslide rates, showing a fast and complete recovery that does not disagree with the non-linear evolution observed in the ChiChi case. The peak change of $V*$ was 16x, 9x, and 5x, and t_r = 1.5-2.7 yr, 1.0-2.4 yr and 0.5-0.9 yr, for the Finisterre, Iwate, and Niigata, earthquakes, respectively. This suggests a correlation between the earthquake magnitude and the recovery timescale (Fig. 4.6).
During this transient geomorphic response, landsliding at elevated rates adds to the debris volume mobilized by an earthquake. In all four cases considered here, these post-seismic landslides represent only $\sim 2\%-5\%$ of the volume of coseismic landslides. The post-seismic landslide volume for the ChiChi earthquake is considerably smaller than previously suggested based on analysis of river suspended load measurements (Hovius et al., 2011), implying that post-seismic landsliding may not be the principal cause of heightened fluvial sediment transport rates after large earthquakes.

4.5 Temporary substrate weakening

Despite differences in substrate and climate the four earthquakes have induced a common geomorphic response, with a rapid, possibly exponential recovery phase, unrelated to aftershocks and rainfall forcing. This could have had several causes.
Oversteepened slopes can form in the crowns of landslides, promoting subsequent failures and expansion of erosion scars. Such secondary failures in the scarps of coseismic landslides make up $15\% - 20\%$ of the total volume of post-seismic landslides in the Finisterre and ChiChi areas and $30\% - 50\%$ in the Niigata and Iwate areas. Thus, this mechanism alone cannot explain the transient geomorphic response.
The root system of the verdant hillslope vegetation in all study areas may have been damaged by shaking, leading to bulk ground strength reduction. Studies at the tree scale in seismically perturbed mountain terrain in New Zealand found very little damage or growth disturbance caused by strong ground motion (Allen et al., 1999; Vittoz et al., 2001). Moreover, in the ChiChi case, where the landslide rate excursion was the strongest, no significant reduction of the canopy Normalized Difference Vegetation Index could be found (Suppl. Fig. 4.7). In as far as the health of above ground biomass is tied with its root mass state, we have no indication that the latter was pervasively affected by the earthquake, resulting in a geomorphologically significant decrease of ground strength.
Pore pressure variations due to seismically induced groundwater level changes were also not a likely driver of the observed trends in landsliding, as they typically dissipate within months (Muir-Wood and King, 1993). After the ChiChi earthquake, the groundwater system recovered in 3 months (Wang et al., 2004), an order of magnitude faster than landslide rates.
Finally, hillslope strength reduction could be due to mechanical damage affecting the superficial layers, by decompaction of soil and colluvium, or an extension and dilation of cracks, joints and bedding planes in regolith and rocks. Field investigations have reported extensive ground cracking in earthquake epicentral areas (e.g., Tutton and Browne, 1994; Owen et al., 2008), with possibly lasting geomorphic effects.

If reduced hillslope strength is indeed a dominant cause of elevated post-seismic landslide rates, then their systematic decrease might be attributed to the erosional removal of damaged layers, or to a healing mechanism. Although damaged layers may be removed by post-seismic landsliding during the recovery time, this only involves $5-10\%$ of all steep slopes affected by strong ground motion. Spatial heterogeneity of the shaking intensity and ground strength could explain why relatively few slopes fail during recovery. However, if the removal of damaged slope materials would dominate the recovery, then the recovery of $V*$ should be proportional to the occurrence of post-seismic landslides. In that case, we would expect a very slow recovery during relatively inactive periods and a sudden drop of $V*$ after major landslide episodes. In the well documented ChiChi case, $V*$ decreased steeply over the relatively dry interval 10/1999-06/2001, preceding the typhoon Toraji. In contrast, it did not change much over this first large typhoon after the earthquake, which caused substantial landsliding (Fig 4.1 and 4.2, Appendix 4.7), suggesting that erosional damage removal was not an important mechanism of recovery. Instead, the occurrence of non-linear soil strength recovery after shaking has been shown by (Lawrence et al., 2009). This may be due to rearrangement of aspherical clasts under overburden weight and enhanced by groundwater percolation. Bedrock "healing" could be due to crack closure under pressure, infilling with sediment and/or rapid mineral precipitation.
The size of landslides in the aftermath of an earthquake may hold information about the depth range affected by seismic reduction of the substrate strength. As landslide surface area and average depth are linked (Larsen et al., 2010), (see Appendix 4.7), the range of landslide depths can be derived from the frequency distribution of mapped landslide areas. In all four cases, this distribution can be described by a power-law for large landslides with a roll-over at the mode of the distribution (Fig. 4.3), consistent with earlier work (e.g., Malamud et al., 2004a). Area-frequency distributions of landslides during the recovery periods were similar to those of background intervals, albeit with higher rates. Hence, more landslides occurred at all sizes, implying uniform ground strength decrease at all depths relevant to the observed slope failure ($\sim 0-10m$). It also means that the post-earthquake increase in volumetric landslide rate corresponds to an equivalent increase in areal landslide rate and landslide frequency (Suppl. Fig. 4.8).

In the Finisterre Mountains and in the ChiChi area, many landslides had depths $> 2m$ (Fig. 4.3). In these steep terrains soil is mostly discontinuous and thin implying that the underlying bedrock and regolith were damaged. Ultimately, further study is required to understand the damage process and the relative contributions of damage removal and healing to the landslide rate recovery.
Our data suggest that damage recovery is near complete, even though one might expect at least some damage to be permanent. Because seismically active areas have damaged rock as a matter of cause, some additional damage due to a single earthquake might easily blend in this background. Moreover, permanent damage is probably more likely to accumulate in relatively intact rock below the soil and regolith layer, at depths $> 5m$, which are only rarely sampled by landsliding. For these reasons our analysis may not be able to detect permanent damage.

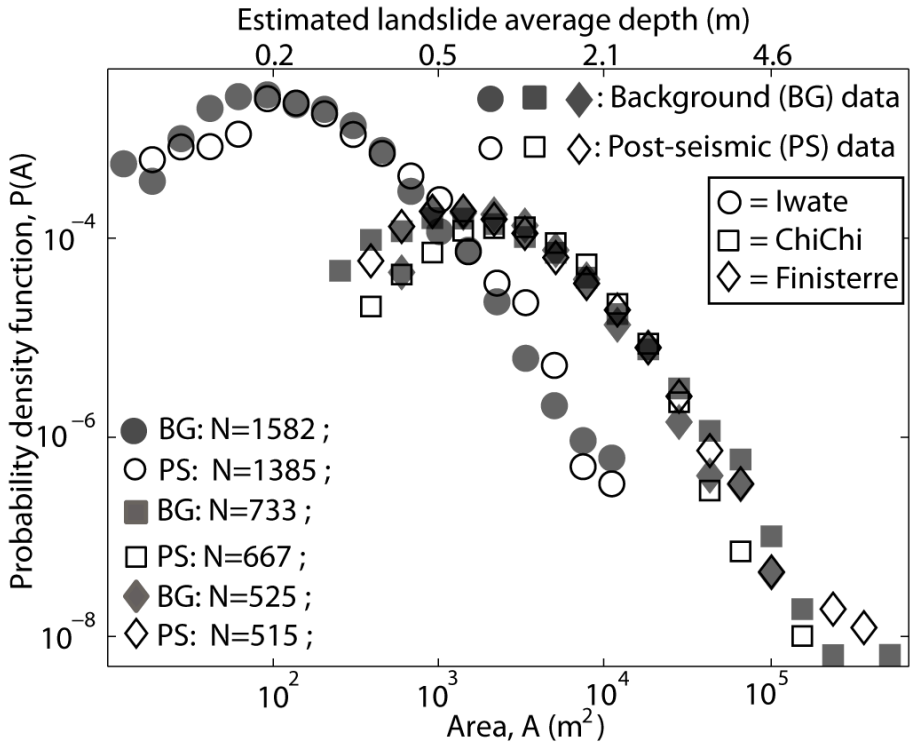

Figure 4.3 – Area-frequency distributions for the background and post-seismic intervals in the ChiChi, Taiwan, Iwate, Japan, and Finisterre, Papua New Guinea earthquake epicentral areas (See Appendix B). The equivalent mean depth derived from area-volume scaling relationships (Larsen et al., 2010) is also reported.

4.6 Conclusion

We have estimated evolving landslide rates in four areas affected by shallow thrust earthquakes ranging from M_w 6.6-7.6. These rates reflect external forcing and propensity to failure of local topography. To isolate the lasting effect of earthquakes, we have empirically normalized observed rates of landsliding by the magnitude of rainfall forcing. Our findings reveal that intense and widespread mass wasting during an earthquake is followed by a possibly exponential recovery of landslide rates over many months to years, unrelated to aftershock activity. In the studied examples, normalized post-seismic landslides rates were initially 5-22x higher than equivalent pre-seismic rates, recovering to background values in $0.7 \pm 0.2 - 3.8 \pm 0.9$ yr, apparently with greater peak rates and longer recovery times for larger earthquakes. However, enhanced landsliding following initial coseismic shaking does not add significantly to the volume of coseismic landsliding, $2\% - 5\%$ in our cases. Because the evolving landslide rates could not be linked to any external forcing we posit that they relate to a transient ground strength decrease. Excluding root damage and water table change, the most likely processes are reversible decompaction of soil and colluvium and/or bedrock damage caused by the earthquake strong motion. Uniformity of changes in the frequency of slope failure across the full size range of landslides indicates that strength decrease is not limited to soil but also affects shallow bedrock.
These results underscore that landslide hazard may remain elevated several years after intermediate and large earthquakes and that improved understanding of reversible,

seismically induced changes of ground strength may aid effective planning of socio-economic recovery of earthquake epicentral areas. Importantly, regional ground strength is not a static, but a dynamic parameter, that may vary significantly due to earthquake disturbance and then recover through active but as yet unidentified processes.

4.7 Supplementary materials to Chapter 4

4.7.1 Landslide mapping

We used pairs of satellite images or aerial photographs to map new landslides in forested catchments at high temporal resolution and compute landslide rates (see Table 4.1). Landslide areas are detected because they clear standing vegetation that contrasts strongly with bare rock or sediment. The resolution did not generally allow adequate distinction between landslide scars and deposits. Therefore, landslides were mapped as a single disturbed area. However, where landslides generated debris flows, or river aggradation, we only mapped what appeared as the landslide source. In case of landslide reactivation we only mapped the portion of the previous slide where the new collapse occured. We never mapped old landslide scar textural changes (where only the interior of an existing scar appeared with a different texture), as they are likely to be only minor reactivation and rockfalls with negligible volume. Mapping of anthropogenic clearings, often characterized by sharp, straight boundaries, was avoided as much as possible. Areas with slopes gentler than 10°, or corresponding to field or human activities in higher resolution, more recent imagery (e.g., Google Earth) were also avoided. The landslide polygons were all delineated by hand, using DEM (at 10m resolution for Japan, 30m elsewhere), and GoogleEarth high resolution image to avoid amalgamation of different, adjacent failures that would cause volume over-estimation (Marc and Hovius, 2015). Thus we are confident that our landslide area mapping is rather conservative and well suited to be converted into volumes with area-volume empirical scaling (Larsen et al., 2010).

4.7.2 Landslide volume computation

We have used published area-volume relationships (Larsen et al., 2010) to estimate the volume of landslides from the mapped disturbed areas. It was assumed that landslides with area $> 10^5 m^2$ involved bedrock, and that smaller landslides were mixed bedrock and soil failures. Landslide maps typically do not distinguish between scar and deposit, lumping the two in one area measure. According to Larsen et al. (2010) scars and deposits have area-volume relations with the same power-law exponent (Larsen et al., 2010), implying constant size ratios between scar and deposit areas of 1.1 and 1.9 for mixed and bedrock landslides, respectively. Hence, we have estimated the scar area by dividing the mapped landslide area by 2.1 and 2.9 for mixed and bedrock landslides, respectively, assuming that runout was equal to the scar length. This may lead to an overestimation of landslide scar volume where runout was much longer, mostly for small slides, which do not contribute significantly to the total eroded mass. Conversely some large landslides on gentle slopes have overlapping scar and deposit areas, meaning that our correction causes a significant underestimation of the scar size and thus the landslide volume. As a systematic way to constrain runout variations is not available, we have applied a blanket correction for every slide, thus obtaining a conservative total volume. We have calculated the volume of every individual landslide in a catalogue, and summed to obtain a total volume of landslides for each earthquake. The average depth of each landslide was simply obtained by dividing the scar area by its estimated volume. Uncertainties in this approach include the coefficient and exponent of the landslide area-volume relations, $V = \alpha A^{\gamma}$, for which

standard deviations have been reported as $\sigma_\alpha = \sigma_\gamma = 0.005$ for mixed bedrock-soil landslides and$\sigma_\alpha = 0.02$ and $\sigma_\gamma = 0.03$ for bedrock landslide scars (Larsen et al., 2010). For potential mapping errors a standard deviation of 20% of the mapped area was arbitrarily assumed. Assuming no covariance between these three sources of uncertainties we used gaussian propagation of error to obtain $1 - \sigma$ uncertainties on the volume of each mapped landslide. The standard deviation on the total landslide volume for an earthquake was calculated assuming that the volume of each individual landslide was unrelated to that of any other, thus, ignoring possible co-variance. In all areas, the uncertainties on the total volume of an interval was typically about 10 to 15% of the total volume and reaching 30% for a few intervals where total volume is dominated by individual events.
For one interval in the Niigata and Iwate time series we had non-homogeneous mapping and had to apply a specific correction. In the Iwate area, the last mapping, in 2013, covered only $143km^2$ in the upper part of our regular $430km^2$ mapping area. However, this area was among the most affected by landslide in the previous intervals, containing on average 60% of the landslide volume mobilized between 2009 and 2012. Therefore, we normalized the 2013 interval by multiplying its total volume by 1.4.
In the Niigata area, no airphotos were available to constrain the pre-earthquake landslide rates and we could only map landslide activity based on 15 m resolution pan-sharpened Landsat 7 imagery (Table 4.1). Only a few landslides were detected and we added landslides in neighbouring catchments, assuming that they must have similar average landsliding rate. Given that we accessed only low resolution imagery the 1999-2003 minimum landslide area we could detect was about $1000m^2$ compared to $\sim 10m^2$ in more recent years. In the recent mapping, the average proportion of total volume coming from landslides $> 1000m^2$ is about 30% and hence it is likely that we underestimate our pre-earthquake rate by a factor of 3 and have corrected this rate accordingly. This relies on a constant ratio between small and large landslides, before and after the earthquake. This is consistent with our observation of constant size-frequency distributions in the other study areas (Fig. 4.3).

4.7.3 Climatic forcing

In Japan we used daily precipitation data from rain gauges located near to the mapped catchments (JMA, http://www.data.jma.go.jp/gmd/risk/obsdl/index.php, last accessed February 2015). We averaged data from the Matsurube station (39.01°N, 140.86°E) and the Komanoyu station (38.94°N, 140.82°E) for the Iwate area. For the Niigata area, we used data from the Sumon station (37.34°N, 139.03°E). In this two cases snow precipitations were measured by the rain gages but we could not differentiate the effects of rainfall and snowmelt on landslide triggering. In the Finisterre range of Papua New Guinea local climatic data are completely absent. Therefore we used interpolated monthly total precipitation, derived from surrounding rain gauge data (Meyer-Christoffer et al., 2011). The closest stations are near the towns of Lae and Madang in the coastal plains, about 130 km to the South-East and 90 km to the North-West, respectively. These stations may have a markedly different rainfall pattern compared to the mountain range and certainly do not provide better than an estimate of the relative variations of the average regional climate.
In Taiwan, we have used long-term daily record of river discharge, Q, near the outlet

of the Chenyoulan catchment (23.72°N, 120.84°E) (Fig. 4.4). These measurements were almost continuous with only a small data gap in 2001 that was filled in using a downstream station (cf., Hovius et al., 2011). The runoff discharge, Qr, that can be turned into a rainfall proxy if divided by the station drainage area, was obtained by removing the base-flow of the hydrograph with the two parameters iterative filter proposed by Eckhardt (2005):

$$B_k = \frac{(1 - BFImax)aB_{k-1} + (1 - a)BFImaxQ_k}{(1 - aBFImax} \tag{4.2}$$

With B_k and Q_k the baseflow and total discharge at timestep k following $B_k < Q_k$, a the groundwater recession constant and $BFImax$ (defining the maximum long term ratio between the baseflow and total discharge). The parameters used were $a = 0.93$ and $BFImax = 0.85$, apparently well suited to our data and consistent for perennial, porous aquifers (Eckhardt, 2005). The runoff discharge was converted into a daily flux and divided by the upstream area of the Chenyoulan catchment to obtain an equivalent daily precipitation averaged over the whole catchment. River channel shifts occur frequently and lead to inconsistent estimation of the baseflow that would significantly bias any cumulative discharge estimate. In removing the baseflow our analysis becomes relatively insensitive to such issues. We have checked the empirical correlation between the unfiltered river discharge and V, the landslide volume per mapped unit area, and found it to be much lower ($R^2 = 0.6$) than what we found with the filtered hydrograph ($R^2 = 0.89$) (Fig. 4.1), supporting our method. Note that, this river gauge in the Chenyoulan catchment was the only one covering our whole period of analysis (1994 -2014). Therefore the inferred precipitation based on the Chenyoulan river is assumed to represent the precipitation forcing in the whole landslide mapping area, encompassing the Chenyoulan catchment, and its neighbouring catchment to the East and the West.

4.7.4 Landslide statistics and probability density function

Further insights on the characteristics of the landslides can be obtained from the landslide area-frequency distribution. To be able to compare different inventories with different number of events we computed the probability density function of a given area of landslide (Malamud et al., 2004a), $P(A_L)$ as:

$$P(A_L) = \frac{N_L}{N_T dA_L} \tag{4.3}$$

with N_T the total number of landslides considered, A_L the landslide area and N_L the number of landslides with area between A_L and dA_L . The bin widths, dA_L , are set to increase linearly in logarithmic space. For each earthquake area, we used 20 bins distributed between the smallest and largest landslide recorded. The robustness of the probability density function will depend on the number of landslides used to compute it, therefore we had to merge all the post seismic intervals together and all the pre-seismic intervals together, to obtain catalogue of a reasonable size. For the Niigata case, the number of landslides in the single post-seismic interval was not large enough to obtain a robust distribution.

Table 4.1 – Summary of the different images used to produce the landslide inventories. L5, 7 and 8 stands for Landsat 5, 7 and 8. AP, AS, EO and IK stand for Airphotos, Aster, EO-ALI and Ikonos satellites, respectively. The year and Julian day follows. The multiple airphotos used for the mapping in Japan were typically taken over the course of one or two weeks hence an approximate day is given only. Image resolution is sub-meter for the airphotos, 1m for Ikonos, 10m for EO-ALI, 15m for Aster and Landsat 7 and 8 and 30m for Landsat 5.

Finisterre	Niigata	Iwate	ChiChi	ChiChi (cont.)
L5-1989-171	L7-1999-189	AP-2006-∼255	L5-1994-86	L7-2001-225
L5-1990-142	L7-2002-245	AP-2008-169	L5-1994-246	L7-2001-257
L5-1992-260	AP-2004-∼315	AP-2009-∼165	L5-1995-109	L7-2001-321
L5-1993-262	AP-2005-∼135	AP-2010-∼325	L5-1995-204	L7-2002-132
SPOT-1994-60	AP-2005-∼255	AP-2011-138	L5-1995-249	L7-2002-180
L5-1994-201	AP-2006-∼165	IK-2012-176	L5-1995-345	L7-2003-71
L5-1995-156	AP-2006-∼315	AP-2013-∼295	L5-1996-204	L7-2003-151
L5-1996-111	AP-2007-∼315		L5-1996-236	AS-2003-189
L5-1996-223			L5-1997-94	AS-2004-58
L5-1997-161			L5-1997-238	AS-2004-282
L5-1997-225			L5-1997-318	L5-2004-306
L5-1998-181			L5-1998-113	L5-2005-228
L7-2000-355			L5-1998-225	L5-2006-71
L7-2003-027			L5-1999-84	L5-2006-199
L5-2008-022			L5-1999-228	L5-2009-175
L5-2010-150			L7-1999-316	EO-2009-244
			L7-2000-79	EO-2012-187
			L7-2000-175	EO-2012-297
			L7-2000-271	L8-2013-106
			L7-2001-49	L8-2013-154
			L7-2001-177	L8-2013-278

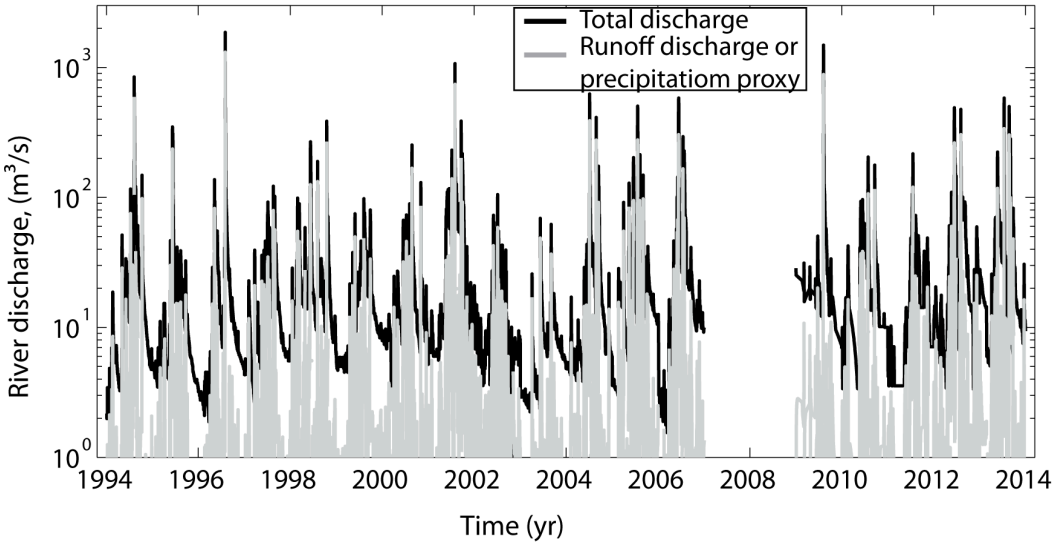

Figure 4.4 – Hydrograph from station 1510H049, on the Chenyoulan river, Choshui catchment, Taiwan. Using Eckhardt (2005) filter we removed the baseflow and obtained a direct discharge that relates to precipitation events. A precipitation proxy was formed by dividing the direct discharge by the drainage area of the station ($367km^2$).

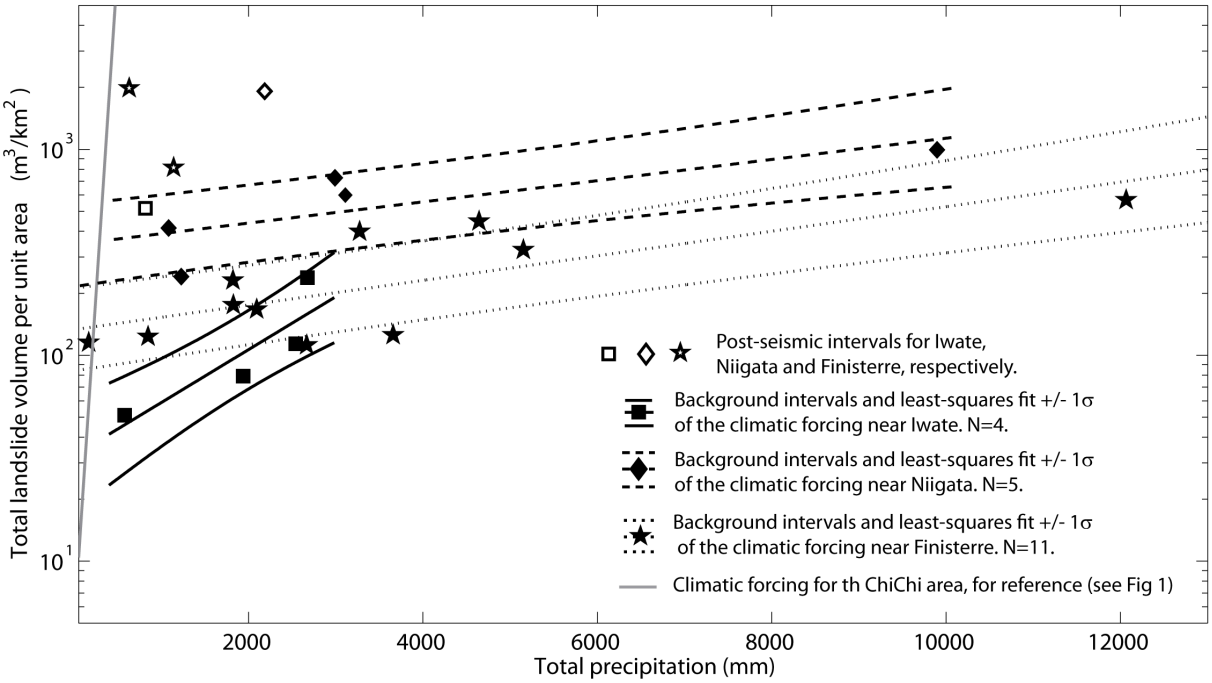

Figure 4.5 – Total landslide volume per unit area for each mapping interval plotted against the total rainfall during the same interval. Note that the open symbols representing the intervals directly following the earthquakes plot largely above the exponential relationship defined by the other intervals. The background intervals are regrouping pre and post earthquake intervals, with 3, 1 and 0 pre earthquake intervals for the Finisterre, Niigata and Iwate cases, respectively.

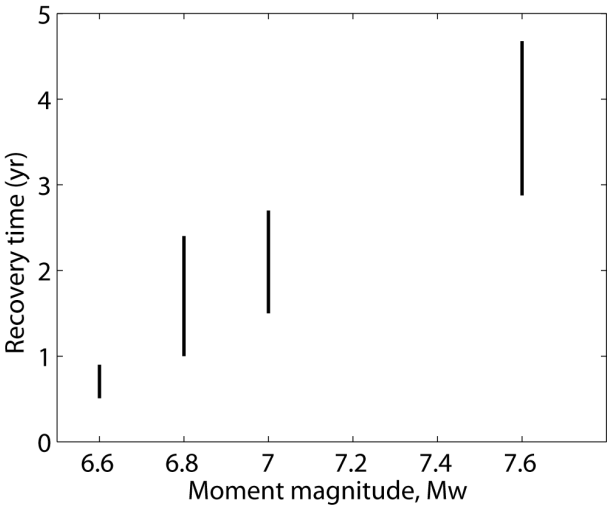

Figure 4.6 – Recovery time estimated for the 4 studied earthquakes against their moment magnitude. Vertical bars give the range of estimated recovery time for each case.

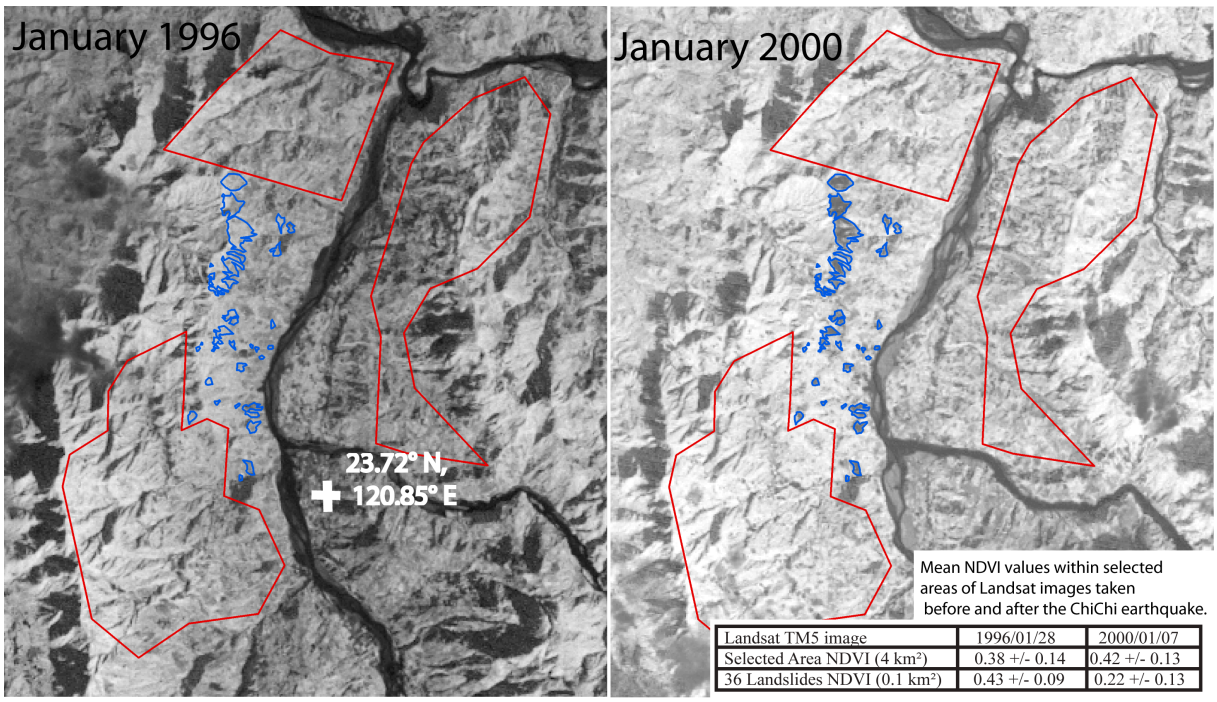

Figure 4.7 – Normalized Difference Vegetation Index (NDVI) map derived from Landsat 5 imagery of January 1996 . NDVI values are strongly affected by seasonnal changes, or in place of actual forest clearing due to landsliding (blue polygons). However, in significant portion of hillslopes unaffected by landslides shades or clouds (red polygons), the mean NDVI values remain fairly constant between January 1996 (pre-earthquake) and January 2000 (3 months after the ChiChi earthquake).

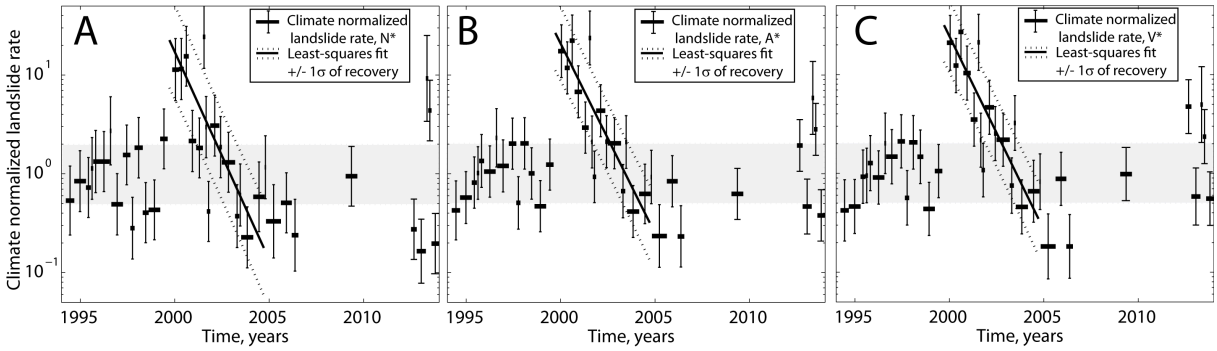

Figure 4.8 – Time series of climate normalized landslide rate in (A) Number, (B) Area and (C) Volume (Thus (C) is equivalent to Figure 4.2 A). The total landslide number or area was first correlated to the total precipitation proxy (Same as Fig. 4.1), and then normalized by the empirical relation based on the fit of the 14 pre-earthquake intervals. Note that the scatter is significantly larger for the normalized number rate, $N*$, probably because this number is much more sensitive to censoring or mapping errors due to variations in resolution, shades coverage or amalgamation.

Link

In Chapter 4, I have shown that landslide rates have increased by a large amount in the epicentral areas of 4 earthquakes, independently of rainfall forcing, and then recovered to background levels over 1 to 4 years. These changes in landslide susceptibility seem independent of biological or hydrological processes and were attributed to bedrock damage and subsequent healing. In contrast to previous estimates, I have found that the volumetric contribution of post-seismic landsliding is small compared to the coseismic one, less than 5%.
The small amount of post-seismic landsliding in these 4 different cases suggests that post-seismic landsliding can be ignored in the long-term modeling of the topographic evolution of epicentral areas, studied in Chapter 6. Nevertheless, we lack in-situ geophysical data to assess and constrain the ground strength decrease and its healing mechanism. Chapter 5 aims to better constrain these coseismic and post-seismic mechanical changes of the subsurface with the use of seismic monitoring methods and GPS data.
In Chapter 5, I use ambient noise recorded by seismometers in 3 out of the 4 earthquakes studied in Chapter 4 to monitor the local changes of elastic properties of the subsurface. These temporal evolutions are compared to the temporal dynamics of strength, inferred from landslide data, and to the surface deformation during the post-seismic period, recorded by GPS networks, in order to assess which process can explain short-term and longer-term mechanical evolution of the ground.

Chapter 5

Co-evolution of shallow seismic velocity changes and landslide rates after earthquakes.

Abstract

Strong ground motion during earthquakes can result in damage at and below the Earth's surface. This is manifest in widespread co-seismic landsliding and may be a cause of the drop in seismic velocity, commonly observed after earthquakes. A link between these two, through changes in rock mechanical properties, is likely but has not been demonstrated. If they are related, then landslide rates and seismic velocities should co-evolve during but also after an earthquake, when both are known to restore toward background values. Here, we compare landslide rate and seismic velocity in the epicentral areas of three crustal earthquakes. These observables show significantly different evolution between events but striking similarities for each earthquake, suggesting that they are both associated with significant weakening of the very shallow substrate, and that this effect diminishes over time. We attribute this to pervasive cracking at and near the Earth's surface due to strong ground motion and subsequent, progressive crack closure that we suggest to be driven by agitation during post seismic deformation. [1]

1. This work is about to be submitted to *Science*.

5.1 Introduction

Ambient noise interferometry and seismic wave deconvolution studies have revealed significant changes of subsurface seismic velocity (0.1-10 km depth) after medium to large earthquakes (e.g., Brenguier et al., 2008; Sens-Schönfelder and Wegler, 2011; Takagi et al., 2012; Sawazaki and Snieder, 2013; Hobiger et al., 2014; Richter et al., 2014; Gassenmeier et al., 2016), but the processes driving these changes and the depth at which they occur have remained poorly resolved. Consistently, these studies have found a velocity drop followed by a progressive, non-linear recovery of the seismic velocity over months to years. The spatial pattern of these changes excludes changes of the stress state or ground water level as cause in most cases. Instead substrate damage related to strong motion or faulting at depth has been invoked (Rubinstein and Beroza, 2004, 2005; Sens-Schönfelder and Wegler, 2011; Sawazaki and Snieder, 2013; Takagi and Okada, 2012; Richter et al., 2014). Accordingly, the post earthquake recovery has been attributed to crack healing and was compared with the recovery of strength or healing of damaged concrete and sandstone samples in laboratory experiments, reflected in the increase of elastic moduli over logarithmic time-scales (e.g., TenCate et al., 2000; Tremblay et al., 2010). Notably, after the 2004 Parkfield, California earthquake the seismic velocity recovery appeared to coincide with post-seismic deformation, which was interpreted to reflect stress variations in the fault zone at depth (5-10 km) (Brenguier et al., 2008). However, the depth at which the velocity change occurred was unconstrained and others have suggested that the Parkfield observations could also be explained by healing of shallow damage (0-100 m) (Sleep, 2009). The correlation of seismic velocity recovery and post-seismic deformation has otherwise remained largely unexplored, and the relations between coseismic velocity changes, superficial damage and post-seismic deformation are poorly understood.
Earthquake-induced landsliding offers a different perspective on the shallow damage caused by earthquake strong-motion (Meunier et al., 2007, 2013). It has been demonstrated that elevated landslide activity, resulting from a loss of substrate strength, persists for months to years after an earthquake, decaying exponentially towards pre-earthquake levels (Marc et al., 2015). Consequently, landslide activity does not only reflect the coseismic excitation, but it may also be a measure of the landscape ´ s increased susceptibility to failure resulting from structural damage of the hillslope material. Three earthquakes for which this geomorphic transient has been shown, occurred in areas with pre-existing networks of seismometers and GPS stations, and therefore offer an opportunity to explore the links between slope failure, seismic velocity and post-seismic deformation. Using joint geomorphic, seismic and geodetic observations at these three sites, we aim at resolving the process responsible for the change of seismic velocity and landslide rate, its characteristic depth, and the mechanism driving long-term substrate healing.

5.2 Cases, data and methods

Time-dependent changes in ground strength have been inferred from landslide susceptibility in the epicentral areas of the 1999 M_w 7.6 Chi-Chi (Taiwan) earthquake, the 2004 M_w 6.6 Mid-Niigata, and the 2008 M_w 6.9 Iwate-Miyagi earthquakes in Japan (Supplementary Methods, Fig 5.1, 5.2, 5.3-5.5). In these areas, we have assessed seis-

Table 5.1 – Summary of the relaxation times estimated for landsliding, seismic velocity and post-seismic displacement for the three earthquakes considered in this study. For the relaxation times τ_S and τ_G we report the mean value with standard error of the mean based on N measurements obtained at different stations and different frequencies or directions, respectively. * indicates that τ_L was estimated from T_L (Supplementary methods).

Earthquake	M_w6.6+6.3 Niigata	M_w6.9 Iwate	M_w7.6 Chi-Chi
Recovery duration, T_L, year	0.5-0.9	1-2.4*	3.8 ± 0.9
Landslide relaxation, τ_L, year	0.25-0.45*	0.5-1.2*	1.11 ± 0.2
Seismic relaxation, τ_S, year	0.32 [0.26-0.49]	0.83 [0.52-1.6]	1.10 [0.5-2.5]
Geodetic relaxation, τ_G, year	0.29 [0.18-0.43]	0.75 [0.55-1.05]	1.22 [1.10-1.47]

mic velocity variations by passive image interferometry (Sens-Schönfelder and Wegler, 2011), based on the correlation of the ambient seismic wavefield, and post-seismic deformation was constrained with GPS station time series in the epicentral areas (Supplementary Methods, Fig 5.1, 5.2). The seismic and geodetic data were fit with a function accounting for the different components of the signal, from which the relaxation time constant, τ, could be deduced (Supplementary Methods).

5.3 Results

Near the epicenter of the Chi-Chi earthquake, a velocity drop of about 1% followed by a non-linear recovery was found at station SSLB (Fig 5.1). A strong seasonal cycle overprints this signal, likely related to seasonal variations of the groundwater level (Hillers et al., 2014). Accounting for this cyclic component, the seismic velocity recovers exponentially with a time constant of $\tau_S = 1.1[0.5 - 2.5]$ yr (Suppl. methods, Figure 5.4) . Meanwhile, the landslide rate recovery after the Chi-Chi earthquake had $\tau_L = 1.1 \pm 0.2$ yr. (Fig 5.1, Table 5.1). Thus, the post-seismic evolution of these two observables was substantially synchronous, even if at the end of 2003 the seismic velocity recovery was incomplete (Fig 5.1).

More extensive seismic and geodetic observations in the two Japanese cases show clearly that recovery time constants vary within a given epicentral area, but that this intra-earthquake variability is small compared to the inter-earthquake differences. The average seismic velocity recovery constants in the Iwate and Niigata epicentral areas are 0.67+/-0.07 and 0.37+/-0.05 years, respectively (Fig 5.2, 5.3, 5.5). The post-seismic evolution of landslide rates in the Iwate and Niigata epicentral areas are less well resolved, and only allow to constrain the total recovery duration. Assuming the duration is 2 times τ (see Supplementary methods), we estimate $\tau_L = 0.5 - 1.2$ and $\tau_L = 0.25 - 0.45$, in good agreement with τ_S for the Iwate and Niigata areas, respectively (Fig 5.2, Table 5.1, Suppl Methods). We note that the magnitude of the seismic velocity recovery varied between cases, from 30% to 100% of the coseismic drop, without apparent correlation with seismic wave frequency (Fig S1,S2). These differencee are probably related to the lithological and rheological diversity of the materials in the epicentral areas and at different depths.

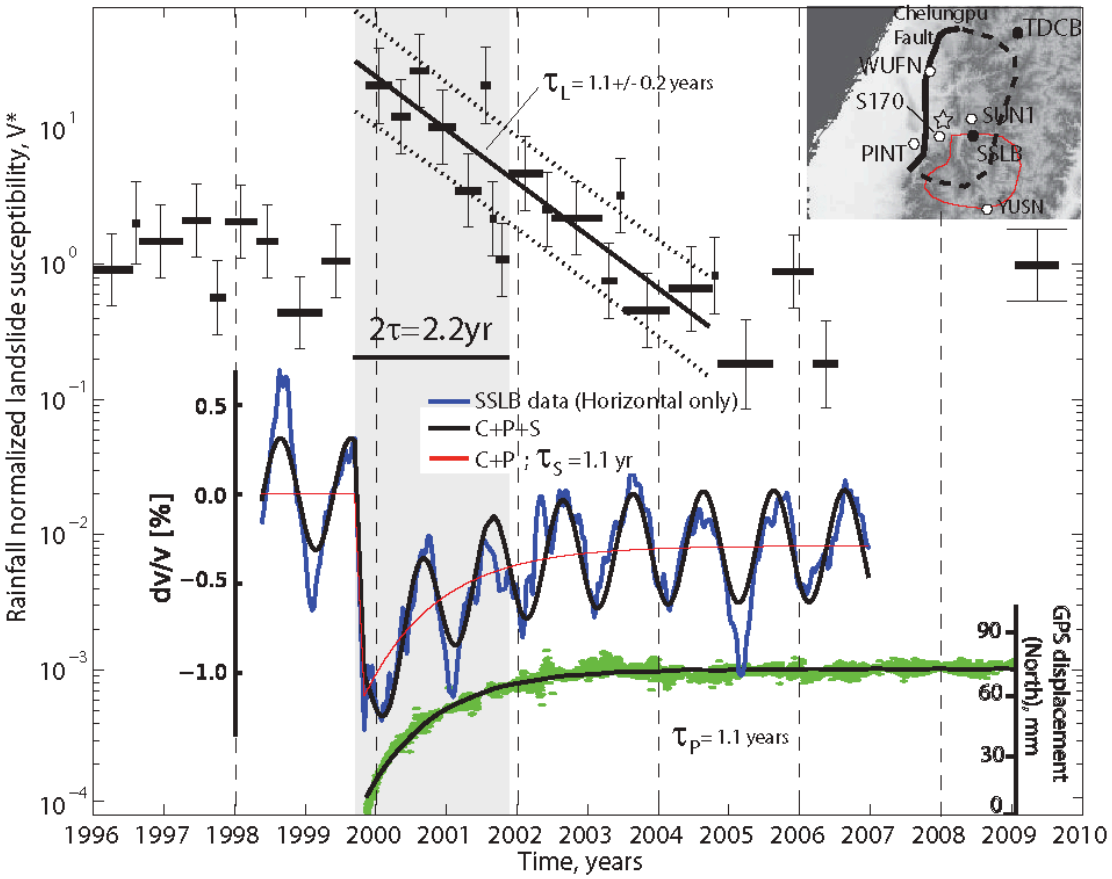

Figure 5.1 – Time series of rainfall normalized landslide susceptibility (black bars), relative velocity changes (in blue) and GPS measurements of surface displacements (in green) after the Chi-Chi earthquake in Taiwan. The best least-square fit of the landslide data yield a relaxation time of 1.1 ± 0.2 year. Inset: Map with the seismic and GPS stations as black and white dots, the fault as dashed polygon with the thick line indicating the surface rupture, the epicenter as a star, and landslide mapping area as a red polygon, respectively.

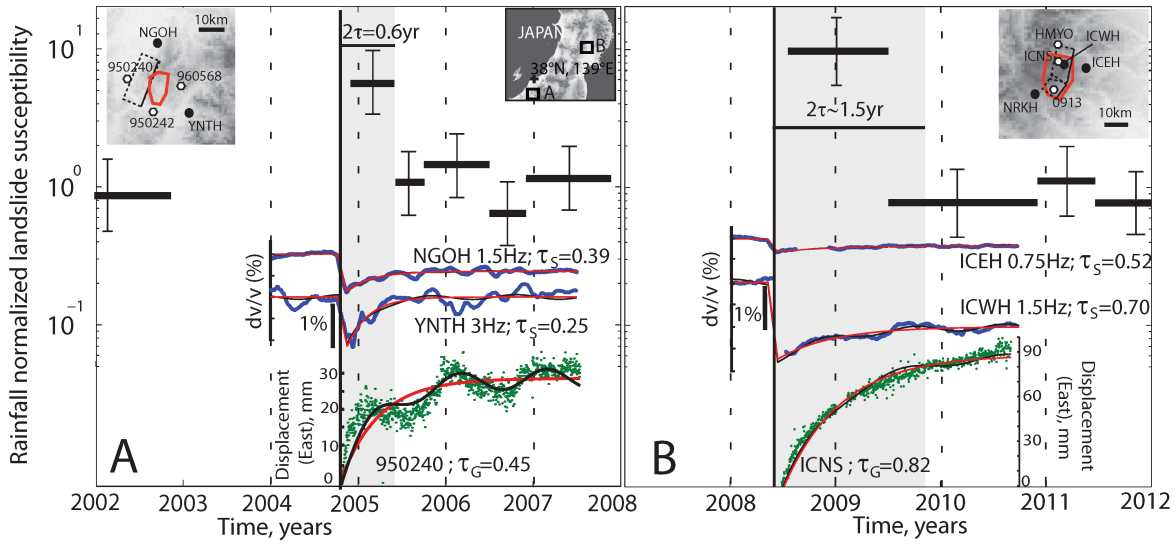

Figure 5.2 – Same as Figure 5.1, for the 2004 Niigata and 2008 Iwate earthquake in Japan.

5.4 Discussion

We have shown that for 3 earthquakes in different locations, post-seismic landslide rates and seismic velocities have evolved simultaneously. Each event displays the same consistent pattern of observations but with its own recovery period, suggesting that these apparently unconnected measurements are linked by an underlying mechanism.
It is well accepted and directly observed that strong motion causes a non-linear response of the subsurface related to the formation of cracks and an increase of pore space (Sleep, 2010). Opening of cracks in the substrate during earthquakes has also been inferred from coseismic changes of river discharge (e.g., Wang et al., 2004), and from the anisotropy of seismic wave propagation (Nakata and Snieder, 2012). Because coseismic changes of seismic velocity cannot be explained by static stress changes or hydrological effects but correlate well with coseismic shaking (Gassenmeier et al., 2016) they are also interpreted as damage and crack opening (Sens-Schönfelder and Wegler, 2011; Hobiger et al., 2014), consistent with theoretical considerations (Ma, 2008; Sleep, 2009, 2010). This effect is strongest very near the Earth's surface, where the confining pressures are smallest. The immediate and strong increase of landslide rates after large, shallow earthquakes is further evidence for significant coseismic cracking near the surface. Marc et al. (2015) proposed that the post seismic decrease of landslide rates is related to the reestablishment of material strength. The co-evolution of landslide rates and seismic velocities after earthquakes suggests that they both relate to progressive closure of cracks and the attendant recovery of strength in the shallow subsurface.
Landslide attributes can be used to put a minimum bound on the depth extent of substrate weakening and healing. In all cases, landslides during the post-seismic recovery period indicated failure depths between 0.5 and 10m, and a homogeneous landslide susceptibility increase, and thus a ground strength reduction within this very shallow layer (Marc et al., 2015). In this very shallow depth range, rock deformation on or near the seismogenic fault (Brenguier et al., 2008; Obermann et al., 2014) cannot be responsible for laterally extensive weakening. Notably, very large earthquake-induced seismic velocity changes (5% or more) in the first 100 m below the surface have been found in boreholes (Nakata and Snieder, 2012; Takagi et al., 2012; Sawazaki and Snieder, 2013). Although the material weakening implies that the velocity changes are maximal at the surface with the strongest deformation, it is likely that part of the signal and/or some seismic stations are influenced by changes at deeper levels (Obermann et al., 2014; Hobiger et al., 2014).

To investigate possible mechanisms responsible for the recovery of strength and elastic moduli of the shallow substrate, we have evaluated the post-seismic displacement measured by GPS stations in the epicentral areas of the 3 earthquakes (See Suppl.), and found that it evolved like the seismic velocities and landslide rates (Table 1, Fig 1, 2). The geodetic relaxation times, τ_G, varied somewhat from station to station but averaged to 1.10 [1.10-2.00], 0.75 [0.55-1.05] and 0.29 [0.18-0.43] years, in the epicentral areas of the Chi-Chi, Iwate and Niigata earthquakes, respectively (Table 5.2, Fig. 5.6-5.9), closely matching the relaxation times of the seismic velocity recovery and of the landslide susceptibility in all cases. Healing is likely due to a mixture of mechanical and chemical effects (Brantut, 2015), but our observations do not yield further information about the detailed nature of these processes. Nevertheless, the match of the

healing of near surface materials as documented in the landslide and velocity data, and the post-seismic deformation allows for three possible explanations: (1) coincidence, (2) the two processes depend on a common mechanism, and (3) one of the two processes causes the other.
We exclude coincidence as the observation of matching geodetic and seismic recovery times, T, does not only hold for our three cases, but also exists for the 2011 Tohoku earthquake, with $T \sim 10$ months (Sawazaki and Snieder, 2013; Delorey et al., 2015), and for the 2004 Parkfield earthquake with $T \sim 3$ years (Brenguier et al., 2008). A possible mechanism underpinning both the recovery of rock mechanical properties and the post-seismic deformation could be associated with afterslip and healing of the fault interface. Post seismic deformation may be the result of the reduction of fault friction during earthquake rupture, allowing creep for a transient period set by the fault gouge healing (e.g., Gratier et al., 2014; Kaproth and Marone, 2014). Moreover, fault gouge healing, and healing of the shallow substrate may be due to similar internal processes that could be depth independent. But, even though this scenario appears possible it is very unlikely as the relaxation times of these processes should be vastly different since they depend on temperature (TenCate et al., 2000), pressure and fluid availability (Brantut, 2015), all of which differ strongly between the near-surface and mid-crustal depths. Considering a possible causal link between processes, we deem unlikely any significant influence of near surface healing on the post-seismic deformation. This is because the thin near-surface layer is the weakest part of the rock column, which cannot support more than a marginal part of the tectonic stress without any possibility to affect fault behavior or mantle relaxation. Instead, this layer could well be affected by geodetically recorded deformation, as contraction of the damaged substrate would be accompanied by closure of cracks and increasing strength and seismic velocity. However, in all our cases, some parts of the earthquake-affected areas have experienced enhanced contraction over timescales compatible with the seismic recovery, while others underwent little deformation or even dilation (Fig 5.10). Hence, large-scale ($> 10km$) compression cannot explain the inferred crack closure directly. In addition, any relation between crack closure and large-scale strain is likely complicated by the local effect of topography on shallow stress redistribution and by the fact that crack distributions may be anisotropic.
We suggest an alternative explanation based on observations of granular materials, which exhibit pronounced "slow dynamics" (Richard et al., 2005). Experiments have shown that disturbed granular materials progressively compact and strengthen when activation energy is supplied by vibration or shear (Richard et al., 2005). This compaction is typically exponential, with a relaxation time set by the magnitude of the agitation (Richard et al., 2005). We hypothesize that in the epicentral areas of shallow, large earthquakes, the near surface materials, including rock mass, regolith and sediment behave as granular materials, damaged by strong dynamic strain and compacting and strengthening subsequently at lower activation levels, induced by post-seismic deformation in the epicentral area. Testing this hypothesis requires data on crack density and stress or strain observations at higher spatial resolution and remains a challenge for future work. However, if proven correct, our hypothesis would offer an explanation of Nakata and Snieder (2012) observation of anisotropy of the propagation of shallow (0-200 m) shear waves in Japan, with a fast axis that is consistently oriented in the arc-normal direction. Assuming that cracks opened due to coseismic shaking have no preferred azimuth the observed anisotropy could result from preferential closure

perpendicular to the convergence direction.

5.5 Conclusion

We conclude that geomaterials in the first tens of metres below the Earth's surface can be significantly weakened by earthquake strong ground motion, leading to lower seismic velocities and higher propensity to failure of topographic slopes. Like in disturbed granular material, the subsequent healing of this damage may be driven by persistent agitation due to post-seismic deformation, the intensity and duration of which are tracked by the recovery of seismic velocities and landslide rates. This implies that geodetic constraints on surface deformation, and systematic monitoring of shallow seismic velocities using passive image interferometry and borehole waveform deconvolution may be a key to better understanding of the time-dependent evolution of landslide hazard after an earthquake and the management of associated risks, but also of the spatio-temporal patterns of seismically affected erosional, hydrological and sedimentological processes in tectonically active areas.

5.6 Supplementary materials to Chapter 5

5.6.1 Supplementary methods

Landslide susceptibility changes

Ground strength variations have been inferred from landslide susceptibility observed in the epicentral areas of three shallow earthquakes the 1999 M_w 7.6 Chi-Chi (Taiwan) earthquake, and the 2004 M_w.6.6 Niigata and the 2008 M_w 6.8 Iwate earthquakes in Japan. We focus on these 3 earthquakes because they are the only ones for which seismological data may be compared to time series of landslide rates. Landslides triggered by rainfalls were mapped using time-series of satellite imagery. To correct for the variable amount of rainfall an empirical relationship between precipitation and landsliding was developed based on time periods unaffected by earthquakes, and used to normalize the whole dataset, thus creating a non-dimensional landslide susceptibility (Marc et al., 2015). Variations of the landslide susceptibility in the Chi-Chi earthquake epicentral area are best constrained and strongly supports an exponential recovery with a relaxation time of $1.1 + / - 0.2$ years. Post-seismic landslide susceptibility is indistinguishable from background level after 3.8 ± 0.9 years, defining a full recovery time, T_L.
For the two Japanese cases, the landslide data did not allow for the determination of a relaxation time but only for the estimation of an upper bound of the complete recovery process duration, T_L. Moreover, because the landslide rate remains noisy we are limited to an accuracy of about 2-fold, meaning that as soon as the landslide susceptibility perturbation L/L_0 has decayed to less than 2 it may be hard to detect. Because we can write $L/L_0 = 1 + A_0 exp(-t/\tau_L)$, we considers that when $t = 2\tau_L$, the perturbation has decayed to 10% of A_0 and is likely undetectable with our data which indicates $A_0 \sim 5 - 10$, for the two Japanese cases. Therefore, we bracket T_L with the first time interval in which the landslide susceptibility is close to background, that is $T_L = 0.5 - 0.9$ yr and $T_L = 1 - 2.4$ years and found $\tau_L = 0.25 - 0.45$ yr and $\tau_L = 0.5 - 1.2$ yr, for the Niigata and Iwate areas, respectively (Fig 5.2).

Seismic velocity changes

Seismic velocity variations were observed with passive image interferometry (PII, (Sens-Schönfelder and Wegler, 2011)) that is based on the correlation of the ambient seismic wavefield. Here we use single station cross-correlation (See (Hobiger et al., 2014)) because of the superior susceptibility to shallow variations in the high frequencies (Figures 5.3-5.5). The seismic velocity change and recovery in the Iwate area have already been constrained (Hobiger et al., 2014; Takagi et al., 2012) and we present here our analysis of the velocity changes at stations ICEH and ICWH. Although NRKH station show important changes we ignore it as it has been shown to be dominated by deep processes (Hobiger et al., 2014; Takagi et al., 2012). Seismic velocity drop and recovery were estimated for seismic stations YNTH and NGOH, nearby the Niigata earthquake epicenter. For the Chi-Chi earthquake in Taiwan we have used records from the seismic stations SSLB and TDCB, near the epicenter and at the northern extremity of the rupture, respectively. For the two Japanese earthquakes the selected stations are within or very close to the area where landslides were mapped. They have

the largest signal to noise ratio and show the strongest signal of velocity changes. In Taiwan the two stations are the only ones of the BATS array that were recording before the main shock. However, TDCB signal does not exhibit significant velocity changes after the earthquake.

Post-seismic displacement and deformation

Post-seismic deformation was constrained based on GPS station displacement time series in the fault zone nearby the seismic stations and the landslide mapping area (Figures 5.6-5.9). As for the seismic stations, we focus on the stations closest to the fault area and with a good signal to noise ratio and therefore the largest post-seismic displacements. The collected GPS data are processed with GAMIT 10.42/GLOBK 5.16 software packages using the double-differenced ionosphere-free carrier phase observations (L3) as the basic observables. The residual tropospheric zenith delay is estimated every 2 hours per station simultaneously with the station coordinates by a least squares adjustment. Fourteen IGS sites in the Asia-Pacific region are constrained to their International Terrestrial Reference Frame 2008 coordinates and velocities in GLOBK processing, together with the parameter estimates from GAMIT solutions to obtain ITRF2008 coordinates of other GPS sites. In the Niigata area, we limited our analysis to the period just before the occurrence of the Niigata-Chuetsu-Oki 2007 earthquake that impacted significantly the area. In the Iwate area, the data were only recorded until August 2010. Nearby the Chi-Chi epicenter the post-seismic behavior of the stations we use have been presented and analyzed in detail by (Rousset et al., 2012). They showed that variable relaxation occurred along the fault. As our seismic and landslide data are limited to the southern part of the rupture we have focussed on the GPS station bracketing this zone only, SUN1 and YUSN. For each station we have fitted Eq 1 to all components exhibiting a significant post-seismic relaxation while components without transient behavior have been ignored (Table 5.2, Fig 5.6-5.9).
To assess the surface deformation associated with the post-seismic surface displacements we computed areal strain. We estimate average areal strain within a polygon composed by a number of cGPS sites using the method proposed by Shen et al. [1996]. Areal strain can be derived from variations of GPS displacement gradients on the nodes of polygon. The contribution of each cGPS site is weighted as a function that decays with increasing distance from the centroid of the polygon.

Relaxation times and confidence intervals

To estimate the relaxation time constant from the seismic velocity changes and the displacement data we model the signal with a superposition of a background level, A, a coseismic step change decaying exponentially, (C), and a sinusoidal function with an annual pulsation w=2pi / yr and a phase Φ to account for the seasonal variations. The model for the seismic velocity variations contains an additional permanent offset following, B_{sismo} Hobiger et al. (2014). For the GPS time series, we have first removed the linear interseismic trend from the whole time series, and then proceeded to fit the same function, with $B_{sismo} = 0$.

$$F(t) = A + \left(B_{sismo} + Cexp\left(-\frac{t - t_{eq}}{\tau} \right) \right) H(t - t_{eq}) + sin(2\pi t + \Phi) \qquad (5.1)$$

Table 5.2 – Summary of the relaxation time constants and confidence intervals for post seismic GPS displacement on different directions. Components without value do not show significant transient post-seismic displacement.

Earthquake/ GPS station	Relaxation time (East)	Relaxation time (North)	Relaxation time (Up)
Niigata - 950240	0.45 [0.29-0.61]	x	x
Niigata - 950242	0.25 [0.10-0.45]	x	x
Niigata - 960568	0.16 [0.08-0.25]	x	x
Iwate - ICNS	0.82 [0.70-0.95]	x	x
Iwate - 0913	0.10 [0.06-0.14]	0.61 [0.34-1.10]	0.39 [0.22-0.61]
Iwate - HMYO	0.29 [0.25-0.34]	0.82 [0.61-1.10]	x
Chi-Chi - SUN1	1.10 [1.10-1.27]	1.10 [1.10-1.10]	1.47 [1.10-1.98]

To estimate the relaxation time and its interval of confidence from the seismic and geodetic data we used non-linear least-square fitting of models with fixed relaxation time logarithmically spaced between 0.1 and 10 years. We computed the variance for all model residuals and the variance ratio between each model and the best model. With an F-test we assessed which models are statistically indistinguishable from the best model at a 95% confidence level. The relaxation time interval producing models with fits similar to the best model gives the confidence interval of the relaxation time. Because the variance weights equally all parts of the signal, forcing models to adjust to various relaxation times resulted in poor estimates of the coseismic offset of GPS signals, and for the determination of GPS signal confidence intervals, we kept the coseismic offset constant and equal to the value determined by the best non-linear least-square fit, with unconstrained relaxation time.
To obtain a regional average relaxation time comparable with the landslide data we had to merge estimates and confidence interval from different seismic and GPS observations. For each seismic station in Japan, we performed an F-Test on the merged residuals obtained from each of the 3 frequency bands to obtain a best relaxation time and confidence interval. Then we consider that the averaged relaxation and intervals for each station pair are representative for the epicentral area. The GPS displacement is a vectorial measurement and in some cases different relaxation are visible along different directions, implying some rotation of the source process driving these displacements. In any case, when comparable amplitudes of post-seismic displacement occur with different temporal dynamics, the longest one is representative for the surface activity. Therefore in the Iwate case, we have neglected the Up and East components of stations 0913 and HMYO (Fig. 5.9). As for the seismic stations, we averaged relaxation time and intervals boundaries to obtain a single, regional, estimate of the relaxation dynamics in the epicentral area.

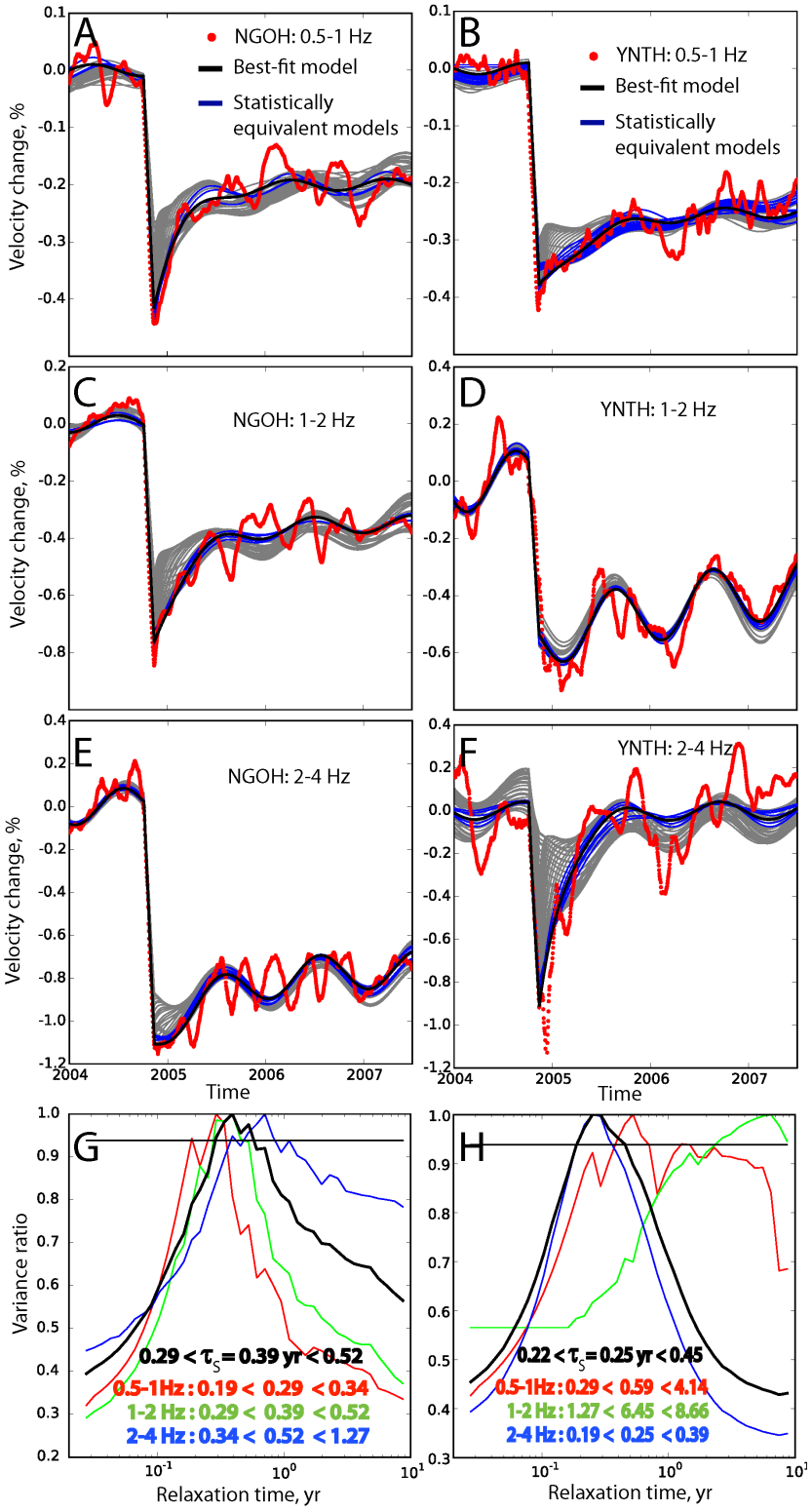

Figure 5.3 – Model fit and estimation of the best relaxation time and confidence interval for the relative velocity variations, at different frequency ranges, of the seismic station NGOH (A,C,E) and YNTH (B,D,F) in the epicentral area of the 2004 Mid-Niigata earthquake. Data is in red, best model in black, acceptable models in blue and other tested models in grey. The variance of the best model over the variance of models with different relaxation times, used to determine confidence intervals and best estimate of τ_S are shown for each frequency for both station in (G) and (H). The black curve is combining the residuals at each frequency to determine a the best relaxation time and confidence interval for a given station. The critical variance ratio above which models are indistinguishable from the best model (at a 95% confidence level given the number) is indicated with the black horizontal line.

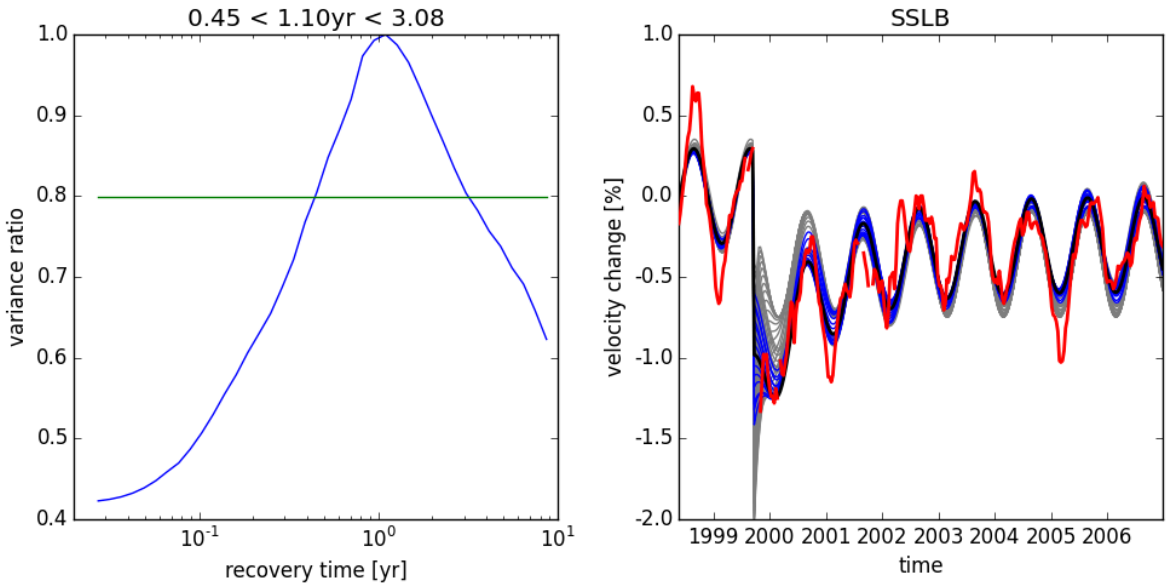

Figure 5.4 – Same as Figure S1 but for stations SSLB in the 1999 Chi-Chi earthquake epicentral area.

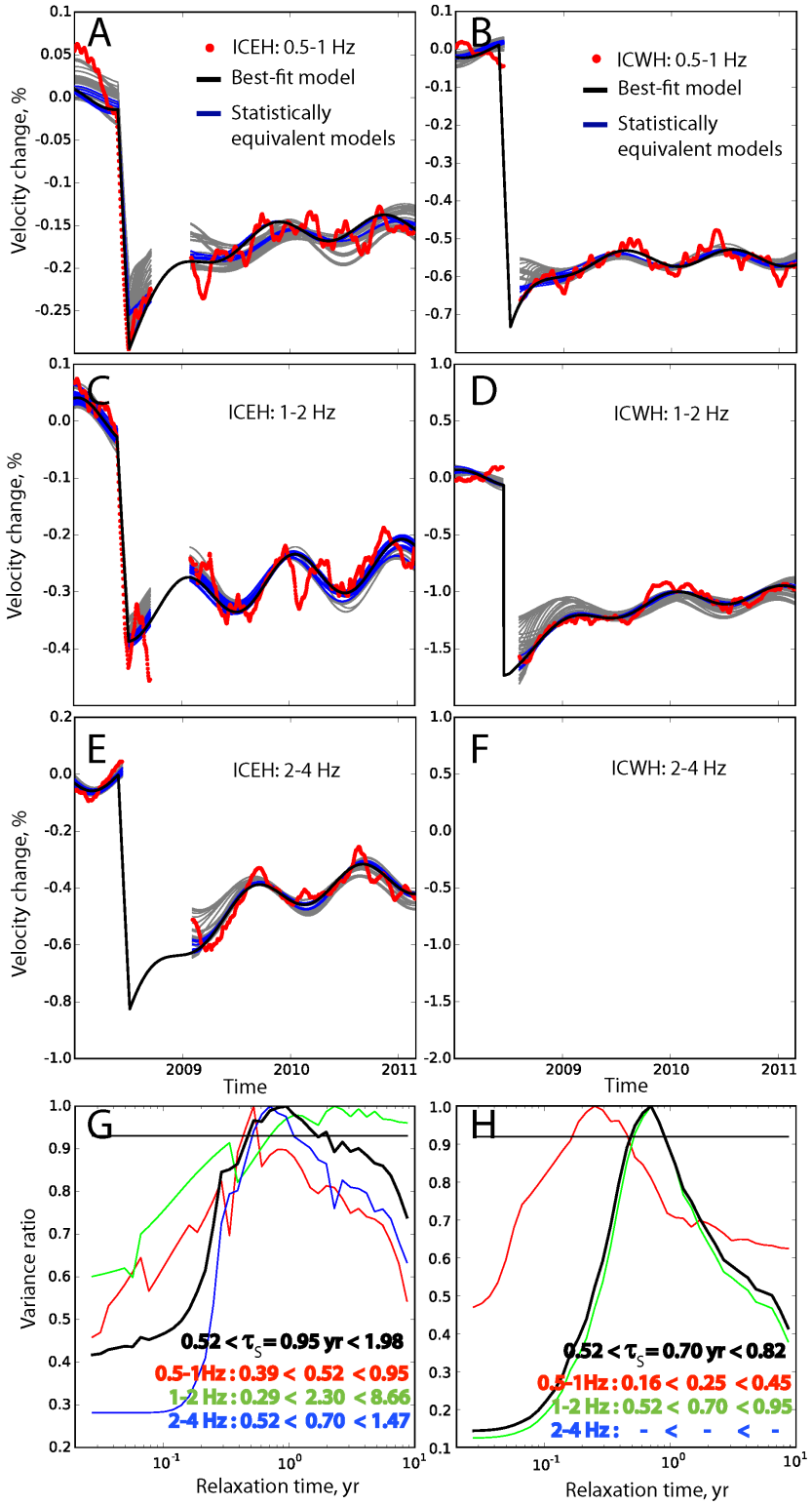

Figure 5.5 – Same as Figure S1 but for stations ICEH and ICWH in the 2008 Iwate earthquake epicentral area. For station ICWH, at 2-4Hz, the signal does not allow to determine dv/v.

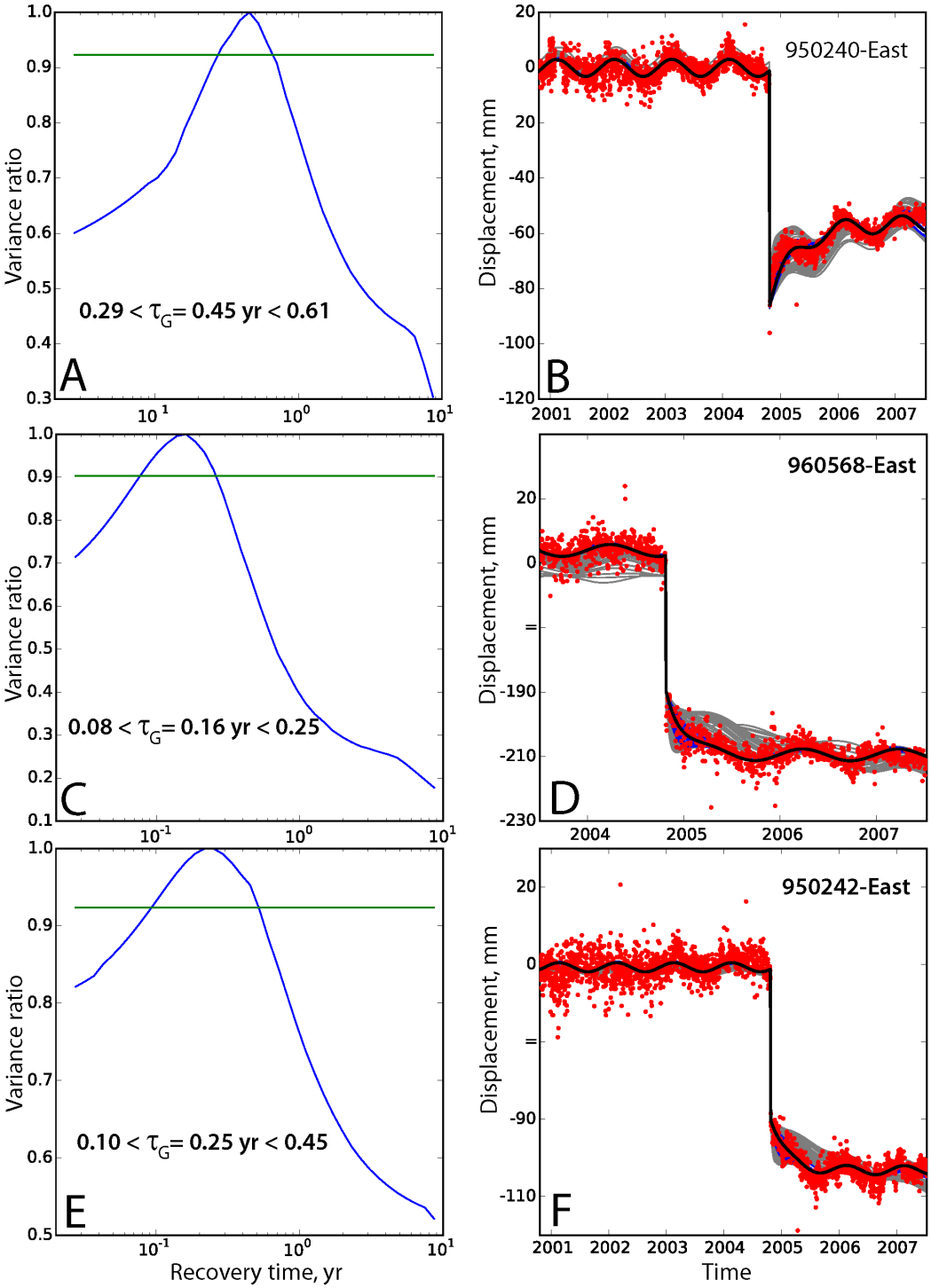

Figure 5.6 – Model fit (B,D,F) and estimation of the best relaxation time and confidence interval (A,C,E) for the continuous GPS stations in the Niigata epicentral area. Data is in red, best model in black, acceptable models in blue and other tested models in grey. Station name and selected direction are in the panels. To improve visibility of the interseismic and post-seismic signals the amplitude of the coseismic drop has been cut.

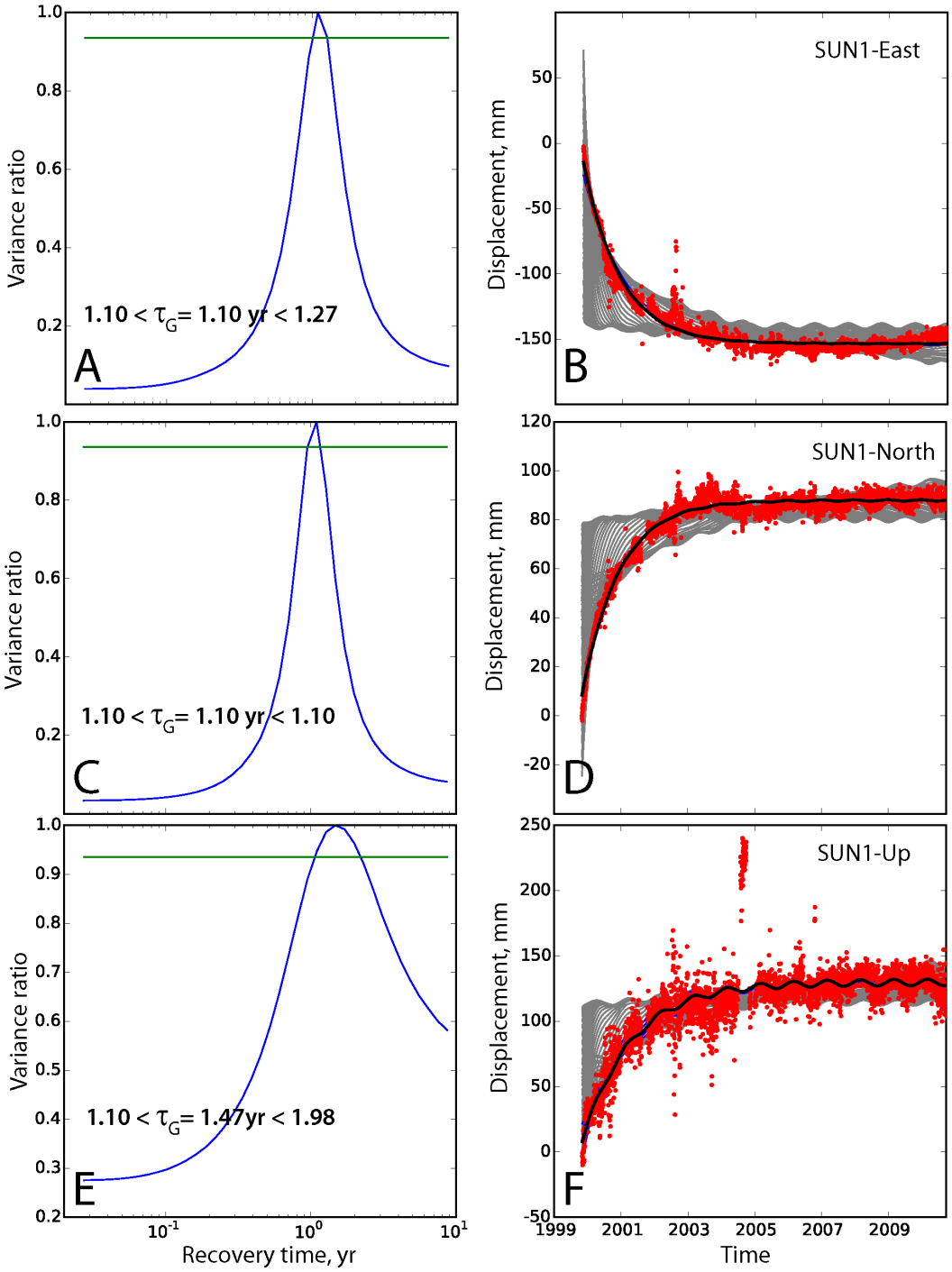

Figure 5.7 – Same as Figure 5.6, for continuous GPS station in Chi-Chi area, Taiwan.

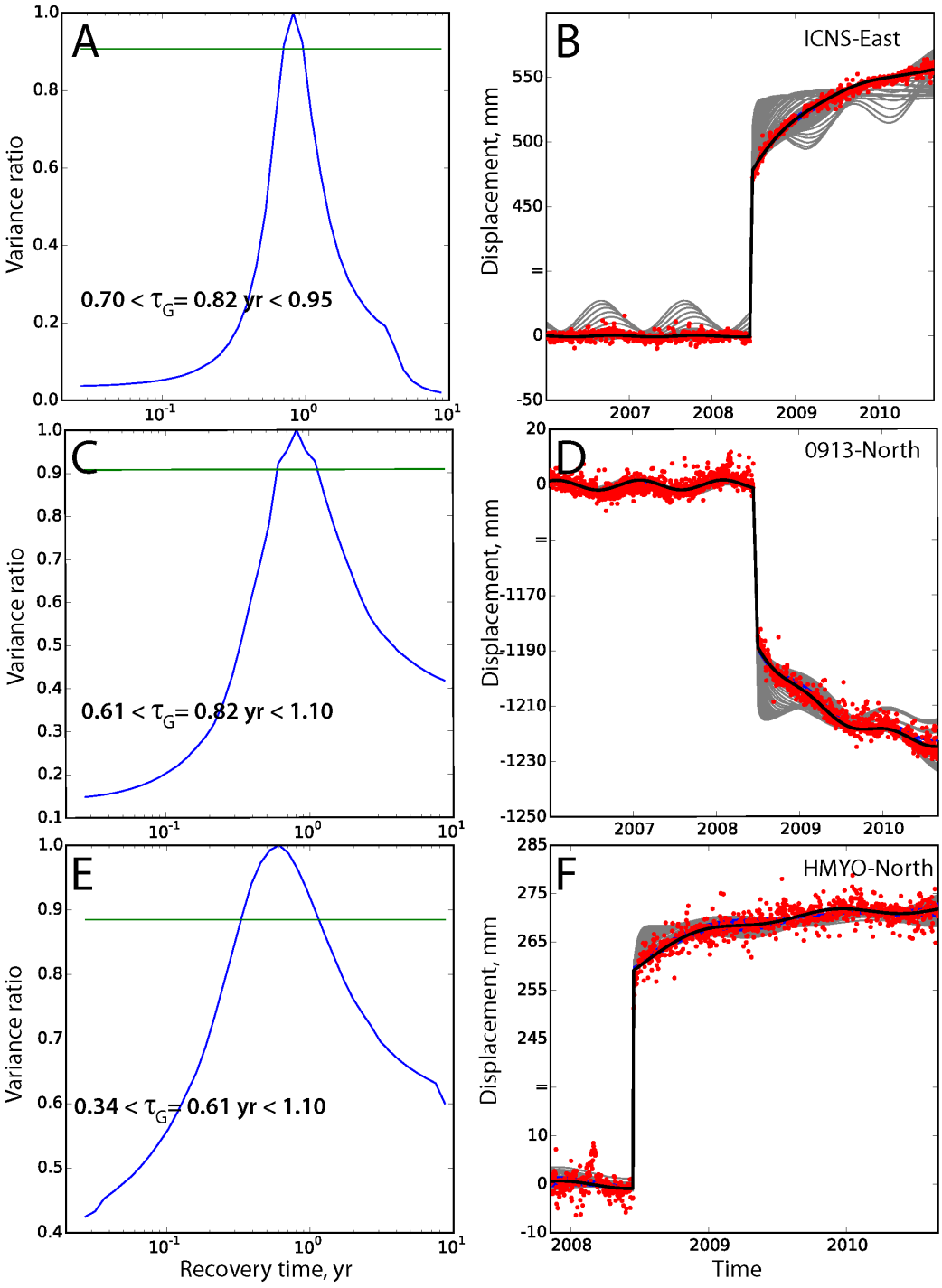

Figure 5.8 – Same as Figure 5.6, for continuous GPS station in Iwate area, Japan.Only the directions with a long transient behaviour are shown

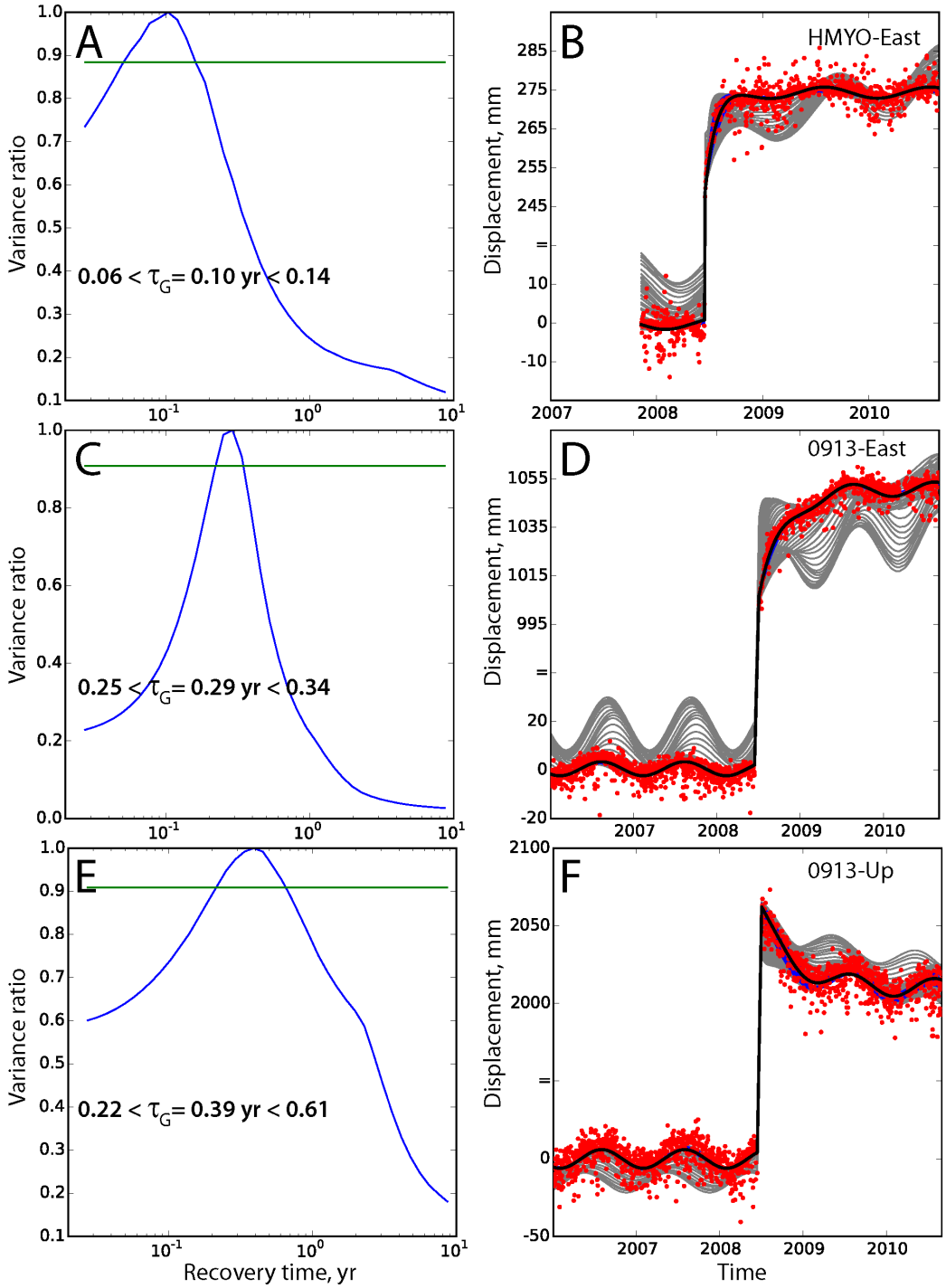

Figure 5.9 – Same as Figure 5.6, for continuous GPS station in Iwate area, Japan. Only the directions with a shorter transient behaviour are shown

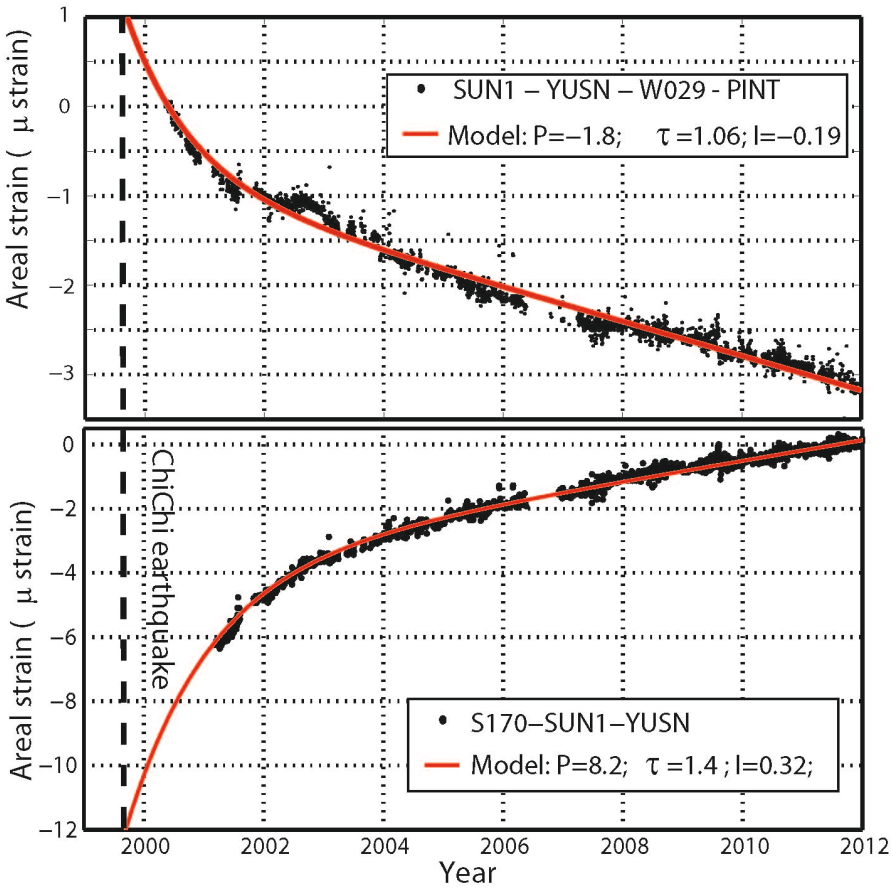

Figure 5.10 – Areal strain computed between different cGPS stations in the 1999 Chi-Chi earthquake epicentral area (See Suppl.Methods). The areal strain indicates average, large scale contraction (upper panel) and dilation (lower panel) occur in the hanging wall of the fault where landslide susceptibility and seismic velocity changes were measured.

Link

In Chapter 5, I have shown that the post-seismic relaxation times for landslide rate, seismic velocity and GPS surface displacement appear to vary from earthquake to earthquake, though they are strikingly similar for the 3 different observables in a given epicentral area. This supports the common interpretation that the seismic velocity drop relates to very shallow extensive coseismic ground cracking, and that thesubsequent crack healing is responsible for the recovery of strength and elastic moduli. Further, the recovery is consistent with the surface displacement but not with the inter-station normal strain, suggesting the superficial regolith and fractured bedrock may compact, and heals as a granular material agitated by the post-seismic deep deformation.
Although the landslide susceptibility presented in Chapter 4 suggested a complete recovery of the bedrock damage, the seismic velocity considered in Chapter 5 does not always recover fully. This mismatch could arise if permanent damage occured deeper than 10-20m, at depths that are sampled by the seismic velocity but not by landsliding. It could also arise if specific, relatively rare, lithologies did not heal completely and were coincidentally present at the seismic station sites. For now, these hypotheses are difficult to test, and we cannot exclude that a small amount of permanent damage is simply unresolved by our landslide susceptibility estimates. This issue will need further attention, but in Chapter 6 I simply ignore any long lasting effects of earthquakes on erosional dynamics of hillslopes, neglecting the relatively small amount of post-seismic landsliding, and a potential cumulative weakening of hillslope materials.
In Chapter 5, I combine the coseismic prediction for earthquake-induced landsliding developed in Chapter 3 with a standard solution for the surface displacement caused by earthquakes. This allows me to evaluate in which conditions earthquakes may cause more erosion than uplift, i.e., have a negative mass balance, and therefore, limit rather than build average topography. I compute the mass balance for individual earthquakes as well as for earthquake sequences, assuming that faults either produce characteristic earthquakes with fixed magnitude or a range of earthquakes with magnitudes following a Gutenberg-Richter distribution.

Chapter 6

The mass balance of earthquakes and earthquake sequences.

Abstract

Large, compressional earthquakes cause surface uplift as well as widespread mass wasting. Knowledge of their trade-off is fragmentary. Combining a seismologically-consistent model of earthquake-triggered landsliding and an analytical solution of coseismic surface displacement, we assess how the mass balance of single earthquakes and earthquake sequences depends on fault size and other geophysical parameters. We find that intermediate size earthquakes ($M_w 6.3-7.3$) may cause more erosion than uplift, controlled primarily by seismic source depth and landscape steepness, and less so by fault dip and rake. Such earthquakes can limit topographic growth, but our model indicates that smaller earthquakes and large events ($M_w > 7.5$) systematically cause mountain building. Earthquake sequences with a Gutenberg-Richter distribution have a greater tendency to have predominant erosion, than repeating earthquakes of the same magnitude, unless a fault can produce earthquakes with $M_w > 8$ or more. [1]

1. The work reported here was in the final round of review at GRL. By the time of the final thesis publication it has been typo-edited, formatted and published as: Marc, O., Hovius, N., and Meunier, P.: The mass balance of earthquakes and earthquake sequences, Geophysical Research Letters, 43, 2016GL068 333, doi: 10.1002/2016GL068333, 2016a.

6.1 Introduction

At the Earth's surface, geological processes creating topographic relief compete with geomorphic processes that level it. Where crustal deformation is fast, shallow earthquakes can dominate the displacement of rocks and the surface (Avouac, 2007). In the steep landscapes that prevail in such areas, shallow earthquakes can also induce widespread landsliding (e.g., Keefer, 1994) by short-lived, cyclic changes of the normal and shear stresses in hillslopes due to strong ground motion, shattering of the bedrock and rapid changes in groundwater distribution. In active mountain belts most valleys contain only small amounts of sediment, suggesting that, over multiple seismic cycles, most landslide debris is evacuated. Therefore, erosion due to landslides should be included in the mass balance of an earthquake. Here, this is defined as the difference between the change in rock mass volume above a reference plane (e.g., sea level) due to seismic and post-seismic surface deformation, and the volume of surface material mobilized by seismically-induced mass wasting, adjusted for the local effects of isostatic compensation. Strictly, this mass balance pertains to the area located above or in the direct vicinity of shallow faults that are locked during most of the seismic cycle, where seismic deformation is predominant. It does not include inter-seismic deformation or erosion, which are not considered here.

Recent studies suggest that the mass balance differs between earthquakes. Despite intense mass wasting, the 1999, M_w7.6 Chi-Chi earthquake in Taiwan caused growth of the hanging wall topography (Hovius et al., 2011), but landsliding due to the 2008 M_w7.9 Wenchuan earthquake in China matched seismic surface uplift (Parker et al., 2011; Li et al., 2014). And, Barlow et al. (2015) showed that tectonic subsidence was much greater than topographic lowering due to seismically induced mass wasting for the 2010 M_w7.2 El Cucapah Mayor earthquake. Li et al. (2014) also developed a more general treatment of the balance of seismically-induced landsliding and uplift, assuming that the rate of landsliding scales linearly with earthquake moment (Keefer, 1994). Notably, they predicted that earthquakes larger than a critical magnitude ($\sim M_w8$) would systematically have more erosion than uplift. If correct, this would have significant consequences for the emergence and growth of mountain ranges due to seismic processes. However, consideration of the spreading and attenuation of seismic waves with increasing distance from their earthquake source, and the geometry of faults likely to produce earthquakes of different magnitudes, suggests that the landslide rate is non-linear in earthquake moment (Marc et al., 2016b). Moreover, beside the influence of local climate (Barlow et al., 2015), the amount of landsliding due to a given earthquake should depend importantly on the steepness of the perturbed topography. Tested against a comprehensive compilation of estimates of earthquake-induced landslide volumes, the seismologically-consistent model of Marc et al. (2016b) performed better than any direct fit between earthquake moment and estimated landslide volume. We consider that this new model provides, for the first time, a robust basis for comparison with the uplift volume, which can be computed for any given earthquake from the surface deformation field using the approach of Okada (1985).

Here, we explore the parameters controlling the mass balance of earthquakes with a thrust component, combining the approaches of Marc et al. (2016b) and Okada (1985). In addition, we investigate the evolution of this mass balance for a fault experiencing many earthquakes over the long-term. We finish by discussing the implications of our results for the topographic evolution of fault-bounded structures and for mountain

building.

6.2 Methods

6.2.1 Uplift Modeling

Okada (1985) has developed an analytical solution for the surface displacement produced by slip on a plane in an elastic infinite half space. Fault slip distributions calculated by inversion of geodetically measured surface deformation, using this solution tend to be consistent with those derived from seismological inversions(e.g., Weston et al., 2012). The vertical displacement caused by a thrust fault is dome-shaped, with an extent scaling with the size and centroid depth of the fault (Figure 6.1A). This uplifted area is paired with two subsiding lobes, a major one above the footwall and a minor one in the hanging wall, above the down-dip extremity of the fault. This solution requires specification of the fault dimensions (length and width), geometry (strike, dip and depth centroid) and the amount of slip. We derived length, L, width, W, and average slip, D, from fault scaling relationships with seismic Moment, Mo, (Leonard, 2010) and obtained the total uplifted volume, V_u, for earthquake scenarios by numerically integrating all vertical surface displacement $> 0.5\%$ of the maximum, thus accounting for near-field subsidence at the periphery of uplift areas (Suppl. Methods). The modeled uplifted volume V_u is approximately proportional to the earthquake moment and independent of the fault centroid depth, as the large increase in the total uplifted area with increasing centroid depth is balanced by the decrease in maximum surface displacement (Suppl. Methods). The main parameters determining the uplifted volume are, therefore, the earthquake moment, Mo, and the dip, d, and rake, r, of the fault (Figure 6.1). At $d = 45°$ and $r = 90°$ the amount of subsidence relative to uplift due to earthquake slip is minimized and V_u is maximized. V_u decreases as d departs from 45 °, tending to zero (with subsidence cancelling uplift) when r tends to zero or 180 (strike-slip) and becomes negative with net subsidence when r is negative (normal fault).

6.2.2 Landslide Modeling

Complementing the surface displacement model, we have used a seismologically-consistent model predicting the total volume of landslides triggered by an earthquake, V_p, as a function of seismic moment, seismic source depth, R_0, and landscape modal slope, Smod (Marc et al., 2016b) Figure 6.1). The modal slope is easily extracted from a Digital Elevation Model and is a first order indicator of the landscape sensitivity, that is its propensity to failure (Marc et al., 2016b). This model derives from explicit consideration of processes modulating the ground shaking that controls landsliding (Khazai and Sitar, 2004; Meunier et al., 2007, 2013; Yuan et al., 2013), such as the amplitude of high frequency waves emitted at the source and the wave attenuation due to geometric spreading. In our model, the critical magnitude, above which an earthquake causes discernable landsliding and Vp assumes a non-zero value, is modulated by R_0 and ranges between M_w5 to 6 (Figure 6.1). Above this critical magnitude, V_p rises sharply, driven by the exponential increase of the ground shaking with increasing earthquake moment and by fault length increase. After reaching the hinge magnitude, $M_h = 6.75$,

the acceleration term saturates (Boore and Atkinson, 2008; Baltay and Hanks, 2014) and V_p is primarily increasing due to fault length growth with moment, $V_p \sim L \sim Mo^{2/5}$ (cf. Marc et al., 2016b) (Figure 6.1). This model differs from the classic, empirical relationship proposed by Keefer (1994), in which landslide volume increases linearly with earthquake moment.
The landslide model has been shown to be more accurate than empirical relationships, with predicted landslide volumes within a factor of 2 of independent estimates for earthquakes with magnitudes between 5 and 8 in two-thirds of 40 documented cases (Marc et al., 2016b). However, it has been found to over-predict landslide volumes where exceptionally strong lithologies, such as massive carbonates, are present, and for earthquakes with complex rupture mechanisms, such as super-shear.

6.3 Mass Balance of single earthquakes

The mass balance of earthquakes is found as the ratio of the curves for total uplift and total landsliding. Here, we explore the role of earthquake magnitude and the effects of source depth and landscape steepness, which modulate landsliding.
For a given fault geometry, the uplift term increases linearly with the seismic moment, but the relation between landsliding and the seismic moment is more complex. In small earthquakes, the ground shaking is insufficient to cause substantial landsliding and uplift always dominates. However, above the threshold for slope failure, the landslide term increases much faster with moment than the uplift term, up to the hinge magnitude, $M_h = 6.75$. Beyond this magnitude, landsliding scales with moment to the power 2/5, and triggered landslide volume increases much slower than the uplift volume. Therefore, for a given source depth and landscape steepness, the landslide volume may exceed the uplifted volume around the $M_h = 6.75$, and intermediate size earthquakes, with $M_w 6$ to 7, may have a negative mass balance (Figure 6.1). But for large earthquakes we find, in contrast to (Li et al., 2014), that the net surface uplift always exceeds the expected landsliding (Figure 6.1).
The range of earthquake magnitudes with a negative mass balance is strongly controlled by the source depth and landscape steepness and is smallest for earthquakes rupturing at greater depth or below gentle topography. For example, according to our model, an earthquake with source at 8km or deeper below topography with modal slope less than 23°will never be erosive (Figure 6.1B). Even in very steep landscapes with modal slope of 32°, earthquakes deeper than 14 km will never be erosive (Figure 6.1C). These considerations apply to a thrust fault with a dip of 30°and pure dip-slip (Rake=90°). The net surface uplift would be reduced if the rake increased or the dip decreased (Figure 6.1), affecting the earthquake mass balance. For example, shallow earthquakes on a fault with dip of 15°and a rake of 120°, could still have excess erosion at $M_w \sim 7.3$ However, for values consistent with thrust earthquakes (i.e. $120° > Rake > 60°$ and $10° > dip > 45°$) these parameters have limited importance compared to topographic steepness and source depth (Figure 6.1). .In summary, our results indicate that the mass balance of earthquakes depends critically on the earthquake characteristics and that above a certain magnitude, uplift always dominates. For a given earthquake the typical uncertainty of the total landslide volume predicted by the model we use here is about a factor of two (Marc et al., 2016b), meaning that even for a $M_w 6.8$ event, uplift and erosion are the same within error for most earthquake

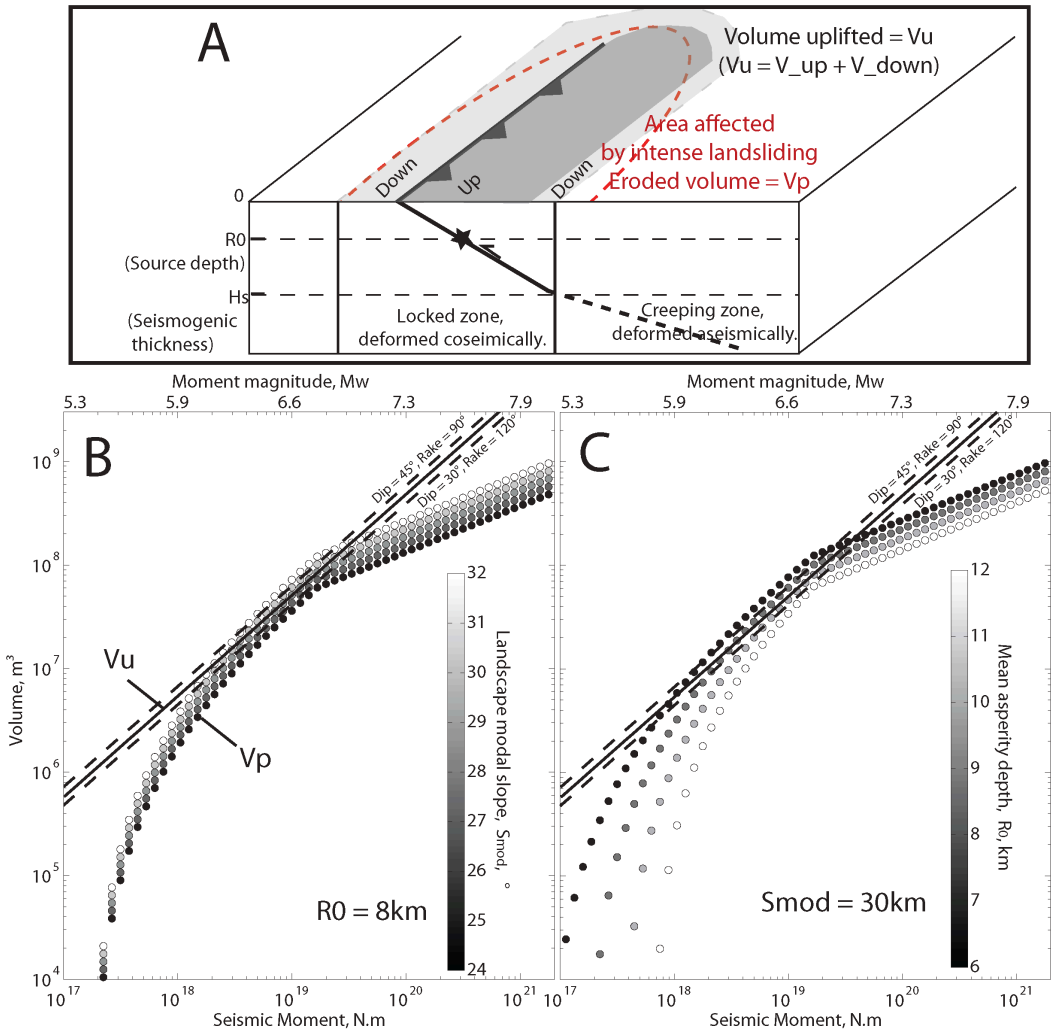

Figure 6.1 – Sketch of the uplift and erosion caused by an earthquake above its causative fault, (A), and coseismic uplift and landsliding against seismic moment for earthquakes with different landscape modal slope (B) and different asperity depth (C).

settings (Figure 6.1).

6.4 Mass balance of earthquake sequences

We have explored the effects of different physical parameters on the mass balance of single earthquakes. However, growth of fault-controlled structures and mountain ranges occurs over many earthquake cycles (King et al., 1988). To assess the long-term mass balance of the locked portion of a seismogenic fault we have modeled two end-member scenarios. One is a fault dominated by repeating earthquakes of characteristic magnitude. Although such faults are relatively rare, the Alpine Fault of New Zealand may be an example (Berryman et al., 2012). The other is a fault rupturing in earthquakes of various magnitudes on random sub-segments. In this second scenario, we assume that the distribution of earthquake magnitudes follows a Gutenberg-Richter (GR) relationship (Gutenberg and Richter, 1954), described by a power-law decay with exponent ~ 1, with at least one earthquake of maximum magnitude, $M_w X$, rupturing the entire fault. The Gutenberg-Richter relationship applies at regional scales and although we have limited empirical evidence, it seems to hold, for example for the Himalayan front (Avouac, 2015). Therefore, both end-members are relevant as they apply to specific, major fault systems, but many fault systems may have intermediate behavior.

For these two scenarios, the long-term mass balance of a seismogenic structure, defined as the mean volumetric change (MVC), is obtained by summing the erosion and uplift caused by all earthquakes on the structure with $5 < M_w < M_w X$, and dividing by the total number of earthquakes. In this calculation, the effects of smaller earthquakes, $M_w < 5$, are neglected because our model predicts little or no landsliding for such events in most settings, and because the long-term surface uplift is dominated by the largest events. The variations or evolution of other model parameters over the long term must also be constrained. We find that the characteristic time needed for a master fault to generate enough earthquakes to populate a full and representative distribution, is typically shorter than a million years for both types of sequences (Supplementary Methods) and therefore short compared to the structural evolution of a mountain belt. Thus, it is reasonable to assume that the fault geometry and rupture mode remain fairly constant over this period and that we can use mean values of dip and rake angle. Moreover, we keep $M_w X$ fixed and neglect any fault growth, therefore our calculations are best suited to relatively large and mature faults, the width and length of which are constrained by structural discontinuities. Climate and erosional conditions acting on the landscape may change importantly over such time scales but for simplicity we assume a constant topographic slope distribution.

Finally, the distribution of source or asperity depths over the long-term must be considered. For a seismogenic layer of thickness H_s and a fully locked fault (i.e., moving only in earthquakes), the cumulative seismic slip on the fault must be uniform over the full depth range, and is set by the convergence rate. This is important because the landslide volume assigned by our model is very sensitive to the depth of the main slip patch (Meunier et al., 2013; Marc et al., 2016b), or asperity, that emits most of the high frequency waves triggering landslides (Ruiz et al., 2011; Avouac et al., 2015). Therefore, long-term mass balance calculations depend critically on the depth range over which all earthquakes are distributed equally in order to satisfy equal slip. This range is set

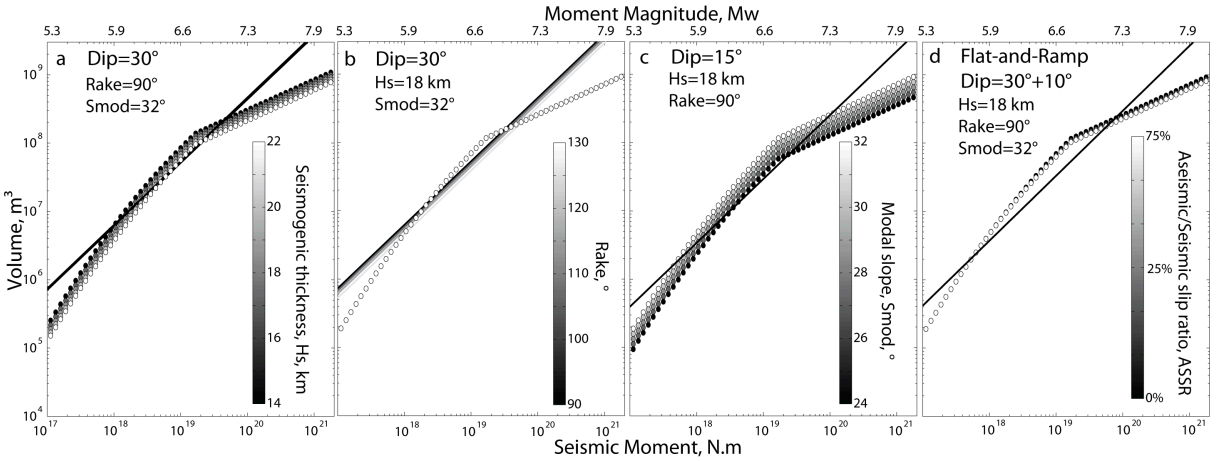

Figure 6.2 – Mean uplifted volume and landsliding for repeating earthquakes of a given seismic moment or magnitude. Four fault geometries are considered, a 30°dip thrust with varying seismogenic thickness, H_s, (A) or rake (B), a 15 °dipping thrust with varying modal slope (C) and a flat-and-ramp thrust (10°and 30°dip, respectively) with a varying ratio of aseismic over seismic slip on the flat portion (ASSR, see Suppl. Methods) (D).

between the surface (1km depth for numerical convenience) and H_s, typically between 15 and 20km (Leonard, 2010). Additionally, for a given dip angle and seismogenic thickness there is a critical earthquake magnitude beyond which the width of a fault can't increase. This mechanical boundary yields a break in fault size scaling, which is clearly observed for strike slip faults (Leonard, 2010), but not for dip-slip faults, suggesting that very large dip-slip earthquakes may extend to smaller depths because of the low angle or flat-and-ramp geometry of the active fault.
Hence, our calculations of the long-term mass balance of seismogenic faults depend on the fault geometry, fault length or maximum earthquake magnitude and the thickness of the seismogenic layer. Here, our analysis can't be exhaustive with respect to the range of geometries. Instead, we consider three typical settings. The first is a textbook thrust at 30°dip. The second is a thrust gently dipping at 15°, as representative of the geometry of megathrusts in the Himalayan range. The third fault has a flat-and-ramp geometry, with a ramp dipping at 30°and a flat dipping at 10°, as can be found in fold and thrust belt settings. The flat is set to be twice wider than the ramp with a transition between the two segments at a constant depth of 12 km, and with a variable ratio of seismic and aseismic slip (seismic slip ratio, SSR) (Suppl. Methods).

6.5 Long-term Mass balance of faults

In the first end-member scenario, repeating earthquakes with a constant magnitude and geometry occur on a fault. The main difference with respect to a single earthquake is that to maintain equal slip on the locked portion of the fault, earthquakes must rupture asperities at all depths, and the thickness of the seismogenic layer becomes the relevant parameter in the long-term. For large events, the average erosion of all earthquakes is similar to the erosion of a single earthquake occurring at a characteristic depth of approximately half the thickness of the seismogenic layer (Figure 6.2). Earthquakes larger than $M_w \sim 7.0$ or $M_w \sim 7.3$ are constructive, even under steep land-

scapes, for 30°dip faults or gently dipping and flat-and-ramp faults, respectively (Figure 6.2). For smaller earthquakes, the scaling of the landslide volume with earthquake moment is different because deeper earthquakes do not trigger landslides (Figure 6.2). The transition between these two regimes occurs below $M_w 6.5$ when earthquakes at the base of the seismogenic layer are expected to cause ground shaking which does not exceed the threshold for landsliding. In either case, the averaging of landslide erosion over N earthquakes of equal magnitude means that the standard error on the long-term erosion is that of a single earthquake divided by the square root of N. For a time interval covering a few tens of earthquakes the standard error on the average long-term erosion is $\sim 20\%$.

As a second end-member scenario, we consider a sequence of earthquakes with magnitudes distributed according to the Gutenberg-Richter relation, where the many small and intermediate earthquakes modulate the effect of rare, large earthquakes. Notably, because the exponent on the earthquake frequency-magnitude distribution is one, or 2/3 in moment, the surface uplift, which is linear in moment, is controlled by the largest earthquakes. However, the landslide model has a break in scaling with seismic moment at $M_w = 6.75$ (Figure 6.1), and erosion is optimal around this break. Thus, with a GR distribution, the long-term total erosion and its uncertainty are dominated by the events between $M_w 6.5 - 7$, which become more numerous as $M_w X$ increases. The uncertainty on the total erosion is about 22%, 12% and 7% , for a fault with $M_w X = 7.0, 7.5$ and 8.0, respectively. In any case, we find that the long-term mass balance behaves similar to that of the repeated earthquake scenario, but with a wider range of erosive faults. This is due to the large number of net erosive earthquakes of $M_w \sim 7$, the effect of which must be overcome by a few $M_w \sim 8$ earthquakes with a positive volume change to yield an overall increase in topographic volume.

Even in steep, landslide-prone landscapes with modal slopes around 32°, single faults with a dip of 30°are never erosive unless earthquakes have a strike-slip component or the seismogenic layer is thin (Figure 6.2, 6.3). However earthquakes on such faults would break a seismogenic layer of thickness 18 km in its entirety at an earthquake magnitude $M_w 7.6$, and they would not be able to grow after this. Therefore, other fault geometries with gentler dip or flat-and-ramp structure are especially relevant for $M_w >= 7.5$. For steep landscapes, and especially with a Gutenberg-Richter scenario, we observe that gentle dipping faults and faults with flat-and-ramp geometry are dominated by erosion unless the fault system can generate earthquakes with $M_w 7.8 - 8$, requiring a fault length of about 150-200 km (Figure 6.3). Even larger earthquakes would be necessary for a positive long-term mass balance if some amount of strike-slip occurred.

6.6 Discussion and conclusions

We have modeled the mass balance of earthquakes by comparing the coseismic surface deformation with the volume of earthquake-triggered landslides, accounting for the seismic source depth and topographic sensitivity. In contrast to previous studies that have not considered the specifics of faulting and topography, we have found that earthquakes with a net erosive effect are not those with a large magnitude above $M_w \sim 8$, but rather those with intermediate magnitudes between $M_w 6.3$ and 7.3. For deeper earthquakes and/or landscapes with gentle topography this range may nar-

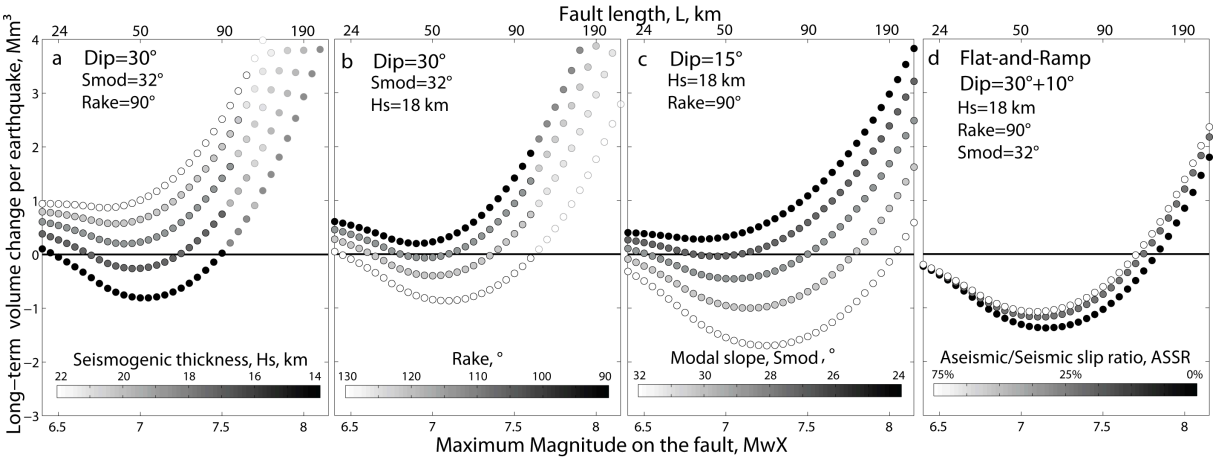

Figure 6.3 – Long term mass balance for a Gutenberg-Richter distribution of earthquake on a master-fault of length L and maximum magnitude M_wX. Same scenarios as in Figure 6.2. Transparent symbols indicate unrealistic setting where the fault width exceeds the seismogenic thickness H_s.

row or disappear. Our model predicts that earthquakes deeper than 15 km or under landscapes with topographic modal slopes less than 20°are always constructive. We also modeled the cumulative mass balance of a fault with repeating earthquakes of similar magnitude and a fault with earthquakes following a Gutenberg-Richter distribution. In steep landscapes, we found that faults with repeating earthquakes will systematically be constructive as soon as these earthquakes reach $M_w \sim 7 - 7.3$, that is when the length reaches 50 to 70km. In contrast, faults with earthquakes with a Gutenberg-Richter distribution may remain dominated by erosion until they can generate earthquakes of $M_w 8$ or more, which requires fault lengths in excess of 150km. This is especially so if they dip gently or have a flat-and-ramp geometry, as we would expect for settings with a normal thickness of the seismogenic layer. Such faults, which are common in fold-and-thrust belts, may limit orogenic growth until the fault system has grown enough to produce very large earthquake ($M_w > 8$), when net topographic growth can resume.

Our model has important limitations. First, we have not considered the isostatic rebound, which would occur due the removal of any substantial amount of landslide debris from the uplifted topography. As previously discussed, isostasy is certainly an important part of the problem but it is largely under-constrained because we do not know the rate at which the landslide debris is exported, nor if it is redeposited close to or distant from the affected topography (Molnar, 2012; Densmore et al., 2012). Moreover, the elastic thickness that sets the length scale over which the rebound is distributed is variable (e.g., Jordan and Watts, 2005). For an elastic thickness of 20 or 40km, landslide erosion distributed over 50 km across a fault would solicit 38% and 25% compensation through isostatic rebound, respectively (Densmore et al., 2012). Even for a very large earthquake, intense landsliding is unlikely to reach more than 25km away from the earthquake source because the ground shaking saturates, and the area affected could be much smaller for earthquakes of $M_w 6 - 6.5$ (Marc et al., 2016b). With constant elastic thickness this would reduce the amount of isostatic compensation within the eroded area. Although isostatic compensation may change the sign of the earthquake mass balance where the sum of surface uplift and erosion is relatively small, our findings re-

main generally robust away from these cusps. For example in settings where $M_w 6.5-7$ earthquakes induce 2 to 3 times more erosion than uplift the mass balance would remain negative even after accounting for 25-40% of isostatic rebound (Figure 6.2).
Further, we have neglected complexities such as aseismic slip and interactions with neighboring faults. Neighboring faults may be close enough to cause uplift and/or landsliding in the topography above the fault in question, and possibly also to affect the way earthquake magnitudes on that fault are distributed in time. Therefore, depending on the setting, seismic activity on neighboring faults can shift the long-term mass balance of a fault in any direction. The effects of aseismic slip are more tractable because, whether it occurs as post-seismic slip or as creep during the interseismic period, it will build topography as earthquakes do, but without associated landsliding, as modeled in the case of a fault with flat-and-ramp geometry (Figure 6.3). When aseismic slip is limited to the deeper part of the fault, as often observed for post-seismic afterslip (e.g., Rousset et al., 2012), it has a limited impact on the mass balance because it "replaces" the less effective earthquakes of a long-term sequence (Figure 6.3). On faults where creep is significant at shallow depth the mass balance will be more strongly shifted towards uplift. However, examples of such faults are rare, but may include the Longitudinal Valley Fault in Taiwan (Avouac, 2015), and our treatment likely applies to most settings.
Finally, we have neglected any progressive evolution of the topography and effects of fault growth. This is likely reasonable over 10^5 years, but not at the scale of mountain building, that is $10^6 - 10^7$ years. The spatial and temporal extent to which earthquakes may limit topographic growth will depend on how fast the landscape reaches a high modal slope, on the geometry of the fault and the rate and mode of fault growth, and on whether repeated or distributed earthquakes occur on it. We suggest that in order to decipher the long term influence of faults and earthquakes on mountain building, and to explore the feedbacks between erosion and fault mechanical behavior, a mechanical model describing fault and crustal properties (e.g., Mary et al., 2013) would need to be effectively coupled with a landscape evolution model characterizing topography and incorporating earthquake-induced landsliding (cf. Steer et al., 2014). Short of this full geodynamic approach, our mass balance model indicates that incipient faulting in a relatively gentle landscape will always lead to the construction of topography because coseismic landsliding is limited by the steepness of that topography, whatever the fault and earthquake size. However, as topography rises and steepens, then intermediate size earthquakes will quickly become destructive, limiting the rate of mountain building and eventually halting net mountain growth. During a certain period such faults and associated topography may continue to expand laterally, while their average topography is reduced. But when faults become large enough to produce earthquakes of $M_w > 7.8 - 8.2$, effective mountain building could resume. Therefore, our study does not challenge the role of earthquakes as a key mechanism of mountain building. Rather, it demonstrates that earthquakes are ambivalent agents, which may limit topographic growth during a given period or in a certain part of a mountain belt. For example, historical records attest that very large continental earthquakes ($M_w > 8.3$) have occurred relatively frequently on faults bounding the Himalayas (Bollinger et al., 2014), and the earthquake sequences likely drive topographic growth. In contrast, in many smaller mountain belts such as Taiwan, Papua New Guinea, or the mountain ranges flanking Tibet to the north, such large faults may be absent and the average topographic growth may be limited rather than supported by earthquakes.

6.7 Supplementary materials to Chapter 6

6.7.1 Supplementary methods

Volume uplifted by an earthquake

Okada (1985) has developed an analytical solution for the surface displacement produced by slip on a plane in an elastic infinite half space, which we have used to model the uplifted volume due to an earthquake. We derived length, L, width, W, and average slip, D, from fault scaling relationships with seismic moment, Mo, (Leonard, 2010) and obtained the total uplifted volume, V_u, for earthquake scenarios by numerically integrating all vertical surface displacement $> 0.5\%$ of the maximum. This threshold is imposed to account for near-field subsidence at the periphery of uplift areas, but avoid inclusion of the effects of far field elastic oscillations, which are unrealistic. In order to always allow integration over areas of uplift and subsidence within a distance of 2-3 fault lengths away from the fault centroid (i.e., the distance required to reach displacement smaller than our threshold), our model space is set to grow with fault length, and width. V_u varies almost linearly with earthquake moment, typically $V_u \sim Mo^{0.95}$, and the fault attributes L, W and D. Therefore, the uncertainty within the scaling relationship is not an important source of error for our uplifted volume estimate, and only the uncertainty on the seismic moment is important. Notably, the analytical solution that we have used assumes an Earth surface without topography.
The uplifted volume Vu predicted by the model is mostly independent of the fault centroid depth, as the large increase in the total uplifted area with increasing centroid depth is balanced by the decrease in maximum surface displacement. However, the use of a threshold of displacement, at 0.5% of the maximum displacement does not exactly preserve the relative importance of uplifting and subsiding areas when centroid depth is varied, especially for large earthquakes. This gives rise to variations of Vu of up to 5-10% with centroid depth that have been ignored in further calculations.
We have tested for the sensitivity of solutions to effects of topography, using 3D Boundary Element Modeling (cf. **?**) and found that although local surface displacement could differ by as much as 20%, the bulk effect of topography on the total uplifted volume was typically of the order of 0.1-1% due to canceling effects of local uplift and subsidence.

Characteristic time of earthquake sequences

We have considered sequences of repeating earthquakes of identical magnitude, and of earthquakes with a magnitude-frequency distribution as described by Gutenberg and Richter (1954). For repeating earthquakes, typical recurrence times for large earthquakes in rapidly converging settings is on the order of 100 to 1000 years, meaning that in 10,000 to 100,000 years, we can average the mass balance of 10^2 earthquakes. Longer time is needed for a master fault to generate enough earthquakes to populate a GR distribution, as many small and intermediate earthquakes are associated with a major event of M_wX, rupturing the whole fault. This characteristic time is computed by summing the total horizontal slip caused by the largest earthquake of M_wX and the thousands of associated smaller earthquakes, and dividing by the shortening rate. For $M_wX \sim 8.2$ and $\sim 13,000$ earthquakes with $M_w > 5$, and a convergence rate of 3

cm/yr, as might be found in an active mountain belt, a characteristic time over which a master fault may display a GR distribution is $\sim 150,000$ years. If several fault systems together accommodate the total convergence, then this characteristic time must be multiplied by the number of major structures in the shortening zone.

Prescriptions for the flat-and-ramp scenario

For the flat-and-ramp scenario we allow the amount of seismic slip on the flat portion of the fault as a proportion of total slip to vary. We consider that the amount of seismic slip taken on the ramp may be equal to, or twice or four times larger than that occurring on the flat, defining a seismic slip ratio. We assume that this ratio determines the relative probability for an asperity to be on the ramp rather than on the flat. These prescriptions represent a flat detachment that may be "smoother" or weaker than the ramp and therefore less likely to rupture seismically. This implies that a proportion of the total slip on the flat occurs aseismically, during post-seismic or inter-seismic periods. For example, for constant cumulative slip conditions, a seismic slip ratio between ramp and flat of 1, 2 or 4 implies that the long-term ratio of aseismic over seismic slip on the flat (ASSR in the main text) is 0%, 50% or 75%, respectively. For a given seismic slip, an increase of the ASSR implies that the earthquake asperities are located higher on the fault and produce more erosion. However, for a given long-term total slip, a larger ASSR favors topographic growth because the aseismic slip will produce as much uplift as seismic slip, but without any erosion.

Chapter 7

Conclusions

Chapter 2 detailed how amalgamation, a mapping error in which multiple landslides are bundled into a single mapped polygon, can bias landslide volume estimates and landslide size statistics. Short of an adequate way to automatically correct for this effect I proposed an algorithm to automatically detect erroneous polygons, which can inform manual correction.
For four earthquake induced landslide inventories, obtained by manual or automatic mapping methods, I found various degrees of amalgamation. The simple screening of mapped polygons over a Digital Elevation Model revealed geometric or topographic inconsistencies that allowed me to manually split the larger polygons. Based on this partial correction I estimated a minimal bias on the total landslide volume and the area-frequency power-law exponent of up to 300% and 50%, respectively. Furthermore, I devised a simple algorithm implementing a systematic check of the geometric and topographic characteristics of the mapped polygons, and able to detect potentially erroneous polygons. Tested on the landslide inventory for the Northridge earthquake (Harp and Jibson, 1996), the algorithm reached an accuracy of 92.5% with only 2.7-3.6% of amalgams missed and 3.9-4.8% correct mapped polygons incorrectly classified. This should permit checking of other inventories with such issues and guide and accelerate manual corrections.

Chapter 3 presented a seismologically-consistent model predicting the total volume and area of landslides induced by an earthquake. I tested this new model with an extensive database of earthquakes with information on their induced landsliding and seismological characteristics. I have developed an analytical expression for the total area or volume of landslides, by combining wave emission and fault size scaling relationships with magnitude, together with the theory of seismic wave attenuation and a statistical description of the landscape properties. In this treatment, the dependence on the distribution of slope and ground strength of the landscape required empirical calibration. The calibration and accuracy of the model were assessed with a database of 40 earthquakes for which I gathered total landslide volume, moment, depth, and characteristics of the overlying topography. I found that landscape steepness, characterized by the mode of the topographic slope distribution, has an exponential influence on the total landslide volume. Therefore, this prediction requires knowledge of parameters controlling the shaking intensity and extent, controlled by the earthquake magnitude,

fault size and depth, as well as constraints on the abundance of steep slopes that sets the landscape sensitivity to shaking. The model performs relatively well, with a success rate about twice that of previous models (Keefer, 1994) or empirical fits that can be obtained between landslide volume and seismic moment. In absolute terms, the model prediction is within a factor two of the estimate for 63% of the cases ($R^2 = 0.76$, N=40), while most outliers had specific environmental or seismological conditions. For example, all three cases underlain by massive, unfractured limestone units - with an above average rock mass strength - produced much less landsliding than predicted. These cases underscore the need to develop methods to obtain quantitative estimates of rock strength that are representative at the landscape scale (Clarke and Burbank, 2010; Gallen et al., 2015). Extremely dry conditions and peculiar earthquake ruptures can also explain some outliers, and further data should be acquired to integrate these aspects in the model. Though fewer estimates exist for total landslide area, the prediction seems less dependent on the landscape modal slope than total volume, and more on parameters affecting the area frequency distribution, possibly the shaking duration. Nevertheless, our model predictions are also good with 65% of the events predicted within a factor of 2 of the estimated area ($R^2 = 0.73$, N=17).

Chapter 4 investigated the effect of earthquakes on landscape properties and dynamics. I assessed the changes of landslide rate due to earthquakes and their possible mechanism by repeated landslide mapping. In the epicentral areas of four intermediate to large earthquakes I normalized landslide rates for rainfall forcing, empirically estimated with cumulative precipitation, and found that landslide rates systematically increased, by up to 20 times, after an earthquake. These elevated rates are unrelated to aftershocks and normalized for rainfall and therefore indicate ground strength reduction. Further, I observed that normalized landslide rates decayed and returned to pre-earthquake rates over 1-4 years, in a non-linear fashion for at least one case. I discarded root-system damage, as trees damaged by the shaking seem rare (Allen et al., 1999) as well as hydrological disturbance that typically dissipates in a few months to a year (Wang et al., 2004). The favoured explanation is that the shaking was strong enough to open or elongate existing fractures in the regolith or to cause decompaction of soils. Based on landslide depth estimates I inferred that the damage could not be limited to the soil layer, and must have affected the regolith and shallow bedrock. The strength recovery, though it may be in part due to removal of the damaged layer, may also be due to clast re-arrangement (Lawrence et al., 2009) or cracks closing under pressure or through filling. An active healing mechanism is favoured because it could explain the observed non-linear recovery apparently independent of the intensity of subsequent episods of landsliding directly following the earthquake, contrary to what would be expected if the recovery would be driven by the removal of damaged layers.

Chapter 5 presented the temporal evolution of seismic velocity, obtained through autocorrelation of ambient noise registered at seismic stations located in the epicentral areas of three out of the four earthquakes presented in Chapter 4. I compared the temporal dynamics of seismic velocity to the dynamics of rainfall normalized landslide susceptibility and to the post-seismic deformation measured through GPS station displacements. While each area has different relaxation time-scales, I found a striking match between these three independent signals. The correlation between the dynam-

ics of landsliding and seismic velocity supports the common interpretation that velocity drops co-seismically because of new cracks opening in the shallow ground due to strong motions. This work also supports the idea that the change of elastic moduli must occur at very shallow depths (0-20m), decreasing the ground strength (or cohesion) enough to significantly increase landslide hazard. The correlation between post-seismic surface displacement and the shallow mechanical properties may be causal and analogous to the compaction and strengthening of granular material agitated by shear or vibration, observed in laboratory experiments (Richard et al., 2005). In any case, my observations suggest that the temporal evolution of mechanical properties of the ground, key to many surface processes, may be driven by tectonic processes to a larger extent than previously thought.

Chapter 6 aimed to model the competition between uplift and erosion caused by earthquakes, making use of the newly built model of landsliding. The modelling compared predicted landslide volumes based on the relation from Chapter 3 and analytic prediction of coseismic surface deformation due to single earthquake scenarios or to a series of earthquakes on a fault. First, I showed that large earthquakes, $M_w > 7.5$, are always constructives because for $Mw > 6.75$ the ground shaking saturates, and the landslide volume increase with moment is smaller than the increase in the uplifted volume. This result contrasts with earlier work by Li et al. (2014). For a single earthquake, source depth and landscape steepness are the main controls on the mass balance, modulating the range of moments that can be destructive. Over the long term I considered that either repeated earthquakes or a distribution of earthquakes with moments following the Gutenberg-Richter (GR) distribution could occur on a master fault. Then, the seismogenic thickness controls the distribution of depth over which the slip must be distributed and replaces earthquake source depth as a control on the long term mass balance. In the case of GR-faults I found that common fault settings could remain destructive until the fault is able to produce very large earthquakes, $M_w > 8$ or 8.2, suggesting that seismic faults in many mountain ranges may limit the topographic growth until they reach very large dimensions ($> 200km$) that are able to produce very large earthquakes. Faults may need a significant amount of time before reaching such a large size, implying that their contribution to the building of topography will vary during their lifetime and the evolution of a mountain belt. Currently some small and young mountain belts, such as Taiwan or the Finisterre range in Papua New Guinea may not have such large faults and may not build topography through earthquakes. The co-evolution of landscape topography and fault geometry and behavior through time has been neglected but should be studied to unravel possible feedbacks between earthquake-induced erosion and fault mechanical behavior.

The results obtained through the different chapters have added some new constraints on the interactions between tectonics and erosion, mediated by earthquake-induced landslides, and inform discussion of the ambiguous role of earthquakes in the long-term evolution of the topography in seismically active areas. However, many of the results derived from this thesis not only have geophysical or geodynamical implications, but also a significant importance for natural hazard assessment and mitigation, and the potential for applications will be explored in the following synthesis.

Chapter 8

Synthesis

8.1 Discussion

In this thesis I have addressed the feedbacks between tectonics and erosion that are associated with earthquakes, and their consequences for erosion and landscape evolution over different timescales. Finally, I would like to go beyond the individual studies presented in the previous chapters and attempt to draft a more general picture of the understanding acquired through this thesis.

8.1.1 Coseismic landsliding

The importance of direct feedbacks between tectonics and erosion through earthquake induced landslides has been recognized for a long time (Keefer, 1994; Dadson et al., 2004). I have tried to deepen our understanding of the contribution of earthquakes to erosion by better quantifying the amount of landsliding triggered by an earthquake. This was accomplished by collecting a database summarizing observations of earthquake-induced landslides and physical modeling of the seismic shaking that triggers the landslides. This analytical approach is well suited for broad-brush applications such as comparing erosion driven by climate and earthquakes, assessing the impact of past or future earthquakes, evaluating damage and mitigating risk immediately after an earthquake. The efficacy of this approach suggests that a simplified earthquake and ground shaking model captures a large part of the variability in terms of total landsliding from earthquake to earthquake. The model also predicts a depth dependent cutoff for small earthquakes, predicting that $M_w < 4.5$ earthquakes will not trigger significant slope failure, even when they occur at depths of only a few kilometers. This is consistent with earlier compilations (Keefer, 1984). Further, the model predicts that for deeper earthquakes, with sources at 5-10 km depth, $M_w > 5 - 5.5$ are required for significant landsliding. The model also predicts a total area affected by landsliding, based on the fault length and on the maximum distance before waves emitted at the source are attenuated to the critical acceleration required for landsliding. This could be compared to early compilations (Keefer, 1984; Rodriguez et al., 1999) and to currently available landslide maps. Obviously, as the model considers the statistical density of landsliding, rare or distant individual landslides may complicate the

comparison with minimum earthquake magnitude for landsliding and the total area affected by landsliding predicted by the model. The limitations of this approach lie mainly in the fact that individual landslide locations are not modeled, as most parameters are averaged over the epicentral area. As long as geotechnical parameters are not available at fine scales across landscapes, accurate prediction of landslide locations will remain an open challenge (Dreyfus et al., 2013). However, refining the spatial pattern of landsliding at intermediate scales seems possible, either through forward modeling, or through statistical assumptions about the general behaviour of earthquake-induced landslides, requiring far fewer details about the seismic source. This model is, by design, broadly consistent with the forward modeling of the spatial pattern of landslide density proposed by Meunier et al. (2013). Therefore, knowing or assuming a slip distribution on a fault plane, the analytical prediction could be combined with this forward model and both the total landslide area and volume predicted, together with their spatial distribution. However, a-priori knowledge of earthquake slip distribution remains intractable and renders this approach of limited social utility, as it can be performed only after the earthquake has been studied in detail. Alternatively, various empirical observations made on different earthquakes could be combined in a set of statistical relationships about the relative probability of occurence of earthquake-induced landslides as a function of slope angle and a proxy of lithological strength (Parise and Jibson, 2000; Lin et al., 2008; Gorum et al., 2013; Meunier et al., 2013), distance from the ridge (Meunier et al., 2008) and slope aspect relative to the seismic source (Meunier et al., 2008; Barlow et al., 2015). These different factors could be integrated in a single set of equations, which, together with the simple assumption of a line source propagating at a given depth on a given fault plane, would give a spatial pattern of relative probability of landsliding, according to which the total landslide volume and area could be distributed. Although this would still ignore seismic effects that cannot be predicted a priori, such as source directivity, such an approach is now within reach and should certainly be developed and tested.

8.1.2 Bedrock fracturing and earthquake strong-motion

Bedrock fracturing and rockmass weakening is another important feedback between tectonics and erosion according to some studies (Molnar et al., 2007; Clarke and Burbank, 2010). However, this is mainly attributed to large scale, homogeneous processes, such as microseismicity or displacement on bent faults (Molnar et al., 2007). The importance of earthquakes and dynamic fracturing has been invoked (Sleep, 2010; Owen et al., 2008) but not clearly established. Combining remote-sensing observations and ambient noise correlation techniques I have shown in Chapters 4 and 5 that several earthquakes have induced simultaneous increases in landslide rate and decreases in seismic wave velocity. This strongly suggests that dynamic fracturing is common and has a strong effect on the mechanical properties of the shallow rocks. Such effects are of first order at the annual time scale, with 5-20 fold increases in landslide susceptibility. It is unclear whether or not dynamic fracturing due to earthquakes may accumulate and leave a long term signature in the landscape (e.g., Sleep, 2011b; Parker et al., 2015). The landslide data are relatively noisy and may not be able to detect small permanent damage. In contrast, the fact that seismic velocities do not recover fully at all sites suggests that some permanent damage may occur within some parts of the landscape. Further that analysis of the status of ground cracks and their healing

with in-situ measurements would certainly help in assessing where and how damage is healed.
The study of increased landslide activity following earthquakes was largely motivated by observations of enhanced post-seismic fluvial sediment transport (Koi et al., 2008; Hovius et al., 2011; Howarth et al., 2012; Wang et al., 2015). My data indicate relatively fast recovery times of only a few years for the disturbance on the hillslopes, whereas studies of sediment transport reported disturbances up to 50 years long. Therefore, I propose that enhanced suspended sediment transport is likely due to a lag in transport and delivery of coseismic landslide materials to the river network, as observed after intense landsliding due to typhoons (Huang and Montgomery, 2013). Hence, most of what is transported in rivers in the years following an earthquake is probably still coseismic landslide material and my data shows that the additional mass wasting due to elevated hillslope susceptibility is a minor contribution compared to the total volume of coseismic landslides. This highlights the need to better constrain the transport and evacuation dynamics of the landslide debris, particularly of the bedload fraction.

8.1.3 Earthquake mass balance

Several studies have suggested that, over longer timescales, the erosion due to earthquake-induced landsliding is larger than the coseismic uplift for very large earthquakes, raising questions about the role of earthquakes in mountain building (Parker et al., 2011; Li et al., 2014). The new predictive equation that I have developed, allows better integration of the different physical effects that control the mass balance of earthquakes. I have modeled the mass balance as the ratio or difference between coseismic landsliding and coseismic surface deformation, neglecting post-seismic erosion or deformation. In Chapter 4, I showed that the contribution of post-seismic landslides to the total erosion caused by earthquakes was small in comparison to the coseismic mass wasting. Still, permanent damage of shallow rocks remains possible (e.g., Parker et al., 2015) and in this case progressive fracturing due to strong shaking may increase the erosion term of the mass balance estimates. The post-seismic deformation that is known to occur generally amounts to $\sim 10-15\%$ or less of the coseismic moment (e.g., Hsu et al., 2007; Ryder et al., 2007; Barbot et al., 2008), and is therefore a minor contribution that would only nudge the mass balance towards construction.
Long-term storage of sediment produced through landsliding, if it happens significantly within the epicentral areas, would also change the mass balance. For the Chi-Chi earthquake, models suggested that the river transport capacity may be vastly exceeded and that landslide debris may take centuries to be evacuated (Yanites et al., 2010). These estimates are uncertain and require updating for various earthquakes for which accurate estimates of the volume of landslide debris have been presented in Chapter 3. Nevertheless, landslide dams and giant landslide deposits have been identified in many mountain belts (Korup et al., 2007, 2010) and probably contribute to long-term storage. Recent work has estimated the total sediment stored in the Himalayan belt in such deposits, as well as other valley fills, to $\sim 900km^3$, with age and/or residence time varying between 50-200 kyr for the largest fills (Blöthe and Korup, 2013). This estimate can be compared to the frequency of large, shallow earthquakes that rupture the Himalayan front and produce significant landsliding, such as the recent 2005 M_w 7.5 Kashmir or the 2015 M_w 7.9 Nepal earthquakes (Owen et al., 2008; Kargel et al., 2015).

Earthquakes of M_w 7, 7.5 and 8 occur every 100, 300 and 900 years (Avouac, 2015) on 5 or more major fault segments along the range, and produce, about 0.15, 0.3 and 0.6 km^3 of debris, respectively, assuming an average earthquake source depth of 8 km. Neglecting any larger or smaller earthquake contributions, as well as other erosion terms, these large earthquakes would produce 150 km^3 in 9 kyr, and more than the total volume of all valley fills in 60 kyr, a time shorter than the age of most large fills (Blöthe and Korup, 2013). This suggests that only a fraction of coseismic landslide debris is stored and that a significant amount is effectively exported over the long-term. The amount of export and its duration will likely vary significantly depending on the regional setting, with a complex role of climate, topography and erosional dynamics, as suggested by the large difference in storage between the Western, Central and Eastern Himalayas (Blöthe and Korup, 2013).

8.1.4 Landslide hazard

I have discussed in detail the geophysical and geomorphological significance of findings on earthquake-induced landsliding, but less so in terms of natural hazard applications. Secondary hazards such as landslides, and their indirect consequences such as landslide dams, debris flows or floodplain aggradation and river avulsion, are a significant part of the hazards induced by earthquakes in mountain regions. For some earthquakes, coseismic landsliding may be the primary source of infrastructure damage (Bird and Bommer, 2004), and the cause of a large proportion of casualties, as for the 2008 Wenchuan (China) earthquake, where 25% of the total death toll (i.e., 20,000 out of 80,000 deaths) were attributed to landslides (Yin et al., 2009). These estimates do not usually consider casualties or costs associated with the post-seismic period, in which a part of landslides and sediment transport are still an indirect effect of the earthquake (Huang and Li, 2014). My results have multiple implications for these issues. First, the equations presented in Chapter 3 allow exploration of the magnitude of secondary hazard associated with expected earthquake scenarios. Even if forecasting of the location of landslides is the ultimate goal for risk assessment, the ability to predict or rapidly assess the magnitude of landsliding, that may vary by orders of magnitude with landscape properties and earthquake depth, is of definite value. Coupling my prediction to estimation of the spatial patterns of landslides, as discussed at the outset of the synthesis, is an important step to better constrained hazard estimates. Second, the constraints on the elevated landslide rates after earthquakes, presented in Chapter 4, indicate that landslide hazards in epicentral areas may increase by an order of magnitude, and persist for one to several years. This should be taken into account when planning remediation measures in rugged epicentral areas. The magnitude of the landslide susceptibility increase appears to increase with the earthquake magnitude, but likely relates to additional earthquake characteristics. Indeed, the ground damage and weakening is expected to be strongly dependent on ground shaking, scaling non-linearly with moment and depth, as modeled in Chapter 3. The recovery time is also important for risk management as it allows anticipation of the period over which elevated risk and costs are likely. In Chapter 5, I observed that the material healing dynamics correlate with post-seismic displacement and may be driven by it. This would mean that the recovery is not related to landscape properties, but rather to crustal behaviour that may be hard to anticipate after an earthquake. In contrast, Chapter 5 also suggests that the progressive recovery of shallow bedrock strength could be monitored

through the monitoring of shallow seismic velocities. Therefore, ambient noise correlation techniques could be used after earthquakes to constrain the initial phase of the recovery and anticipate the total duration of the elevated risk period.

8.2 Future work

The results obtained through this thesis have also highlighted the need for further research on several key aspects which are presented below.

8.2.1 Automatic mapping of individual landslides

First, with the rapid proliferation of landslide inventory maps, it becomes urgent to define quality standards for mapping. Guzzetti et al. (2012) recognized that the diversity of imagery and mapping techniques would lead to variable results, limiting the credibility of landslide maps, unless standards and best practice methods were developed. Accurate and comparable maps are important in order to build databases or time series of landslide inventories, as exemplified in Chapter 3 and 4. The algorithm to detect amalgamation presented in Chapter 2 is part of such efforts but the real challenge is to implement automatic delineation of various landslide bodies within areas affected by intense landsliding. Developing other criteria and guidelines to assess which derivatives, such as landslide volumes, landslide numbers, landslide locations or size-frequency statistics, can be safely extracted from an inventory map would certainly help to make the best use of these maps. Another important aspect is the delineation of landslide scar, runout and deposit, rather than the whole perturbed area as is usually the case (e.g., Behling et al., 2014; Stumpf et al., 2014). This obviously requires high resolution imagery, probably 5 m or better, and may not be possible for all landslide types and configurations. Nevertheless, even partial inventories with reliable differentiation of the different components of a landslide would allow study of the statistical behaviour of runout, and to better assess the relation between scar and deposit areas and how they vary with landslide size and location. These are important parameters required to improve the accuracy and precision of the conversion from landslide area to volume, as well as to better assess and mitigate hazards.

8.2.2 Quantification of rock strength

Another issue that has been pervasive through the different aspects of this work is the strength of hillslopes. Indeed, quantifying rock or ground strength seems essential to constrain the amount of earthquake-induced landsliding (cf., Chapter 3) but also to understand how it controls landslide dynamics of catchments (cf., Chapter 4). The key problem is that laboratory measurements of strength from field samples are usually orders of magnitude higher than what seems reasonable to explain the failure behaviour of the hillslopes (Hoek and Brown, 1980). This arises from our inability to account for heterogeneity of the material (e.g., fractures, multiple lithologies with variable behaviour) at the hillslopes scale. Such heterogeneity can be partly assessed by

methods yielding qualitative rock strength indices (Selby, 1982), but it is unclear how such methods could be extended to a catchment scale. Still, several avenues may be explored to address this recurrent problem. One is to use geophysical methods based on wave propagation that is sensitive to ground structure and properties (e.g., Clarke and Burbank, 2010, 2011). In this sense, ambient noise techniques introduced in Chapter 5 present the advantage of yielding continuous measurements based on existing networks and averaging properties on various length scales. However, dedicated experiments with these techniques are needed to better understand how to extract ground strength from signals that are also sensitive to many other processes (cf., Richter et al., 2014) and uncertainties. Another option is to try to model and quantify the effects of fracture networks on superficial strength, making use of new theoretical progress in the characterization of these networks (e.g., Davy et al., 2010, 2013) and new ways to measure them in the field through laser scanning or photogrammetry. Finally, in fast eroding threshold landscapes we may expect a specific topographic signature, and therefore might be able to invert slope or relief characteristics to obtain mechanical strength at the landscape scale (e.g., Schmidt and Montgomery, 1995). The potential of such inversion should surely be assessed with newly available high resolution Lidar DEMs (e.g., DiBiase et al., 2012).

8.2.3 Developing software for automatic earthquake-induced landsliding hazard assessment

Although the expression developed in Chapter 3 does not yield information on the location of individual landslides it gives a rapid and accurate estimate of the magnitude of landsliding expected along a seismogenic fault. In order to be useful for rapid response risk management after earthquakes, this expression would need to be implemented in an online platform and coupled to routine earthquake detection. We plan to develop a web based application, that could take as input earthquake information, such as M_w, fault type and location and output the total volume and total area of landslides, as well as some other derivatives such as the percentage of affected hillslopes. The application could be plugged in to an earthquake detection and assessment platform such as the USGS PAGER service. With the fault coordinates and the earthquake depth and magnitude, we would automatically extract the surrounding topography from the ASTER GDEM and compute the local landscape modal slope and the topographic availability correction factor. With these parameters and the earthquake characteristics, the total volume of landslides, total area of landslides and their associated uncertainties would be computed. Therefore, routinely detected shallow earthquakes could be immediately attributed some secondary hazard estimates, based on landsliding expected from our model. The next step to take to improve such an application and widen its potential use would be to combine it with current or future knowledge about the spatial pattern of landslide density.

Bibliography

Abercrombie, R. E., Webb, T. H., Robinson, R., McGinty, P. J., Mori, J. J., and Beavan, R. J.: The enigma of the Arthur's Pass, New Zealand, earthquake: 1. Reconciling a variety of data for an unusual earthquake sequence, Journal of Geophysical Research: Solid Earth, 105, 16 119–16 137, doi: 10.1029/2000JB900008, 2000.

Ahnert, F.: Functional relationships between denudation, relief, and uplift in large, mid-latitude drainage basins, American Journal of Science, 268, 243–263, doi: 10.2475/ajs.268.3.243, 1970.

Alfaro, P., Delgado, J., Garcia-Tortosa, F. J., Lenti, L., Lopez, J. A., Lopez-Casado, C., and Martino, S.: Widespread landslides induced by the Mw 5.1 earthquake of 11 May 2011 in Lorca, SE Spain, Engineering Geology, 137-138, 40–52, doi: 10.1016/j.enggeo.2012.04.002, 2012.

Allen, R. B., Bellingham, P. J., and Wiser, S. K.: Immediate damage by an earthquake to a temperate montane forest, Ecology, 80, 708–714, doi: 10.1890/0012-9658(1999)080[0708:IDBAET]2.0.CO;2, 1999.

Allmann, B. P. and Shearer, P. M.: Global variations of stress drop for moderate to large earthquakes, Journal of Geophysical Research: Solid Earth, 114, B01 310, doi: 10.1029/2008JB005821, 2009.

Anderson, H., Beanland, S., Buck, G., Darby, D., Downes, G., Haines, J., Jackson, J., Robinson, R., and Webb, T.: The 1968 May 23 Inangahua, New Zealand, earthquake: An integrated geological, geodetic, and seismological source model, New Zealand Journal of Geology and Geophysics, 37, 59–86, doi: 10.1080/00288306.1994.9514601, 1994.

Antonini, G., Ardizzone, F., Cardinali, M., Galli, M., Guzzetti, F., and Reichenbach, P.: Surface deposits and landslide inventory map of the area affected by the 1997 Umbria-Marche earthquakes, Bollettino della Societa geologica italiana, 121, 843–853, 2002.

Avouac, J.-P.: 6.09 - Dynamic Processes in Extensional and Compressional Settings - Mountain Building: From Earthquakes to Geological Deformation, in: Treatise on Geophysics, edited by Schubert, E.-i.-C. G., pp. 377 – 439, Elsevier, Amsterdam, 2007.

Avouac, J.-P.: From Geodetic Imaging of Seismic and Aseismic Fault Slip to Dynamic Modeling of the Seismic Cycle, Annual Review of Earth and Planetary Sciences, 43, 233–271, doi: 10.1146/annurev-earth-060614-105302, 2015.

Avouac, J.-P., Meng, L., Wei, S., Wang, T., and Ampuero, J.-P.: Lower edge of locked Main Himalayan Thrust unzipped by the 2015 Gorkha earthquake, Nature Geoscience, advance online publication, doi: 10.1038/ngeo2518, 2015.

Baltay, A., Ide, S., Prieto, G., and Beroza, G.: Variability in earthquake stress drop and apparent stress, Geophysical Research Letters, 38, L06 303, doi: 10.1029/2011GL046698, 2011.

Baltay, A. S. and Hanks, T. C.: Understanding the Magnitude Dependence of PGA and PGV in NGA West 2 Data, Bulletin of the Seismological Society of America, 104, 2851–2865, doi: 10.1785/0120130283, 2014.

Barbot, S., Hamiel, Y., and Fialko, Y.: Space geodetic investigation of the coseismic and postseismic deformation due to the 2003 Mw7.2 Altai earthquake: Implications for the local lithospheric rheology, Journal of Geophysical Research: Solid Earth, 113, n/a–n/a, doi: 10.1029/2007JB005063, 2008.

Barlow, J., Barisin, I., Rosser, N., Petley, D., Densmore, A., and Wright, T.: Seismically-induced mass movements and volumetric fluxes resulting from the 2010 Mw = 7.2 earthquake in the Sierra Cucapah, Mexico, Geomorphology, doi: 10.1016/j.geomorph.2014.11.012, 2015.

Barnes, J. B., Ehlers, T. A., Insel, N., McQuarrie, N., and Poulsen, C. J.: Linking orography, climate, and exhumation across the central Andes, Geology, 40, 1135–1138, doi: 10.1130/G33229.1, 2012.

Baum, R. L., Godt, J. W., and Savage, W. Z.: Estimating the timing and location of shallow rainfall-induced landslides using a model for transient, unsaturated infiltration, Journal of Geophysical Research: Earth Surface, 115, F03 013, doi: 10.1029/2009JF001321, 2010.

Behling, R., Roessner, S., Kaufmann, H., and Kleinschmit, B.: Automated Spatiotemporal Landslide Mapping over Large Areas Using RapidEye Time Series Data, Remote Sensing, 6, 8026–8055, doi: 10.3390/rs6098026, 2014.

Bennett, P. C., Hiebert, F. K., and Choi, W. J.: Microbial colonization and weathering of silicates in a petroleum-contaminated groundwater, Chemical Geology, 132, 45–53, doi: 10.1016/S0009-2541(96)00040-X, 1996.

Berryman, K. and Villamor, P.: Surface rupture of the Poulter Fault in the 1929 March 9 ArthurPass earthquake, and redefinition of the Kakapo Fault, New Zealand, New Zealand Journal of Geology and Geophysics, 47, 341–351, doi: 10.1080/00288306.2004.9515060, 2004.

Berryman, K. R., Cochran, U. A., Clark, K. J., Biasi, G. P., Langridge, R. M., and Villamor, P.: Major Earthquakes Occur Regularly on an Isolated Plate Boundary Fault, Science, 336, 1690–1693, doi: 10.1126/science.1218959, 2012.

Bird, J. F. and Bommer, J. J.: Earthquake losses due to ground failure, Engineering Geology, 75, 147–179, doi: 10.1016/j.enggeo.2004.05.006, 2004.

Blöthe, J. H. and Korup, O.: Millennial lag times in the Himalayan sediment routing system, Earth and Planetary Science Letters, 382, 38–46, doi: 10.1016/j.epsl.2013.08.044, 2013.

Bollinger, L., Perrier, F., Avouac, J.-P., Sapkota, S., Gautam, U., and Tiwari, D. R.: Seasonal modulation of seismicity in the Himalaya of Nepal, Geophysical Research Letters, 34, L08 304, doi: 10.1029/2006GL029192, 2007.

Bollinger, L., Sapkota, S. N., Tapponnier, P., Klinger, Y., Rizza, M., Van der Woerd, J., Tiwari, D. R., Pandey, R., Bitri, A., and Bes de Berc, S.: Estimating the return times of great Himalayan earthquakes in eastern Nepal: Evidence from the Patu and Bardibas strands of the Main Frontal Thrust, Journal of Geophysical Research: Solid Earth, 119, 2014JB010 970, doi: 10.1002/2014JB010970, 2014.

Bonilla, M. G.: Landslides in the San Francisco South quadrangle, California, Tech. Rep. OFR - 60-15, United States Geological Survey, 1960.

Boore, D. M. and Atkinson, G. M.: Ground-Motion Prediction Equations for the Average Horizontal Component of PGA, PGV, and 5% -Damped PSA at Spectral Periods between 0.01s and 10âĂL's, Earthquake Spectra, 24, 99–138, doi: 10.1193/1.2830434, 2008.

Bouchon, M.: Effect of topography on surface motion, Bulletin of the Seismological Society of America, 63, 615–632, 1973.

Brady, P. V.: The effect of silicate weathering on global temperature and atmospheric CO2, Journal of Geophysical Research: Solid Earth, 96, 18 101–18 106, doi: 10.1029/91JB01898, 1991.

Brantut, N.: Time-dependent recovery of microcrack damage and seismic wave speeds in deformed limestone, Journal of Geophysical Research: Solid Earth, p. 2015JB012324, doi: 10.1002/2015JB012324, 2015.

Brardinoni, F. and Church, M.: Representing the landslide magnitudeâĂŞfrequency relation: Capilano River basin, British Columbia, Earth Surface Processes and Landforms, 29, 115–124, doi: 10.1002/esp.1029, 2004.

Braun, J.: The many surface expressions of mantle dynamics, Nature Geoscience, 3, 825–833, doi: 10.1038/ngeo1020, 2010.

Brenguier, F., Campillo, M., Hadziioannou, C., Shapiro, N. M., Nadeau, R. M., and Larose, E.: Postseismic Relaxation Along the San Andreas Fault at Parkfield from Continuous Seismological Observations, Science, 321, 1478–1481, doi: 10.1126/science.1160943, 2008.

Brune, J. N.: Tectonic stress and the spectra of seismic shear waves from earthquakes, Journal of Geophysical Research, 75, 4997–5009, doi: 10.1029/JB075i026p04997, 1970.

Brunetti, M. T., Guzzetti, F., and Rossi, M.: Probability distributions of landslide volumes, Nonlin. Processes Geophys., 16, 179–188, doi: 10.5194/npg-16-179-2009, 2009.

Burbank, D. W., Leland, J., Fielding, E., Anderson, R. S., Brozovic, N., Reid, M. R., and Duncan, C.: Bedrock incision, rock uplift and threshold hillslopes in the northwestern Himalayas, Nature, 379, 505–510, doi: 10.1038/379505a0, 1996.

Burtin, A., Hovius, N., McArdell, B. W., Turowski, J. M., and Vergne, J.: Seismic constraints on dynamic links between geomorphic processes and routing of sediment in a steep mountain catchment, Earth Surface Dynamics, 2, 21–33, doi: 10.5194/esurf-2-21-2014, 2014.

Champagnac, J.-D., Molnar, P., Sue, C., and Herman, F.: Tectonics, climate, and mountain topography, Journal of Geophysical Research: Solid Earth, 117, n/a–n/a, doi: 10.1029/2011JB008348, 2012.

Cheloni, D., DÁgostino, N., DÁnastasio, E., and Selvaggi, G.: Reassessment of the source of the 1976 Friuli, NE Italy, earthquake sequence from the joint inversion of high-precision levelling and triangulation data, Geophysical Journal International, 190, 1279–1294, doi: 10.1111/j.1365-246X.2012.05561.x, 2012.

Chien, F.-C. and Kuo, H.-C.: On the extreme rainfall of Typhoon Morakot (2009), Journal of Geophysical Research: Atmospheres, 116, D05 104, doi: 10.1029/2010JD015092, 2011.

Ching, K.-E., Hsieh, M.-L., Johnson, K. M., Chen, K.-H., Rau, R.-J., and Yang, M.: Modern vertical deformation rates and mountain building in Taiwan from precise leveling and continuous GPS observations, 2000-2008, Journal of Geophysical Research: Solid Earth, 116, n/a–n/a, doi: 10.1029/2011JB008242, 2011.

Cirella, A., Piatanesi, A., Cocco, M., Tinti, E., Scognamiglio, L., Michelini, A., Lomax, A., and Boschi, E.: Rupture history of the 2009 L'Aquila (Italy) earthquake from nonlinear joint inversion of strong motion and GPS data, Geophysical Research Letters, 36, L19 304, doi: 10.1029/2009GL039795, 2009.

Clarke, B. A. and Burbank, D. W.: Bedrock fracturing, threshold hillslopes, and limits to the magnitude of bedrock landslides, Earth and Planetary Science Letters, 297, 577–586, 2010.

Clarke, B. A. and Burbank, D. W.: Quantifying bedrock-fracture patterns within the shallow subsurface: Implications for rock mass strength, bedrock landslides, and erodibility, Journal of Geophysical Research: Earth Surface, 116, F04 009, doi: 10.1029/2011JF001987, 2011.

Clough, R. and Chopra, A.: Earthquake stress analysis in earth dams, ASCE Journal of the Engineering Mechanics Division, 92, 197–211, 1966.

Collins, B. D. and Jibson, R. W.: Assessment of existing and potential landslide hazards resulting from the April 25, 2015 Gorkha, Nepal earthquake sequence, USGS Numbered Series 2015-1142, U.S. Geological Survey, Reston, VA, 2015.

Dadson, S. J., Hovius, N., Chen, H., Dade, W. B., Hsieh, M.-L., Willett, S. D., Hu, J.-C., Horng, M.-J., Chen, M.-C., Stark, C. P., Lague, D., and Lin, J.-C.: Links between erosion, runoff variability and seismicity in the Taiwan orogen, Nature, 426, 648–651, doi: 10.1038/nature02150, 2003.

Dadson, S. J., Hovius, N., Chen, H., Dade, W. B., Lin, J.-C., Hsu, M.-L., Lin, C.-W., Horng, M.-J., Chen, T.-C., Milliman, J., and Stark, C. P.: Earthquake-triggered increase in sediment delivery from an active mountain belt, Geology, 32, 733–736, doi: 10.1130/G20639.1, 2004.

Dai, F. C., Xu, C., Yao, X., Xu, L., Tu, X. B., and Gong, Q. M.: Spatial distribution of landslides triggered by the 2008 Ms 8.0 Wenchuan earthquake, China, Journal of Asian Earth Sciences, 40, 883–895, doi: 10.1016/j.jseaes.2010.04.010, 2011.

Darby, D. J. and Beanland, S.: Possible source models for the 1855 Wairarapa Earthquake, New Zealand, Journal of Geophysical Research: Solid Earth, 97, 12 375–12 389, doi: 10.1029/92JB00567, 1992.

Davis, L. L. and West, L. R.: Observed effects of topography on ground motion, Bulletin of the Seismological Society of America, 63, 283–298, 1973.

Davy, P., Le Goc, R., Darcel, C., Bour, O., de Dreuzy, J. R., and Munier, R.: A likely universal model of fracture scaling and its consequence for crustal hydromechanics, Journal of Geophysical Research: Solid Earth, 115, B10 411, doi: 10.1029/2009JB007043, 2010.

Davy, P., Le Goc, R., and Darcel, C.: A model of fracture nucleation, growth and arrest, and consequences for fracture density and scaling, Journal of Geophysical Research: Solid Earth, 118, 1393–1407, doi: 10.1002/jgrb.50120, 2013.

Delorey, A. A., Chao, K., Obara, K., and Johnson, P. A.: Cascading elastic perturbation in Japan due to the 2012 Mw 8.6 Indian Ocean earthquake, Science Advances, 1, e1500 468, doi: 10.1126/sciadv.1500468, 2015.

Densmore, A. L., Ellis, M. A., and Anderson, R. S.: Landsliding and the evolution of normal-fault-bounded mountains, Journal of Geophysical Research: Solid Earth, 103, 15 203–15 219, doi: 10.1029/98JB00510, 1998.

Densmore, A. L., Parker, R. N., Rosser, N. J., de Michele, M., Yong, L., Runqiu, H., Whadcoat, S., and Petley, D. N.: Reply to 'Isostasy can't be ignored', Nature Geoscience, 5, 83–84, doi: 10.1038/ngeo1385, 2012.

DiBiase, R. A., Heimsath, A. M., and Whipple, K. X.: Hillslope response to tectonic forcing in threshold landscapes, Earth Surface Processes and Landforms, 37, 855–865, doi: 10.1002/esp.3205, 2012.

Doser, D. I., Webb, T. H., and Maunder, D. E.: Source parameters of large historical (1918âĂŞ962) earthquakes, South Island, New Zealand, Geophysical Journal International, 139, 769–794, doi: 10.1046/j.1365-246x.1999.00986.x, 1999.

Dreyfus, D., Rathje, E. M., and Jibson, R. W.: The influence of different simplified sliding-block models and input parameters on regional predictions of seismic landslides triggered by the Northridge earthquake, Engineering Geology, 163, 41–54, doi: 10.1016/j.enggeo.2013.05.015, 2013.

Eckhardt, K.: How to construct recursive digital filters for baseflow separation, Hydrological Processes, 19, 507–515, doi: 10.1002/hyp.5675, 2005.

Egholm, D. L., Nielsen, S. B., Pedersen, V. K., and Lesemann, J.-E.: Glacial effects limiting mountain height, Nature, 460, 884–887, doi: 10.1038/nature08263, 2009.

Elliott, J. L., Freymueller, J. T., and Rabus, B.: Coseismic deformation of the 2002 Denali fault earthquake: Contributions from synthetic aperture radar range offsets, Journal of Geophysical Research: Solid Earth, 112, B06 421, doi: 10.1029/2006JB004428, 2007.

Emberson, R., Hovius, N., Galy, A., and Marc, O.: Chemical weathering in active mountain belts controlled by stochastic bedrock landsliding, Nature Geoscience, 9, 42–45, doi: 10.1038/ngeo2600, 2015.

Evans, S. G., Roberts, N. J., Ischuk, A., Delaney, K. B., Morozova, G. S., and Tutubalina, O.: Landslides triggered by the 1949 Khait earthquake, Tajikistan, and associated loss of life, Engineering Geology, 109, 195–212, doi: 10.1016/j.enggeo.2009.08.007, 2009.

Fagnano, G.: Produzioni matematiche del conte Giulio Carlo di Fagnano, 1750.

Fielding, E. J., Sladen, A., Li, Z., Avouac, J.-P., BÃijrgmann, R., and Ryder, I.: Kinematic fault slip evolution source models of the 2008 M7.9 Wenchuan earthquake in China from SAR interferometry, GPS and teleseismic analysis and implications for Longmen Shan tectonics, Geophysical Journal International, p. ggt155, doi: 10.1093/gji/ggt155, 2013.

France-Lanord, C. and Derry, L. A.: Organic carbon burial forcing of the carbon cycle from Himalayan erosion, Nature, 390, 65–67, doi: 10.1038/36324, 1997.

Frankel, A.: Rupture Process of the M 7.9 Denali Fault, Alaska, Earthquake: Subevents, Directivity, and Scaling of High-Frequency Ground Motions, Bulletin of the Seismological Society of America, 94, S234–S255, doi: 10.1785/0120040612, 2004.

Frattini, P. and Crosta, G. B.: The role of material properties and landscape morphology on landslide size distributions, Earth and Planetary Science Letters, 361, 310–319, doi: 10.1016/j.epsl.2012.10.029, 2013.

Gallen, S. F., Clark, M. K., and Godt, J. W.: Coseismic landslides reveal near-surface rock strength in a high-relief, tectonically active setting, Geology, 43, 11–14, doi: 10.1130/G36080.1, 2015.

Gallo, F. and Lavé, J.: Evolution of a large landslide in the High Himalaya of central Nepal during the last half-century, Geomorphology, 223, 20–32, doi: 10.1016/j.geomorph.2014.06.021, 2014.

Garwood, N. C., Janos, D. P., and Brokaw, N.: Earthquake-Caused Landslides: A Major Disturbance to Tropical Forests, Science, 205, 997–999, doi: 10.1126/science.205.4410.997, 1979.

Gassenmeier, M., Sens-SchÃűnfelder, C., Eulenfeld, T., Bartsch, M., Victor, P., Tilmann, F., and Korn, M.: Field observations of seismic velocity changes caused by shaking-induced damage and healing due to mesoscopic nonlinearity, Geophysical Journal International, 204, 1490–1502, doi: 10.1093/gji/ggv529, 2016.

Given, J. W., Wallace, T. C., and Kanamori, H.: Teleseismic analysis of the 1980 Mammoth Lakes earthquake sequence, Bulletin of the Seismological Society of America, 72, 1093–1109, 1982.

Goes, S. D. B., Velasco, A. A., Schwartz, S. Y., and Lay, T.: The April 22, 1991, Valle de la Estrella, Costa Rica (Mw = 7.7) earthquake and its tectonic implications: A broadband seismic study, Journal of Geophysical Research: Solid Earth, 98, 8127–8142, doi: 10.1029/93JB00019, 1993.

Gorsevski, P. V., Gessler, P. E., Boll, J., Elliot, W. J., and Foltz, R. B.: Spatially and temporally distributed modeling of landslide susceptibility, Geomorphology, 80, 178–198, doi: 10.1016/j.geomorph.2006.02.011, 2006.

Gorum, T., Fan, X., van Westen, C. J., Huang, R. Q., Xu, Q., Tang, C., and Wang, G.: Distribution pattern of earthquake-induced landslides triggered by the 12 May 2008 Wenchuan earthquake, Geomorphology, 133, 152–167, 2011.

Gorum, T., van Westen, C. J., Korup, O., van der Meijde, M., Fan, X., and van der Meer, F. D.: Complex rupture mechanism and topography control symmetry of mass-wasting pattern, 2010 Haiti earthquake, Geomorphology, 184, 127–138, doi: 10.1016/j.geomorph.2012.11.027, 2013.

Gorum, T., Korup, O., van Westen, C. J., van der Meijde, M., Xu, C., and van der Meer, F. D.: Why so few? Landslides triggered by the 2002 Denali earthquake, Alaska, Quaternary Science Reviews, 95, 80–94, doi: 10.1016/j.quascirev.2014.04.032, 2014.

Govi, M. and Sorzana, P. F.: Effetti geologici del terremoto: Frane., Rivista italiana di paleontologia e stratigrafia, 83, 329–368, 1977.

Grandin, R., Doin, M.-P., Bollinger, L., Pinel-PuyssÃľgur, B., Ducret, G., Jolivet, R., and Sapkota, S. N.: Long-term growth of the Himalaya inferred from interseismic InSAR measurement, Geology, p. G33154.1, doi: 10.1130/G33154.1, 2012.

Granger, D. E., Kirchner, J. W., and Finkel, R.: Spatially Averaged Long Term Erosion Rates Measured from in Situ Produced Cosmogenic Nuclides in Alluvial Sediment, The Journal of Geology, 104, 249–257, 1996.

Gratier, J. P., Renard, F., and Vial, B.: Postseismic pressure solution creep: Evidence and time-dependent change from dynamic indenting experiments, Journal of Geophysical Research: Solid Earth, 119, 2013JB010 768, doi: 10.1002/2013JB010768, 2014.

Gutenberg, B. and Richter, C.: Seismicity of the earth and associated phenomena,, Princeton University Press, Princeton, N.J., 1954.

Guzzetti, F., Ardizzone, F., Cardinali, M., Rossi, M., and Valigi, D.: Landslide volumes and landslide mobilization rates in Umbria, central Italy, Earth and Planetary Science Letters, 279, 222–229, 2009a.

Guzzetti, F., Esposito, E., Balducci, V., Porfido, S., Cardinali, M., Violante, C., Fiorucci, F., Sacchi, M., Ardizzone, F., Mondini, A. C., Reichenbach, P., and Rossi, M.: Central Italy seismic sequences-induced landsliding: 1997-1998 Umbria-Marche and 2008-2009 LâĂŹAquila cases., in: Proceedings of the conference "The Next Generation

of Research on Earthquake-induced Landslides: International Conference in Commemoration of 10th Anniversary of the Chi-Chi Earthquake, Taiwan", pp. 52–61, 2009b.

Guzzetti, F., Mondini, A. C., Cardinali, M., Fiorucci, F., Santangelo, M., and Chang, K.-T.: Landslide inventory maps: New tools for an old problem, Earth-Science Reviews, 112, 42–66, doi: 10.1016/j.earscirev.2012.02.001, 2012.

Hampel, A., Hetzel, R., and Densmore, A. L.: Postglacial slip-rate increase on the Teton normal fault, northern Basin and Range Province, caused by melting of the Yellowstone ice cap and deglaciation of the Teton Range?, Geology, 35, 1107–1110, doi: 10.1130/G24093A.1, 2007.

Hamzehloo, H.: Strong ground motion modelling of causative fault for the 2002 Avaj earthquake, Iran, Tectonophysics, 409, 159–174, doi: 10.1016/j.tecto.2005.08.016, 2005.

Hancox, G., Perrin, G., and Dellow, G.: Earthquake-induced landsliding in New Zealand and implications for MM intensity and seismic hazard assessment, GNS Client Report 43601B, 1997.

Hancox, G., Cox, S., Turnbull, I., and Crozier, M.: Reconnaissance studies of landslides and other ground damage caused by the M_W 7.2 Fiordland earthquake of 22 August 2003., Institute of Geological & Nuclear Sciences report 2003/30, 2003.

Hancox, G. T., Dellow, G., Mc Saveney, M., Scott, B., and Villamor, P.: Reconnaissance Studies of Landslides Caused by the M_L 5.4 Lake Rotoehu earthquake and Swarm of July 2004, Institute of Geological & Nuclear Sciences report 2004/24, 2004.

Hanks, T. C. and Kanamori, H.: A moment magnitude scale, Journal of Geophysical Research: Solid Earth, 84, 2348–2350, doi: 10.1029/JB084iB05p02348, 1979.

Hanks, T. C. and McGuire, R. K.: The character of high-frequency strong ground motion, Bulletin of the Seismological Society of America, 71, 2071–2095, 1981.

Harp, E. and Jibson, R.: Landslides triggered by the 1994 Northridge, California, earthquake, Bulletin of the Seismological Society of America, 86, S319–S332, 1996.

Harp, E. L. and Jibson, R. W.: Anomalous Concentrations of Seismically Triggered Rock Falls in Pacoima Canyon: Are They Caused by Highly Susceptible Slopes or Local Amplification of Seismic Shaking?, Bulletin of the Seismological Society of America, 92, 3180–3189, doi: 10.1785/0120010171, 2002.

Harp, E. L., Wilson, R. C., and Wieczorek, G. F.: Landslides from the February 4, 1976, Guatemala earthquake, U.S.G.S., Prof. Pap., 1204 A, 1981.

Harp, E. L., Tanaka, K., Sarmiento, J., and Keefer, D.: Landslides from the May 25-27, 1980, Mammoth Lakes, California, earthquake sequence, US Geological Survey, 1984.

Harp, E. L., Hartzell, S. H., Jibson, R. W., Ramirez-Guzman, L., and Schmitt, R. G.: Relation of Landslides Triggered by the Kiholo Bay Earthquake to Modeled Ground Motion, Bulletin of the Seismological Society of America, 104, 2529–2540, doi: 10.1785/0120140047, 2014.

Hartshorn, K., Hovius, N., Dade, W. B., and Slingerland, R. L.: Climate-Driven Bedrock Incision in an Active Mountain Belt, Science, 297, 2036–2038, doi: 10.1126/science.1075078, 2002.

Has, B., Noro, T., Maruyama, K., Nakamura, A., Ogawa, K., and Onoda, S.: Characteristics of earthquake-induced landslides in a heavy snowfall region-landslides triggered by the northern Nagano prefecture earthquake, March 12, 2011, Japan, Landslides, 9, 539–546, doi: 10.1007/s10346-012-0344-6, 2012.

Hashimoto, M., Fukushima, Y., and Fukahata, Y.: Fan-delta uplift and mountain subsidence during the Haiti 2010 earthquake, Nature Geoscience, 4, 255–259, doi: 10.1038/ngeo1115, 2011.

Herman, F., Seward, D., Valla, P. G., Carter, A., Kohn, B., Willett, S. D., and Ehlers, T. A.: Worldwide acceleration of mountain erosion under a cooling climate, Nature, 504, 423–426, doi: 10.1038/nature12877, 2013.

Hernandez, B., Cocco, M., Cotton, F., Stramondo, S., Scotti, O., Courboulex, F., and Campillo, M.: Rupture history of the 1997 Umbria-Marche (Central Italy) main shocks from the inversion of GPS, DInSAR and near field strong motion data, Annals of Geophysics, 47, doi: 10.4401/ag-3349, 2004.

Hikima, K. and Koketsu, K.: Rupture processes of the 2004 Chuetsu (mid-Niigata prefecture) earthquake, Japan: A series of events in a complex fault system, Geophysical Research Letters, 32, doi: 10.1029/2005GL023588, 2005.

Hillers, G., Campillo, M., and Ma, K. F.: Seismic velocity variations at TCDP are controlled by MJO driven precipitation pattern and high fluid discharge properties, Earth and Planetary Science Letters, 391, 121–127, doi: 10.1016/j.epsl.2014.01.040, 2014.

Hilton, R. G., Galy, A., Hovius, N., Chen, M.-C., Horng, M.-J., and Chen, H.: Tropical-cyclone-driven erosion of the terrestrial biosphere from mountains, Nature Geoscience, 1, 759–762, doi: 10.1038/ngeo333, 2008.

Hilton, R. G., Galy, A., Hovius, N., Horng, M.-J., and Chen, H.: Efficient transport of fossil organic carbon to the ocean by steep mountain rivers: An orogenic carbon sequestration mechanism, Geology, 39, 71–74, doi: 10.1130/G31352.1, 2011a.

Hilton, R. G., Meunier, P., Hovius, N., Bellingham, P. J., and Galy, A.: Landslide impact on organic carbon cycling in a temperate montane forest, Earth Surface Processes and Landforms, 36, 1670–1679, doi: 10.1002/esp.2191, 2011b.

Hobiger, M., Wegler, U., Shiomi, K., and Nakahara, H.: Single-station cross-correlation analysis of ambient seismic noise: application to stations in the surroundings of the 2008 Iwate-Miyagi Nairiku earthquake, Geophysical Journal International, 198, 90–109, doi: 10.1093/gji/ggu115, 2014.

Hoek, E. and Brown, E.: Practical estimates of rock mass strength, International Journal of Rock Mechanics and Mining Sciences, 34, 1165–1186, 1997.

Hoek, E. and Brown, E. T.: Empirical strength criterion for rock masses, Journal of Geotechnical and Geoenvironmental Engineering, 106, 1013–1035, 1980.

Hovius, N. and Meunier, P.: Earthquake ground motion and patterns of seismically induced landsliding, in: Landslides, Cambridge University Press, 2012.

Hovius, N., Stark, C. P., and Allen, P. A.: Sediment flux from a mountain belt derived by landslide mapping, Geology, 25, 231–234, doi: 10.1130/0091-7613(1997)025$<$0231:SFFAMB$>$2.3.CO;2, 1997.

Hovius, N., Stark, C. P., Tutton, M. A., and Abbott, L. D.: Landslide-driven drainage network evolution in a pre-steady-state mountain belt: Finisterre Mountains, Papua New Guinea, Geology, 26, 1071–1074, doi: 10.1130/0091-7613(1998)026$<$1071:LDDNEI$>$2.3.CO;2, 1998.

Hovius, N., Stark, C. P., Hao-Tsu, C., and Jiun-Chuan, L.: Supply and Removal of Sediment in a Landslide Dominated Mountain Belt: Central Range, Taiwan, The Journal of Geology, 108, 73–89, doi: 10.1086/jg.2000.108.issue-1, 2000.

Hovius, N., Meunier, P., Lin, C., Chen, H., Chen, Y., Dadson, S., Horng, M., and Lines, M.: Prolonged seismically induced erosion and the mass balance of a large earthquake, Earth and Planetary Science Letters, 304, 347–355, doi: 10.1016/j.epsl.2011.02.005, 2011.

Howarth, J. D., Fitzsimons, S. J., Norris, R. J., and Jacobsen, G. E.: Lake sediments record cycles of sediment flux driven by large earthquakes on the Alpine fault, New Zealand, Geology, 40, 1091–1094, doi: 10.1130/G33486.1, 2012.

Hsu, Y.-J., Segall, P., Yu, S.-B., Kuo, L.-C., and Williams, C. A.: Temporal and spatial variations of post-seismic deformation following the 1999 Chi-Chi, Taiwan earthquake, Geophysical Journal International, 169, 367–379, doi: 10.1111/j.1365-246X.2006.03310.x, 2007.

Huang, M. Y.-F. and Montgomery, D. R.: Altered regional sediment transport regime after a large typhoon, southern Taiwan, Geology, 41, 1223–1226, doi: 10.1130/G34826.1, 2013.

Huang, R. and Li, W.: Post-earthquake landsliding and long-term impacts in the Wenchuan earthquake area, China, Engineering Geology, 182, Part B, 111–120, doi: 10.1016/j.enggeo.2014.07.008, 2014.

Insel, N., Poulsen, C. J., and Ehlers, T. A.: Influence of the Andes Mountains on South American moisture transport, convection, and precipitation, Climate Dynamics, 35, 1477–1492, doi: 10.1007/s00382-009-0637-1, 2009.

Iverson, R. M.: Landslide triggering by rain infiltration, Water Resources Research, 36, 1897–1910, doi: 10.1029/2000WR900090, 2000.

Iverson, R. M., George, D. L., Allstadt, K., Reid, M. E., Collins, B. D., Vallance, J. W., Schilling, S. P., Godt, J. W., Cannon, C. M., Magirl, C. S., Baum, R. L., Coe, J. A., Schulz, W. H., and Bower, J. B.: Landslide mobility and hazards: implications of the 2014 Oso disaster, Earth and Planetary Science Letters, 412, 197–208, doi: 10.1016/j.epsl.2014.12.020, 2015.

Januzakov, K., Omuraliev, M., Omuralieva, A., Ilyasov, B., and Grebennikova, V.: Strong earthquakes of the Tien Shan (within the Kyrgyzstan territory and adjacent regions of the countries of Central Asia)., Ilim, Bishkek, 2003.

Jibson, R. and Harp, E.: Large rock avalanches triggered by the M 7.9 Denali Fault, Alaska, earthquake of 3 November 2002, Engineering Geology, 83, 144–160, doi: 10.1016/j.enggeo.2005.06.029, 2006.

Jibson, R. W.: Methods for assessing the stability of slopes during earthquakesâĂŤA retrospective, Engineering Geology, 122, 43–50, doi: 10.1016/j.enggeo.2010.09.017, 2011.

Jibson, R. W., Prentice, C. S., Borissoff, B. A., Rogozhin, E. A., and Langer, C. J.: Some observations of landslides triggered by the 29 April 1991 Racha earthquake, Republic of Georgia, Bulletin of the Seismological Society of America, 84, 963–973, 1994.

Jin, Z., West, A. J., Zhang, F., An, Z., Hilton, R. G., Yu, J., Wang, J., Li, G., Deng, L., and Wang, X.: Seismically enhanced solute fluxes in the Yangtze River headwaters following the A.D. 2008 Wenchuan earthquake, Geology, 44, 47–50, doi: 10.1130/G37246.1, 2015.

Jordan, T. and Watts, A.: Gravity anomalies, flexure and the elastic thickness structure of the IndiaâĂŞEurasia collisional system, Earth and Planetary Science Letters, 236, 732–750, doi: 10.1016/j.epsl.2005.05.036, 2005.

Kaproth, B. M. and Marone, C.: Evolution of elastic wave speed during shear-induced damage and healing within laboratory fault zones, Journal of Geophysical Research: Solid Earth, 119, 2014JB011 051, doi: 10.1002/2014JB011051, 2014.

Kargel, J. S., Leonard, G. J., Shugar, D. H., Haritashya, U. K., Bevington, A., Fielding, E. J., Fujita, K., Geertsema, M., Miles, E. S., Steiner, J., Anderson, E., Bajracharya, S., Bawden, G. W., Breashears, D. F., Byers, A., Collins, B., Dhital, M. R., Donnellan, A., Evans, T. L., Geai, M. L., Glasscoe, M. T., Green, D., Gurung, D. R., Heijenk, R., Hilborn, A., Hudnut, K., Huyck, C., Immerzeel, W. W., Liming, J., Jibson, R., Kaab, A., Khanal, N. R., Kirschbaum, D., Kraaijenbrink, P. D. A., Lamsal, D., Shiyin, L., Mingyang, L., McKinney, D., Nahirnick, N. K., Zhuotong, N., Ojha, S., Olsenholler, J., Painter, T. H., Pleasants, M., Kc, P., Yuan, Q. I., Raup, B. H., Regmi, D., Rounce, D. R., Sakai, A., Donghui, S., Shea, J. M., Shrestha, A. B., Shukla, A., Stumm, D., Kooij, M. v. d., Voss, K., Xin, W., Weihs, B., Wolfe, D., Lizong, W., Xiaojun, Y., Yoder, M. R., and Young, N.: Geomorphic and geologic controls of geohazards induced by Nepal's 2015 Gorkha earthquake, Science, p. aac8353, doi: 10.1126/science.aac8353, 2015.

Katz, O. and Aharonov, E.: Landslides in vibrating sand box: What controls types of slope failure and frequency magnitude relations?, Earth and Planetary Science Letters, 247, 280–294, doi: 10.1016/j.epsl.2006.05.009, 2006.

Kawakatsu, H. and Cadena, G. P.: Focal Mechanisms of the March 6, 1987 Ecuador Earthquakes, Journal of Physics of the Earth, 39, 589–597, 1991.

Keefer, D. K.: Landslides caused by earthquakes, Geological Society of America Bulletin, 95, 406–421, doi: 10.1130/0016-7606(1984)95$<$406:LCBE$>$2.0.CO;2, 1984.

Keefer, D. K.: The importance of earthquake-induced landslides to long-term slope erosion and slope-failure hazards in seismically active regions, Geomorphology, 10, 265–284, doi: 10.1016/0169-555X(94)90021-3, 1994.

Keefer, D. K.: Investigating Landslides Caused by Earthquakes âĂŞ A Historical Review, Surveys in Geophysics, 23, 473–510, doi: 10.1023/A:1021274710840, 2002.

Keefer, D. K. and Manson, M. W.: Regional distribution and characteristics of landslides generated by the earthquake, USGS Professional Paper 1551-C, Geological Survey (U.S.), 1998.

Kempton, J. J. and Stewart, J. P.: Prediction Equations for Significant Duration of Earthquake Ground Motions ConsideringâĂL'site andâĂL'near-sourceâĂL'effects, Earthquake Spectra, 22, 985–1013, doi: 10.1193/1.2358175, 2006.

Khazai, B. and Sitar, N.: Evaluation of factors controlling earthquake-induced landslides caused by Chi-Chi earthquake and comparison with the Northridge and Loma Prieta events, Engineering Geology, 71, 79–95, doi: 10.1016/S0013-7952(03)00127-3, 2004.

Kikuchi, M. and Kanamori, H.: Inversion of complex body wavesâĂŤIII, Bulletin of the Seismological Society of America, 81, 2335–2350, 1991.

King, G. C. P., Stein, R. S., and Rundle, J. B.: The Growth of Geological Structures by Repeated Earthquakes 1. Conceptual Framework, Journal of Geophysical Research: Solid Earth, 93, 13 307–13 318, doi: 10.1029/JB093iB11p13307, 1988.

Kober, F., Zeilinger, G., Hippe, K., Marc, O., Lendzioch, T., Grischott, R., Christl, M., Kubik, P. W., and Zola, R.: Tectonic and lithological controls on denudation rates in the central Bolivian Andes, Tectonophysics, 657, 230–244, doi: 10.1016/j.tecto.2015.06.037, 2015.

Koi, T., Hotta, N., Ishigaki, I., Matuzaki, N., Uchiyama, Y., and Suzuki, M.: Prolonged impact of earthquake-induced landslides on sediment yield in a mountain watershed: The Tanzawa region, Japan, Geomorphology, 101, 692–702, doi: 10.1016/j.geomorph.2008.03.007, 2008.

Korup, O.: Rock type leaves topographic signature in landslide-dominated mountain ranges, Geophysical Research Letters, 35, n/a–n/a, doi: 10.1029/2008GL034157, 2008.

Korup, O. and Schlunegger, F.: Rock-type control on erosion-induced uplift, eastern Swiss Alps, Earth and Planetary Science Letters, 278, 278–285, doi: 10.1016/j.epsl.2008.12.012, 2009.

Korup, O., Clague, J. J., Hermanns, R. L., Hewitt, K., Strom, A. L., and Weidinger, J. T.: Giant landslides, topography, and erosion, Earth and Planetary Science Letters, 261, 578–589, doi: 10.1016/j.epsl.2007.07.025, 2007.

Korup, O., Densmore, A. L., and Schlunegger, F.: The role of landslides in mountain range evolution, Geomorphology, 120, 77–90, doi: 10.1016/j.geomorph.2009.09.017, 2010.

Lacroix, P., Zavala, B., Berthier, E., and Audin, L.: Supervised method of landslide inventory using panchromatic SPOT5 images and application to the earthquake-triggered landslides of Pisco (Peru, 2007, Mw8.0), Remote Sensing, 5, 2590–2616, doi: 10.3390/rs5062590, 2013.

Lague, D.: Reduction of long-term bedrock incision efficiency by short-term alluvial cover intermittency, Journal of Geophysical Research: Earth Surface, 115, F02 011, doi: 10.1029/2008JF001210, 2010.

Larsen, I., Montgomery, D., and Korup, O.: Landslide erosion controlled by hillslope material, Nature Geoscience, 3, 247–251, 2010.

Larsen, I. J. and Montgomery, D. R.: Landslide erosion coupled to tectonics and river incision, Nature Geoscience, 5, 468–473, doi: 10.1038/ngeo1479, 2012.

Lawrence, Z., Bodin, P., and Langston, C. A.: In Situ Measurements of Nonlinear and Nonequilibrium Dynamics in Shallow, Unconsolidated Sediments, Bulletin of the Seismological Society of America, 99, 1650–1670, doi: 10.1785/0120080177, 2009.

Lee, S. T., Yu, T. T., Peng, W. F., and Wang, C. L.: Incorporating the effects of topographic amplification in the analysis of earthquake-induced landslide hazards using logistic regression, Nat. Hazards Earth Syst. Sci., 10, 2475–2488, doi: 10.5194/nhess-10-2475-2010, 2010.

Lee, W. H. K., Shin, T. C., Kuo, K. W., Chen, K. C., and Wu, C. F.: CWB Free-Field Strong-Motion Data from the 21 September Chi-Chi, Taiwan, Earthquake, Bulletin of the Seismological Society of America, 91, 1370–1376, doi: 10.1785/0120000744, 2001.

Legrand, D., Barrientos, S., Bataille, K., Cembrano, J., and Pavez, A.: The fluid-driven tectonic swarm of Aysen Fjord, Chile (2007) associated with two earthquakes (Mw=6.1 and Mw=6.2) within the Liquine-Ofqui Fault Zone, Continental Shelf Research, 31, 154–161, doi: 10.1016/j.csr.2010.05.008, 2011.

Legros, F.: The mobility of long-runout landslides, Engineering Geology, 63, 301–331, doi: 10.1016/S0013-7952(01)00090-4, 2002.

Leonard, M.: Earthquake fault scaling: Self-consistent relating of rupture length, width, average displacement, and moment release, Bulletin of the Seismological Society of America, 100, 1971–1988, 2010.

Li, G., West, A. J., Densmore, A. L., Jin, Z., Parker, R. N., and Hilton, R. G.: Seismic mountain building: Landslides associated with the 2008 Wenchuan earthquake in the context of a generalized model for earthquake volume balance, Geochemistry, Geophysics, Geosystems, 15, 833–844, doi: 10.1002/2013GC005067, 2014.

Li, X., Zhou, Z., Yu, H., Wen, R., Lu, D., Huang, M., Zhou, Y., and Cu, J.: Strong motion observations and recordings from the great Wenchuan Earthquake, Earthquake Engineering and Engineering Vibration, 7, 235–246, doi: 10.1007/s11803-008-0892-x, 2008.

Liao, H.-W. and Lee, C.: Landslides triggered by Chi-Chi earthquake, in: Proceedings of the 21st Asian conference on remote sensing, vol. 1, pp. 383–388, 2000.

Lin, G.-W., Chen, H., Hovius, N., Horng, M.-J., Dadson, S., Meunier, P., and Lines, M.: Effects of earthquake and cyclone sequencing on landsliding and fluvial sediment transfer in a mountain catchment, Earth Surface Processes and Landforms, 33, 1354–1373, doi: 10.1002/esp.1716, 2008.

Lucas, A., Mangeney, A., and Ampuero, J. P.: Frictional velocity-weakening in landslides on Earth and on other planetary bodies, Nature Communications, 5, doi: 10.1038/ncomms4417, 2014.

Ma, S.: A physical model for widespread near-surface and fault zone damage induced by earthquakes, Geochemistry, Geophysics, Geosystems, 9, Q11 009, doi: 10.1029/2008GC002231, 2008.

Mackey, B. H. and Roering, J. J.: Sediment yield, spatial characteristics, and the long-term evolution of active earthflows determined from airborne LiDAR and historical aerial photographs, Eel River, California, Geological Society of America Bulletin, 123, 1560–1576, doi: 10.1130/B30306.1, 2011.

Mahdavifar, M. R., Solaymani, S., and Jafari, M. K.: Landslides triggered by the Avaj, Iran earthquake of June 22, 2002, Engineering Geology, 86, 166–182, doi: 10.1016/j.enggeo.2006.02.016, 2006.

Malamud, B. D., Turcotte, D. L., Guzzetti, F., and Reichenbach, P.: Landslide inventories and their statistical properties, Earth Surface Processes and Landforms, 29, 687–711, doi: 10.1002/esp.1064, 2004a.

Malamud, B. D., Turcotte, D. L., Guzzetti, F., and Reichenbach, P.: Landslides, earthquakes, and erosion, Earth and Planetary Science Letters, 229, 45–59, doi: 10.1016/j.epsl.2004.10.018, 2004b.

Maniatis, G., Kurfess, D., Hampel, A., and Heidbach, O.: Slip acceleration on normal faults due to erosion and sedimentation - Results from a new three-dimensional numerical model coupling tectonics and landscape evolution, Earth and Planetary Science Letters, 284, 570–582, doi: 10.1016/j.epsl.2009.05.024, 2009.

Marc, O. and Hovius, N.: Amalgamation in landslide maps: effects and automatic detection, Nat. Hazards Earth Syst. Sci., 15, 723–733, doi: 10.5194/nhess-15-723-2015, 2015.

Marc, O., Hovius, N., Meunier, P., Uchida, T., and Hayashi, S.: Transient changes of landslide rates after earthquakes, Geology, 43, 883–886, doi: 10.1130/G36961.1, 2015.

Marc, O., Hovius, N., and Meunier, P.: The mass balance of earthquakes and earthquake sequences, Geophysical Research Letters, 43, 2016GL068 333, doi: 10.1002/2016GL068333, 2016a.

Marc, O., Hovius, N., Meunier, P., Gorum, T., and Uchida, T.: A seismologically consistent expression for the total area and volume of earthquake-triggered landsliding, Journal of Geophysical Research: Earth Surface, 121, 640–663, doi: 10.1002/2015JF003732, 2016b.

Martha, T. R., Kerle, N., Jetten, V., van Westen, C. J., and Kumar, K. V.: Characterising spectral, spatial and morphometric properties of landslides for semi-automatic detection using object-oriented methods, Geomorphology, 116, 24–36, doi: 10.1016/j.geomorph.2009.10.004, 2010.

Mary, B. C., Maillot, B., and Leroy, Y. M.: Predicting orogenic wedge styles as a function of analogue erosion law and material softening, Geochemistry, Geophysics, Geosystems, pp. n/a–n/a, doi: 10.1002/ggge.20262, 2013.

Mathur, L.: Assam Earthquake of 15th August 1950, a short note on factual observations, in: A compilation of papers on the Assam earthquake of August, 15, 1950., vol. 1, pp. 56–60, The Central Board of Geophysical Publisher, National Geophysical Research Institute, Hyderabad, India, M.B Ramachandra Rao edn., 1953.

McColl, S. T., Davies, T. R. H., and McSaveney, M. J.: The effect of glaciation on the intensity of seismic ground motion, Earth Surface Processes and Landforms, 37, 1290–1301, doi: 10.1002/esp.3251, 2012.

McGinty, P., Darby, D., and Haines, J.: Earthquake triggering in the Hawke's Bay, New Zealand, region from 1931 to 1934 as inferred from elastic dislocation and static stress modeling, Journal of Geophysical Research: Solid Earth, 106, 26 593–26 604, doi: 10.1029/2000JB000031, 2001.

Meunier, P., Hovius, N., and Haines, A. J.: Regional patterns of earthquake-triggered landslides and their relation to ground motion, Geophysical Research Letters, 34, L20 408, doi: 10.1029/2007GL031337, 2007.

Meunier, P., Hovius, N., and Haines, J. A.: Topographic site effects and the location of earthquake induced landslides, Earth and Planetary Science Letters, 275, 221–232, doi: 10.1016/j.epsl.2008.07.020, 2008.

Meunier, P., Uchida, T., and Hovius, N.: Landslide patterns reveal the sources of large earthquakes, Earth and Planetary Science Letters, 363, 27–33, 2013.

Meyer-Christoffer, A., Becker, A., Finger, P., Rudolf, B., Schneider, U., and Ziese, M.: GPCC Climatology Version 2011 at 0.25Âř: monthly land-surface precipitation climatology for every month and the total year from rain-gauges built on GTS-based and historic data., doi: 10.5676/DWD_GPCC/CLIM_M_V2011_025, 2011.

Molnar, P.: Isostasy can't be ignored, Nature Geoscience, 5, 83–83, doi: 10.1038/ngeo1383, 2012.

Molnar, P. and Qidong, D.: Faulting associated with large earthquakes and the average rate of deformation in central and eastern Asia, Journal of Geophysical Research: Solid Earth, 89, 6203–6227, doi: 10.1029/JB089iB07p06203, 1984.

Molnar, P., Anderson, R. S., and Anderson, S. P.: Tectonics, fracturing of rock, and erosion, Journal of Geophysical Research: Earth Surface, 112, F03 014, doi: 10.1029/2005JF000433, 2007.

Mondini, A. C., Guzzetti, F., Reichenbach, P., Rossi, M., Cardinali, M., and Ardizzone, F.: Semi-automatic recognition and mapping of rainfall induced shallow landslides

using optical satellite images, Remote Sensing of Environment, 115, 1743–1757, doi: 10.1016/j.rse.2011.03.006, 2011.

Mondini, A. C., Marchesini, I., Rossi, M., Chang, K.-T., Pasquariello, G., and Guzzetti, F.: Bayesian framework for mapping and classifying shallow landslides exploiting remote sensing and topographic data, Geomorphology, 201, 135–147, doi: 10.1016/j.geomorph.2013.06.015, 2013.

Montgomery, D. R. and Brandon, M. T.: Topographic controls on erosion rates in tectonically active mountain ranges, Earth and Planetary Science Letters, 201, 481–489, doi: 10.1016/S0012-821X(02)00725-2, 2002.

Montgomery, D. R. and Dietrich, W. E.: A physically based model for the topographic control on shallow landsliding, Water Resources Research, 30, 1153–1171, doi: 10.1029/93WR02979, 1994.

Muir-Wood, R. and King, G. C. P.: Hydrological signatures of earthquake strain, Journal of Geophysical Research: Solid Earth, 98, 22 035–22 068, doi: 10.1029/93JB02219, 1993.

Nakata, N. and Snieder, R.: Estimating near-surface shear wave velocities in Japan by applying seismic interferometry to KiK-net data, Journal of Geophysical Research: Solid Earth, 117, B01 308, doi: 10.1029/2011JB008595, 2012.

Newmark, N.: Effects of earthquakes on dams and embankments, Geotechnique, 15, 139–159, 1965.

Obermann, A., Froment, B., Campillo, M., Larose, E., PlanÃĺs, T., Valette, B., Chen, J. H., and Liu, Q. Y.: Seismic noise correlations to image structural and mechanical changes associated with the Mw 7.9 2008 Wenchuan earthquake, Journal of Geophysical Research: Solid Earth, 119, 3155–3168, doi: 10.1002/2013JB010932, 2014.

Oglesby, D. D., Archuleta, R. J., and Nielsen, S. B.: The Three-Dimensional Dynamics of Dipping Faults, Bulletin of the Seismological Society of America, 90, 616–628, doi: 10.1785/0119990113, 2000.

Okada, Y.: Surface deformation due to shear and tensile faults in a half-space, Bulletin of the seismological society of America, 75, 1135–1154, 1985.

Ouimet, W. B.: Landslides associated with the May 12, 2008 Wenchuan earthquake: Implications for the erosion and tectonic evolution of the Longmen Shan, Tectonophysics, 491, 244–252, doi: 10.1016/j.tecto.2009.09.012, 2010.

Owen, L. A., Kamp, U., Khattak, G. A., Harp, E. L., Keefer, D. K., and Bauer, M. A.: Landslides triggered by the 8 October 2005 Kashmir earthquake, Geomorphology, 94, 1–9, doi: 10.1016/j.geomorph.2007.04.007, 2008.

Parise, M. and Jibson, R. W.: A seismic landslide susceptibility rating of geologic units based on analysis of characteristics of landslides triggered by the 17 January, 1994 Northridge, California earthquake, Engineering Geology, 58, 251–270, doi: 10.1016/S0013-7952(00)00038-7, 2000.

Parker, R., Densmore, A., Rosser, N., De Michele, M., Li, Y., Huang, R., Whadcoat, S., and Petley, D.: Mass wasting triggered by the 2008 Wenchuan earthquake is greater than orogenic growth, Nature Geoscience, 4, 449–452, 2011.

Parker, R. N., Hancox, G. T., Petley, D. N., Massey, C. I., Densmore, A. L., and Rosser, N. J.: Spatial distributions of earthquake-induced landslides and hillslope preconditioning in the northwest South Island, New Zealand, Earth Surface Dynamics, 3, 501–525, doi: 10.5194/esurf-3-501-2015, 2015.

Pathier, E., Fielding, E., Wright, T., Walker, R., Parsons, B., and Hensley, S.: Displacement field and slip distribution of the 2005 Kashmir earthquake from SAR imagery, Geophys. Res. Lett, 33, L20 310, doi: 10.1029/2006GL027193., 2006.

Pearce, A. J. and O'Loughlin, C. L.: Landsliding during a M 7.7 earthquake: Influence of geology and topography, Geology, 13, 855–858, doi: 10.1130/0091-7613(1985)13$<$855:LDAMEI$>$2.0.CO;2, 1985.

Pelletier, J. D., Malamud, B. D., Blodgett, T., and Turcotte, D. L.: Scale-invariance of soil moisture variability and its implications for the frequency-size distribution of landslides, Engineering Geology, 48, 255–268, doi: 10.1016/S0013-7952(97)00041-0, 1997.

Picozzi, M., Parolai, S., and Richwalski, S. M.: Joint inversion of H/V ratios and dispersion curves from seismic noise: Estimating the S-wave velocity of bedrock, Geophysical Research Letters, 32, L11 308, doi: 10.1029/2005GL022878, 2005.

Portenga, E. W. and Bierman, P. R.: Understanding Earth's eroding surface with 10Be, GSA Today, 21, 4–10, doi: 10.1130/G111A.1, 2011.

PWRI: Report for basic data collection about seismic landslides, Debris flow and Volcano Team technical report, 56p, in Japanese, Public Work Research Institute, Tsukuba, Japan, 2009.

Qi, S., Xu, Q., Lan, H., Zhang, B., and Liu, J.: Spatial distribution analysis of landslides triggered by 2008.5.12 Wenchuan Earthquake, China, Engineering Geology, 116, 95–108, doi: 10.1016/j.enggeo.2010.07.011, 2010.

Raymo, M. E. and Ruddiman, W. F.: Tectonic forcing of late Cenozoic climate, Nature, 359, 117–122, doi: 10.1038/359117a0, 1992.

Richard, P., Nicodemi, M., Delannay, R., RibiÃĺre, P., and Bideau, D.: Slow relaxation and compaction of granular systems, Nature Materials, 4, 121–128, doi: 10.1038/nmat1300, 2005.

Richter, T., Sens-Schönfelder, C., Kind, R., and Asch, G.: Comprehensive observation and modeling of earthquake and temperature-related seismic velocity changes in northern Chile with passive image interferometry, Journal of Geophysical Research: Solid Earth, 119, 4747–4765, doi: 10.1002/2013JB010695, 2014.

Rodriguez, C. E., Bommer, J. J., and Chandler, R. J.: Earthquake-induced landslides: 1980-1997, Soil Dynamics and Earthquake Engineering, 18, 325–346, doi: 10.1016/S0267-7261(99)00012-3, 1999.

Roering, J.: Tectonic geomorphology: Landslides limit mountain relief, Nature Geoscience, 5, 446–447, doi: 10.1038/ngeo1511, 2012.

Rousset, B., Barbot, S., Avouac, J.-P., and Hsu, Y.-J.: Postseismic deformation following the 1999 Chi-Chi earthquake, Taiwan: Implication for lower-crust rheology, Journal of Geophysical Research: Solid Earth, 117, n/a–n/a, doi: 10.1029/2012JB009571, 2012.

Rubinstein, J. L. and Beroza, G. C.: Evidence for Widespread Nonlinear Strong Ground Motion in the MW 6.9 Loma Prieta Earthquake, Bulletin of the Seismological Society of America, 94, 1595–1608, doi: 10.1785/012004009, 2004.

Rubinstein, J. L. and Beroza, G. C.: Depth constraints on nonlinear strong ground motion from the 2004 Parkfield earthquake, Geophysical Research Letters, 32, L14 313, doi: 10.1029/2005GL023189, 2005.

Ruiz, S., Kausel, E., Campos, J., Saragoni, G. R., and Madariaga, R.: Identification of High Frequency Pulses from Earthquake Asperities Along Chilean Subduction Zone Using Strong Motion, Pure and Applied Geophysics, 168, 125–139, doi: 10.1007/s00024-010-0117-x, 2011.

Ryder, I., Parsons, B., Wright, T. J., and Funning, G. J.: Post-seismic motion following the 1997 Manyi (Tibet) earthquake: InSAR observations and modelling, Geophysical Journal International, 169, 1009–1027, doi: 10.1111/j.1365-246X.2006.03312.x, 2007.

Saba, S. B., van der Meijde, M., and van der Werff, H.: Spatiotemporal landslide detection for the 2005 Kashmir earthquake region, Geomorphology, 124, 17–25, doi: 10.1016/j.geomorph.2010.07.026, 2010.

Sawazaki, K. and Snieder, R.: Time-lapse changes of P- and S-wave velocities and shear wave splitting in the first year after the 2011 Tohoku earthquake, Japan: shallow subsurface, Geophysical Journal International, 193, 238–251, doi: 10.1093/gji/ggs080, 2013.

Schmidt, K. M. and Montgomery, D. R.: Limits to Relief, Science, 270, 617–620, doi: 10.1126/science.270.5236.617, 1995.

Schmidt, K. M. and Montgomery, D. R.: Rock mass strength assessment for bedrock landsliding, Environmental & Engineering Geoscience, II, 325–338, doi: 10.2113/gseegeosci.II.3.325, 1996.

Scholz, C. H.: Scaling laws for large earthquakes: Consequences for physical models, Bulletin of the Seismological Society of America, 72, 1–14, 1982.

Schuster, R. L., NietoThomas, A. S., D O'Rourke, T., Crespo, E., and Plaza-Nieto, G.: Mass wasting triggered by the 5 March 1987 Ecuador earthquakes, Engineering geology, 42, 1–23, 1996.

Selby, M. J.: Hillslope materials and processes., Oxford University Press, 1st edn., 1982.

Sens-Schönfelder, C. and Wegler, U.: Passive image interferometry for monitoring crustal changes with ambient seismic noise, Comptes Rendus Geoscience, 343, 639–651, doi: 10.1016/j.crte.2011.02.005, 2011.

Shin, T.-C. and Teng, T.-l.: An Overview of the 1999 Chi-Chi, Taiwan, Earthquake, Bulletin of the Seismological Society of America, 91, 895–913, doi: 10.1785/0120000738, 2001.

Shou, K.-J. and Wang, C.-F.: Analysis of the Chiufengershan landslide triggered by the 1999 Chi-Chi earthquake in Taiwan, Engineering Geology, 68, 237–250, doi: 10.1016/S0013-7952(02)00230-2, 2003.

Shroder, J. F.: Slope failure and denudation in the western Himalaya, Geomorphology, 26, 81–105, doi: 10.1016/S0169-555X(98)00052-X, 1998.

Sidle, R. C., Ziegler, A. D., Negishi, J. N., Nik, A. R., Siew, R., and Turkelboom, F.: Erosion processes in steep terrain-Truths, myths, and uncertainties related to forest management in Southeast Asia, Forest Ecology and Management, 224, 199–225, doi: 10.1016/j.foreco.2005.12.019, 2006.

Sleep, N. H.: Depth of Rock Damage from Strong Seismic Ground Motions near the 2004 Parkfield Mainshock, Bulletin of the Seismological Society of America, 99, 3067–3076, doi: 10.1785/0120090065, 2009.

Sleep, N. H.: Strong seismic shaking of randomly prestressed brittle rocks, rock damage, and nonlinear attenuation, Geochemistry, Geophysics, Geosystems, 11, Q10 002, doi: 10.1029/2010GC003229, 2010.

Sleep, N. H.: Deep-seated downslope slip during strong seismic shaking, Geochemistry, Geophysics, Geosystems, 12, Q12 001, doi: 10.1029/2011GC003838, 2011a.

Sleep, N. H.: Seismically damaged regolith as self-organized fragile geological feature, Geochemistry, Geophysics, Geosystems, 12, Q12 013, doi: 10.1029/2011GC003837, 2011b.

Stark, C. P. and Guzzetti, F.: Landslide rupture and the probability distribution of mobilized debris volumes, Journal of Geophysical Research: Earth Surface, 114, F00A02, doi: 10.1029/2008JF001008, 2009.

Stark, C. P. and Hovius, N.: The characterization of landslide size distributions, Geophysical Research Letters, 28, 1091–1094, doi: 10.1029/2000GL008527, 2001.

Stark, C. P., Barbour, J. R., Hayakawa, Y. S., Hattanji, T., Hovius, N., Chen, H., Lin, C.-W., Horng, M.-J., Xu, K.-Q., and Fukahata, Y.: The Climatic Signature of Incised River Meanders, Science, 327, 1497–1501, doi: 10.1126/science.1184406, 2010.

Staron, L. and Lajeunesse, E.: Understanding how volume affects the mobility of dry debris flows, Geophysical Research Letters, 36, L12 402, doi: 10.1029/2009GL038229, 2009.

Steer, P., Simoes, M., Cattin, R., and Shyu, J. B. H.: Erosion influences the seismicity of active thrust faults, Nature Communications, 5, doi: 10.1038/ncomms6564, 2014.

Stein, R. S. and Ekstrom, G.: Seismicity and geometry of a 110-km-long blind thrust fault 2. Synthesis of the 1982-1985 California Earthquake Sequence, Journal of Geophysical Research: Solid Earth (1978-2012), 97, 4865–4883, 1992.

Stevens, C., McCaffrey, R., Silver, E., Sombo, Z., English, P., and Van der Kevie, J.: Mid-crustal detachment and ramp faulting in the Markham Valley, Papua New Guinea, Geology, 26, 847–850, 1998.

Storchak, D. A., Giacomo, D. D., Bondar, I., Engdahl, E. R., Harris, J., Lee, W. H. K., Villasenor, A., and Bormann, P.: Public Release of the ISC-GEM Global Instrumental Earthquake Catalogue (1900-2009), Seismological Research Letters, 84, 810–815, doi: 10.1785/0220130034, 2013.

Stumpf, A., Lachiche, N., Malet, J.-P., Kerle, N., and Puissant, A.: Active Learning in the Spatial Domain for Remote Sensing Image Classification, IEEE Transactions on Geoscience and Remote Sensing, 52, 2492–2507, doi: 10.1109/TGRS.2013.2262052, 2014.

Suarez, G., Pardo, M., Dominguez, J., Ponce, L., Montero, W., Boschini, I., and Rojas, W.: The LimÃşn, Costa Rica earthquake of April 22, 1991: Back arc thrusting and collisional tectonics in a subduction environment, Tectonics, 14, 518–530, doi: 10.1029/94TC02546, 1995.

Sun, J., Shen, Z.-K., Burgmann, R., Wang, M., Chen, L., and Xu, X.: A three-step maximum a posteriori probability method for InSAR data inversion of coseismic rupture with application to the 14 April 2010 Mw 6.9 Yushu, China, earthquake, Journal of Geophysical Research: Solid Earth, 118, 4599–4627, doi: 10.1002/jgrb.50244, 2013.

Suzuki, W., Aoi, S., and Sekiguchi, H.: Rupture process of the 2008 Iwate-Miyagi Nairiku, Japan, earthquake derived from near-source strong-motion records, Bulletin of the Seismological Society of America, 100, 256–266, 2010.

Takagi, R. and Okada, T.: Temporal change in shear velocity and polarization anisotropy related to the 2011 M9.0 Tohoku-Oki earthquake examined using KiK-net vertical array data, Geophysical Research Letters, 39, L09 310, doi: 10.1029/2012GL051342, 2012.

Takagi, R., Okada, T., Nakahara, H., Umino, N., and Hasegawa, A.: Coseismic velocity change in and around the focal region of the 2008 Iwate-Miyagi Nairiku earthquake, Journal of Geophysical Research: Solid Earth, 117, B06 315, doi: 10.1029/2012JB009252, 2012.

Tan, O. and Taymaz, T.: Active tectonics of the Caucasus: Earthquake source mechanisms and rupture histories obtained from inversion of teleseismic body waveforms, in: Postcollisional Tectonics and Magmatism in the Mediterranean Region and Asia, edited by Dilek, Y. and Pavlides, S., pp. 531–578, Geological Society of America, 2006.

Tang, C., Ma, G., Chang, M., Li, W., Zhang, D., Jia, T., and Zhou, Z.: Landslides triggered by the 20 April 2013 Lushan earthquake, Sichuan Province, China, Engineering Geology, 187, 45–55, doi: 10.1016/j.enggeo.2014.12.004, 2015.

Tatard, L. and Grasso, J. R.: Controls of earthquake faulting style on near field landslide triggering: The role of coseismic slip, Journal of Geophysical Research: Solid Earth, 118, 2953–2964, doi: 10.1002/jgrb.50215, 2013.

ten Brink, U. S., Geist, E. L., and Andrews, B. D.: Size distribution of submarine landslides and its implication to tsunami hazard in Puerto Rico, Geophysical Research Letters, 33, L11 307, doi: 10.1029/2006GL026125, 2006.

TenCate, J. A., Smith, E., and Guyer, R. A.: Universal Slow Dynamics in Granular Solids, Physical Review Letters, 85, 1020–1023, doi: 10.1103/PhysRevLett.85.1020, 2000.

Terzaghi, K.: Mechanism of landslides, in: Application of Geology to Engineering Practice (Berkey Volume), edited by Paige, S., pp. 83–123, Geological Society of America, New York, NY, 1950.

Tremblay, N., Larose, E., and Rossetto, V.: Probing slow dynamics of consolidated granular multicomposite materials by diffuse acoustic wave spectroscopy, The Journal of the Acoustical Society of America, 127, 1239–1243, doi: 10.1121/1.3294553, 2010.

Tutton, M. and Browne, T.: A Review of Damage Caused by the 1993 Finisterre Range Earthquakes, Papua New Guinea, in: Proceedings of the PNG Geology, Exploration and Mining Conference 1994, Lae, Papua New Guinea: Carlton, Australia, Australian Institute of Mining and Metallurgy, edited by Rogerson, R., vol. 1, pp. 33–41, 1994.

Vittoz, P., Stewart, G. H., and Duncan, R. P.: Earthquake impacts in old-growth Nothofagus forests in New Zealand, Journal of Vegetation Science, 12, 417–426, doi: 10.2307/3236856, 2001.

Voight, B. and Sousa, J.: Lessons from Ontake-san: A comparative analysis of debris avalanche dynamics, Engineering Geology, 38, 261–297, doi: 10.1016/0013-7952(94)90042-6, 1994.

Wald, D., Helmberger, D., and Heaton, T.: Rupture model of the 1989 Loma Prieta earthquake from the inversion of strong-motion and broadband teleseismic data, Bulletin of the Seismological Society of America, 81, 1540–1572, 1991.

Wald, D., Heaton, T., and Hudnut, K.: The slip history of the 1994 Northridge, California, earthquake determined from strong-motion, teleseismic, GPS, and leveling data, Bulletin of the Seismological Society of America, 86, S49–S70, 1996.

Walder, J. and Hallet, B.: A theoretical model of the fracture of rock during freezing, Geological Society of America Bulletin, 96, 336–346, doi: 10.1130/0016-7606(1985)96$<$336:ATMOTF$>$2.0.CO;2, 1985.

Wallace, T. C. and Lay, T.: Chapter 3 - Body Waves and Ray Theory, in: International Geophysics, vol. 58 of *Modern Global Seismology*, pp. 70–115, Academic Press, 1995.

Wang, C.-y., Wang, C.-H., and Manga, M.: Coseismic release of water from mountains: Evidence from the 1999 (Mw = 7.5) Chi-Chi, Taiwan, earthquake, Geology, 32, 769, doi: 10.1130/G20753.1, 2004.

Wang, D. and Mori, J.: The 2010 Qinghai, China, Earthquake: A Moderate Earthquake with Supershear Rupture, Bulletin of the Seismological Society of America, 102, 301–308, doi: 10.1785/0120110034, 2012.

Wang, J., Jin, Z., Hilton, R. G., Zhang, F., Densmore, A. L., Li, G., and West, A. J.: Controls on fluvial evacuation of sediment from earthquake-triggered landslides, Geology, 43, 115–118, doi: 10.1130/G36157.1, 2015.

Wartman, J., Dunham, L., Tiwari, B., and Pradel, D.: Landslides in Eastern Honshu induced by the 2011 Tohoku Earthquake, Bulletin of the Seismological Society of America, 103, 1503–1521, doi: 10.1785/0120120128, 2013.

Wei, S., Fielding, E., Leprince, S., Sladen, A., Avouac, J.-P., Helmberger, D., Hauksson, E., Chu, R., Simons, M., Hudnut, K., Herring, T., and Briggs, R.: Superficial simplicity of the 2010 El Mayor-Cucapah earthquake of Baja California in Mexico, Nature Geoscience, 4, 615–618, doi: 10.1038/ngeo1213, 2011.

Wen, K.-L.: Non-linear soil response in ground motions, Earthquake Engineering & Structural Dynamics, 23, 599–608, doi: 10.1002/eqe.4290230603, 1994.

Weston, J., Ferreira, A., and Funning, G.: Systematic comparisons of earthquake source models determined using InSAR and seismic data, Tectonophysics, 2012.

Willett, S. D.: Orogeny and orography: The effects of erosion on the structure of mountain belts, Journal of Geophysical Research: Solid Earth, 104, 28 957–28 981, doi: 10.1029/1999JB900248, 1999.

Willett, S. D., Hovius, N., Brandon, M. T., and Fisher, D. M.: Introduction, Geological Society of America Special Papers, 398, vii–xi, doi: 10.1130/2006.2398(00), 2006.

Wolinsky, M. A. and Pratson, L. F.: Constraints on landscape evolution from slope histograms, Geology, 33, 477–480, doi: 10.1130/G21296.1, 2005.

Wu, W. and Sidle, R. C.: A Distributed Slope Stability Model for Steep Forested Basins, Water Resources Research, 31, 2097–2110, doi: 10.1029/95WR01136, 1995.

Xu, C., Xu, X., and Yu, G.: Landslides triggered by slipping-fault-generated earthquake on a plateau: an example of the 14 April 2010, Ms 7.1, Yushu, China earthquake, Landslides, 10, 421–431, doi: 10.1007/s10346-012-0340-x, 2013.

Xu, C., Xu, X., Pourghasemi, H. R., Pradhan, B., and Iqbal, J.: Volume, gravitational potential energy reduction, and regional centroid position change in the wake of landslides triggered by the 14 April 2010 Yushu earthquake of China, Arabian Journal of Geosciences, 7, 2129–2138, doi: 10.1007/s12517-013-1020-4, 2014a.

Xu, C., Xu, X., Shyu, J. B. H., Zheng, W., and Min, W.: Landslides triggered by the 22 July 2013 Minxian-Zhangxian, China, Mw 5.9 earthquake: Inventory compiling and spatial distribution analysis, Journal of Asian Earth Sciences, 92, 125–142, doi: 10.1016/j.jseaes.2014.06.014, 2014b.

Xu, C., Xu, X., Yao, X., and Dai, F.: Three (nearly) complete inventories of landslides triggered by the May 12, 2008 Wenchuan Mw 7.9 earthquake of China and their spatial distribution statistical analysis, Landslides, 11, 441–461, doi: 10.1007/s10346-013-0404-6, 2014c.

Yagi, H., Yamasaki, T., and Atsumi, M.: GIS analysis on geomorphological features and soil mechanical implication of landslides caused by 2004 Niigata Chuetsu earthquake, Journal of the Japan Landslide Society, 43, 294–306, 2007.

Yagi, H., Sato, G., Higaki, D., Yamamoto, M., and Yamasaki, T.: Distribution and characteristics of landslides induced by the Iwate-Miyagi Nairiku Earthquake in 2008 in Tohoku District, Northeast Japan, Landslides, 6, 335–344, 2009.

Yanites, B., Tucker, G., Mueller, K., and Chen, Y.: How rivers react to large earthquakes: Evidence from central Taiwan, Geology, 38, 639–642, 2010.

Yin, Y., Wang, F., and Sun, P.: Landslide hazards triggered by the 2008 Wenchuan earthquake, Sichuan, China, Landslides, 6, 139–152, doi: 10.1007/s10346-009-0148-5, 2009.

Yoshida, S. and Koketsu, K.: Simultaneous inversion of waveform and geodetic data for the rupture process of the 1984 Naganoken-Seibu, Japan, earthquake, Geophysical Journal International, 103, 355–362, 1990.

Yuan, R.-M., Deng, Q.-H., Cunningham, D., Xu, C., Xu, X.-W., and Chang, C.-P.: Density Distribution of Landslides Triggered by the 2008 Wenchuan Earthquake and their Relationships to Peak Ground Acceleration, Bulletin of the Seismological Society of America, 103, 2344–2355, doi: 10.1785/0120110233, 2013.

Zeng, Y. and Chen, C.-H.: Fault Rupture Process of the 20 September 1999 Chi-Chi, Taiwan, Earthquake, Bulletin of the Seismological Society of America, 91, 1088–1098, doi: 10.1785/0120000743, 2001.

Zhang, Y., Wang, R., Chen, Y.-T., Xu, L., Du, F., Jin, M., Tu, H., and Dahm, T.: Kinematic Rupture Model and Hypocenter Relocation of the 2013 Mw 6.6 Lushan Earthquake Constrained by Strong-Motion and Teleseismic Data, Seismological Research Letters, 85, 15–22, doi: 10.1785/0220130126, 2014.